



City Research Online

City, University of London Institutional Repository

Citation: Ramirez, Ciro Moreno (2015). Dynamic Analysis of Alternative Suspension Systems for Sport Motorcycles. (Unpublished Doctoral thesis, City University London)

This is the accepted version of the paper.

This version of the publication may differ from the final published version.

Permanent repository link: <https://openaccess.city.ac.uk/id/eprint/14574/>

Link to published version:

Copyright: City Research Online aims to make research outputs of City, University of London available to a wider audience. Copyright and Moral Rights remain with the author(s) and/or copyright holders. URLs from City Research Online may be freely distributed and linked to.

Reuse: Copies of full items can be used for personal research or study, educational, or not-for-profit purposes without prior permission or charge. Provided that the authors, title and full bibliographic details are credited, a hyperlink and/or URL is given for the original metadata page and the content is not changed in any way.

Dynamic Analysis of Alternative Suspension Systems for Sport Motorcycles

Ciro Moreno Ramírez

Thesis submitted for the degree of Doctor of Philosophy



CITY UNIVERSITY
LONDON

School of Mathematics, Computer Science and Engineering
Department of Mechanical Engineering and Aeronautics

June 2015

Contents

Contents	iii
List of Figures	vii
List of Tables	xv
Acknowledgements	xvii
Abstract	xix
1 Introduction	1
1.1 Preliminaries	1
1.2 Summary of objectives	5
1.3 Structure of the thesis	5
2 Literature Review	7
3 Description of the Motorcycle Model	21
3.1 Baseline model	22
3.1.1 Parametric description	22
3.1.2 Tyres modelling	25
3.1.3 Monoshock rear suspension	25
3.1.4 Forward speed and roll angle controllers	26
3.1.5 Braking system	27
3.1.6 Road input	27
3.2 Additional features	28
3.2.1 Modifications on the braking system	28
3.2.2 Modifications on the road input	29

3.2.3	Two dimensional step bump input	29
3.3	Reduced models	32
3.4	Simulations tools	35
3.4.1	VehicleSim	35
3.4.2	State space description	36
3.5	Dynamic behaviour of the nominal model	39
3.6	Conclusions	44
4	Double Wishbone Suspension Systems	47
4.1	Kinematics	49
4.2	Suspension modelling	62
4.2.1	CAD modelling and FEA analysis	62
4.2.2	Mathematical modelling	68
4.3	Dynamic analysis	72
4.3.1	In-plane dynamic response	73
4.3.2	Stability analysis	79
4.4	Conclusions	88
5	Interconnected Suspensions System: Linear Description	93
5.1	Interconnected suspension prototypes	94
5.1.1	Raer Design	94
5.1.2	The Toptrail Project - Citroën 2CV	98
5.1.3	Creuat Suspension Technology	102
5.2	Reduced model with two degrees of freedom	104
5.2.1	Independent suspensions system	104
5.2.2	Interconnected suspension system	111
5.3	Reduced model with four degrees of freedom	118
5.4	Conclusions	127
6	Interconnected Suspensions System: Performance	129
6.1	Modelling of the interconnected suspensions system	131
6.2	Road bump input response	132
6.2.1	Efficiency mapping	134
6.2.2	Optimization of the stiffness and damping coefficients	137

6.3	Frequency response	142
6.3.1	Road profiles generation	143
6.3.2	Simulations and signal processing	145
6.4	Conclusions	158
7	Interconnected Suspensions System: Stability Analysis	161
7.1	Straight running condition	167
7.1.1	Variation of interconnection stiffness coefficient	168
7.1.2	Variation of interconnection damping coefficient	170
7.2	Small roll angle	178
7.2.1	Variation of interconnection stiffness coefficient	179
7.2.2	Variation of interconnection damping coefficient	182
7.3	Medium roll angle	184
7.3.1	Variation of interconnection stiffness coefficient	184
7.3.2	Variation of interconnection damping coefficient	185
7.4	High roll angle	189
7.4.1	Variation of interconnection stiffness coefficient	189
7.4.2	Variation of interconnection damping coefficient	192
7.5	Optimal interconnection coefficients	192
7.6	Conclusions	195
8	Conclusions and Further Work	197
A	Motorcycle Reduced Model	205
B	New Basis for the State Space	211
C	Maximum Loads on the Front End	219
	Bibliography	223

List of Figures

3.1	GSX-R1000 motorcycle.	22
3.2	GSX-R1000 geometrical description.	23
3.3	GSX-R1000 parental structure.	24
3.4	Monoshock rear suspension mechanism.	26
3.5	Motorcycle front wheel passing through a step bump in three different stages.	30
3.6	Motorcycle's reduced model with four degrees of freedom.	33
3.7	Motorcycle's reduced model with two degrees of freedom.	34
3.8	VS Browser graphical user interface.	36
3.9	Auxiliary frames created by VS Lisp with each rotation of a body.	38
3.10	Root locus for the nominal motorcycle model showing the main normal modes.	40
3.11	Normal modes' components for the nominal motorcycle model under straight running conditions.	41
4.1	3D models for a telescopic fork, a girder and a Hossack suspension systems.	48
4.2	Main motorcycle's handling geometric parameters.	49
4.3	Telescopic fork's handling geometric parameters variation with the suspension travel.	50
4.4	Motorcycle's geometry variation with the vertical suspension travel for the telescopic fork, the girder and the Hossack suspension systems.	51
4.5	Design parameters on the four-bar linkage suspension systems.	52
4.6	Effects of varying the design parameters on the wheelbase, the head angle and the normal trail for the girder suspension system.	54

4.7	Effects of varying the design parameters on the wheelbase, the head angle and the normal trail for the Hossack suspension system.	55
4.8	Girder suspension system's kinematic behaviour with <i>prl</i> configuration.	58
4.9	Hossack suspension system's kinematic behaviour with <i>prl</i> configuration.	58
4.10	Girder suspension system's kinematic behaviour with <i>tft</i> configuration.	59
4.11	Hossack suspension system's kinematic behaviour with <i>tft</i> configuration.	59
4.12	Girder suspension system's kinematic behaviour with <i>cnt</i> configuration.	60
4.13	Hossack suspension system's kinematic behaviour with <i>cnt</i> configuration.	61
4.14	Girder suspension system CAD models.	63
4.15	Hossack suspension system CAD models.	64
4.16	FEA results of the girder model with parts' masses approximated to those of the telescopic fork, showing the factor of safety map.	65
4.17	FEA results of the Hossack model with parts masses approximated to those of the telescopic fork, showing the factor of safety map.	65
4.18	FEA results of the girder model with reduced masses showing the factor of safety map.	66
4.19	FEA results of the Hossack model with reduced masses showing the factor of safety map.	66
4.20	Girder suspension system's parental structure.	69
4.21	Hossack suspension system's parental structure.	70
4.22	Motorcycle front end response after a 50 mm road bump input for the girder and Hossack suspension systems with a parallelogram configuration (<i>prl</i>).	73
4.23	Motorcycle front end response after a 50 mm road bump input for the girder and Hossack suspension systems with a telescopic fork's trajectory configuration (<i>tft</i>).	74
4.24	Motorcycle front end response after a 50 mm road bump input for the girder and Hossack suspension systems with a constant normal trail configuration (<i>cnt</i>).	75

4.25	Vertical suspension travel (<i>v.s.t.</i>) and normal trail (t_n) for the girder and Hossack systems with a parallelogram configuration (<i>prl</i>).	76
4.26	Vertical suspension travel (<i>v.s.t.</i>) and normal trail (t_n) for the girder and Hossack systems with a telescopic fork's trajectory configuration (<i>tft</i>).	77
4.27	Vertical suspension travel (<i>v.s.t.</i>) and normal trail (t_n) for the girder and Hossack systems with a constant normal trail configuration (<i>cnt</i>).	78
4.28	Root loci of the nominal motorcycle model fitted with a telescopic fork suspension.	80
4.29	Root loci of the girder suspension for the telescopic fork's trajectory (<i>tft</i>) and the constant normal trail (<i>cnt</i>) configurations.	81
4.30	Root loci of the Hossack suspension system with parallelogram (<i>prl</i>) and constant normal trail (<i>cnt</i>) configurations.	82
4.31	Root loci for girder suspension lighter model with a constant normal trail (<i>cnt</i>) configuration for different values of the twist moment coefficients.	83
4.32	Root loci for Hossack suspension lighter model with a constant normal trail (<i>cnt</i>) configuration for different values of the twist moment coefficients.	84
4.33	Root loci for girder suspension lighter model with a constant normal trail (<i>cnt</i>) configuration for different values of the steering damper coefficient.	85
4.34	Root loci for Hossack suspension lighter model with a constant normal trail (<i>cnt</i>) configuration for different values of the steering damper coefficient.	86
4.35	Root loci for the girder and Hossack suspension systems for the lighter models with the constant normal trail configurations set with steering damper coefficient values that guarantee wobble stability	87
5.1	Raer Design interconnected suspension system bicycle prototype.	94
5.2	Diagram showing the interconnection layout and relevant parameters for the Raer Design system.	95
5.3	Toptrail interconnected suspension system bicycle prototype.	99

5.4	Citroën 2CV chassis with interconnected suspension system	100
5.5	Diagram showing the interconnection layout and relevant parameters for the Toptrail system.	100
5.6	CREUAT interconnected suspension system.	103
5.7	Two degrees of freedom motorcycle model with independent suspen- sions system.	105
5.8	Two degrees of freedom motorcycle model with interconnected sus- pension system.	112
5.9	Two degrees of freedom motorcycle model with symmetrical weight distribution and interconnected suspension system.	115
5.10	Four degrees of freedom motorcycle model.	119
5.11	Root locus of the two degrees of freedom motorcycle model overlapped with that of the four degrees of freedom motorcycle model before the optimization process.	125
5.12	Root locus of the two degrees of freedom motorcycle model overlapped with that of the four degrees of freedom motorcycle model after the optimization process.	127
6.1	Simulink model with a VehicleSim Block to call a simulation that will be run from VS Browser.	130
6.2	Sketches of the interconnected suspension systems.	131
6.3	Precision and comfort variables responses at 80 m/s with intercon- nection coefficients $k_s = 0$ N and $c_s = -548$ Ns.	133
6.4	Efficiency maps of comfort and precision variables for different values of c_s with $k_s = 0$ N for a 0.05m step input at forward speeds starting at 10 m/s up to 80 m/s.	134
6.5	Efficiency maps of comfort and precision variables for different values of k_s with $c_s = 0$ Ns for a 0.05 m step input at forward speeds starting at 10 m/s up to 80 m/s.	135
6.6	Efficiency maps of comfort and precision variables for different values of c_s and k_s for a 0.05 m step input at a constant speed of 50 m/s. . .	137
6.7	Efficiencies of the precision and comfort variables obtained for the four interconnection set-ups.	140

6.8	Wave signal used to build the different roads profiles.	143
6.9	Wave signal, sampling points and frequency variation of road profile function.	145
6.10	Example of the inflection points algorithm application to the front wheel frequency response.	147
6.11	Frequency responses of the precision and comfort variables for the different interconnection set-ups at 40 m/s.	148
6.12	Frequency response maps of the precision and comfort variables for all the forward speeds for the nominal independent suspensions model ($k_s = 0$ N and $c_s = 0$ Ns).	149
6.13	Root locus for the motorcycle model with independent suspensions at 0° roll angle.	150
6.14	Wheelbase filtering for pitch and bounce motions due to the road profile wavelength.	150
6.15	Example of the bounce and pitch normal modes's components.	151
6.16	Frequency response maps of the precision and comfort variables for all the forward speeds with interconnection coefficients $k_s = 0$ N and $c_s = -548$ Ns.	153
6.17	Frequency response maps of the precision and comfort variables for all the forward speeds with interconnection coefficients $k_s = 0$ N and c_s taking negative optimal values depending on the forward speed.	154
6.18	Maximum magnitudes compared to the inverse of the interconnected suspension damping coefficient of set-up b) (negative speed variable damping coefficient).	155
6.19	Frequency response maps of the precision and comfort variables for all the forward speeds with interconnection coefficients $k_s = 0$ N and c_s taking positive and negative optimal values.	156
6.20	Frequency response maps of the precision and comfort variables for all the forward speeds with interconnection coefficients k_s and c_s taking positive and negative optimal values.	157
7.1	Root loci of the motorcycle nominal suspension system for various roll angles.	162

7.2	Out-of-plane normal modes' components for the motorcycle nominal configuration at 0° roll angle.	164
7.3	In-plane normal modes' components for the motorcycle nominal configuration at 0° roll angle.	165
7.4	Root loci for stiffness and damping coefficients variations at 0° roll angle.	167
7.5	In-plane normal modes' components for the maximum and minimum values of stiffness interconnection coefficient at 0° roll angle.	169
7.6	Root loci for the interconnection damping coefficient variation at 0° roll angle divided into positive and negative values.	171
7.7	Front hop mode's components for intermediate values of the interconnection damping coefficient and stiffness coefficient $k_s = 0$ N at 0° roll angle.	172
7.8	Bounce mode's components for intermediate values of the interconnection damping coefficient and stiffness coefficient $k_s = 0$ N at 0° roll angle.	173
7.9	Pitch mode's components for intermediate values of the interconnection damping coefficient and stiffness coefficient $k_s = 0$ N at 0° roll angle.	174
7.10	In-plane normal modes' components for the maximum and minimum values of damping interconnection coefficient for at 0° roll angle.	176
7.11	Root loci for stiffness and damping coefficients variations at 15° roll angle.	179
7.12	Components of normal modes affected by the interconnection coefficients at a roll angle of 15° for the nominal configuration.	180
7.13	Bounce and rider shake modes' components for the maximum and minimum values of the stiffness interconnection coefficient for at 15° roll angle.	181
7.14	In-plane normal modes' components for the maximum and minimum values of the damping interconnection coefficient for at 15° roll angle.	183
7.15	Root loci for stiffness and damping coefficients variations at 30° roll angle.	185

7.16	Components of the normal modes affected by the interconnection coefficients at a roll angle of 30° for the nominal configuration.	186
7.17	Bounce and rider shake modes' components for the maximum and minimum values of the stiffness interconnection coefficient at 30° roll angle.	187
7.18	In-plane normal modes' components for the maximum and minimum values of the damping interconnection coefficient at 30° roll angle. . .	188
7.19	Root loci for stiffness and damping coefficients variations at 45° roll angle.	190
7.20	Components of the normal modes affected by the interconnection coefficients at a roll angle of 45° for the nominal configuration.	190
7.21	In-plane normal modes' components for the maximum and minimum values of the damping interconnection coefficient at 45° roll angle. . .	191
7.22	Root loci for the four optimal interconnected suspension system configurations proposed in Chapter 6.	193
A.1	Motorcycle's reduced model with four degrees of freedom.	205
A.2	Equivalent spring force of the reduced model rear suspension and linear approximation	207
A.3	Equivalent damping coefficient of the reduced model rear suspension and linear approximation.	209
B.1	Auxiliary frames created by VS Lisp with each rotation of a body. . .	211
C.1	Forces appearing under straight line front wheel braking.	220
C.2	Maximum lateral load calculated as the projection of the maximum longitudinal load on the front wheel axis for maximum lean and steering angles.	221

List of Tables

3.1	GSX-R1000 geometrical model main points.	23
3.2	Input values table for the two dimensional step bump description. . .	31
3.3	GSX-R1000 four degrees of freedom reduced model dynamical parameters.	33
3.4	GSX-R1000 two degrees of freedom reduced model's dynamical parameters.	34
3.5	Degrees of freedom of the GSX-R1000 multi-body system.	37
4.1	Design parameters values obtained for the three different girder suspension systems configurations.	57
4.2	Design parameters values obtained for the three different Hossack suspension systems configurations.	57
4.3	Masses of the different suspension systems models bodies	67
5.1	Stiffness and damping coefficients values for the front, rear and interconnection spring-damper units obtained with the two degrees of freedom model.	125
5.2	Stiffness and damping coefficients values for the front, rear and interconnection spring damper units returned by the optimization process.	126
6.1	Target function's weights for the optimization of the interconnection set-up a).	139
6.2	Optimal coefficient values found for the four different interconnection set-ups.	141
7.1	Eigenvectors components of the GSX-R1000 multi-body system considered for the mode motion identification.	163

Acknowledgements

I want to express my sincere appreciation and gratitude to my supervisor Dr. María Tomás-Rodríguez, for her support and guidance throughout this thesis, for inspiring me to reach my highest limits and for allowing me a wide independence on the development of my research within an excellent work atmosphere.

I also would like to thank Dr. Simos Evangelou for the long hours he kindly spent with me discussing the Duolever suspension dynamics and helping me to understand the subtle details of VehicleSim programming. Furthermore, his work has been an important inspiration for me during the development of this research.

I am also very grateful to Prof. Fernando Viadero Rueda, Dr. Alfonso Fernández del Rincón, Dr. Pablo García Fernández, Dr. Ana M. de Juan de Luna and all the other staff of the Department of Structural and Mechanical Engineering of the Universidad de Cantabria for giving me the opportunity to carry out an enriching and stimulating collaboration in a friendly and warm environment during my stay there.

This thesis would not have been possible without my family. I wish to express my deepest gratitude to them: To my parents, for providing a home with a commendable environment for inquisitiveness and learning, being always an example of the highest human values. And to my brother, for being invariably prone to help me with any of the mathematical questions I brought to him, but, above all, for sharing with me his way of looking at life, thoughtful and plenty of goodness and generosity.

Finally, my most sincere love and gratefulness go to Cristina, for her unconditional support even in the long distance and despite all the sacrifices this implied to her. Her endless optimism and the trust she always put in me have been a very powerful encouragement during all these years.

Abstract

In this thesis, VehicleSim multi-body software is used to extend and modify an existing motorcycle model by including different non-conventional suspension systems. Girder and Hossack double wishbones front suspension systems are designed, implemented and tested. Using a synthesis of mechanism methodology, they are designed with different kinematic configurations that allow different behaviours of the motorcycle front end. By means of CAD tools and finite element analysis, realistic three dimensional models of the suspension systems designs are developed. The dynamical properties of the mechanical assemblies are obtained from the CAD models and used to build a realistic mathematical model of a sport motorcycle fitted with these alternative suspension systems. Dynamical and stability analyses of the alternative front suspension systems are performed. For the different kinematic configurations, anti-dive properties and variation of the motorcycle's handling geometric parameters are studied by non-linear dynamical simulations. Stability analyses are performed by means of the motorcycle linear models eigenvalues.

Passive interconnection of front and rear suspension systems of a sport motorcycle is also investigated. The effects of an interconnected suspensions system on the motorcycle in-plane motions are studied by means of reduced order linear models. The baseline model is modified to include passive interconnection forces between the front and rear suspension systems. The possible improvement introduced by an interconnected suspensions system in terms of suspension accuracy is investigated through non-linear simulations with delayed step tyres inputs. Appropriate values of the interconnection passive components for different possible mechanical implementation are found by means of optimization processes. Linear stability analyses are performed for each of the different optimal interconnected configurations. Non-linear frequency analyses of the motorcycle wheels and chassis responses are also performed considering the delay between the front and rear tyre inputs. Non-linear simulations with variable frequency sinusoidal road inputs are run for this purpose. Finally, modal analyses of the motorcycle model are carried out for variable interconnection parameters in order to understand the effect of the interconnected suspensions system on the motorcycle's motion.

Chapter 1

Introduction

1.1 Preliminaries

Motorcycles are a largely extended means of transport used around the world. Whilst in some developing countries motorcycles are essential for commuting and transportation, in developed countries, these machines have been more associated to sport and leisure activities, although the popularity of these vehicles for commuting has increased globally over the years. Whatever the motorcycle's use might be, there exist safety hazards associated with these vehicles. Some of them depend on the interaction with other vehicles, the state of the roads and unpredictable traffic events. But other risks depend solely on the motorcycle's design and dynamics.

In order to gain a complete understanding of these machines' behaviour, motorcycle dynamics have been thoroughly studied in the past. Substantial amount of research has been carried out to date by taking advantage of the relatively recent automated multi-body mechanical systems software and high fidelity motorcycle models. Nowadays, these models are able to simulate the behaviour of real machines accurately over a wide range of normal operating conditions. These tools allow the study and evaluation of different experimental mechanisms and devices before prototyping and physically testing them on a real motorcycle, which becomes an advantage over the trial-and-error methods traditionally employed by manufacturers in the past.

The aim of this thesis is to investigate alternative suspensions systems for sport motorcycles taking advantage of a high fidelity model developed by (Sharp et al.

2004) which has been extensively used and validated by many, e.g. (Shaeri et al. 2004), (Evangelou et al. 2006), (Sharp 2007), (Evangelou et al. 2008), (Evangelou et al. 2010) and (Sharp 2012). In here, the Sharp motorcycle model has been modified to include the dynamics corresponding to two alternative suspension systems and, in this way, explore the impact these would have on the motorcycle dynamics and stability. Two reduced models are as well derived in order to facilitate the analysis of certain features that will be presented in this thesis.

Suspension systems are probably the most relevant elements influencing motorcycle dynamics. They are responsible for the isolation of the motorcycle's chassis from the road irregularities, keeping certain comfort levels for the rider whilst allowing the wheels to follow the road profile as close as possible. Several isolation methods and devices have been developed along the history of these machines. However, nowadays the most extended configurations consist of two separate suspension systems, one for the front and the other for the rear motorcycle's ends. For the rear suspension system, most motorcycle manufacturers have adopted a swinging arm with a mono-shock system. It consists of a single shock-absorber connected to the rear swinging arm through a mechanical linkage that provides progressive stiffness-damping properties to the rear suspension structure. On the other hand, the telescopic fork is the manufacturers' most common option for the front suspension system in the commercial and racing motorcycles. This system consists of a pair of sliding tubes inside two stanchions which contain springs and dampers which are responsible for the shock absorption.

Although the contemporary high end telescopic fork suspension systems are engineered with the most advanced technology and provide excellent performance, they are limited in some features by their geometrical conception. Unlike the rear swinging arm, that can provide a good anti-squat behaviour depending on its design, the telescopic fork suspension system is not compatible with anti-dive characteristics for realistic head angles. On the other hand, a progressive stiffness and damping behaviour cannot be implemented in the telescopic fork suspension design as it can be done with mono-shock system on the rear suspension.

There exist alternative suspension systems based on mechanical double wishbone linkages that overcome the telescopic fork geometrical limitations and introduce new

features. The two most representative systems, due to their mechanical simplicity and kinematics configuration possibilities, are the "girder" and the "Hossack" suspension systems. An extensive description of them is given in Chapter 4, where their kinematic and dynamic behaviours are investigated. These suspension systems present several advantages in terms of their construction. The mechanical simplicity and the increase in the overall rigidity allow for lighter and cheaper implementations maintaining high performance levels and a large number of design options.

However, nowadays, the girder suspension system is rarely seen in custom motorcycles whilst the Hossack suspension system is only adopted in a few commercial models. BMW marketed this suspension system as "Duolever" and included it on its high end sport-touring machines. On the other hand, Bultaco Motors has recently launched two new electric commuter prototypes incorporating the "Dual Link Evolution" front suspension system, which is a Hossack system. None of the commercial models adopting this solution are sport motorcycles, nevertheless some experimental racing motorcycles have been developed and fitted with this system obtaining good racing results. It is the case of the electric e-Moto created by LGN Tech Design, from which Bultaco Motors takes its technology (Bultaco Motors 2015).

The system's stability is a fundamental aspect on the motorcycle's design in order to guarantee the machine performance and, more importantly, the rider's safety. The machine's stability can be greatly affected by modifications on the suspension system. However, a lack of research about the alternative suspension systems effects on the motorcycles' stability was found in the literature. There exist some studies on the performance and response of some alternative suspension systems including the Hossack system. (Mavrouidakis & Eberhard 2006) and (Watanabe & Sayers 2011) obtained promising results for this type of suspension system. Nevertheless, stability analyses of sport motorcycle including either girder or Hossack systems have not been found. One of the goals of this thesis has been to create realistic mathematical models of a sport motorcycle including the girder and the Hossack suspension systems and to investigate the potential advantages and disadvantages that these types of systems may introduce in the sport machines from a kinematics and dynamics point of view, with special attention to their effects on the motorcycle's stability.

Another main goal of this research is to investigate the improvements on the suspension's overall performance that an interconnected suspension system could introduce in the sports motorcycles. As it has been said before, the standard configuration for all the commercial models consists of independent suspension systems for the front and rear motorcycle ends. In the car industry, it is very common the inclusion of anti-roll bars connecting the two wheels of the front and rear axle separately. This method allows to obtain independent stiffness and damping properties for bounce and roll movements that otherwise would be coupled. The connection between the front and rear ends is not as common as the anti-roll bars, although there exist some remarkable examples, such as the case of the historical Citroën 2CV. Nowadays, Creuat Suspension Technology (Creuat 2015) has developed a passive integral interconnected suspension system that connects the four wheels of a car allowing higher levels of suspension settings and performance (see Fontdecaba i Buj 2002).

In the two-wheeled vehicles field, the interconnection of front and rear ends has not been explored except for a couple of individuals' bicycle demonstrators. Interesting results are presented in their respective web pages (RaerDesign 2015) and (Toptrail 2015). In this thesis, the research of this new suspension configuration is extended to the sport motorcycles case. It is organized in three chapters for three different approaches to the interconnected suspension system dynamics.

The present research is intended to explore the promising features of three alternative suspension systems. All of them are passive systems easy to be implemented in any motorcycle. Furthermore, they might be combined in order to enhance their individual characteristics. Although further research work is required for the implementation of these systems on specific real motorcycle models, this thesis can be a starting point for this research. It demonstrates the advantage that these systems provide to the sport motorcycles and points out the issues that need to be carefully considered in their design and development.

As a result of this research, some academic publications were made during the time it was carried out: (Moreno-Ramírez et al. 2011), (Moreno-Ramírez et al. 2012*b*), (Moreno-Ramírez et al. 2012*a*), (Moreno-Ramírez et al. 2014), (García-Fernández et al. 2014) and (Moreno-Ramírez & Tomas-Rodríguez 2014). Never-

theless, by the time this thesis is completed, more relevant results are been written into various journal articles.

1.2 Summary of objectives

With the aim of simplifying the understanding of the contents of this thesis, the main goals and objectives can be summarized as follows:

- a) Investigate two existing alternative front suspension methods for sport motorcycles: girder and Hossack suspension systems.
- b) Contribute to the current knowledge on motorcycle modelling by implementing, in a widely accepted benchmark model (Sharp et al. 2004), the dynamics and kinematics of the two alternative suspension systems under study.
- c) Analyse the stability characteristics of a sport motorcycle fitted with either girder or Hossack suspension systems.
- d) Investigate a new arrangement in which front and rear suspensions become interconnected through passive components.
- e) Introduce the interconnected suspensions system as a new feature in the motorcycle's existing model.
- f) Study the possible improvements this new arrangement may imply in terms of performance and stability.
- g) Understand the effect of the interconnection system on the motorcycle's linear motion associated to its normal modes.

1.3 Structure of the thesis

Chapter 2 contains a thorough literature review of the state of the art in the field of motorcycle dynamics and stability as well as alternative suspension systems.

Chapter 3 provides a description of the simulation model used to carry out the research presented in this thesis as well as details of the modelling software used for these purposes.

Chapter 4 provides an extensive description of the girder and Hossack suspension systems. The systems' modelling and their kinematic and dynamic behaviours are

studied in this chapter as well as their effect on the motorcycle's stability.

In Chapter 5, the interconnected suspension system is defined for a sport machine with conventional mono-shock and telescopic fork suspensions. Then, following the approach in (Fontdecaba i Buj 2002), two motorcycle's reduced models are used in order to investigate the interconnected suspension system configuration possibilities in terms of bounce and pitch in-plane normal modes resonance frequency and damping ratio.

In Chapter 6, the accuracy of the interconnected suspension system is studied for different road inputs for a wide forward speed range. Optimal values of the interconnection parameters for different possible configurations of the interconnected suspension system are obtained, resulting in a significant suspension accuracy improvement for all of them. Finally, the system's frequency response is investigated taking into consideration the coupling between the front and rear wheels motion.

In Chapter 7, a stability analysis of the interconnected suspension system is carried out for different running conditions. Special attention is paid to the motorcycle's normal modes evolution for different values of the interconnection parameters. The normal modes are studied in terms of resonance frequency and damping ratio through the motorcycle's state space eigenvalues. On the other hand, the pattern of motion evolution of each normal mode provided by the associated eigenvector is investigated in order to understand how the motorcycle's motion is affected by the interconnected suspension.

Chapter 8 summarizes the conclusions obtained and gives an account of further research lines.

Chapter 2

Literature Review

This chapter is intended to provide a general view of the most relevant literature on the different areas involved in the research presented in this thesis. The evolution of motorcycle mathematical models, the theoretical and experimental results that have configured the scientific knowledge on motorcycle stability and the study of motorcycle alternative suspension systems in the framework of modelling and stability analysis are covered in chronological order.

Evolution of motorcycle mathematical modelling

Research on two-wheeled vehicles motion has been conducted for over a century. One of the earliest works on bicycle dynamics is found in (Rankine 1869). In this article, the author explained the constant lean angle under steady-cornering assuming an inverted pendulum approximation for the bicycle model, although the formal justification of this approximation was performed later by (Routh 1899). At the same time (Whipple 1899) presented the first analysis of a bicycle self-stability concept using the Routh-Hurwitz stability criterion to determine the stability regimes of the proposed bicycle model. In his work, (Whipple 1899) presented the bicycle linearised equations of motion under straight running conditions. Although these equations contained two typographical errors, as (Hand 1988) pointed out, once these errors are corrected, the equations presented by (Whipple 1899) correspond with the accepted benchmark equations obtained by (Meijaard et al. 2007).

The early research on bicycle and motorcycle dynamics progressed slowly and contradictory results were obtained at first. For those readers interested in detailed

historical development of this topic, comprehensive reviews of the existing literature can be found in (Meijaard et al. 2007) and (Limebeer & Sharp 2006).

A significant step forward in the motorcycle theoretical analysis was presented by (Sharp 1971). In this paper, a Lagrangian analysis of a motorcycle-rider system was performed by the author. The motorcycle model consisted in two rigid frames articulated by an inclined steering axis where the rider was considered to be rigidly attached to the rear frame. The tyre forces and moment were defined as linearly dependent on the camber and the side-slip angles. A first order differential equation that modelled the tyre relaxation properties was used to obtain the instantaneous tyre forces and moments from the steady state angles. Yaw, roll, steer and lateral motion were the four degrees of freedom allowed in the system. Only straight running conditions with small perturbations were considered in this contribution. A linear analysis was carried out, obtaining the eigenvalues of the linear system as functions of the forward speed for a range of different constant speeds. Two different cases regarding the steering degree of freedom were considered. One of them assumed the steering to be locked. This is, no degree of freedom was allowed for the steering. In this case, a "fixed control" analysis was performed. In the other case, the front frame was considered free to rotate about the steering axis allowing a "free control" analysis.

The predicted instability through the entire speed range under study made the "fixed control" characteristic unattractive. However, the "free control" analysis returned relevant results. Important modes were predicted along the entire speed range, being some of them oscillatory. These were "capsize", "weave" and "wobble". Capsize is a low speed instability experienced by the motorcycle falling onto its side. It is easily controlled by the rider by means of the weight and steering torque. Weave is a low frequency oscillating mode in which roll, yaw and steer degrees of freedom are the most relevant involved motions. Its typical resonance frequency was found to be about 2 Hz – 3 Hz, being well damped at moderate speeds whilst it becomes less damped and possibly unstable at high speeds. The resonance frequency of the wobble mode is higher, about 7 Hz – 9 Hz. The main degree of freedom involved in this mode is the steering oscillation relative to the rear frame. In (Sharp 1971) the study of model predicted that wobble was highly damped for low speeds

whilst it became less damped at higher speeds. This model represented minimum requirements that led to qualitative correct predictions; in fact, the tyre relaxation was an important new feature in the model that introduced the destabilization of the wobble mode, approximating the theoretical results to the physical observations.

(Sharp 1971) used this model to demonstrate the impact of a steering damper on the weave and wobble modes. An increase on the steering damper coefficient stabilized the wobble mode whilst destabilized the weave mode and vice versa. The author demonstrated the critical effect on the motorcycle stability of the steering angle, the trail and the front frame moment of inertia about the steering axis. (Sharp 1971) obtained the stability characteristics for many other parameters variation with results that qualitatively agreed with real motorcycle behaviour.

(Cooper 1974) investigated the effect of aerodynamic forces on a high-speed motorcycle stability and performance. Several wind tunnel experiments were performed for a wide range of motorcycle-rider configurations. Steady aerodynamic forces and moments were measured on each of their three components for different values of constant wind speed. The results suggest that the main aerodynamics influence comes from drag, lift and pitching moment, which affects the tyre side forces through the change produced in the tyre load changing with the speed. (Cooper 1974) included these aerodynamic forces and moment in the (Sharp 1971) motorcycle dynamical model in order to investigate the high speed weave stability problem. The stability analysis performed by the author showed low weave damping at high speed when unsteady aerodynamic forces were included. However, these results did not reveal considerable changes in the wobble mode stability.

Aiming to investigate the components flexibility on the motorcycle lateral dynamics, (Sharp 1974) extended the original motorcycle model to introduce a torsional degree of freedom between the rear wheel and the rear frame. This newly considered motion was restrained by a linear spring and a linear damper. The results showed that whilst the capsize and wobble modes remained relatively unaffected, the weave mode damping would deteriorate at medium and high speeds for reduced stiffness in the new degree of freedom.

(Jennings 1974) observed how the weave mode was modified under cornering conditions and how the suspension systems were relevant in their initiation and

maintenance. After several laboratory experiments and riding tests in the front and rear suspension dampers, the author concluded that motorcycle suspension damping characteristics do influence the system weave stability on cornering. It was also noticed that as the speed was increased, a weave oscillation appeared for smaller roll angles. Later, by means of mathematical analysis, (Sharp 1976*a*) demonstrated the possible interaction between pitch and weave modes for high forward speeds due to the proximity of the natural frequencies of both modes under this running condition. Whilst the interactions between the in-plane and out-of-plane degrees of freedom were weak for straight running condition, they became more relevant for higher values of roll angle in steady-cornering.

(Sharp 1976*b*) was the first attempt to study the effect of the acceleration and deceleration on the motorcycle dynamics. The author found some unsubstantiated results due to the simple approach used in this work, where the acceleration was considered as a parameter in the equations of motion and the lateral and longitudinal equations were defined as uncoupled. However, the stabilising effect of the acceleration on the capsize mode became evident. This result suggested the main influence on the capsize mode of a roll angle to yawing moment feedback term introduced by the rear frame inertia.

(Roe & Thorpe 1976) pointed out the existing inconsistency between the theory predictions and the observed wobble oscillations. The authors measured the steer angle fluctuations on different machines ridden in free steering control, this is, hands off. They observed that the wobble mode self-excitation became stronger at midrange speeds whilst the theory at the time predicted higher speeds for this instability to appear. The experiment showed that by the stiffening of the telescopic forks and increasing the rear frame torsional stiffness, the vehicle stability could be considerably improved.

The discrepancy between the theory and the observation regarding to the wobble mode was explained by (Sharp & Alstead 1980). The motorcycle theoretical model at that time assumed the chassis to be rigid. (Sharp & Alstead 1980) improved the existing models by introducing frame flexibility and by using a more elaborated tyre model based on the "taught string" theory previously developed by (Sharp & Jones 1977) which included considerations of tread width, longitudinal tread rubber

distortion and tread mass gyroscopic effects. The tyre parameters were adjusted according to the load and a parabolic approximation to the exact response was carried out. The frame torsional flexibility was addressed under three different approaches. In the first of them, torsional flexibility of the front frame about an axis parallel to the steering axis was included in the model. The second configuration consisted in the lateral flexibility of the wheel relative to the forks along the spindle axis. Finally, the third of them included torsional flexibility at the steering head about an axis normal to the steering axis and belonging to the motorcycle symmetry plane. The new degree of freedom motion was restrained by linear springs and damper in all cases. The stability analyses of four different large production motorcycle models were performed by obtaining the linear models eigenvalues for straight running conditions. The two first frame flexibility modelling proposals did not return satisfactory results able to predict wobble mode behaviour. However, the rear frame torsional flexibility about an axis perpendicular to the steering axle obtained the required results, for which the wobble mode damping was reduced at midrange forward speeds and increased at higher speeds, without affecting its natural frequency in a strong manner. Also, the weave mode damping at higher speeds was slightly reduced, becoming closer to the experimental observations. In the light of those results, it was suggested that higher values of torsional stiffness would increase the motorcycle stability. The main results of this work were independently confirmed by (Splerings 1981).

By static and dynamic loading at the wheel rim of a large conventional road motorcycle, (Giles & Sharp 1983) obtained its rear and front frame stiffness properties. A sinusoidally driven shaker introduced dynamic loads on the frame. The deflection of the chassis was obtained by using an accelerometer and the frequency response information was obtained through the electronic data processing, which returns a single resonance frequency for the front frame about 12 Hz. It was concluded that the lumped mass assumption was correct for the frame flexibility modelling. However, the location of the twist axis at the steering head of the front frame and the value of the torsional stiffness predicted by the static and dynamic loading were remarkably different. Regarding to theoretical wobble mode prediction, these differences were shown to be very significant.

Moving forward in the motorcycle stability analysis and building on his previous work (Koenen & Pacejka 1980) and (Koenen & Pacejka 1982), (Koenen 1983) developed a mathematical model which considered small perturbations about the straight running conditions but also about the steady cornering conditions. The author calculated the eigenvalues of the small perturbation linearised motorcycle model and obtained consistent results for straight running conditions with the conventional knowledge of that time. Whilst weave and wobble modes were predicted varying with speed, the front and rear suspension pitch and wheel hop modes depended very slightly on it. However, for the steady cornering conditions, it was predicted that the stability of the cornering weave mode would be hardly affected if the suspension dampers were removed. This results were contrary to the previous experiences of (Jennings 1974).

At that time, a considerably number of tyres models were available. These models can be categorized in three groups: 1) physically founded models which require computation for their solution. For example, the multi-radial model developed by (Sharp & El-Nashar 1986) and (Sharp 1992). 2) Sufficiently simplified physically based models which allow analytical solution, such as the brush model described in (Fujioka & Goda 1995). 3) Formula based empirical models as described in (Bakker et al. 1989), (Pacejka & Bakker 1992) and (Pacejka & Besselink 1997).

The more relevant and widely used tyre model nowadays falls in the third category. It is the so called Magic Formula model and it matches a real tyre behaviour with high accuracy. The steady state longitudinal force, side force, aligning moment and overturning moment are described as functions of longitudinal slip, side-slip, camber angle and normal load. The model parameters are constrained to prevent unrealistic behaviour in any operating condition. The other two models will not be considered, however, the interested reader is referred to (Pacejka & Sharp 1991) for a detailed review.

The magic formula model was developed representing a car tyre behaviour, where side-slip is the dominant input. For motorcycles, large camber angles are common. Aiming to overcome this deficiency, (de Vries & Pacejka 1998) updated the original equations to make them suitable for the motorcycle case. By means of a tyre test trailer, the authors performed a series of measurements on public roads. They

acquired steady state forces and moments for front and rear tyres for different side-slip angles, camber angles and normal load values. The data obtained were used for identification of the different parameters. Physically correct representations outside the measured data range were also sought. Two different dynamic models were considered in order to process the results: one of them was a first order relaxation model consistent with the "taut string" theory. The other was a rigid ring model which was found to describe very accurately the tyre response. Using velocity independent tyre parameters only, it provides results with a high precision for a greater range of frequencies than for the relaxation model. Magic formula equations for motorcycle tyres were further improved in (Tezuka et al. 2001) and (Pacejka 2002).

By this time, several computer softwares for assisted mechanical modelling were already available. One of them was AutoSim. This tool was developed by Mechanical Simulation Corporation. It was a symbolic code generation language designed for multi-body modelling and built on top of the artificial intelligence standardised language Common LISP (Steele 1990). It follows a tree topology for the multi-body system description, so that the constituent system bodies were arranged in a parental structure (Sayers 1991). The method to obtain the equations of motion is based on (Kane & Levinson 1983) and (Kane & Levinson 1985), which is an alternative statement of the Jourdain's virtual power principle. Compared to the Lagrange's energy-based method, the Kane's equations becomes a more efficient method as it needs significantly less operations to obtain the equations of motion. The AutoSim package became a powerful and efficient tool for the multi-body modelling. Its input was in the form of a high level intuitive language whilst its outputs could be either a low-level computer language code, such as FORTRAN or C, ready to compile and solve the equations to obtain motion time histories, or a MATLAB M-file containing symbolic state-space description for linear analysis in the form of matrices A, B, C and D. AutoSim evolved to the newer VehicleSim software suite that keeps a high backwards compatibility. Its core features are maintained but the whole tool has been widely improved with the addition of external advanced features, such as the Simulink compatibility or the VS Browser. It consists in a graphical user interface built in different solvers that allows the end user to run the different simulations with different external inputs and events directly from it. VehicleSim is the multi-body

modelling tool used in this thesis.

(Sharp & Limebeer 2001) used AutoSim to reproduce the (Koenen 1983) motorcycle model as accurate as possible using the same parameters values. Equivalent straight running and steady cornering root-loci were calculated. The predictions obtained were not the same but they were qualitatively equivalent to those in (Koenen 1983).

(Sharp & Limebeer 2001) investigated the inconsistency between the experimental measurement obtained by (Jennings 1974) and (Weir & Zellner 1979) and the (Koenen 1983) prediction regarding to the negligible influence of the suspension damping on the weave mode under steady cornering conditions. Root-loci for suspension damping variation under cornering were calculated obtaining a significant relevance of this parameter on the weave mode. This work pointed out the need for a computer assisted method for the analysis of the, each time more complex, motorcycle models and reveals a possible error in (Koenen 1983) calculations. Indeed, a variable geometry active rear suspension was demonstrated to stabilise the cornering weave (Sharp 2000).

(Cossalter & Lot 2002) implemented an eleven degrees of freedom nonlinear motorcycle model in a Fortran code named Fatbike. An original tire model which took into account the tires geometric shape and the elastic deformation of its carcasses was developed, describing the tire dynamics in a similar manner than the existing relaxation models. The approach followed by the authors allowed to obtain simple equations of motion based on the natural coordinates. A set of fully cartesian coordinates were used to describe each rigid body. Then, the links between the rigid bodies are described with algebraic equations. Although with this approach the coordinates were redundant, it allowed to reduce the complexity of the equation of motion. As a result, the FastBike performance becomes fast enough to run real time simulations, becoming an adequate engine for motorcycle simulators. Real experiments for slalom and lane change manoeuvres were carried out and then compared to the equivalent simulations using the FastBike code. The results showed a good agreement between both numerical and experimental tests.

Motorcycle dynamics and stability

Once the computer assisted modelling tools became a standard and the mathematical models reach an adequate fidelity, the research on motorcycle dynamics and stability could move forward. External events, experimental motorcycle designs and, in general, different conditions from the classic steady cornering and constant forward speed could be now investigated.

(Limebeer et al. 2001) used the model developed by (Sharp & Limebeer 2001) to revisit motorcycle stability under acceleration and braking firstly presented by (Sharp 1976*b*). The authors proposed that the stability properties of an accelerating/braking motorcycle are equivalent to those of a constant speed machine running uphill/downhill. They gave a summary of some of the problems that appear with time-varying systems in classical control theory and numerically showed that both the constant speed motorcycle running uphill/downhill eigenvalues and the frozen-time eigenvalues of the accelerating/braking machine can qualitatively predict the transient of the accelerating/braking motorcycle when it is perturbed. These results demonstrated qualitatively the acceleration/braking action effects on motorcycle stability, coinciding with recorded motorcyclists' experience.

(Limebeer et al. 2002) investigated the road undulations effects on the motorcycle stability with special emphasis on cornering conditions and on the mechanism by which the road undulations can affect the motorcycle lateral dynamics. The coupling terms between the in-plane and out-of-plane dynamics allow an energy transmission from the road to the out-of-plane degrees of freedom. So that a perturbation in the road profile can induce steering oscillations. It was found that both wobble and front hop modes resonance frequencies are mostly dominated by the front wheel road input and an adequate design of the front end can address some of the difficulties experienced with these modes. Regarding to the weave mode, it was found that both front and rear wheels' road inputs affect in a similar manner to its resonance frequency and stability problems related to this mode appear more difficult to be resolved.

(Evangelou 2003) used AutoSim to develop both linear and nonlinear models for the hand derived motorcycle models presented in (Sharp 1971) and (Sharp 1994). Then, a more comprehensive model, based on previous work (Sharp & Limebeer

2001) was extended. Using the advanced model, the author investigated the acceleration and braking on motorcycle stability. The result confirmed those obtained by (Limebeer et al. 2001) showing the equivalence between uphill/downhill and acceleration/braking. Furthermore, the wobble mode was proved to be significantly destabilised when the motorcycle brakes on a level surface or descends an incline at constant speed, whilst it becomes more stable for opposite running conditions, this is when the machine accelerates or ascends an incline. Regarding to the weave mode, the inclines, acceleration and deceleration do not present significant influence on its damping and frequency. Finally, (Evangelou 2003) improved further the advanced motorcycle model including a more precise tyre modelling based on Magic Formula methods combined with modern tyre data. A more realistic tyre-road contact geometry, parameters describing a modern high performance motorcycles and other features of contemporary machines designs were also included.

(Sharp et al. 2004) improved the advanced model presented by (Evangelou 2003) and set up a high fidelity mathematical model of a sport motorcycle dynamics based on the parameters of a Suzuki GSX-R1000 motorcycle. The new model is used for steady turning, stability, design parameter sensitivity and response to road forcing calculations. The predictions of this model are in agreement with observations of motorcycle behaviour, suggesting that, despite improvements in frame designs over recent years, the frame flexibility represents an important study field in the motorcycle dynamics.

(Evangelou et al. 2006) presented a framework to design steering passive compensators to stabilize the wobble and weave modes simultaneously. By means of classical passive filter techniques, the authors designed and tested several compensator designs with optimized parameters. To do so, the force-velocity to current-voltage pairing was introduced to obtain an electro-mechanical correspondence between resistor, inductors and capacitors to dampers, springs and inerters. This last component was developed by (Smith 2002) and became an essential component in this work.

The road camber influence on the motorcycle stability was investigated by (Evangelou et al. 2008) by means of the GSX-R1000 motorcycle model developed by (Sharp et al. 2004). In order to obtain the steady-state running conditions, a circular cone

was used as road surface. This allows the vehicle to keep a constant forward speed and roll angle, being the road camber constant. The results showed that at low speed both weave and wobble modes stabilities reach their maximums when the motorcycle symmetry plane and the road surface are perpendicular. However, for high speeds the opposite behaviour was found. The weave and wobble modes stability increased for higher values of the motorcycle roll angle relative to the road plane. And for those running conditions in which the machine was perpendicular to the road, the damping of these modes was minimized. Therefore, the positive road camber usually adopted in the road designs to enhance the friction limit of the four-wheeled vehicles and to aid the rain drainage becomes detrimental for the motorcycles stability.

An example of the high relevance achieved by the computer assisted multi-body models in the motorcycle dynamics research can be appreciated in (Cossalter et al. 2008). The chatter of motorcycles consists in a vibration of the front and rear unsprung masses during the machine braking manoeuvres with a resonance frequency about 17 Hz – 22 Hz, depending on the motorcycle characteristics. In this paper the authors could study the chatter phenomenon from experimental evidences but also from a numerical point of view. This led on to a better understanding of this phenomenon and also allowed to propose a physical interpretation of it.

Other oscillatory phenomenon that can affect the motorcycle stability is the burst of oscillations appearing under high-speed cornering and firm-acceleration conditions as a consequence of wobble and weave modes interaction. Whilst the wobble mode frequency decreases under these conditions, the weave mode frequency increases and a destabilizing interaction can occur at certain point. (Evangelou et al. 2010) and (Evangelou et al. 2012) studied this source of instabilities and proposed a method to suppress them by means of a mechanical compensator. Assuming that the bursting occurs on a time scale over which the variation in the speed could be neglected, the authors utilized time invariant models with constant motorcycle forward speed in the design process of the proposed compensator. In order to maintain the constant speed requirement for the time invariant model, the influences of the acceleration and braking in the system were modelled as d’Alambert inertial forces applied to the mass centre of each of the bodies constituting the motorcycle model. The design

and optimization of the compensator was made from robust control theory in order to address the inevitable uncertainties and nonlinearities affecting the machine local behaviour. It was found that the resulting compensator was a simple mechanical network comprising a linear spring in series with a damper.

Alternative suspension systems

A high fidelity motorcycle model combined with computer assisted modelling and numerical simulation tools bring the possibility of testing new ideas, concepts and motorcycle arrangements before a more resources-demanding prototyping stage. Several authors have taken advantage of these tools obtaining satisfactory results in their research.

(Mavroudakos & Eberhard 2006) investigated a number of alternative motorcycle's front suspension systems modelled as a highly detailed multi-body system. The suspension systems were compared in terms of kinematics and dynamics in order to improve the insight into the aspects that need to be considered if one of these alternative systems is to be adopted in an eventual motorcycle design. The paper included four suspension systems alternative to the conventional telescopic fork and presented their responses to different motorcycle manoeuvres, highlighting the performance potential of such systems. However, stability analyses of the different suspension arrangement were not performed in this work.

Following the ideas in (Sharp 2000), (Evangelou 2010) proposed a variable geometry active rear suspension system to control the weave oscillations on sport motorcycle operating at high speeds. The design analysis makes use of the previously used model based on the Suzuki GSX-R1000 motorcycle. Its conventional monoshock rear suspension arrangement was modified and extended allowing the variations of the leverage ratio between the spring damper unit and rear wheel vertical displacement. An actuator varies the geometry by controlling the displacement between the moving parts related to the shock-absorber junction. Classical Bode-Nyquist frequency response ideas were used to develop the control strategy and an integrator anti-windup scheme was introduced in the system to satisfy the limited displacement space, and to limit the maximum actuator force and power requirements. So that a feasible device of practical dimensions could be designed.

Simulation results demonstrated that significant improvements could be obtained with this kind of actuators.

BikeSim is a VehicleSim tool (formerly named AutoSim) specifically designed to simulate the dynamic behaviour of motorcycles whose mathematical model is based on a core model developed and validated by Prof. Robin Sharp, Prof. David Limebeer and Dr. Simos Evangelou, at Imperial College, London, using the AutoSim code generator. (Watanabe & Sayers 2011) described the modelling methods used in the commercial BikeSim simulation package to represent alternative front and rear suspension motorcycle arrangements. More precisely, these alternative systems corresponded to the Duolever and Paralever BMW's suspensions designs. The Duolever is a Hossack front suspension system redesigned and re-branded by BMW, whilst the Paralever is the commercial name of its four-bar linkage rear suspension system. Different simulations for braking, acceleration, and cornering manoeuvres were performed comparing the dynamical responses of the conventional and the multi-link suspension systems. The results showed that alternative suspension systems could provide advantages over conventional suspension systems. Similar comparisons were made with a chain-drive powertrain and a shaft-drive powertrain, which demonstrated the need for a multi-link rear suspension system when a shaft-drive is used for the powertrain. Although the VehicleSim tool presents exceptional capabilities in terms of model linearisation and state space representation and a high compatibility with scientific software such Matlab-Simulink, a stability analysis is not performed in this paper.

Finally, it is important to mention the work done by (Fontdecaba i Buj 2002). Although this work was orientated to four-wheeled vehicles, the approach followed by the author in the study of an interconnected suspension system represents the starting point for a part of the research developed in the current doctoral thesis. (Fontdecaba i Buj 2002) presented an interconnected suspension system for four-wheeled vehicles based on passive components. The author first exposed the theory behind the interconnection system by means of a four degrees of freedom car model for which the wheel masses were neglected and whose main general motions were bounce, pitch, roll and axle crossing. These motions were defined as functions of the individual wheel displacement, thus a change of basis on the model degrees of

freedom allowed to obtain the adequate individual terms for each wheel suspension system that could define the general motions independently. This was possible thanks to the interconnection terms in the dynamics equations between the four wheel suspension forces. Experimental tests were conducted by an independent third party company on a 1990 Range Rover model fitted with an interconnected suspension system to prove that the free axle crossing configuration proposed by the theory became an advantage in terms of traction, comfort and performance of the whole suspension system. The results also highlighted the two major improvements of this system. On one hand, the better weight distribution on static and dynamic conditions reduced the effect of road irregularities on the vehicle steering control. On the other hand, the availability of new parameters allowed configuring the four normal modes stiffness and damping characteristics independently. However, as it will be shown in Chapter 5, the introduction of the wheels degrees of freedom into the interconnected suspension models, increases the complexity of the normal modes and make the independent tuning of these modes to be a complicated task.

Chapter 3

Description of the Motorcycle

Model

The different mathematical models derived in this thesis for the analysis of alternative suspension systems are modifications of the model presented in (Sharp et al. 2004). This mathematical model was built during several years of research underpinned by wide literature and experimental data. In Chapter 2 it was introduced the evolution of the previous motorcycle models, which explained different phenomenologies of two-wheeled vehicles dynamics but presented some lacks. (Sharp et al. 2004) developed a consistent model whose predictions closely follow the results obtained in numerous experiments carried out within the motorcycle dynamics field and which was able to address the contradictions found in previous models. This model has been extensively used in the past in several contributions such as (Shaeri et al. 2004), (Evangelou et al. 2006), (Sharp 2007), (Evangelou et al. 2008), (Evangelou et al. 2010) and (Sharp 2012). Furthermore, it has been widely tested and adopted by the industry. BikeSim software is a motorcycle dynamics simulator which is based on this model and it is used by a large number of manufacturers to obtain high fidelity prediction on the dynamics of their machines (Mechanical Simulation Corporation 2015).

In order to obtain a high-fidelity representation of the motorcycle dynamics, (Sharp et al. 2004) used in their model the parameters of a Suzuki GSX-R1000 K1 motorcycle, which is the superbike manufactured by Suzuki in 2001 (see Fig. 3.1). With 170 kg of mass, powered by an in-line four cylinder and four stroke engine with

988 cc able to deliver 160 hp, this machine is a good representative of contemporary commercial high performance motorcycles.



Figure 3.1: GSX-R1000 motorcycle. www.gsxr.es

3.1 Baseline model

The motorcycle consists of seven bodies: rear wheel, swinging arm, main frame (comprising rider's lower body, engine and chassis), rider's upper-body, steering frame, telescopic fork suspension and front wheel. It involves 13 degrees of freedom: three rotational and three translational for the main frame, two rotational for the wheels spin, one rotational for the swinging arm, one rotational for the rider's upper body, one rotational for the frame flexibility, one rotational for the steering body and one translational for the front suspension fork. What follows in this section is a description of the model developed by (Sharp et al. 2004).

3.1.1 Parametric description

A precise parametric description of a real motorcycle was performed in (Sharp et al. 2004). A Suzuki GSX-R1000 was acquired and its key geometry points and the dynamical properties of the different motorcycle parts were obtained in a process combining the technical information in the workshop manual with the direct measurements of the main motorcycle parts mechanical properties, which were disas-

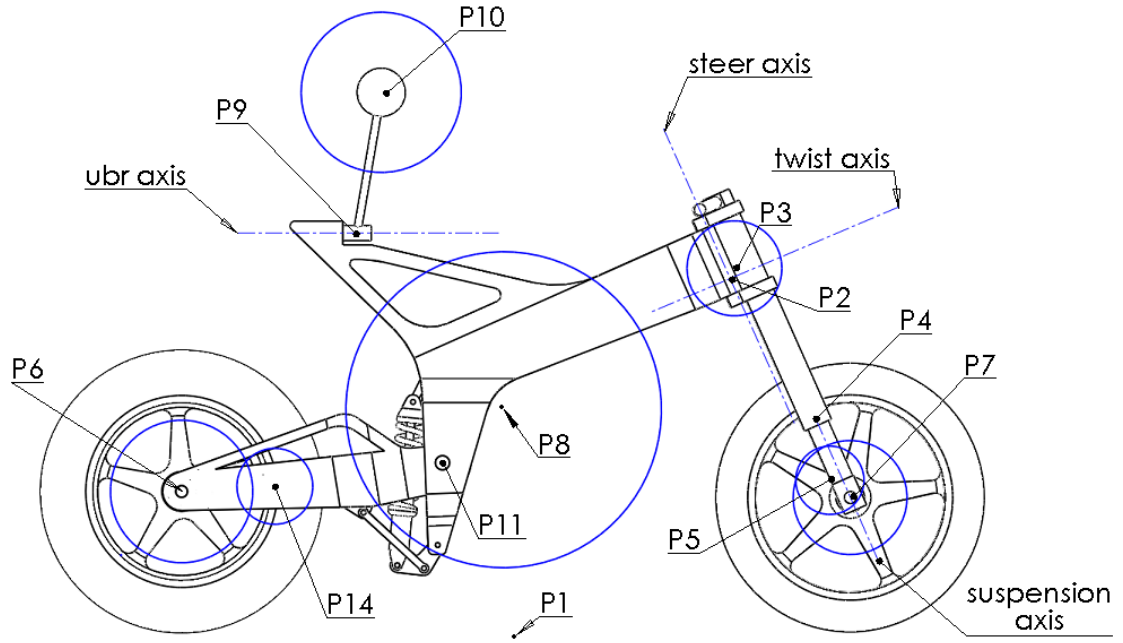


Figure 3.2: GSX-R1000 geometrical description. Blue circles are plotted on the bodies' centre of masses. The diameters are proportional to the corresponding bodies' masses

Point	Description
P1	Aerodynamic reference point.
P2	Twist axis joint with rear frame.
P3	Centre of mass of front frame steer body.
P4	Joint between front suspension and steer bodies.
P5	Centre of mass of front suspension body.
P6	Centre of mass and attachment point of the front wheel.
P7	Centre of mass and attachment point of the rear wheel.
P8	Centre of mass of the main frame.
P9	Attachment point for rider on rear frame.
P10	Centre of mass of the rider's upper body.
P11	Point of attachment for swinging arm onto main frame.
P14	Centre of mass of swing arm.

Table 3.1: GSX-R1000 geometrical model main points.

sembled from it to individually test them. The elastic properties of the suspension elements were tested in a standard dynamic materials testing machine obtaining the stiffness and damping parameters values of the corresponding elastic elements. Being these the front and rear shock absorbers and the steering damper unit. On the other hand, the main frame's torsional stiffness, between the steering head and the power unit, was estimated from previous works, (Giles & Sharp 1983) and (Koenen 1983), based on different motorcycles models. The flexibility is modelled as a rotation degree of freedom restrained by a parallel spring/damper system between the front and the rear frames about the twist axis. This axis is contained in the motorcycle's symmetry plane, perpendicular to the steering axis and passes through the joining points of the steer body.

The rider's upper body has a degree of freedom relative to the main frame rotating about its x axis, whilst the lower body is considered as part of the main frame. A parallel spring/damper system restrains the upper body. Their stiffness and damping coefficients are obtained from the experimental results of (Nishimi et al. 1985), by identifying the rider's stiffness and damping parameters in forced vibration on a motorcycle frame. The three aerodynamic coefficients (drag, lift and pitch) are obtained from wind tunnel testing data of a Triumph motorcycle which presented similar style and dimensions to the GSX-R1000 (Sharp 2001).

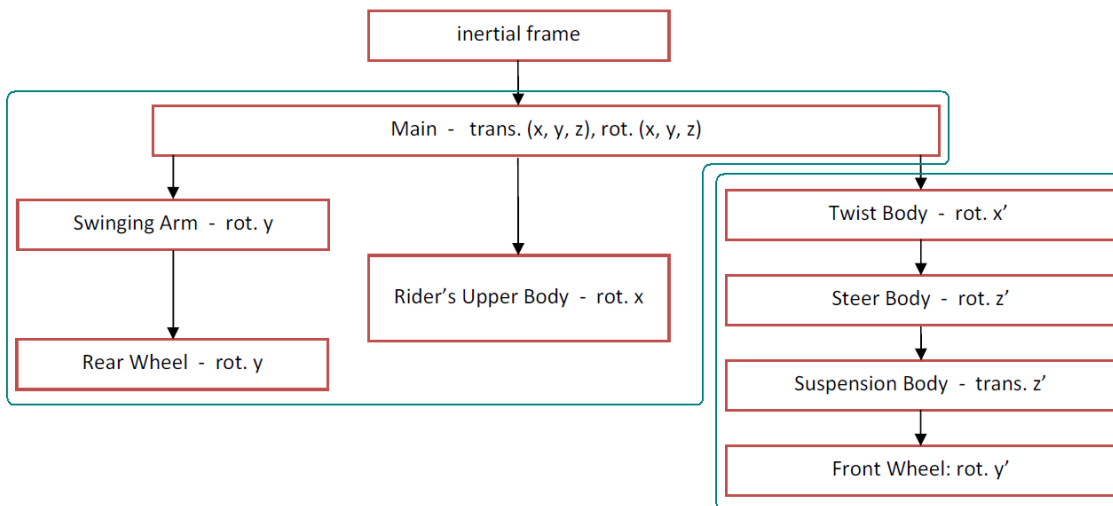


Figure 3.3: GSX-R1000 parental structure.

Figure 3.2 represents the main geometric points and axes in the motorcycle's geometry. The centre of mass of each of the seven constituent bodies is represented

as a blue circle with a diameter proportional to its mass. Table 3.1 contains the indexes of these points. In terms of multi-body systems, the motorcycle can be modelled with the parental structure shown in Fig. 3.3.

3.1.2 Tyres modelling

The tires modelling is a fundamental part on the motorcycle modelling process. Following the work presented by (Cossalter et al. 1999), (Cossalter & Lot 2002) and (Cossalter et al. 2002), the (Sharp et al. 2004) model includes tyres width in their descriptions – contrary to the models existing by that time where the tyres were commonly assumed as thin. In the wide tyre model, the lateral migration of the contact point occurs automatically, so that the overturning moment appears as a consequence of that displacement, whilst a realistic self aligning moment results from the application of the longitudinal forces to the cambered tyre.

(Sharp et al. 2004) modelled the tyres forces applying Pacejka’s ”Magic Formula” (Pacejka 2002). This is a set of parametric equations relating load, slip ratio (longitudinal slip), slip angle and camber angle to longitudinal force, side force and aligning moment. Very limited parameter values were found in the literature, but taking advantage of the amount of relevant experimental data available, the equation parameters could be identified. The steady-state force and moment system for any realistic operating condition can be calculated with a complete set of parameters values for a given tyre. To determine a full set of these parameters for modern front and rear high performance motorcycle tyres, the already available data such those on (de Vries & Pacejka 1998) and (Pacejka 2002) were used in (Sharp et al. 2004). Different optimization processes were used to improve iteratively the elements of a starting vector of parameters appearing in the equations, which finally return close predictions to the data measured.

3.1.3 Monoshock rear suspension

For the GSX-R1000 motorcycle, a single spring-damper unit with a mechanical linkage connection to the swinging arm is used as rear suspension system. Figure 3.4a shows a sketch with the geometric description of this monoshock system, whilst Fig. 3.4b shows a 3D model of the assembly. It involves a closed kinematic loop

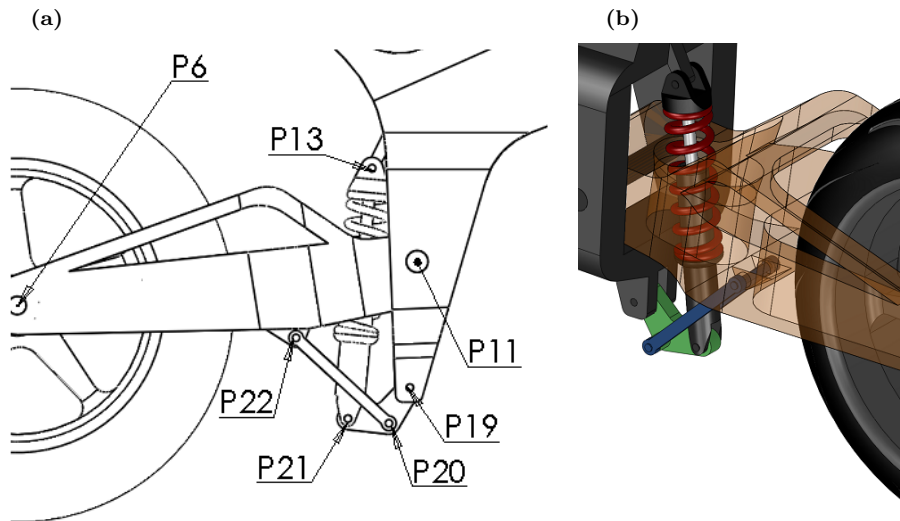


Figure 3.4: a) Monoshock geometrical description. b) Monoshock 3D model.

that provides variable stiffness and damping responses depending on the swinging arm position. (Sharp et al. 2004) performed a geometric pre-analysis of this system and coded the resulting equations into the model programming. Those equations must be solved in-line during the simulations. A resulting rear suspension moment is applied to the swinging arm reacting on the main frame depending on the rotated angle and the rotational speed.

3.1.4 Forward speed and roll angle controllers

Forward speed controller

In the (Sharp et al. 2004) model the forward speed is maintained by a driving torque applied to the rear wheel and reacting on the main frame. This torque is modelled as a proportional-integral (*PI*) controller on the speed error with fixed gains. This representation corresponds to a shaft drive system. However, the baseline motorcycle model uses a chain drive to transmit the torque to the rear wheel. This can represent considerable differences on the machine dynamics under heavy acceleration manoeuvres. Nevertheless, these kind of manoeuvres are not considered neither in (Sharp et al. 2004) nor in this thesis and little differences between the two transmission systems appear on the different manoeuvres under study in both works. In the baseline model, the target forward speed was provided as data in a table function, with time being the independent variable. However, in this thesis this model has

been modified to support a speed reference depending on only two parameters: a constant initial speed and a linear speed ratio corresponding to the acceleration. In this way, a linear function of the forward speed with respect of time is obtained.

Roll angle controller

For some manoeuvres, the motorcycle is not self-stable; in order to stabilise the machine in such situations, (Sharp et al. 2004) implemented a roll angle feedback controller. This allows to obtain different steady turning equilibrium states through simple simulations, which will not be stable without the roll angle controller. The controller developed was a proportional-integral-derivative (*PID*) feedback of motorcycle lean angle error to steering torque. The lean angle target is set by an initial value and a constant change rate. Thus, the target lean angle is a ramp function of time which can be easily modified. The *PID* gains are defined as speed adaptive in order to achieve an effective stabilisation of the motorcycle for the difficult cases involving very low or very high speeds. Finally, the steering control torque is applied to the steer body reacting on the rider's upper body.

3.1.5 Braking system

A full braking system is modelled in (Sharp et al. 2004) as two torques that oppose the wheels' spin. The front wheel braking torque reacts to the suspension body and is proportional to the front braking force applied by the rider. The rear wheel braking torque reacts on the swinging arm and is proportional to the rear braking force applied by the rider. The relations that convert both rider braking forces into the wheels braking torques are mathematically calculated from the braking system: this is, hydraulic circuit, braking pads areas, friction coefficients and braking disk diameters. The desired front/rear braking distribution is modelled as two rider braking forces defined as constant inputs that the user must provide during simulation if a braking manoeuvre is performed.

3.1.6 Road input

In the (Sharp et al. 2004) model, the road inputs are defined as vertical compressions of the tyres' carcass produced by a road elevation and they do not take into

account the contact point longitudinal displacement that an eventual step input may produce. In order to simulate a sinusoidal road perturbation, the model includes a built-in sinusoidal function which acts as tyres' inputs. This capability was first introduced in (Limebeer et al. 2002) and exploited further in (Shaeri et al. 2004) where road undulations influence on motorcycle stability was investigated. The sinusoidal function can be activated/deactivated and programmed with the desired frequency and amplitude characteristics.

3.2 Additional features

In the present work some capabilities which extend the (Sharp et al. 2004) model are needed in order to run the adequate simulations. (Sharp et al. 2004) model was built taking advantage of the Autosim multi-body software developed by (Mechanical Simulation Corporation 2015). This software has evolved to an even more powerful tool called VehicleSim. Nowadays, the modifications introduced in Vehiclesim software allow new capabilities that have been exploited to perform three main modifications, regarding to the road inputs and the braking control, as part of the work of this thesis.

3.2.1 Modifications on the braking system

In Chapter 4 two alternative front suspension systems are tested on the GSX-R1000 baseline model. Apart from these motorcycle's front end modifications, which are explained in chapter 4, other common parts have been modified. The first of them is the braking system. In order to study the response of the new suspension systems and their anti-dive properties, a braking system capable of delivering a constant deceleration is needed. For this purpose, the speed reference input is now defined depending on two parameters: the initial speed and the acceleration. With these two constant inputs, a speed ramp function is obtained. The driving torque control remains as described in section 3.1.5 whilst the braking system is slightly modified following the work in (Evangelou 2003). The rider's braking forces inputs are substituted by a braking distribution ratio that the user may set for each simulation.

The braking torque is now calculated by the same *PI* controller than the driving torque. If the acceleration is set as negative, the driving torque is switched off, whilst the braking torques are applied, depending on the braking distribution ratio, to the front and rear wheels reacting in the front suspension body and the swinging arm respectively. In the case that the acceleration is set as positive, the braking torques are switched off and the speed controller output is applied to the rear wheel through the driving torque reacting on the chassis (main body) in a similar manner than in the baseline model.

3.2.2 Modifications on the road input

The second baseline model modification corresponds to the road input on the tyres. Previously, these inputs were defined as a vertical compression of the tyre carcass introduced by a built-in sinusoidal function. Now, taking advantage of VS Browser (the simulation tool included in Vehiclesim) capabilities, this function can be substituted by two variables (one for each wheel, front and rear), whose values are read from an external table by the solver program during the simulation. The road profile can be externally designed and imported into the final simulation. In Chapter 6, the motorcycle model is tested through a variable sinusoidal road profile specifically designed in order to have a constant frequency density. The road profile is designed in Matlab as a two-dimensional table containing distances and heights. Then, it is exported as a plain-text comma-separated values file (csv file) to the VS Browser, which takes from this file the value of the height for each of the wheels input variables depending on its longitudinal position for each simulation's time step. Taking advantage of this modification, an optimized road profile could be used for the simulations.

3.2.3 Two dimensional step bump input

The third modification introduced by this thesis into the baseline motorcycle model, is also related to the road input modelling. In this case, the objective is to consider the effect of the longitudinal contact point migration produced by a step bump. In Chapter 4 and Chapter 6 the different suspension systems are tested in straight forward running simulations passing through a step bump with a considerable height.

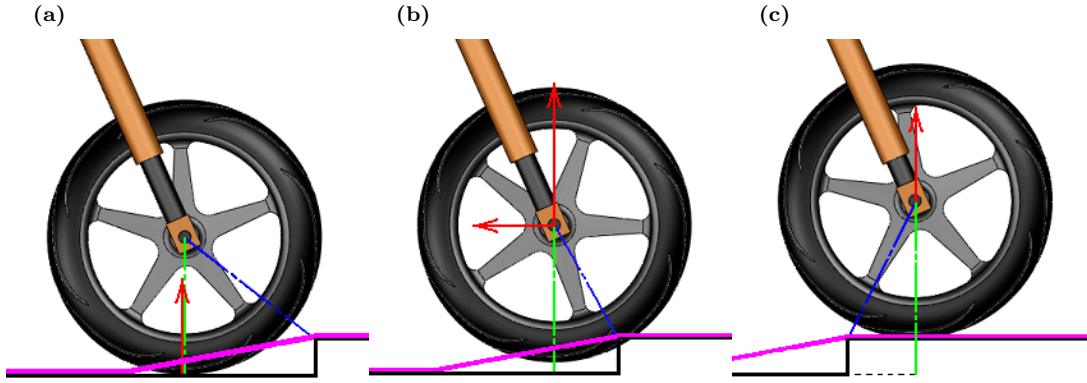


Figure 3.5: Motorcycle front wheel passing through a step bump in three different stages.

Several strategies are considered to find the best computing approximation. It was found that the most natural manner to reproduce a road step bump into the model was by introducing additional radial forces applied to the centre of the wheels in parallel to the forces generated in the tyres carcasses by the original model. In this context, two complementary descriptions of the step are needed as inputs to correctly track its position. The first input is a ramp table of coordinates (x, z) whose values allow to calculate the distance from the centre of the wheels to the step corner. The height of the ramp has the same value as the step height (h_{st}), whilst the ramp horizontal distance (l_{st}) can be any value larger than the rear tyre radius (r_r), which is the largest of both tyres. The second input is a pair of constants containing the l_{st} and the h_{st} values. The input table is externally introduced during the simulation, the equation in the solver need these values to correctly read the table's information. The table's values are plotted in Fig. 3.5 in magenta overlapped to the actual step bump which is represented in solid black. The projection of the front wheel centre on the road, used to read the table values for its corresponding position in the x direction, is plotted with dashed green lines. Finally, the distance between the wheel centre and the step corner (d_{sf}) is represented by a dashed blue line. In order to simplify the description of this feature, only the front wheel is explained here, nevertheless the same development can be applied to the rear wheel.

If the step corner is located at the global coordinates (x_b, z_b) , where the z_b coordinate takes the value of the step height (h_{st}), then the input table must take the values on Table 3.2. During the simulation, the centre of the wheel is dynamically tracked. The z coordinates of the input ramp table is read for the x coordinates of

\mathbf{x}	\mathbf{z}
$(-\infty, x_b - l_{st})$	0
$[x_b - l_{st}, x_b]$	$(x - x_b + l_{st}) \cdot \frac{h_{st}}{l_{st}}$
$(x_b, +\infty)$	h_{st}

Table 3.2: Input values table for the two dimensional step bump description.

the wheel (x_{wf}) and is stored in $road_f$ variable to calculate the step corner position relative to the wheel's centre by means of Eq. 3.1 and Eq. 3.2.

$$x_{sf} = x_{fw} + l_{st} - road_f \cdot \frac{l_{st}}{h_{st}} \quad (3.1)$$

$$z_{sf} = h_{st} \quad (3.2)$$

Whilst x_{sf} value is the horizontal relative distance from the front wheel centre to the step corner, the value of z_{sf} is the step corner z coordinates which is constant. The absolute x coordinate of the front wheel is x_{fw} . With these coordinates the relative distance between the wheel's centre and the step corner (d_{sf}) is computed. Note that for the interval $(-\infty, x_b - l_{st}]$ the relative coordinates of the step take the values $((x_{fw} + l_{st}, 0)$. On the other hand, for the interval $[x_b, +\infty)$ the coordinates correspond to (x_{fw}, h_{st}) . The force produced by the carcass compression (F_{tf}) is calculated by Eq. 3.3, which represents the Hook's law applied to the existing length difference between the nominal tyre radius and the distance d_{sf} . The front tyre's stiffness coefficient is k_{tf} . The tyres' elastic force only appears under the carcass compression. However, when the distance d_{sf} is larger than the tyre radius, the computed force F_{tf} is positive. In order to properly model this force, a discontinuity must be added to the model, so that the force magnitude can only achieve either zero or negative values.

$$F_{tf} = \begin{cases} -k_{tf} \cdot (r_f - d_{sf}) & : d_{sf} < r_f \\ 0 & : d_{sf} \geq r_f \end{cases} \quad (3.3)$$

Figure 3.5 represents the three different stages in which the wheel passes through the road step bump. In Fig. 3.5a the wheel's centre has gone through the first table

values different from zero. The distance to the step corner is larger than the wheel radius (r_f) and thus, the force appearing on the tyre is the normal load provided by the nominal force calculations and plotted with a red arrow. In Fig. 3.5b, the tyre has impacted with the step corner, d_{sf} is shorter than the wheel's radius and, consequently, the corresponding radial force is applied to the wheel's centre. The figure shows the force's vertical and horizontal components with red arrows. In Fig. 3.5c the wheel's centre has overcome the step corner. Equation 3.1 returns a step corner x coordinate value which is equal to the wheel's centre x coordinate for any position of the wheel after this point. Consequently, the horizontal component of the radial force becomes zero. Only the wheel vertical displacements will affect this force. At this last stage, the radial force is equal to the normal load provided by the tyre nominal force calculations. Being the two forces (the nominal model carcass load and the new step radial force) applied in parallel, the nominal normal load becomes zero as the tyre is separated from the nominal ground. And the resultant force, represented by the red arrow, is now that corresponding to the radial force applied to the wheel's centre.

This road step bump model does not consider manoeuvres in which the motorcycle is leant. It is only suitable for straight forward running simulations in which this kind of bumps are tested. However, it introduces a higher level of accuracy in the road step bump description compared to the former description in which the longitudinal forces were not considered.

3.3 Reduced models

The GSX-R1000 mathematical model is a three dimensional high fidelity model able to reproduce realistic motorcycle dynamics. However, for some part of this work, a reduced model is needed in order to study the motorcycle's in-plane dynamics with approximate analytic equations. This is the case of Chapter 5, where the front and rear suspensions interconnection are studied through two reduced in-plane models. One of them is a uni-body model with two degrees of freedom, vertical displacement and rotation about y axis. The other one is a four degrees of freedom model including the main frame and the two wheels.

Figure 3.6 shows a sketch of a motorcycle reduced model composed by three

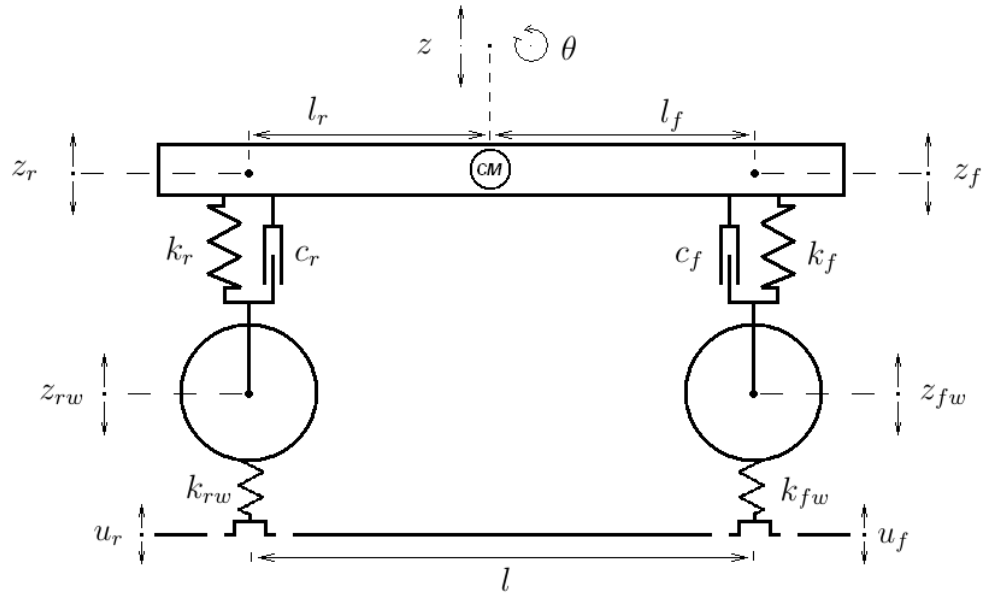


Figure 3.6: Motorcycle's reduced model with four degrees of freedom.

bodies and four degrees of freedom. These are the front and rear wheels vertical displacements, the main frame vertical displacement and the main frame pitch rotation.

Parameter	Value	Units	Description
m_m	208.80	kg	Main body mass.
I_m	42.35	kgm ²	Main body inertia moment.
m_{fw}	19.15	kg	Front wheel mass.
m_{rw}	17.61	kg	Rear wheel mass.
l_f	0.663	m	Distance from the center of mass to front end.
l_r	0.659	m	Distance from the center of mass to rear end.
k_f	29.96	kNm ⁻¹	Front suspension stiffness coefficient.
k_r	19.30	kNm ⁻¹	Rear suspension stiffness coefficient.
c_f	2.56	kNsm ⁻¹	Front suspension damping coefficient.
c_r	3.57	kNsm ⁻¹	Rear suspension damping coefficient.
k_{fw}	130.00	kNm ⁻¹	Front tyre stiffness coefficient.
k_{rw}	141.00	kNm ⁻¹	Rear tyre stiffness coefficient.

Table 3.3: GSX-R1000 four degrees of freedom reduced model dynamical parameters.

The wheels' motion in this model are considered as vertical with linear stiffness and damping forces acting between the main body and the wheels. On the other

hand, the tyres' forces are modelled as linear springs whose stiffness coefficients are the corresponding to those in the original GSX-R1000 model. The dynamic properties of the reduced model are obtained from the original model as it is shown in Appendix A. The suspensions coefficients and the masses and inertia moment of the four degrees of freedom reduced model are shown in Table 3.3.

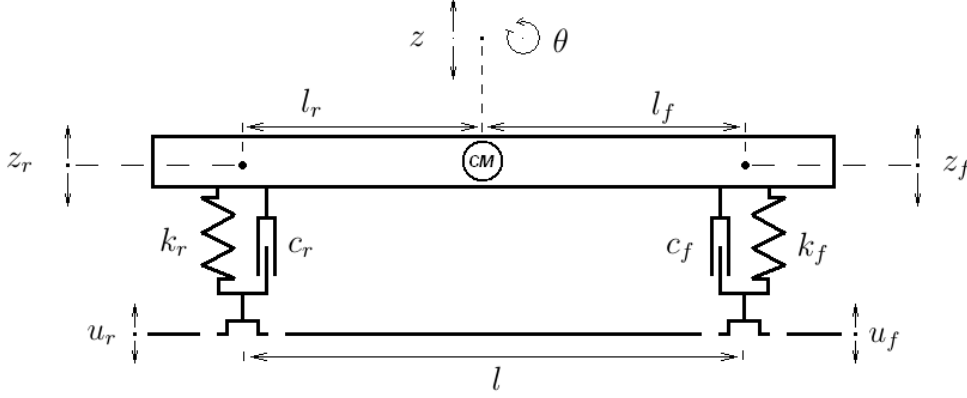


Figure 3.7: Motorcycle's reduced model with two degrees of freedom.

The four degrees of freedom model can be reduced to a simpler model of two degrees of freedom. This model (shown in Fig. 3.7) comprises the main body and the front and rear suspension systems only.

Parameter	Value	Units	Description
m_m	208.80	kg	Main body mass.
I_m	42.35	kgm ²	Main body inertia moment.
l_f	0.663	m	Distance from the center of mass to front end.
l_r	0.659	m	Distance from the center of mass to rear end.
k_f	24.35	kNm ⁻¹	Front suspension stiffness coefficient.
k_r	16.98	kNm ⁻¹	Rear suspension stiffness coefficient.
c_f	2.56	kNsm ⁻¹	Front suspension damping coefficient.
c_r	3.57	kNsm ⁻¹	Rear suspension damping coefficient.

Table 3.4: GSX-R1000 two degrees of freedom reduced model's dynamical parameters.

In this case, the masses of the wheels are not taken into account, considering that they are significantly smaller than the main body mass. Consequently, each stiffness coefficient of the front and rear suspension is calculated as the resultant stiffness coefficient of two in-line springs. These two spring coefficients correspond

to the tyre stiffness and to the reduced suspension spring coefficient in the four degrees of freedom model. The values of the damping coefficients remain similar to those of that model. The parameters of the two degrees of freedom model are shown in Table 3.4.

3.4 Simulations tools

3.4.1 VehicleSim

The GSX-R1000 mathematical model is built and simulated taking advantage of the VehicleSim multi-body simulation software from (Mechanical Simulation Corporation 2015). This suite consists of two separated tools. One of them is VS Lisp and the other is VS Browser. VS Lisp is the tool used to generate solvers for the different vehicles models under study. It uses a computer language designed to automatically generate computationally efficient simulation programs for mechanical systems composed of multiple rigid bodies. VS Lisp can be used in two possible ways: First, the symbolic equations generated by VS Lisp can be directly obtained and used with other software. The second option allows to build new solvers with the same architecture and behaviour as those existing in commercial packages such as CarSim and fully compatible with the VS Browser.

VS Browser is the main program included in all the VehicleSim products, that provides a graphical context with a standard graphical user interface from which the nonlinear simulation can be run and the different databases can be managed. This includes the solvers created with VS Lisp, the external inputs and events and data post processing and visualization. VS Browser has a high flexibility; it allows from introducing on-line model parameters up to third party software compatibility. This is the case of Matlab-Simulink, that can be directly connected to the VS Browser through its own Simulink block. This last feature is very helpful for the nonlinear optimization processes exploited in Chapter 6. On the other hand, once a model solver has been built, it can be tested for different running conditions and for different inputs using the imported tables and events. Furthermore, the parameters defining the model dynamics, such as the suspensions or the aerodynamics coefficients, can be modified directly on VS Browser without modifying the model solver. Figure 3.8

shows the most used functionalities in the VS Browser front end.

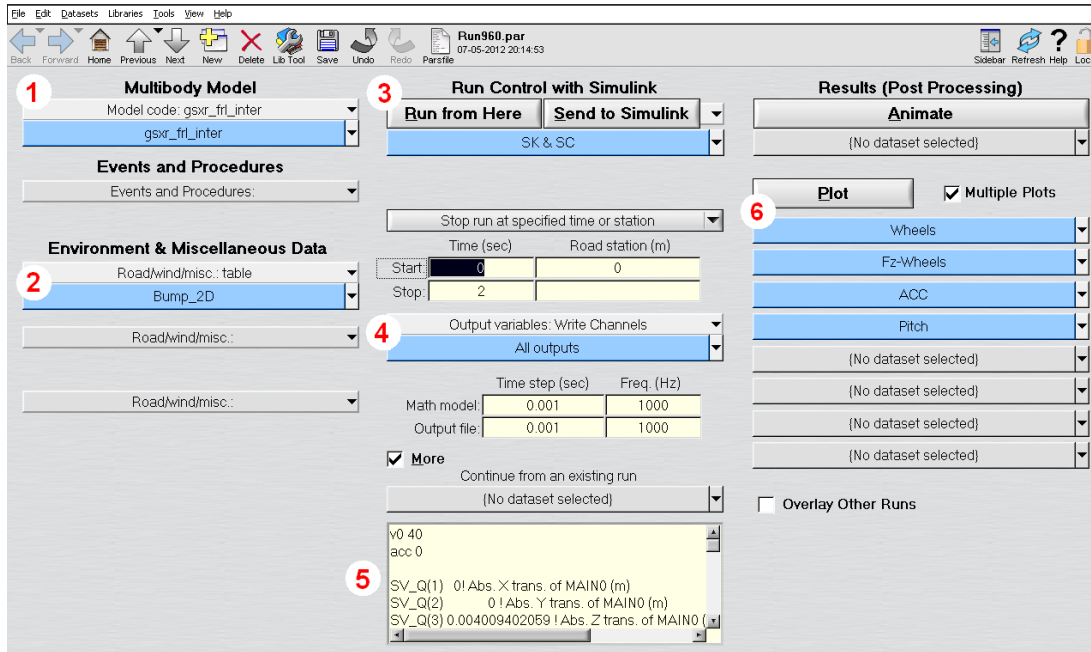


Figure 3.8: VS Browser graphical user interface. 1) Selection menu for the different mathematical models. 2) External event such as road profiles, bump inputs, etc. can be configured and imported from here. Several external event can be imported in the same simulation. 3) The Simulink block and the different solvers are configure and run from these menus. 4) The simulation time, the time step and the outputs sampling frequency are set up from here. 5) The model’s physical parameters and the state variables’ initial values can be directly modified by the user. 6) The plotting tool can be configured to automatically return the time-story of the chosen variables. Several plots can be configured at the same time.

Another good advantage of VehicleSim is that it can be configured to return the linearised symbolic equations of motion. A Matlab file with the state space description can be obtained containing the A, B, C and D matrices depending on the inputs and outputs defined during the model programming. These matrices are symbolically described and depend on the state variables values. In order to obtain an adequate description of the model, they must be fed with equilibrium states variable values. Then, the numerical matrices obtained, represent the linear equations of motion for small displacements around the considered equilibrium state.

3.4.2 State space description

From the numerical representation of the state matrix A, the eigenvalues and eigenvectors can be computed. The stability of the system around an equilibrium state can be studied through the root locus of this matrix. On the other hand, the system’s normal modes are described by the matrix A eigenvectors. The basis in which

this matrix is represented is that of the system’s generalized coordinates and velocities, in this case, they correspond to the motorcycle degrees of freedom listed in Table 3.5.

The building up of a model process in VS Lisp follows a parental structure in which the degrees of freedom of each body are expressed on its parent reference frame. Each body in the system has its own reference frame whose origin is located at the point where it is connected to its parent. Its centre of masses is defined in this local reference frame. When a body lacks of a parent it is referred to the inertial reference frame.

DOF	Description
XT, YT, ZT	Motorcycle chassis x , y and z translation.
ZR, YR, XR	Motorcycle chassis yaw , $pitch$ and $roll$ rotations.
SWA	swinging arm rotation about the main frame’s y axis.
UBR	Rider upper-body rotation about the main frame x axis.
TWS	Front frame rotation about the $twist$ axis.
STR	Front frame rotation about the $steering$ axis.
SUS	Front fork compression/extension.
FW	Front wheel rotation about its y axis.
RW	Rear wheel rotation about its y axis.

Table 3.5: Degrees of freedom of the GSX-R1000 multi-body system.

The generalized coordinates that VS Lisp uses to describe the system are the degrees of freedom of all the bodies related to their parents’ reference frames, following the user definition of the bodies. However, when a body is described with several rotational degrees of freedom, VS Lisp does not describe all of them in the same reference frame, but it introduces intermediate coordinates systems for each rotational degree of freedom, keeping the order specified by the user when the body’s degrees of freedom are introduced.

In the case of the GSX-R1000 model, the main body of the motorcycle assembly is the chassis. It is defined in the inertial reference frame and it has six degrees of freedom: three translational and three rotational. The three translational ones are related to the inertial reference frame (S_0) and they describe the rectilinear motion

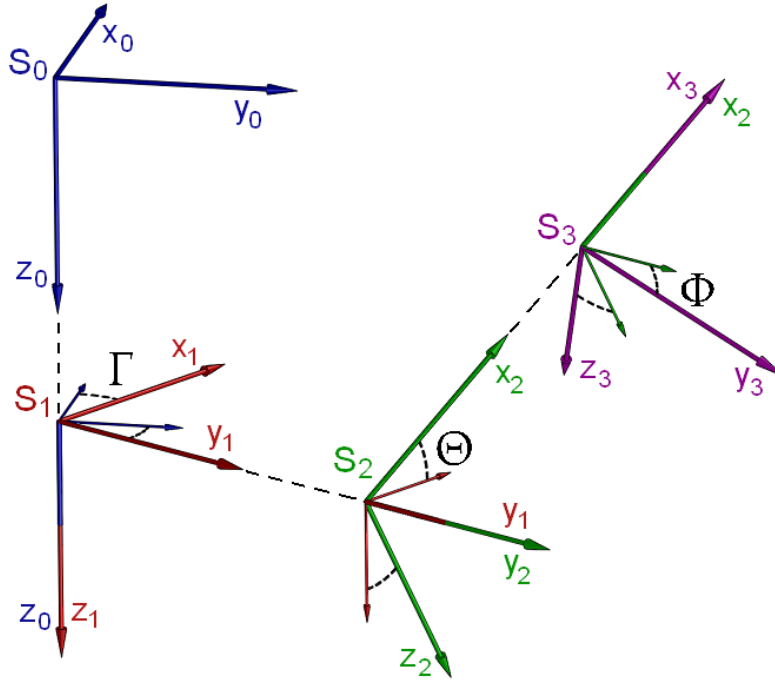


Figure 3.9: Auxiliary frames created by VS Lisp with each rotation of the body. Note that the frames are represented separately in order to show a clearer view of each rotation, nevertheless, the origins of all of them are coincident.

along the x , y and z axis of the origin of the chassis reference frame (S_1). Regarding to the rotational degrees of freedom, three possible rotations are defined. The yaw angle is the rotation about the inertial reference frame z axis. This rotation creates a new reference frame (S_1) sharing the z axis with S_0 and rotated Γ° about it. The pitch angle is the rotation about the y axis of S_1 . This rotation introduces another reference frame (S_2) which shares the y axis with the S_1 frame and which is rotated Θ° about it. Finally, the roll angle is the rotation about the S_2 x axis. The final reference frame is S_3 and it is rotated Φ° about the S_2 x axis, which is shared by both S_2 and S_3 . Figure 3.9 shows the three auxiliary reference frames created by each rotation about the main axes.

The rest of the motorcycle's bodies are defined with one degree of freedom each. The swinging arm y rotation, the rider's upper body x rotation and the twist body rotation about the twist axis are defined in the chassis reference frame S_3 . The steer body rotation about its z axis is defined in the twist body reference frame and the front suspension body z translation is defined in the steer body's reference frame. The rear and front wheels y rotations are related to the swinging arm and the front suspension reference frames respectively.

The eigenvectors of matrix A are mathematical representations of the system's normal modes; each component of these eigenvectors represents the relative amplitude and phase angle of the corresponding degree of freedom within the normal mode associated to this eigenvector. For the motorcycle's normal modes, the small oscillations of the chassis six degrees of freedom are not expressed on its own reference frame (S_3). The eigenvector components for the yaw (ZR), the pitch (YR) and the roll (XR) angles are related to S_1 , S_2 and S_3 reference frames respectively. Whilst those components for the translational oscillations (XT , YT and ZT) are related to the S_0 reference frame. Therefore, the modal description depends on the motorcycle's trajectory and the chassis orientation. In order to obtain understandable normal modes descriptions, all these components are translated into the chassis reference frame S_3 , as it is explained in Appendix B. So that, a normal mode can be understood as a small oscillation of each degree of freedom related to the motorcycle's symmetry plane.

3.5 Dynamic behaviour of the nominal model

Once the motorcycle model has been programmed and the corresponding solver has been built, nonlinear simulations can be performed for any running conditions and with several external inputs, obtaining in this way the response of the outputs. On the other hand, a Matlab file with the state space description can be obtained and used to study the stability of the motorcycle models.

In most of the following chapters of this thesis, several root loci of different motorcycle systems are provided and used as a graphical tool to study the stability properties of those systems. The normal modes characteristics are studied through the eigenvectors. Both eigenvalues and eigenvectors are obtained from the system's matrix A , which has to be fed with the frozen-time values of the equilibrium states in order to accurately reproduce the system's dynamics.

The nonlinear equations of motions obtained by VS Lisp are used to integrate the state variables time histories for either straight running conditions or steady turns, which feed the state space matrix A . Speed and roll angle feedback controllers are used to reach the equilibrium states during the simulation. However, in the model's

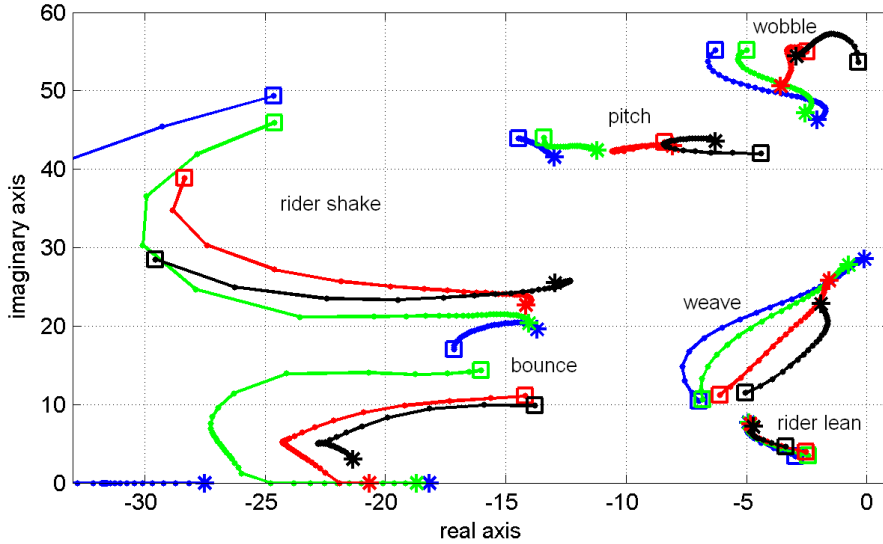


Figure 3.10: Root locus for the nominal motorcycle model showing the main normal modes. The speed is increased from 10 m/s (□) to 80 m/s (*) and different roll angles are considered: 0° (blue), 15° (green), 30° (red) and 45° (black).

state space description these feedback controls are disabled in order to study the open-loop system stability. Figure 3.10 shows the typical root loci for the nominal GSX-R1000 model. Four different roll angles are shown (0°, 15°, 30° and 45°) for forward speeds ranging from 10 m/s up to 80 m/s. The main normal modes affecting the motorcycle’s stability are shown. Four out-of-plane modes and two in-plane modes can be seen. The out-of-plane modes are wobble, weave, the rider’s lean and the rider’s shake modes, which affect the degrees of freedom corresponding to motions out of the motorcycle’s symmetry plane. On the other hand, pitch and bounce modes are in-plane modes affecting the motions inside the symmetry plane. However, when the motorcycle is leant, the various degrees of freedom become coupled and all the modes contain in-plane and out-of-plane components. Although some of these modes, such as pitch, bounce and rider’s shake, are highly damped for the system’s nominal configuration, in the following chapters of this thesis, it will be shown how these mode’s damping properties change under other suspension configurations and a deep study will be carried out.

In order to obtain an idea on how the motion involved in each mode is, its corresponding associated eigenvector is studied. For any given equilibrium state, the magnitude and the phase of each eigenvector’s component are obtained. With these results, similar plots to those in Fig. 3.11 can be drawn. In Fig. 3.11 the magnitude

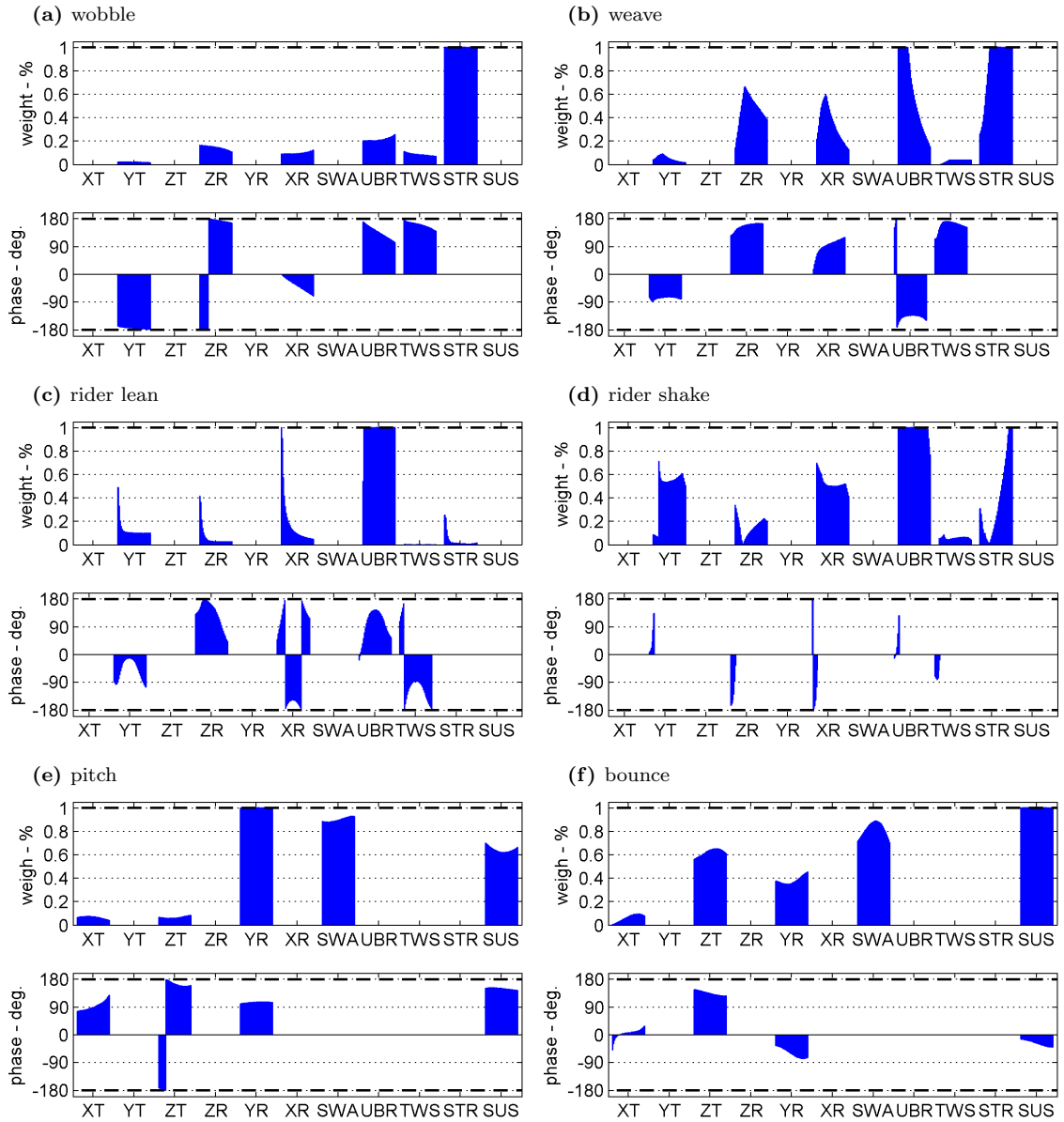


Figure 3.11: Normal modes' components for the nominal motorcycle model under straight running conditions. The speed evolution of each component's weight and phase is represented by the bars profile, varying the speed from left (10 m/s) to right hand side (80 m/s). For each mode, the upper bar diagram represents the normalized weight of its components in the general mode motion. The lower bar diagram represents the phase angle. The steering angle component's phase is taken as reference for the out-of-plane modes. For the in-plane mode, the swinging arm component's phase is taken as reference.

and phases of the eigenvectors' components for zero roll angle running condition are shown. These eigenvectors correspond to the eigenvalues in Fig. 3.10 for straight running conditions (blue \times). The upper bar diagram represents the eigenvector's components magnitudes (these are the relative amplitudes of the degrees of freedom involved in the normal mode motion) whilst the lower diagram shows the phases of the components (the relative phase angle of the oscillation of each degree of freedom). The motorcycle's system has thirteen degrees of freedom and the eigenvectors obtained from the matrix A have twenty-six components, thirteen generalized positions and thirteen generalized speeds. In order to obtain a clear understanding of the motion that a normal mode represents with a simplified view, the attention will be focussed on eleven of these twenty-six variables: six degrees of freedom of the chassis, front suspension translation and rider's upper body, twist, steer and swinging arm rotations.

The magnitude and phase bars that represent each eigenvector's component show shaped edges. The heights of these edges are the values of either the magnitude or phase of this component at the corresponding forward speed, ranging from 10 m/s (at the left-hand side) up to 80 m/s (at the right-hand side).

Both weave and wobble modes have been deeply studied in the literature (Sharp 1971, Cooper 1974, Koenen 1983, Limebeer & Sharp 2006, Evangelou et al. 2008, etc.) due to their proximity to the unstable area, which in some cases becomes a risk for the rider's safety and system's integrity. Figure 3.11a shows the bar diagram for the wobble mode at zero roll angle. This mode is characterized by a violent front frame shaking about the steering axis whilst the rear frame is only slightly affected. The typical frequencies of wobble oscillation in sport motorcycles may vary between 40 rad/s and 60 rad/s and this mainly depends on the mechanical trail, the front tire cornering stiffness and the steer body inertia.

The weave mode eigenvector components are shown in Fig. 3.11b. This mode is characterized by roll, yaw and steering angle oscillations at medium and high forward speeds. At low speed, the rider's upper-body oscillation has main relevance, whilst for higher speeds this component magnitude is quickly reduced and the steering oscillation is increased. This mode is well damped at moderate speeds, but becomes less at high speeds. Its natural frequency rises from zero at very slow speeds to

about 30 rad/s for higher speeds. This frequency highly depends on the motorcycle's velocity, mass and size. Lower frequencies correspond to heavier motorcycles and vice versa.

The rider's lean mode (shown in Fig. 3.11c) appears when the rider's upper-body degree of freedom is included in the model's description. It consists in a low frequency (3 rad/s – 9 rad/s) and high amplitude oscillation of this body. For very low speeds the roll and chassis lateral displacement show high amplitudes, being the roll angle the most relevant degree of freedom. However, these components are quickly reduced when the speed is increased. It is a well damped mode that hardly affects the motorcycle's stability.

The rider's shake mode is also associated to the rider's upper-body degree of freedom. Its motion consists in the shaking of the rider with high frequencies at low speeds (about 50 rad/s). Nevertheless, when the speed is increased, it quickly becomes over-damped for the zero roll angles running conditions. Figure 3.11d shows how the relative phase of all its components become zero as the imaginary part of its associated eigenvalue does so too. However, when the motorcycle is leant, this trend with the speed reverts and, although the frequency is reduced, the mode remains oscillating.

The pitch mode is shown in Fig. 3.11e. It consists in the chassis pitching with large oscillations of the front and rear suspensions. The phase angle existing between the motorcycle's front suspension with respect to the swinging arm is about 180°. The differences in terms of masses, stiffness and damping between the front and the rear motorcycle's ends on this model, introduce other oscillations components such as vertical and horizontal chassis displacements. For a fully symmetrical model, these last oscillation components would not exist. This mode is well damped, observing smaller values of damping for higher roll angles. Its frequencies for all running conditions studied are constricted between 40 rad/s and 45 rad/s and do not significantly depend on the speed.

Figure 3.11f shows the bounce mode's components. This mode is a main frame's vertical oscillation. This motion is in phase opposition with front and rear suspensions. Due to the asymmetry around the model's centre of masses, pitch and longitudinal oscillation are involved on the bounce mode. At zero roll angle, its fre-

quency is not affected by the forward speed and remains around 20 rad/s. However, once the motorcycle starts leaning, the evolution of this mode with the speed results in a reduction of its frequency until it becomes non-oscillating at higher speeds, whilst its damping ratio is increased.

All these modes and their interactions are studied further in Chapter 7 in which the interconnection of the front and rear suspension systems is investigated as a method of improving the overall suspension's performance.

3.6 Conclusions

In this chapter the basis of the mathematical model used along this thesis has been presented. It consists in a variation of an existing high fidelity model of a Suzuki GSX-R1000 sport motorcycle, which has been widely used and tested in the existing literature. Some necessary additional features have been included in the model in order to obtain some specific results on the dynamics of the different alternative suspension systems under study in this work.

Two in-plane linearised reduced models of the GSX-R1000 have been provided. This is a full dimensional nonlinear model, however, for some mathematical derivations in Chapter 5, the reduced models are needed. First, a single body model with two degrees of freedom is used to study the basis of the pitch and the bounce motion in the motorcycle's planar dynamics. Then, a second model with four degrees of freedom, including the wheels, becomes necessary for a better understanding on these dynamics.

VehicleSim MBS software, used to build the model's equations of motion is introduced. The state space description obtained with this software is presented. It is found that a change of basis is necessary in order to obtain an understandable representation of the normal modes through the eigenvectors and eigenvalues description.

Finally, the typical results expected from this model are shown. Root loci of the main oscillating modes are plotted and a pattern of motion of the different modes is obtained via the model's eigenvectors. The amplitudes and phases of their corresponding degrees of freedom are presented for the nominal motorcycle

model under straight running conditions. This is a useful tool to understand the motorcycle's motion behaviour for each normal mode.

The mathematical framework in which all the simulation work performed in this thesis is based on, has been introduced in this chapter. In the subsequent chapters, several references to it will be found.

Chapter 4

Double Wishbone Suspension Systems

The motorcycle's front end links the front wheel to the motorcycle's chassis and has two main functions: the front wheel suspension and the vehicle steering. Up to this date, several suspension systems have been developed in order to achieve the best possible front end behaviour, being the telescopic fork the most extended one. It consists of a couple of outer tubes which contain the suspension components (coil springs and damper) internally and two inner tubes which slide into the outer ones allowing the suspension travel. Traditionally the inner tubes are attached to the frame through two triple trees which connect the front end to the main frame through the steering bearings and allow the front wheel to turn about the steering axis. This system keeps the front wheel's displacement in a straight line parallel to the steering axis. There exist alternative suspension designs that allow different trajectories of the front wheel with the suspension travel. The aim of this chapter is to study the effect of this type of systems on a sport motorcycle's dynamics. These systems can be divided into two main groups. One of them presents the steering axle located between the chassis and the suspension elements (wishbones in most of the cases). And on the other, this axle is placed between the suspension elements and the front wheel. Two double wishbone systems are considered in this chapter as representative of these two groups: the girder suspension and Hossack system. In both cases, the system can be designed in order to provide a desired front wheel trajectory, however whilst the girder suspension keeps the steering angle

fixed in the chassis reference frame, the Hossack system modifies it with the travel of the suspension. Other double wishbone suspension systems behave similarly to the girder suspension, as is the case of the leading link. On the other hand, there also exist different systems that, being of a different construction, result in a similar behaviour to the Hossack system. This is the case of most of the hub-centre steering suspension systems. Figure 4.1 shows 3D models of a telescopic fork, a Hossack system and a girder suspension.

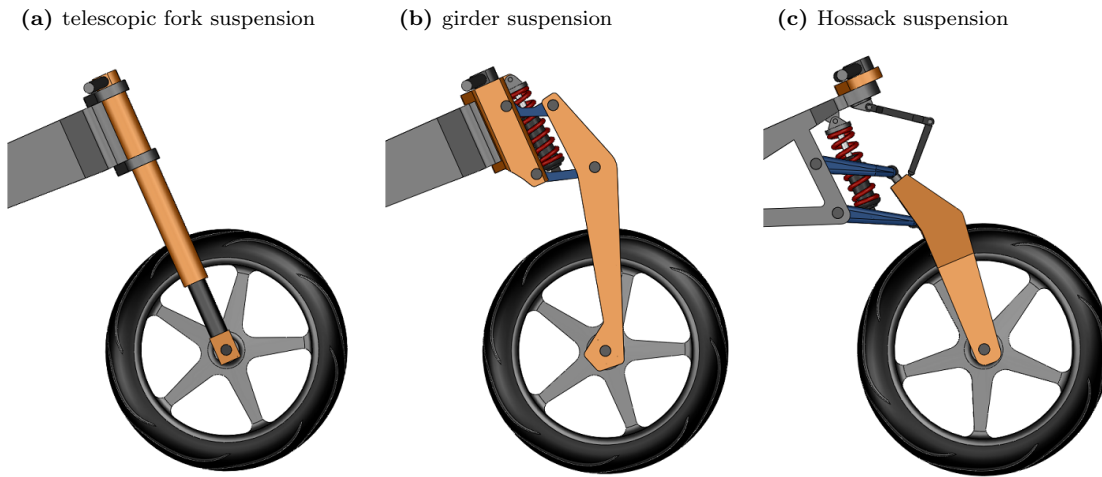


Figure 4.1: 3D models for a telescopic fork (a), a girder (b) and a Hossack (c) suspension systems.

The girder's fork consists of a pair of long uprights where the front wheel is attached to. These uprights are linked to the triple trees by an upper and a lower wishbones which perform the suspension motion. Both triple trees rotate about the steering axle which is fixed to the motorcycle chassis. A spring-damper unit is usually attached between the lower wishbone and the upper triple tree providing the shock absorption function. On the other hand, the Hossack suspension system consists of a double wishbones structure directly attached to the chassis. The two wishbones rotate about both axes perpendicular to the symmetry plane of the motorcycle, providing the suspension motion. An upright is linked to the front tips of the wishbones by two ball joints, which allow it to turn left and right as well as to move up and down. Therefore, the steering axis becomes defined by the imaginary line passing through the geometric centre of the ball joints. The control over the steering angle is applied by the rider to the handlebar which is connected to the upright through the steering linkage. This is a system of two levers connected by

an axis, which can be compressed or elongated in order to reach the length between the handlebar and the upright. The front wheel is attached to this upright and the suspension reaction is provided by a spring-damper unit attached between the lower wishbone and the motorcycle chassis. In terms of kinematics, it can be said that these two types of designs cover most of the existing double wishbone suspension system.

4.1 Kinematics

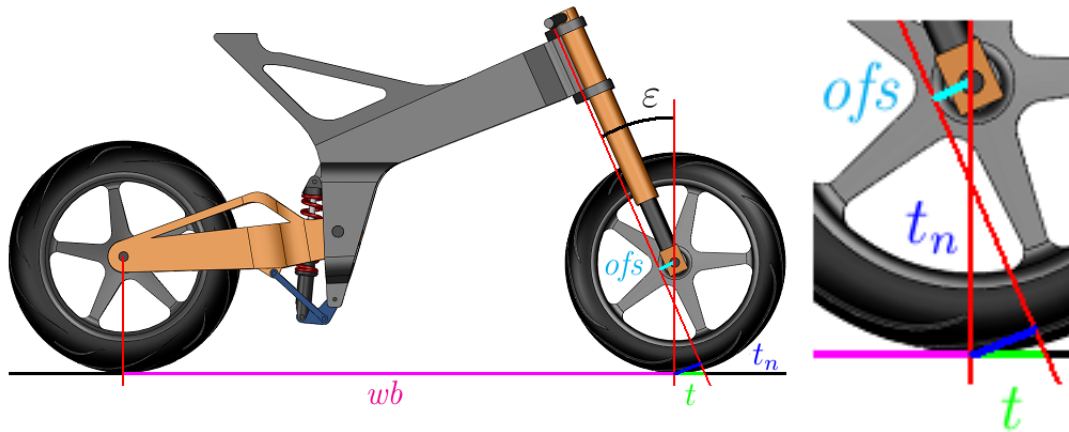


Figure 4.2: Main motorcycle's handling geometric parameters. The wheelbase (wb) is plotted in a solid magenta line, the trail (t) in green, the normal trail (t_n) in blue and the head angle (ε) in black. The fork offset (ofs) is also shown in solid cyan line.

The motorcycle handling is affected for some geometric parameters which are defined by the front end design. Figure 4.2 presents the four more relevant geometric parameters for the motorcycle handling. These are the trail (t), the normal trail (t_n), the head angle (ε) and the wheelbase (wb). The wheelbase is the distance between the front and rear wheels contact points. The head angle is the angle between the steering axis and the vertical. The trail is the distance between the front wheel contact point and the point where the steering axis intersects with the ground. Finally, the normal trail is the trail distance projection into a plane perpendicular to the steering axis. This is the lever arm of the front tyre forces appearing on its contact point, which result in a torque about the steering axis. The trail (t), the normal trail (t_n) and the head angle (ε) are related to each other by the following

expressions:

$$t_n = r_{fw} \cdot \sin(\varepsilon) - ofs \quad (4.1)$$

$$t = \frac{t_n}{\cos(\varepsilon)} \quad (4.2)$$

r_{fw} is the tyre's radius and ofs is the front wheel's spindle offset from the steering axis. The wheelbase also depends on the rear frame construction including the swinging arm. In the case of a conventional telescopic fork, the steering axle is rigidly inserted into the chassis whilst the offset is a constant value. Therefore, when the fork is compressed the wheelbase and the head angle decrease and, thus, the trail and the normal trail. Figure 4.3 shows the behaviour of these magnitudes with the vertical suspension travel ($v.s.t.$). The vertical suspension travel is defined as the vertical travel of the front wheel centre when the suspension system is compressed ($v.s.t. > 0$) or extended ($v.s.t. < 0$) considering the chassis fixed in the inertial frame. This definition is valid for all the different suspension systems and provides a general magnitude that can be used to compare various behaviours.

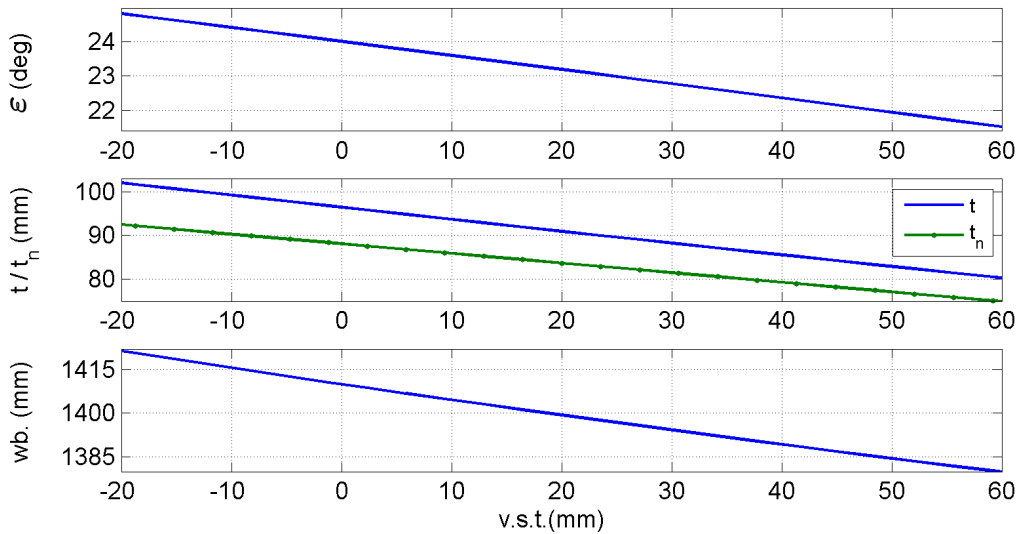


Figure 4.3: Telescopic fork's handling geometric parameters variation with the suspension travel. The head angle (ε), the trail (t), the normal trail (t_n) and the wheelbase (wb) variation with the vertical suspension travel ($v.s.t.$).

For the double wishbones systems this behaviour can be modified. In the case of the girder system, the offset is variable with the travel of the suspension, this is the turn of the wishbones. For the Hossack system, it is the steering axis which varies with respect to the chassis when the suspension is compressed. In both cases, and

according to Eq. 4.1, different behaviour of the handling geometric parameters can be achieved along the suspension travel. Figure 4.4 illustrates this concept for these three mechanical arrangements.

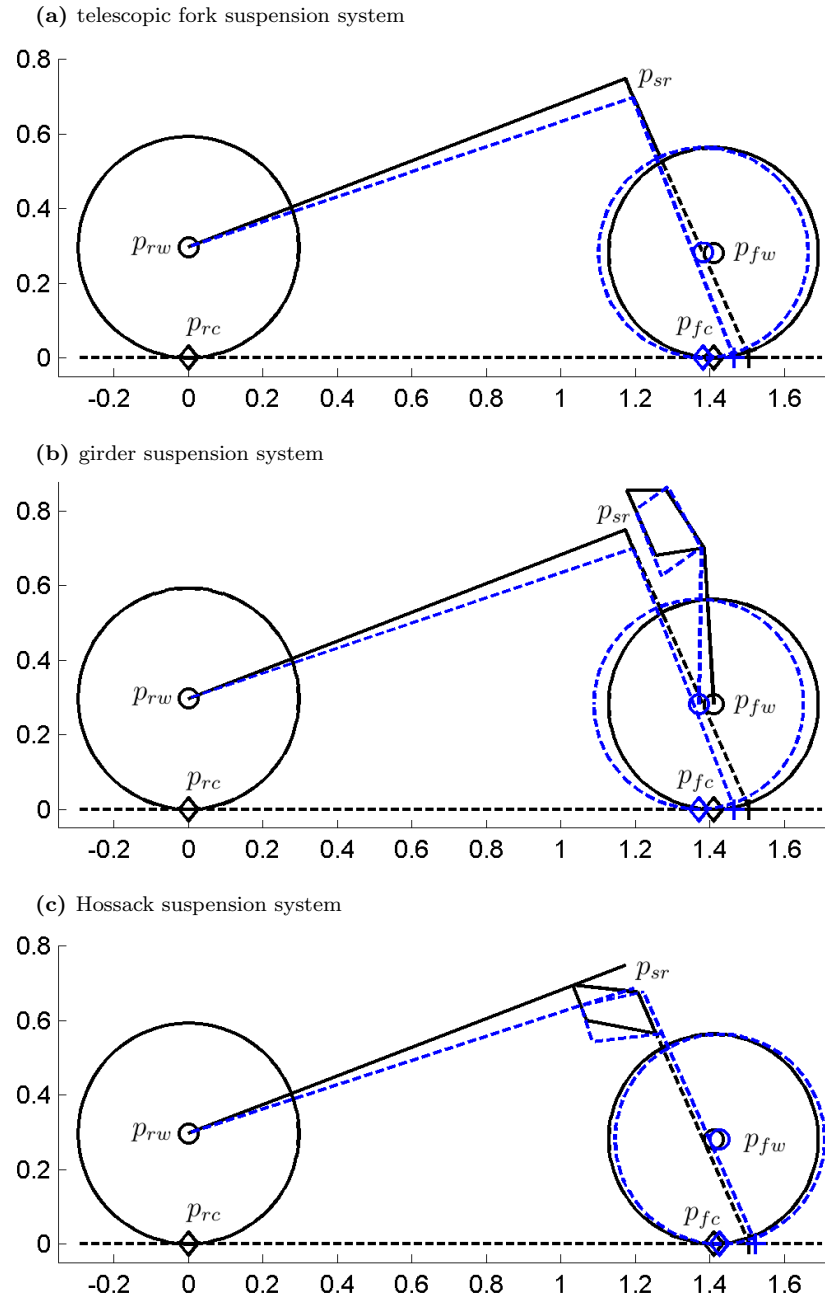


Figure 4.4: Motorcycle's geometry variation with the vertical suspension travel for the telescopic fork (a), the girder (b) and the Hossack (c) suspension systems. Solid blue line represents the motorcycle's nominal position. The motorcycle with compressed suspension appears as dashed blue lines. The axes units are expressed in metres.

It can be observed how for the telescopic fork case in Fig. 4.4a, the wheelbase, normal trail and head angle are decreased when the suspension is compressed. In the example of the girder suspension system in Fig. 4.4b, the mechanical layout results

in a constant normal trail. In this case, a constant normal trail implies a wheelbase decrease. Due to the fact that the steering axle is fixed to the motorcycle chassis, the offset on the uprights must be increased negatively. Therefore, the front wheel contact point is moved backwards whilst the head angle is inevitably reduced. In Fig. 4.4c, the Hossack system layout, also shows a constant normal trail. For this system, the front wheel offset is constant and the steering axle changes with respect to the chassis. Therefore, a constant normal trail is achieved with a constant head angle, which results in an increase of the wheelbase with the suspension travel.

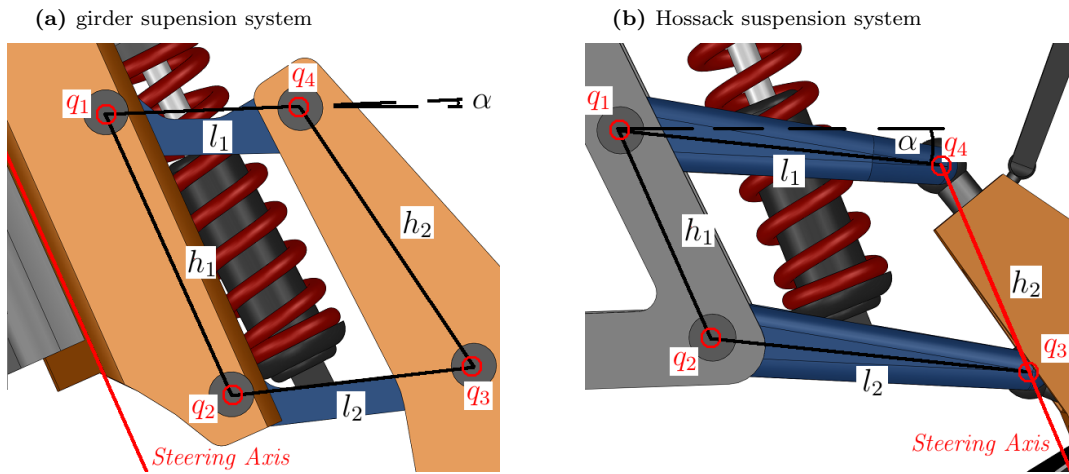


Figure 4.5: Design parameters on the four-bar linkage suspension systems. a) Girder suspension system. b) Hossack suspension system.

Both girder and Hossack systems consist in a four-bar linkage. The difference between them is the edge of the quadrilateral to be considered as steering axis. Figure 4.5 shows the design parameters of the four-bar linkage for these two systems: the lengths of the upper (l_1) and lower (l_2) wishbones, the distances between the attachment points of the wishbones (h_1 on the chassis side and h_2 on the uprights side) and the angle between the upper wishbone and the horizontal at the nominal position (α). With these five parameters full assembly kinematics are defined. The variation of one of them will affect the overall behaviour of the handling geometric parameters with the suspension travel. Different configurations of these five parameters can be calculated to obtain different behaviours of the front suspension systems.

Both suspension systems can be defined by equivalent four-bar linkages geometric points (q_1 , q_2 , q_3 and q_4) which are shown in Fig. 4.5b and Fig. 4.5a. The coordinates

of these points in the motorcycle chassis reference frame for the motorcycle nominal position depend on the design parameters (l_1, l_2, h_1, h_2 and α) and in the front and rear frames geometric points. Figure 4.4b and Fig. 4.4c show a motorcycle sketch with the girder and the Hossack systems respectively. The rear frame geometric points are the rear wheel contact point (p_{rc}), the rear wheel centre point (p_{rw}) and the steering point (p_{rs}). On the other hand, the front frame geometric points are indicated as the front wheel centre point (p_{fw}), the front wheel contact point (p_{fc}) and the point in which the steering axis intersects with the road (p_{fs}). For the synthesis of the suspension mechanisms, the rear frame is considered as rigid, thus the variation in the geometry is produced exclusively by the suspension system deformation.

In order to study the variation of the suspension systems kinematic behaviour, an automated mechanism synthesis approach is developed under a modular methodology. Three main functions are built for each of the suspension systems in order to calculate the geometry variation of the motorcycle fitted with those systems:

- a) Front End Positions (*FEP*): This function depends on which suspension system is considered (girder or Hossack) and calculates the 4-bar linkage points nominal coordinates (q_1, q_2, q_3, q_4) taking as inputs the design parameters (l_1, l_2, h_1, h_2 and α) and considering the coordinates of the default rear and front frames' geometric points.
- b) Suspension Kinematics Loop (*SKL*): This function calls the *FEP* function to obtain the motorcycle nominal geometry depending on the design parameters. Once the nominal geometry is set, the different coordinates of q_3, q_4 and the front frame geometric points (p_{fw}, p_{fc} and p_{fs}) can be calculated in a loop for different values of α , corresponding to a full suspension travel. The function returns the trajectory of the front wheel contact point (p_{fc}) in the inertial frame and the handling geometric parameters values (wheelbase, head angle, trail and normal trail) for each loop's iteration.
- c) Target (*Tgt*): This function uses the *SKL* function outputs. It allows to choose between different targets, which can be either a defined p_{fc} trajectory or a desired value of any of the handling geometric parameters. The function returns the error between the defined target and the corresponding *SKL* function output. The

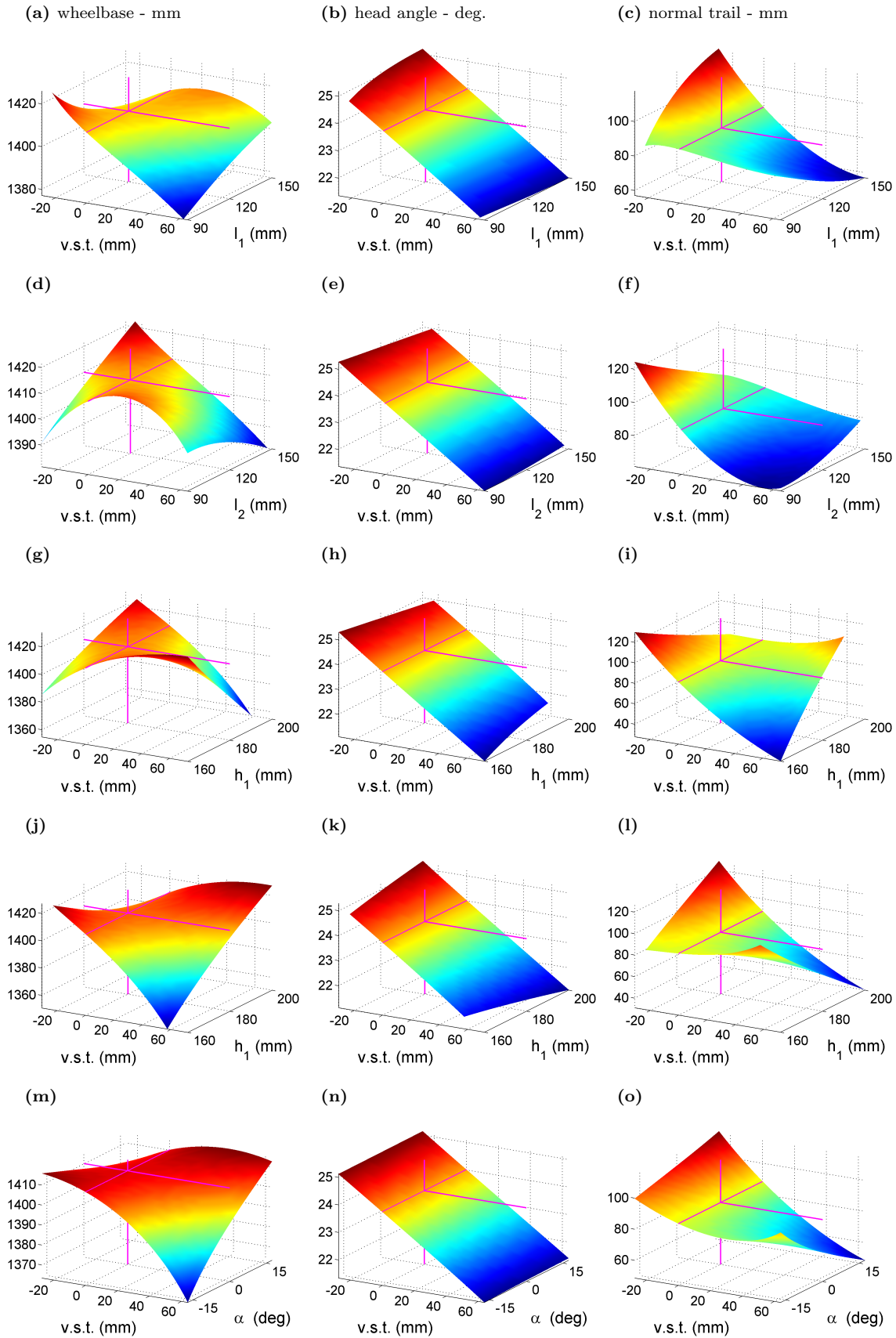


Figure 4.6: Effects of varying the design parameters on the wheelbase, the head angle and the normal trail for the girder suspension system.

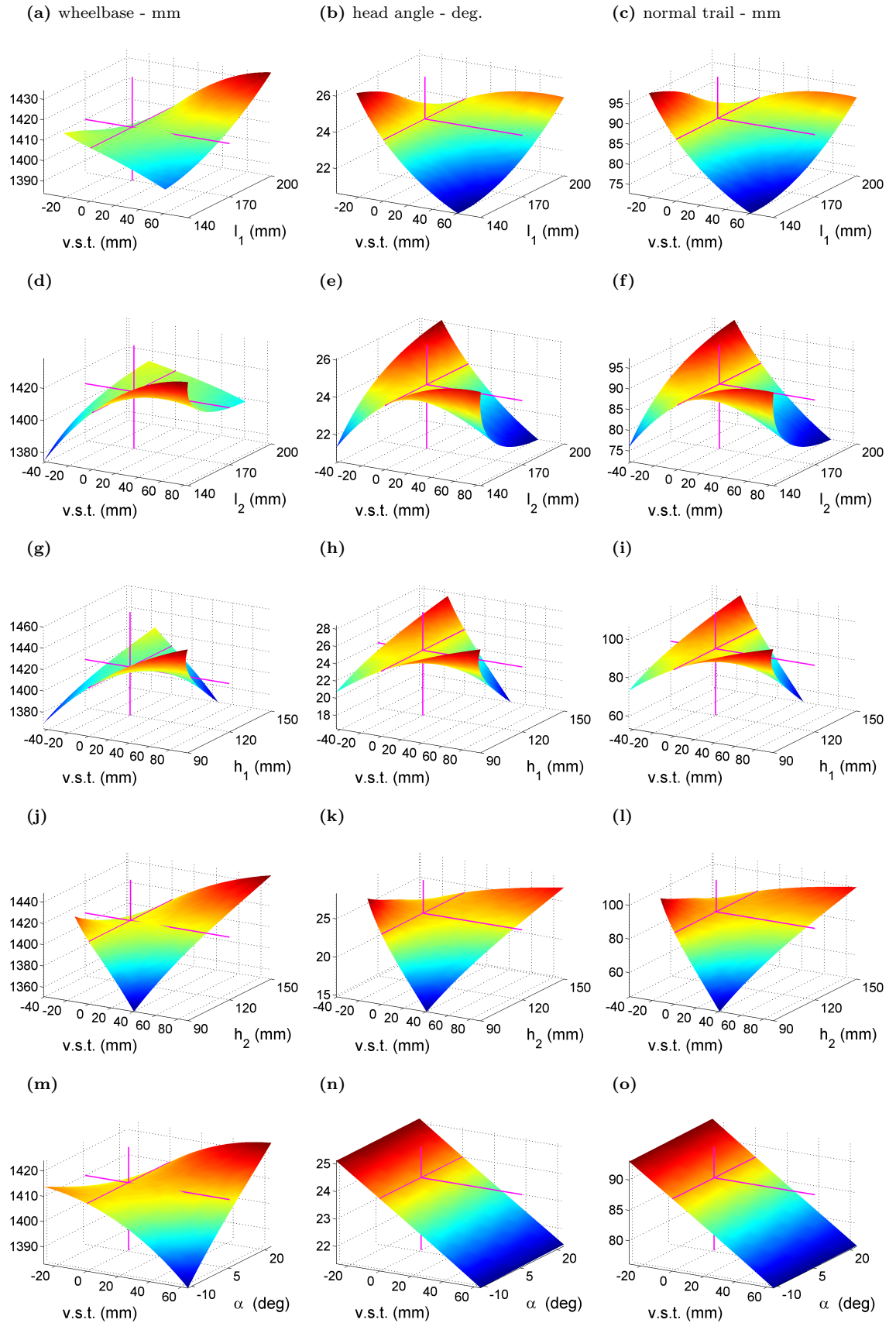


Figure 4.7: Effects of varying the design parameters on the wheelbase, the head angle and the normal trail for the Hossack suspension system.

error is calculated as the square mean of the difference between the target variable value and the variable value returned by the *SKL* function in each iteration point.

With these functions, the impact of varying each design parameter value on the handling geometric parameters can be mapped. Figure 4.6 shows the effects of modifying these parameters on the variation with the vertical suspension travel of the wheelbase, the head angle and the normal trail for the girder suspension system. Only the normal trail will be taken into consideration as it is the actual lever arm of the front wheel force about the steering axis, whilst the trail can be obtained as a simple function of the former as indicated in Eq. 4.2.

As it can be expected, as the steering axle is fixed to the chassis, the head angle behaviour does not change with the variation of any of the design parameters. However, the wheelbase and the normal trail behaviours are affected by these parameters values. This suspension system can be designed to perform a prescribed behaviour of the wheelbase and the normal trail whilst the head angle behaviour cannot be modified.

Similar results are shown in Fig. 4.7 for the Hossack system. In this case, a close relation between the head angle and the normal trail behaviours can be observed due to the variable steering axis and the constant offset. The wheelbase variation does not present such a relation. Different values of α affect the wheelbase behaviour whilst the head angle and the normal trail keep their nominal response. Therefore, either the desired wheelbase or head angle variations given certain vertical suspension travel can be found with the Hossack suspension system. The trail and the normal trail are closely related to the head angle in this system.

In order to obtain a desired behaviour of the suspension system under study, several optimization processes are carried out. These processes take advantage of the Matlab optimization toolbox, which is proven to be an adequate framework for this kind of problems. The *fminsearch* function is used to minimize the error returned by the *Tgt* function. It quickly converges returning the necessary parameters values that result in the desired suspension behaviour. Three different configurations are designed for both the girder and the Hossack suspension systems:

- a) Parallelogram (*prl*): The suspension systems are designed with l_1 , l_2 , h_1 and h_2 as two pairs of parallel sides and with $\alpha = 0$, being this the simplest configuration.

No optimization process is needed.

- b) Telescopic fork's trajectory (*tft*): The suspension systems are designed to allow for a front wheel trajectory similar to that followed by the front wheel in the case of motorcycle being fitted with a telescopic fork system.
- c) Constant normal trail (*cnt*): The suspension systems are designed to allow for a constant normal trail along the full suspension travel.

After the synthesis processes, the values of the design parameters obtained are given in Table 4.1 and Table 4.2.

Girder configurations	l_1 (mm)	l_2 (mm)	h_1 (mm)	h_2 (mm)	α (deg.)
Parallelogram	120	120	180	180	0.0
Fork trajectory	107	135	171	172	0.0
Constant t_n	106	131	192	185	0.0

Table 4.1: Design parameters values obtained for the three different girder suspension systems configurations.

Girder configurations	l_1 (mm)	l_2 (mm)	h_1 (mm)	h_2 (mm)	α (deg.)
Parallelogram	170	170	120	120	5.7
Fork trajectory	155	183	127	117	5.8
Constant t_n	173	190	102	123	6.0

Table 4.2: Design parameters values obtained for the three different Hossack suspension systems configurations.

The handling geometric parameters behaviour of the girder and the Hossack suspension systems for the parallelogram (*prl*) configuration are presented in Fig. 4.8a and Fig. 4.9a respectively. Whilst Fig. 4.8b and Fig. 4.9b show the front wheel's contact point trajectory along the full suspension travel (black) for both systems with this configuration. The trajectory corresponding to that of the telescopic fork (magenta) is plotted as a reference in both figures. It can be observed that in both cases the head angle (ε), the trail (t) and the normal trail (t_n) are reduced in compression and increased in extension whilst the wheelbase is always reduced out of the nominal position.

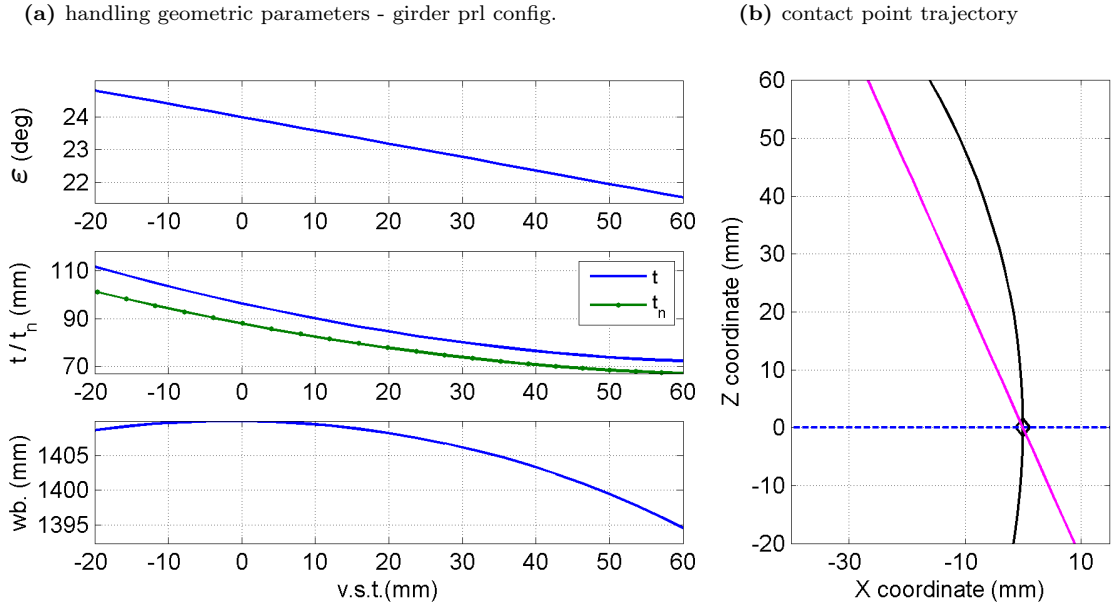


Figure 4.8: Girder suspension system's kinematic behaviour with *prl* configuration. The head angle (ε), the trail (t), the normal trail (t_n) and the wheelbase (wb) variation with the vertical suspension travel ($v.s.t.$) are presented in a). In b) it is plotted the front wheel contact point trajectory along the full suspension travel (black). As a reference, the trajectory corresponding to that of the telescopic fork is plotted in magenta.

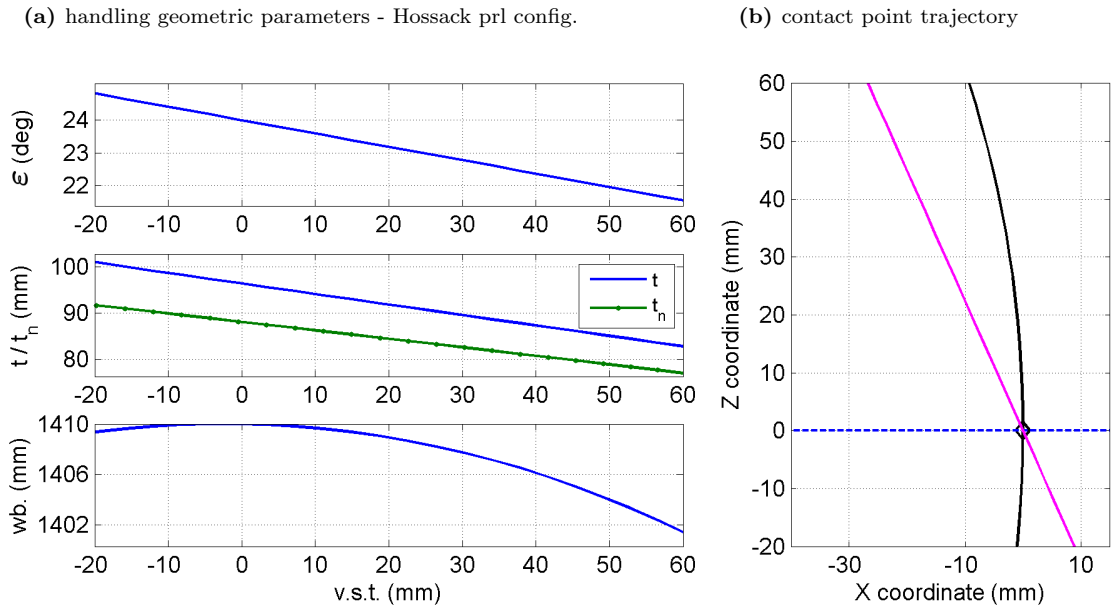


Figure 4.9: Hossack suspension system's kinematic behaviour with *prl* configuration. The head angle (ε), the trail (t), the normal trail (t_n) and the wheelbase (wb) variation with the vertical suspension travel ($v.s.t.$) are presented in a). In b) it is plotted the front wheel contact point trajectory along the full suspension travel (black). As a reference, the trajectory corresponding to that of the telescopic fork is plotted in magenta.

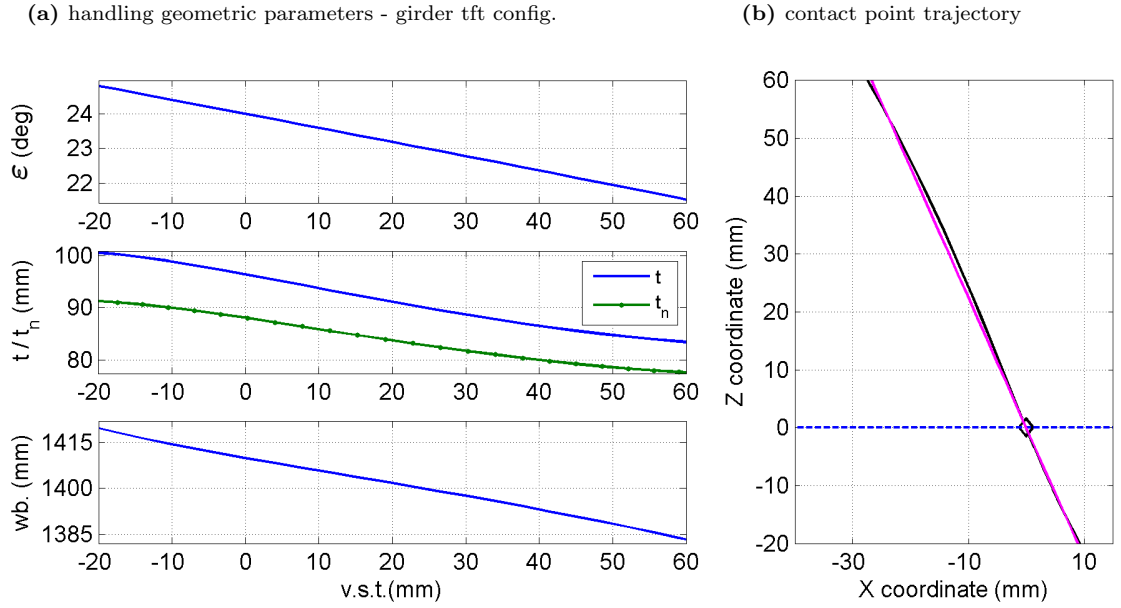


Figure 4.10: Girder suspension system's kinematic behaviour with *tft* configuration. The head angle (ε), the trail (t), the normal trail (t_n) and the wheelbase (wb) variation with the vertical suspension travel ($v.s.t.$) are presented in a). In b) the front wheel's contact point trajectory is plotted along the full suspension travel (black). As a reference, the trajectory corresponding to that of the telescopic fork is plotted in magenta.

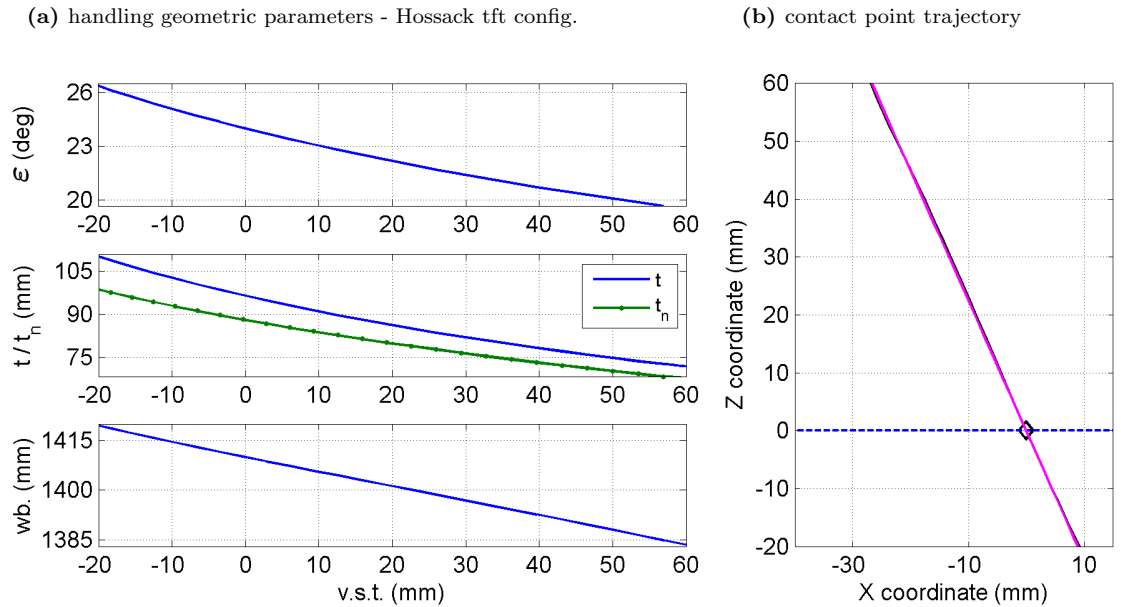
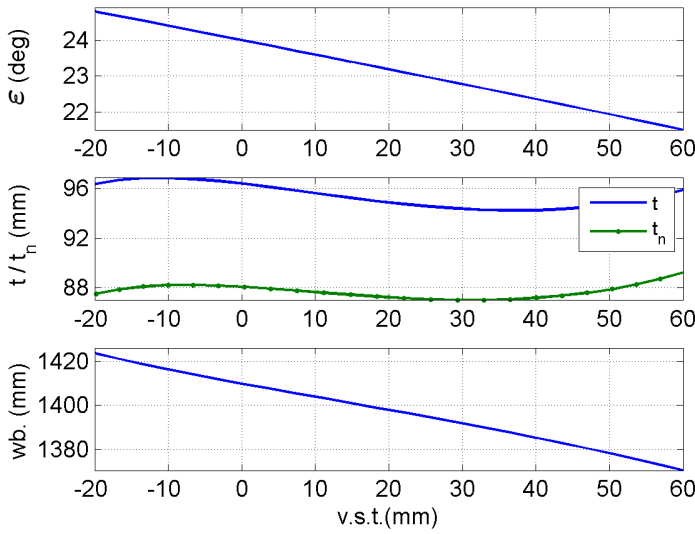


Figure 4.11: Hossack suspension system's kinematic behaviour with *tft* configuration. The head angle (ε), the trail (t), the normal trail (t_n) and the wheelbase (wb) variation with the vertical suspension travel ($v.s.t.$) are presented in a). In b) the front wheel's contact point trajectory is plotted along the full suspension travel (black). As a reference, the trajectory corresponding to that of the telescopic fork is plotted in magenta.

(a) handling geometric parameters - girder cnt config.



(b) contact point trajectory

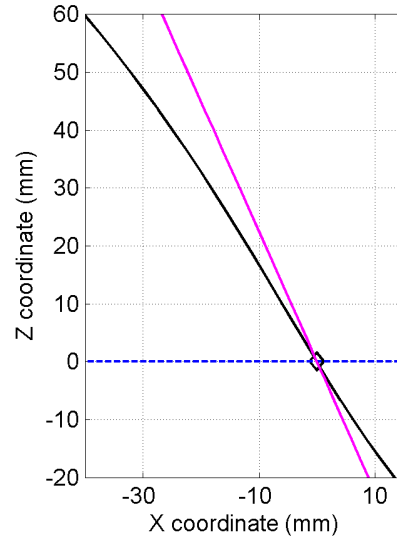


Figure 4.12: Girder suspension system's kinematic behaviour with *cnt* configuration. The head angle (ε), the trail (t), the normal trail (t_n) and the wheelbase (wb) variation with the vertical suspension travel ($v.s.t.$) are presented in a). In b) the front wheel's contact point trajectory is plotted along the full suspension travel (black). As a reference, the trajectory corresponding to that of the telescopic fork is plotted in magenta.

Both systems have similar head angle behaviour. However, the trail, the normal trail and the wheelbase show a wider variation for the girder system case, where the trail and normal trail follow concave curves in comparison to the Hossack trail and normal trail straight lines. Regarding to the front wheel's contact point, both systems show curved trajectories, being the Hossack system's trajectory slightly more vertical.

Similar plots are obtained for the telescopic fork's trajectory (*tft*) configuration of the girder (Fig. 4.10) and the Hossack (Fig. 4.11) systems. The trajectories reached by both systems are almost identical to that of the telescopic fork. In the case of the girder suspension system, the handling geometric parameters behave similarly to those with the telescopic fork suspension shown in Fig. 4.3. This is the expected behaviour once the steering axle and the wheel trajectories are equal in both systems. However, for the Hossack suspension system, the steering axle varies with the suspension travel, which leads to different behaviours of the handling geometric parameters. The variation in the head angle, the trail and the normal trail with the vertical suspension travel are significantly larger for the Hossack system than for the telescopic fork suspension. However, the wheelbase is modified in a

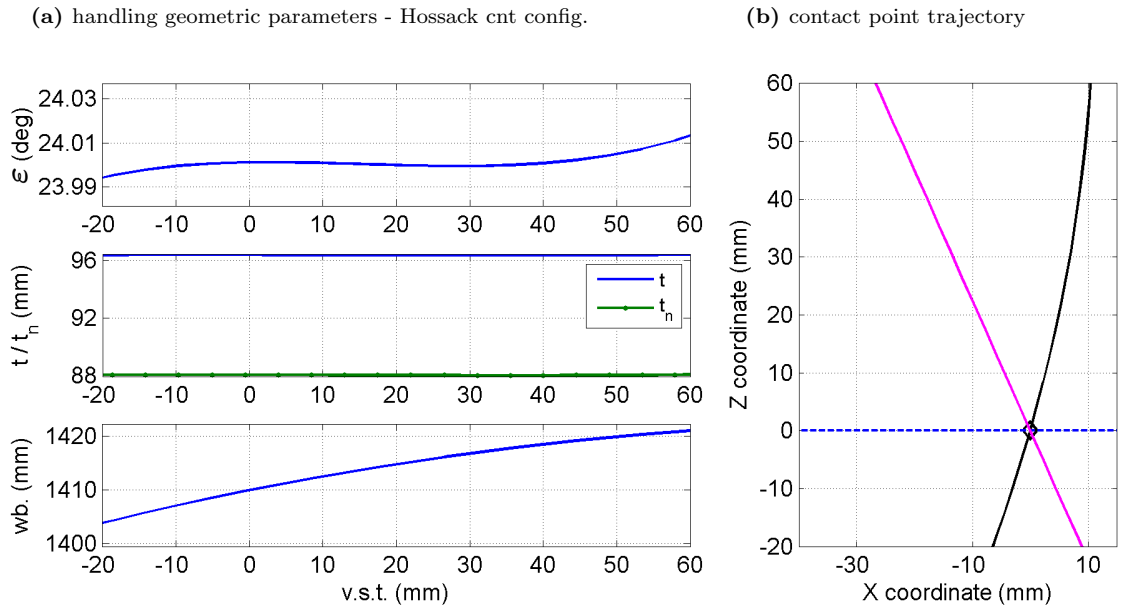


Figure 4.13: Hossack suspension system’s kinematic behaviour with *cnt* configuration. The head angle (ε), the trail (t), the normal trail (t_n) and the wheelbase (wb) variation with the vertical suspension travel (*v.s.t.*) are presented in a). In b) the front wheel’s contact point trajectory is plotted along the full suspension travel (black). As a reference, the trajectory corresponding to that of the telescopic fork is plotted in magenta.

similar way, as the front wheel follows the same trajectory in both cases.

Being the normal trail a crucial parameter in the motorcycle handling, it would be an interesting feature for a suspension system to maintain this value constant at any position of the suspension travel. Kinematic behaviours of the girder and Hossack suspension systems with a constant normal trail (*cnt*) configuration are represented in Fig. 4.12 and Fig. 4.13 respectively. Almost constant trail and normal trail are achieved for the girder suspension system, with small deviations from their nominal values. As expected, the head angle maintains its nominal behaviour with the vertical suspension travel whilst the wheelbase is reduced. On the other hand, for the Hossack suspension system, the trail and normal trail are constant along the full suspension travel. Oppositely to the girder system, the constant normal trail configuration for the Hossack suspension system implies an almost constant head angle, whilst the wheelbase is increased in extension and decreased in compression.

Regarding to the front wheel’s contact point, it can be observed that in the girder system case, the trajectory is mostly a straight line at an angle with the vertical which is greater than that on the fork suspension’s trajectory case. In the case of the Hossack system, the front wheel follows a curved trajectory. The angle with

the vertical becomes negative in this case, reducing its value under compression and increasing it under extension. These trajectory angles will directly affect the suspension systems' anti-dive capabilities. Contrary to the telescopic fork system's behaviour, both systems show a wide range of possible kinematic configurations, either Hossack or girder systems could be a good choice depending on the motorcycle's kinematics requirements.

4.2 Suspension modelling

In order to study the girder and Hossack suspension systems' dynamic properties, two mathematical models have been built using VehicleSim. Each of these models geometry has been modified with the design parameters values obtained in the previous section for the three kinematic configurations: parallelogram (*prl*), telescopic fork's trajectory (*tft*) and constant normal trail (*cnt*). Therefore, three different configurations of each of the girder and Hossack suspension systems are obtained and will be dynamically tested in the following sections.

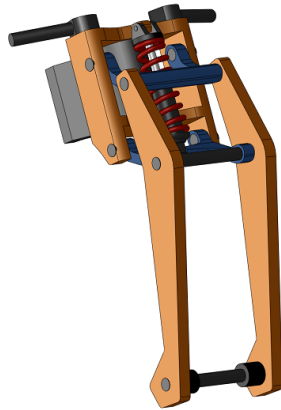
The mathematical models here presented are developed as modifications of the Suzuki GSX-R1000 nominal model, derived in (Sharp et al. 2004), which was built considering the actual physical properties of the original motorcycle's parts. The masses, the moments of inertia and the centres of masses were directly measured for each part. Unfortunately, it does not exist a real GSR-R1000 motorcycle fitted with either a girder suspension or a Hossack system. Therefore, the physical properties of these parts cannot be measured and included in the mathematical model. In order to obtain these values, a 3D computer-aided design (CAD) for each suspension system has been developed as part of the work in this thesis. The software used for this task was SolidWorks (Dassault Systems 2015), which also allowed to perform the different finite element analysis (FEA) through its SolidWorks Simulation tool, needed to determine the designs consistency and reliability.

4.2.1 CAD modelling and FEA analysis

It is important to note that this part of the research is not intended to obtain a high performance commercial suspension systems, but to provide with a good approx-

imation of the mechanical parts involved on each suspension system under study. Therefore, the masses, the centre of masses, the inertia moments, etc. represent close values to those of a possible real suspension system implementation.

(a) girder suspension heavy desing



(b) girder suspension lighth desing

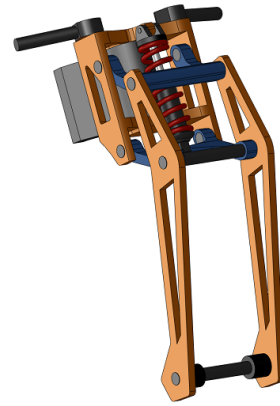
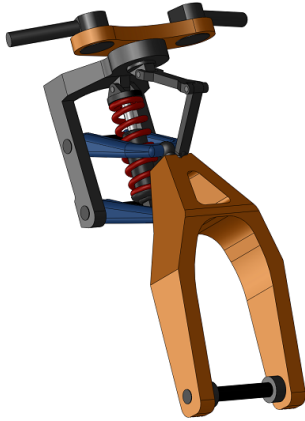


Figure 4.14: Girder suspension system CAD models. a) Girder design with equivalent parts masses to those of the telescopic fork. b) Girder design with reduced parts masses.

Two different models have been developed for each of the two systems, girder and Hossack. The first of them is developed keeping the same front end assembly's mass as that of the original telescopic fork of the GSX-R1000 model. Each part tends to keep the mass equal to the equivalent part in the telescopic fork case. However, due to the structural differences between the three suspension systems, this is not always possible. For instance, in the case of the Hossack system, the steering assembly consists only of a triple tree, being lighter than the telescopic fork's steering body. In this case, the excess of mass of the whole assembly is added to the chassis body as a mass placed in the same coordinates than those of the steering body's centre of mass. The second model of each suspension system has been designed in order to explore the mass reduction allowed by these systems and its effects on motorcycle dynamics. Thus, all the parts involved in the assembly have been lightened as much as possible. Figure 4.14 shows the heavier and the lighter CAD models of the girder suspension whilst the CAD models for the Hossack system are shown in Fig. 4.15.

Once each part is designed, a construction material is associated to it, so the dynamic properties of that particular part can be returned by SolidWorks. The material chosen for both girder and Hossack suspension systems was aluminium

(a) Hossack suspension heavy desing



(b) Hossack suspension light desing

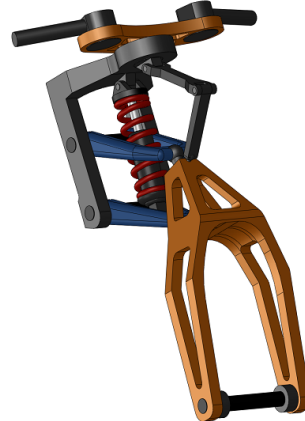


Figure 4.15: Hossack suspension system CAD models. a) Hossack design with equivalent parts masses to those of the telescopic fork. b) Hossack design with reduced parts masses.

alloy 7075-T6. It is widely used in automotive industry due to its strength and light weight, being a good candidate for the suspension system designs in these cases. These systems have been designed in order to support maximum loads during extreme running condition. Various finite element analyses were carried out for each suspension system taking into consideration the maximum loads calculated in Appendix C.

The factor of safety is considered to be the multiplication factor of the maximum loads allowed before a structure failure occurs following the von Misses criterion (Boresi & Schmidt 2002). In order to ensure the integrity of the suspension systems, a factor of safety greater than one ($f_{os} > 1$) was required at any point of the assemblies. For these conditions, the maximum resultant of the deformation vector obtained was always smaller that $U_{res} = 8$ mm, which could be considered as an acceptable limit taking into account that a minimal deformation of the systems' geometry takes place.

During the FEA simulation process, the spring-damper unit is substituted by a rigid connection and the two extreme positions of the assemblies (extended and compressed) are tested. In this way, the factor of safety and the resultant of the deformation vector are obtained for both suspension systems and both extreme positions. Figure 4.16b and Fig. 4.16c show these results respectively for the girder model with a parallelogram configuration. Figure 4.16a shows the analysis results of the same model under maximum lateral loads. For this design, the minimum factor

of safety is $fos = 3.86$. The maximum deformation magnitude was found for the longitudinal maximum load in the extended system, with a value of $U_{res} = 3.4$ mm.

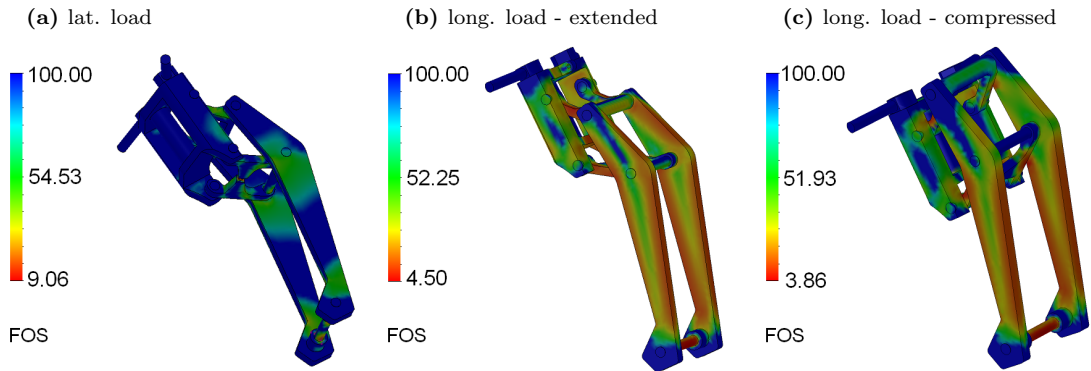


Figure 4.16: FEA results of the girder model with parts' masses approximated to those of the telescopic fork, showing the factor of safety map.

A similar study was performed for the Hossack suspension system. The results shown in Fig. 4.17 show a minimum factor of safety of $fos = 2.23$ found for the maximum longitudinal load, being the suspension system on its compressed position (Fig. 4.17c). In terms of the maximum deflection, this value is also achieved for longitudinal maximum load, now in the suspension extended position (Fig. 4.17b), whose magnitude becomes $U_{res} = 1.6$ mm.

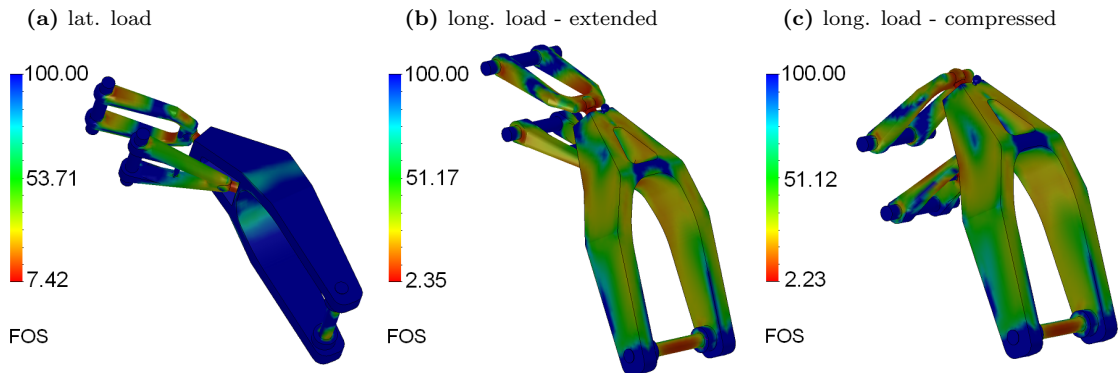


Figure 4.17: FEA results of the Hossack model with parts masses approximated to those of the telescopic fork, showing the factor of safety map.

The finite element analysis becomes very helpful for the task of designing the lighter models for both suspension systems, able to meet the maximum loads requirements. The analyses of these lighter models are presented in Fig. 4.18 for the girder suspension and in Fig. 4.19 for the Hossack system. For the girder lighter model with reduced masses, the minimum factor of safety is $fos = 1.02$, found

in the compressed suspension for the maximum longitudinal load. The maximum deflection is also found under this load with a magnitude of $U_{res} = 7.9$ mm.

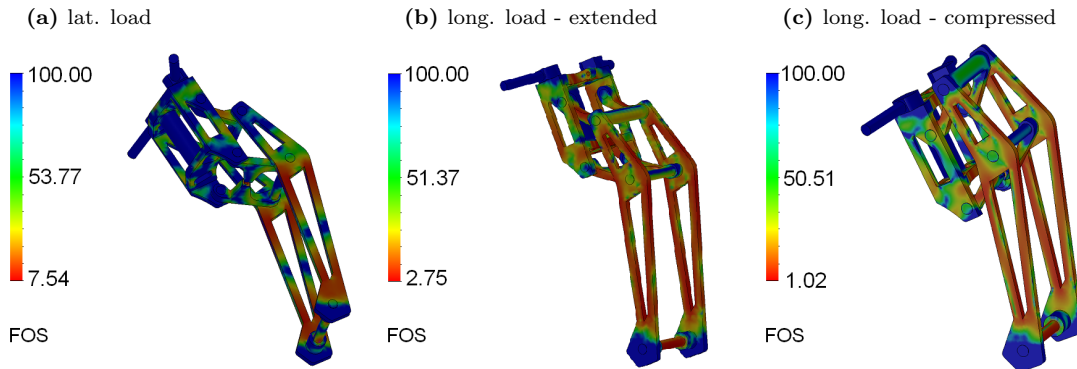


Figure 4.18: FEA results of the girder model with reduced masses showing the factor of safety map.

In the case of the Hossack lighter model, the minimum factor of safety takes the value of $f_{os} = 2.2$ for the compressed assembly under maximum longitudinal load. Whilst the maximum deflection is achieved under the same condition for the extended assembly, taking a value of $U_{res} = 3.6$ mm.

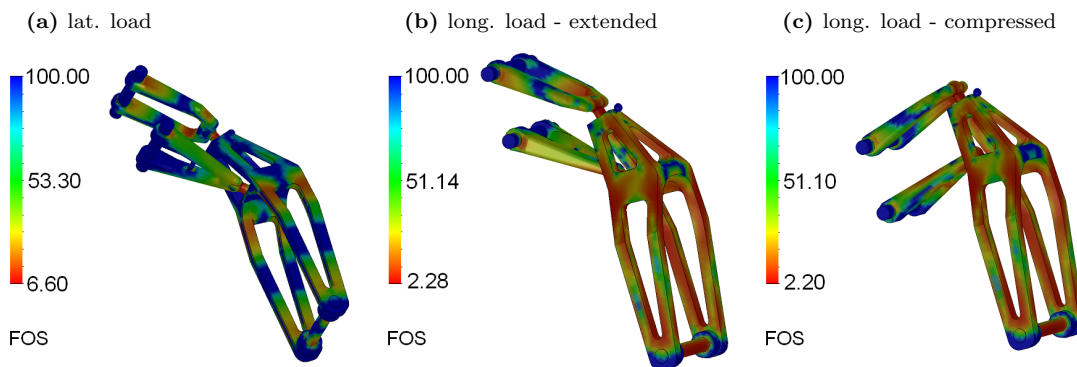


Figure 4.19: FEA results of the Hossack model with reduced masses showing the factor of safety map.

With the double wishbones suspension system, a significant front end mass reduction can be achieved. In order to compare the three different systems mass distributions, they have been divided in four subsystems containing different parts each of them. The parts belonging to each subsystem depend on which suspension system is considered:

- a) STR: It is the body that allows the steering action. It comprises the triple trees and eventually other parts depending on the model under consideration. In the

- case of the telescopic fork it also includes the upper tubes. In the case of the girder, the mass of the upper part of the spring damper unit is included too. In the case of the Hossack system, it includes the upper lever of the steering linkage.
- b) SUS: It represents the body holding the front wheel. In the case of the telescopic fork it comprises the lower tubes of the fork. In the case of the girder and Hossack suspension systems, this body corresponds to the uprights, the lower part of the spring-damper unit and, only for the Hossack system, the lower lever of the steering linkage.
- c) UWB: This part is exclusively defined for the girder and Hossack systems. It only consists of the upper wishbone.
- d) LWB: This part is exclusively defined for the girder and Hossack systems. It only consists of the lower wishbone.

Table 4.3 shows the masses of each part on the different suspension systems compared to the original telescopic fork parts masses. In order to study separately the effects of the geometry variation of these systems from the mass reduction effects on the motorcycle dynamics, the heavier models maintain the whole mass of the original front end assembly. In the case of the Hossack heavier model, the remaining mass needed to equal that of the original telescopic fork (4.986 kg) is added (in the mathematical model) to the main frame on the attachment point of the steering body. A second study of the lighter models allows to obtain an insight of the mass reduction effect of this motorcycle components.

Parts masses	STR (kg)	SUS (kg)	UWB (kg)	LWB (kg)	Total (kg)
Fork	9.990	7.250	—	—	17.240
Girder heavy	7.863	7.930	0.666	0.764	17.223
Girder light	4.333	4.231	0.666	0.764	9.994
Hossack heavy	2.681	7.673	0.976	0.924	12.254
Hossack light	2.165	3.988	0.976	0.924	8.053

Table 4.3: Masses of the different suspension systems models bodies

4.2.2 Mathematical modelling

Once the masses and inertias of the different parts of both suspension systems are calculated, the motorcycle's mathematical models with the alternative suspension systems can be built. These mathematical models are conceived as multi-body systems where a parental structure is followed. They are coded in VS Lisp, which returns the equations of motion and the linear state-space representation for each of them.

Multi-body description

The GSX-R1000 model presented in Chapter 3 has been modified to include both the girder and the Hossack suspension systems. In both cases, and similarly to the original nominal model, a massless body is included (the twist body) that represents the frame's flexibility. The flexibility is defined as a rotational degree of freedom between the motorcycle chassis (rear frame) and the front suspension (front frame) about the twist axis. This is an axis perpendicular to the steering one and contained into the motorcycle's symmetry plane, which passes through the attachment point of the twist body. This point is defined in both suspension systems as the middle point between the upper and the lower wishbones joint coordinates. For each of the suspension models, a different parental relation between the different bodies is implemented. The parental structure of the girder suspension is shown in Fig. 4.20.

The steer body is attached to the twist body, allowing the rotation about its z axis. The twist's body reference frame shares its y axis with the main frame's y axis. The twist body's reference frame is rotated about the y axis making coincident its x axis with the twist axis in the main frame. All the bodies after the twist body have a similar reference frame orientation. Therefore, the z axes of the twist and the steer bodies are collinear with the steering axis in the main body reference frame. The mass, the inertia moments and the inertia products of this body correspond to those of the girder's STR subsystem stated in the previous section. The rider's steering moment and the steering damper moment are applied to the steer body about its z axis and react on the rider's upper body the first of them, and on the main body the second. The upper wishbone and lower wishbone bodies are sons of the steer body and both of them rotate about the y axis. Their masses and their moments

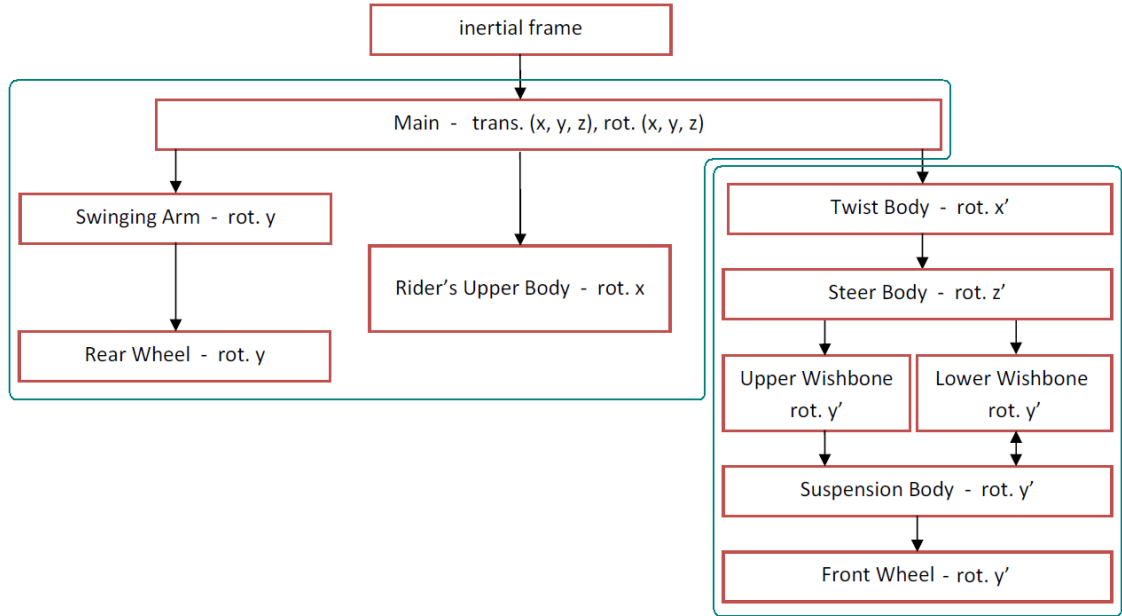


Figure 4.20: Girder suspension system's parental structure.

and products of inertia are obtained from the CAD designs and correspond to the girder's UWB and LWB subsystems respectively. Finally, the suspension body is son of the upper wishbone body and closes the four bar linkage loop with the lower wishbone at its front extreme. It also rotates about the y axis and its mass and moments and products of inertia correspond to those of the girder's SUS subsystem. This body is the front wheel body's father which has same properties and kinematics as the original GSX-R1000 nominal model, rotating about its y axis.

Following the different mechanical configuration of the Hossack suspension system, in which the steering axle is on the four bar linkage opposite side, a different parental structure must now be considered. This is shown in Fig. 4.21. In this case, the two wishbones are connected directly to the twist body and rotate about their y axis corresponding to that of the twist body. Their mass and inertia properties were found in the previous section as those of the Hossack's UWB and LWB subsystems. The suspension body in the Hossack model also performs the system's steering action; it can rotate about its y and z axes. It is a child of the upper wishbone body and closes the four bar linkage loop with the lower linkage one. Its mass, inertia moments and inertia products (calculated through the CAD design), correspond to the Hossack SUS subsystem presented in previous section. The front

wheel body is connected to the suspension body and rotates about its y axis. It has a similar definition to that in the telescopic fork and the girder suspension models. Considering that the inertia moment and products obtained for the Hossack STR subsystem are negligible and that it does not play a significant role on the front end kinematics, its mass is directly lumped into the main body's mass, which centre of masses is modified according to the relative position of this subsystem. In the Hossack suspension systems, the rider's steering and the steering damper moments are directly applied to the suspension body about its z axis. The first reacts on the rider's upper body whilst the second does so on the main body.

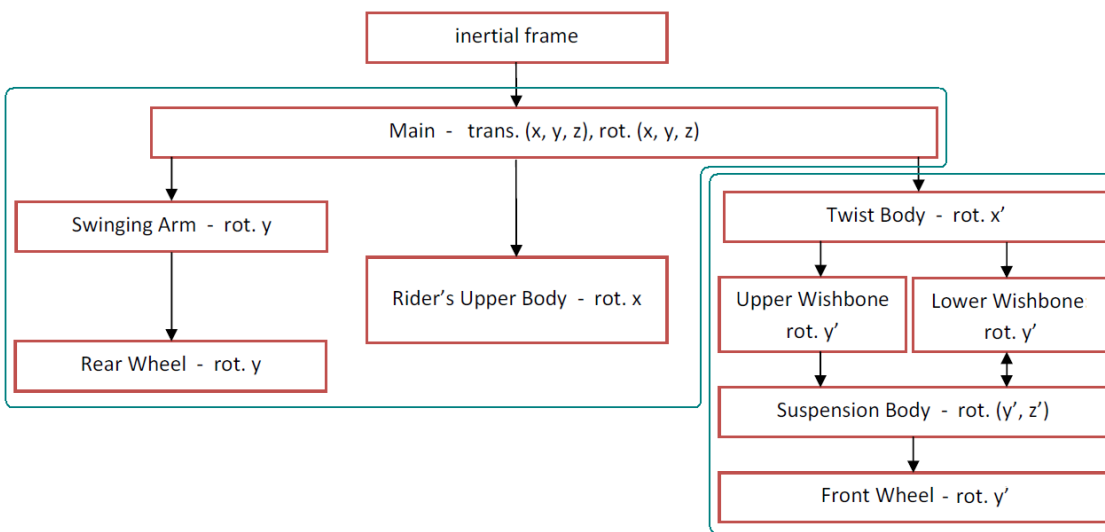


Figure 4.21: Hossack suspension system's parental structure.

Suspension tuning

The suspension forces in both girder and Hossack systems are modelled as two moments applied to the lower wishbones and reacting on the steer body and the twist body respectively. These suspension moments depend on the lower wishbones angular displacements and speeds, producing the reactive and the dissipative suspension actions. The focus of this work is to compare the two alternative suspension systems performance with that of the telescopic fork system. Thus, a similar suspension tuning is sought to introduce the minimum systems variations. The equivalent suspension moments to the linear suspension force of the telescopic fork can be calculated considering a conservation of energy condition. The sum of the energy stored and dissipated by the torsional spring and damper respectively in the double

wishbone system is the same as for the linear spring and damper in the telescopic fork, for the same vertical displacement of the front wheel attachment point and in the same time. In the spring case, this condition is expressed by Eq. 4.3.

$$F_s \cdot \frac{dx_f}{dt} = M_s \cdot \frac{d\theta}{dt} \quad (4.3)$$

θ is the angle rotated by the lower wishbone and x_f is the compressed/extended distance of the telescopic fork. M_s is the double wishbone suspension systems' equivalent stiffness moment. F_s is the force in the fork's spring for a longitudinal displacement equivalent to a front wheel's vertical displacement z , being the motorcycle chassis fixed to the inertial reference frame. This force is calculated for the telescopic fork spring stiffness coefficient ($k_f = 25$ kN/m) as:

$$F_s = -k_f \cdot \frac{z}{\cos(\varepsilon)} \quad (4.4)$$

Where ε is the telescopic fork head angle. Then, the equivalent moment for the double wishbone system can be obtained as:

$$M_s = -k_f \cdot \frac{z}{\cos(\varepsilon)} \cdot \frac{\partial x_f}{\partial \theta} \quad (4.5)$$

Taking advantage of the kinematic model obtained in section 4.1, x_f and θ are calculated numerically as functions of the vertical displacement z and then differentiated. Finally, a polynomial fit is performed for M_s and θ , finding an equivalent stiffness moment as a third order polynomial function of the lower wishbone angle expressed by the Eq. 4.6.

$$M_s = -k_{w3} \cdot \theta^3 - k_{w2} \cdot \theta^2 - k_{w1} \cdot \theta - k_{w0} \quad (4.6)$$

A similar approach is followed to find the equivalent damping moment (M_d). The energy conservation equation is:

$$F_d \cdot \frac{dx_f}{dt} = M_d \cdot \frac{d\theta}{dt} \quad (4.7)$$

If the equivalent damping moment is considered as a linear moment with the

rotational speed of the lower wishbone, Eq. 4.7 can be rewritten as:

$$-c_w \cdot \left(\frac{d\theta}{dt}\right)^2 = -c_f \cdot \left(\frac{dx_f}{dt}\right)^2 \quad (4.8)$$

Where $c_f = 2134$ Ns/m is the nominal value of the telescopic fork damping coefficient and c_w is the damping coefficient of the equivalent damping moment applied to the lower wishbone. The equivalent damping coefficient can be then obtained as:

$$c_w = c_f \cdot \left(\frac{\partial x_f}{\partial \theta}\right)^2 \quad (4.9)$$

Similarly than for the spring case, $\frac{\partial x_f}{\partial \theta}$ is calculated numerically. Therefore, the damping moment can be written as follows:

$$M_d = -c_w \cdot \frac{d\theta}{dt} \quad (4.10)$$

A polynomial fit is performed for c_w as a function of θ obtaining a third degree polynomial relation. Finally, the equivalent damping moment is expressed by equation 4.11. For both girder and Hossack suspension systems and for the three geometrical configurations, different values of the stiffness and damping fit coefficients are found.

$$M_d = (-c_{w3} \cdot \theta^3 - c_{w2} \cdot \theta^2 - c_{w1} \cdot \theta - c_{w0}) \cdot \frac{d\theta}{dt} \quad (4.11)$$

4.3 Dynamic analysis

Once the different models have being implemented in VehicleSim, VS Lisp returns the nonlinear equations of motion and the model's state-space representation based on the linear approximation of these equations. The nonlinear equation of motion can be integrated for different running conditions. In this chapter, they are used, on one hand, to study the in-plane response of the motorcycle fitted with the different suspension system. On the other hand (and following the approach in Chapter 3), they are solved obtaining the quasi-equilibrium states necessary to feed the state space matrices in order to perform a stability analysis for various forward speeds

and roll angles.

4.3.1 In-plane dynamic response

VehicleSim contains the VS Browser tool. By means of a graphical user interface, different events can be introduced on each simulation, such as various road inputs. Each suspension system has been tested under two different running conditions: passing through a road bump input and braking with the front wheel in straight line with constant deceleration.

Road bump input

The road bump input simulation is performed with the motorcycle running in straight line at a forward speed of $v = 40$ m/s. A step input of a height of $h_b = 50$ mm is introduced after a few meters. This step bump is implemented in VehicleSim using an external table. This table has been built as explained in Chapter 3 in order to take into consideration the vertical and horizontal forces on the tyres.

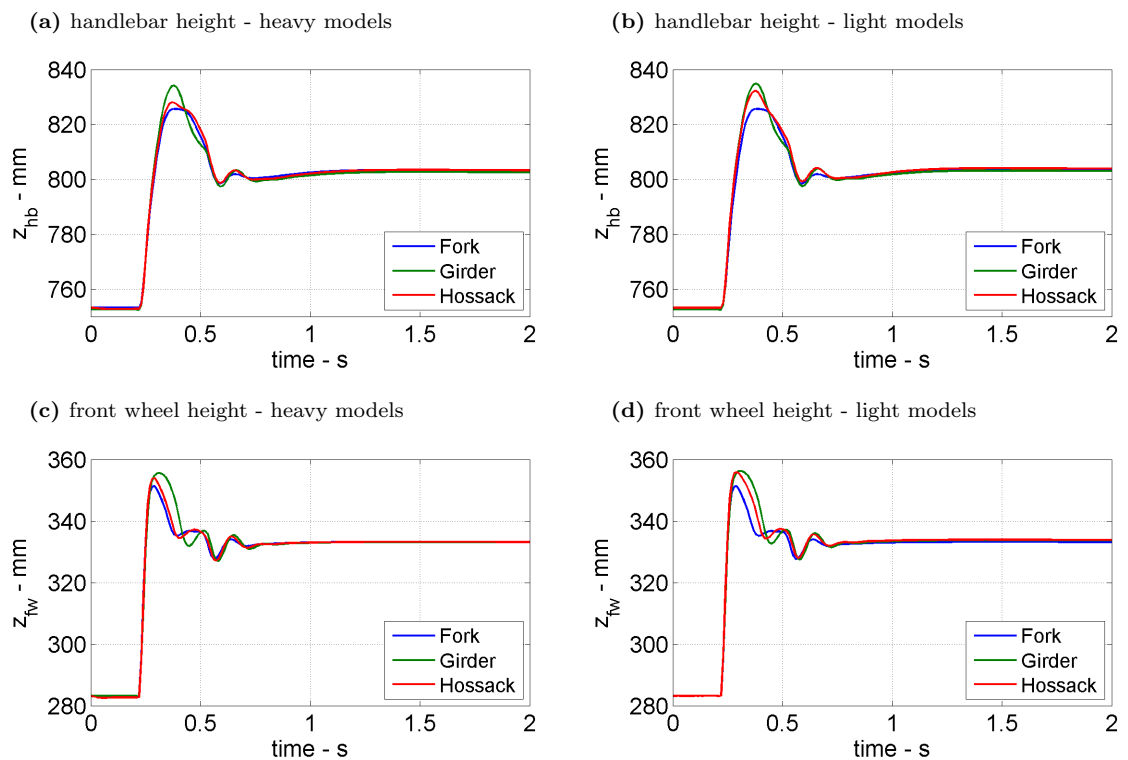


Figure 4.22: Motorcycle front end response after a 50 mm road bump input with a forward speed of $v = 40$ m/s for the telescopic fork suspension compared to the girder and Hossack suspension systems with a parallelogram configuration (*prl*).

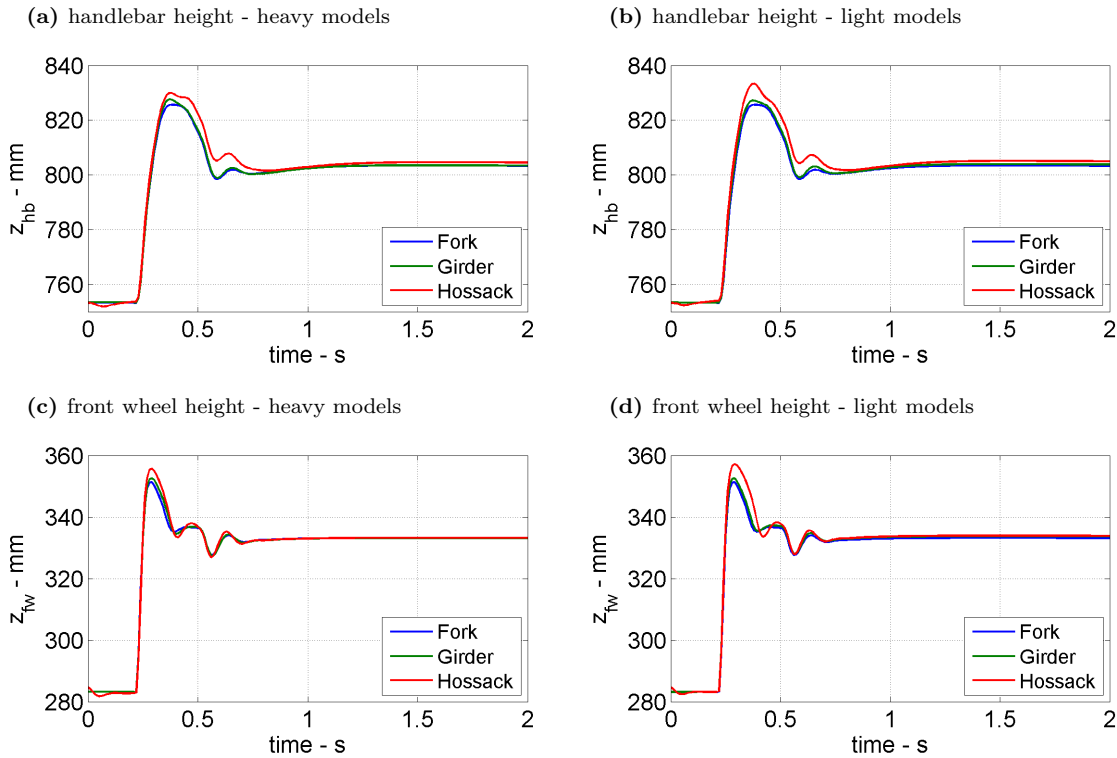


Figure 4.23: Motorcycle front end response after a 50 mm road bump input with a forward speed of $v = 40$ m/s for the telescopic fork suspension compared to the girder and Hossack suspension systems at the telescopic fork’s trajectory configuration (*tft*).

Figure 4.22 shows the front end responses of the telescopic fork, the girder and the Hossack suspension systems for a bump input simulation. Both the girder and the Hossack systems have been designed with a parallelogram (*prl*) configuration. Figure 4.22a and Fig. 4.22c show the behaviours of the heavier models whilst Fig. 4.22b and Fig. 4.22d those of the lighter models. It can be appreciated that in any case, the behaviours of the three models are very similar. The Hossack suspension’s front end follows more closely the behaviour of the telescopic fork suspension case. Whilst in the case of the girder system there exist a slight deviation. On the other hand, the mass reduction does not affect significantly the suspensions’ responses. Nevertheless, the Hossack system’s response is more affected than the girder suspension’s response.

When both suspension systems are designed with a fork’s trajectory (*tft*) configuration, the girder system shows a response almost identical to the telescopic fork suspension case. It is the Hossack suspension system which introduces small behaviour differences. Again, the mass reduction modifies the Hossack system response whilst the girder’s one remains mostly unaffected. These results, shown in

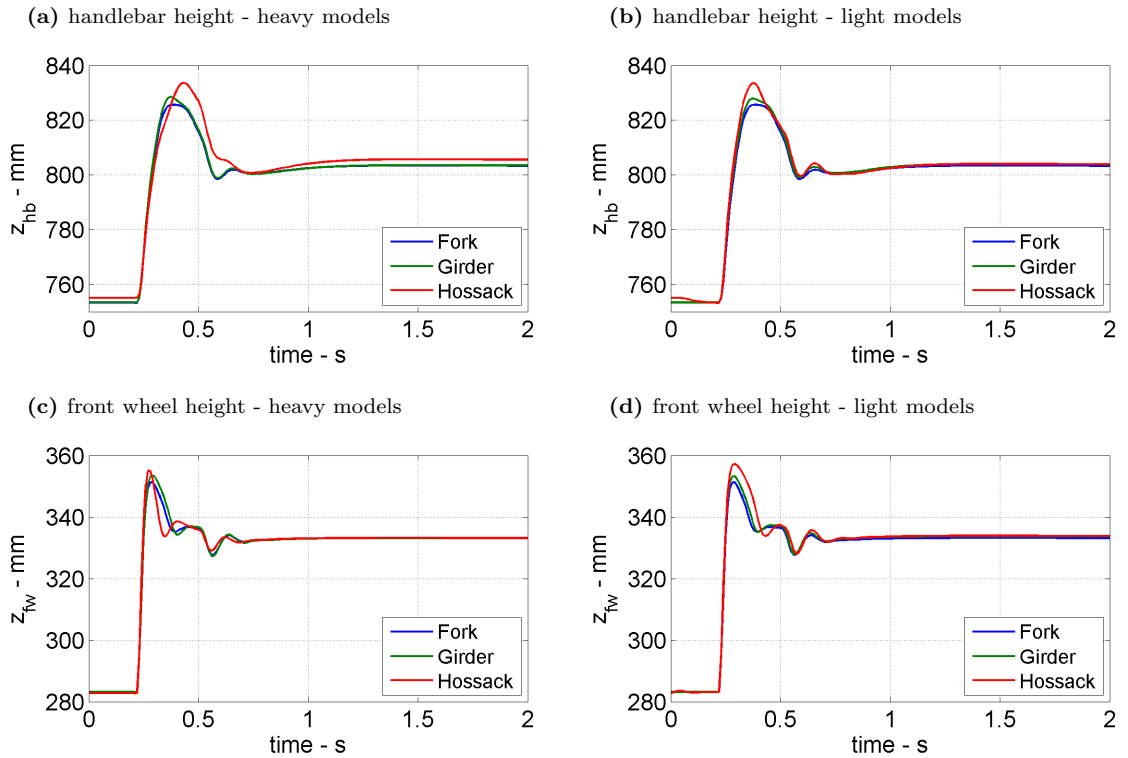


Figure 4.24: Motorcycle front end response after a 50 mm road bump input with a forward speed of $v = 40$ m/s for the telescopic fork suspension compared to the girder and Hossack suspension systems with a constant normal trail configuration (*cnt*).

Fig. 4.23, are coherent with the fact that the steering axle in the girder and the fork suspension systems is fixed to the chassis, and in both cases, the front wheel follows the same trajectory. Consequently, a small deviation in the masses motion is produced in both front ends.

Figure 4.24 shows the results for the road bump input simulation for the two designed alternative suspension systems in order to introduce a minimal normal trail variation. A similar behaviour in both systems is observed. Whilst the girder suspension response is closer to that of the telescopic fork, the Hossack system response differs slightly. Additionally to this, the Hossack suspension system is the one that shows more influence on the mass reduction.

For both suspension systems (girder and Hossack) with the three different kinematics configurations (*prl*, *tft* and *cnt*), the road bump input responses are similar to that of the telescopic fork. Although it can be said that they show some differences and are slightly affected for the mass variations, the increase in the front ends height responses are not larger than 5 mm in any case.

Front wheel braking

A front wheel braking manoeuvring simulation is set up for the motorcycle running on a straight line, at a initial forward speed of $v = 40$ m/s which is forced to decelerate with a negative acceleration of $a = -0.5$ G. This deceleration is obtained by applying a braking moment into the front wheel, whose magnitude is controlled by a PD controller implemented in the model as in Chapter 3.

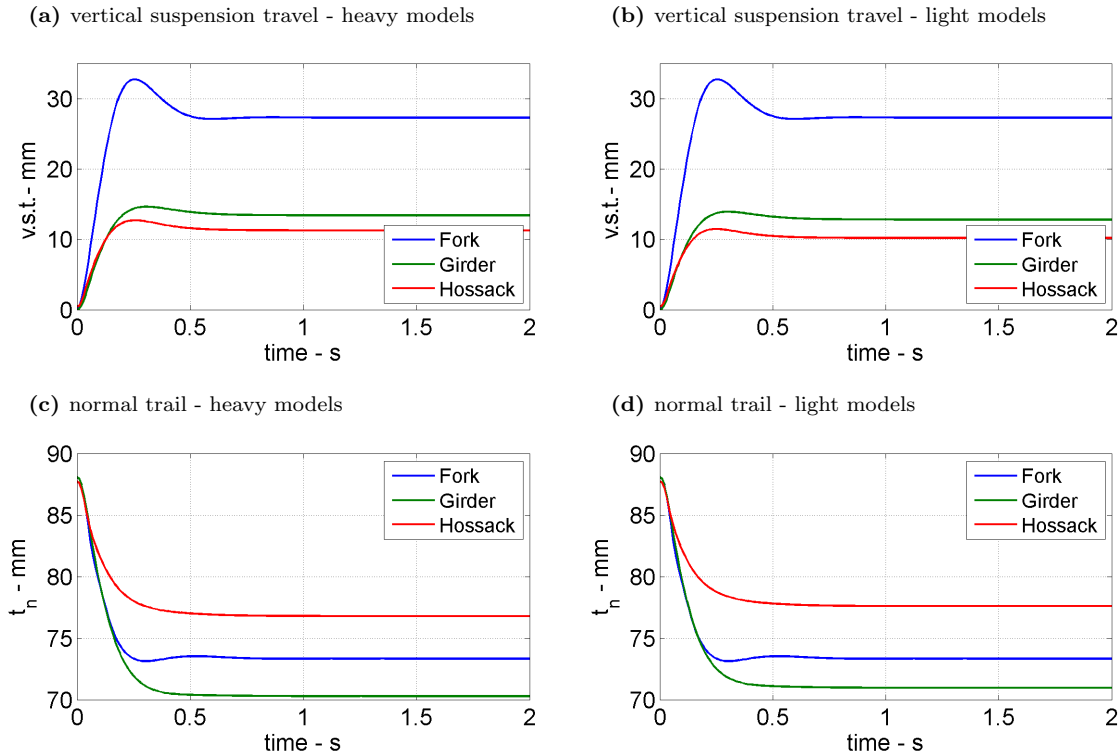


Figure 4.25: Vertical suspension travel ($v.s.t.$) and normal trail (t_n) for the telescopic fork suspension compared to the girder and Hossack systems with a parallelogram configuration (prl). A straight line front wheel braking manoeuvre at an initial forward speed of $v = 40$ m/s with a constant deceleration of $a = -4.9$ m/s² is performed.

In order to focus on the pure braking effects only, the aerodynamic forces have not been taken into account by setting the drag, lift and pitch aerodynamic coefficients to zero during this simulation. Figure 4.25 shows the vertical suspension travel and the normal trail variation of the three different motorcycle models fitted with the telescopic fork, the girder suspension and the Hossack system with a parallelogram configuration (prl). The anti-dive effect is shown to increase in Fig. 4.25a and 4.25b for both double wishbone suspension systems. This is produced by their front wheels contact points trajectories which can be observed in Fig. 4.10a and 4.9. The mass reduction slightly increases this effect due to a decrease on the inertia.

However, regarding to the normal trail variation, the girder and the Hossack system behave opposite to each other. Whilst the girder suspension reaches smaller normal trail values than the telescopic fork, the Hossack system presents larger normal trail values than the fork for all the suspension travel. The lighter models' normal trail are similarly affected, presenting slightly larger values of this parameter than in the heavier models cases.

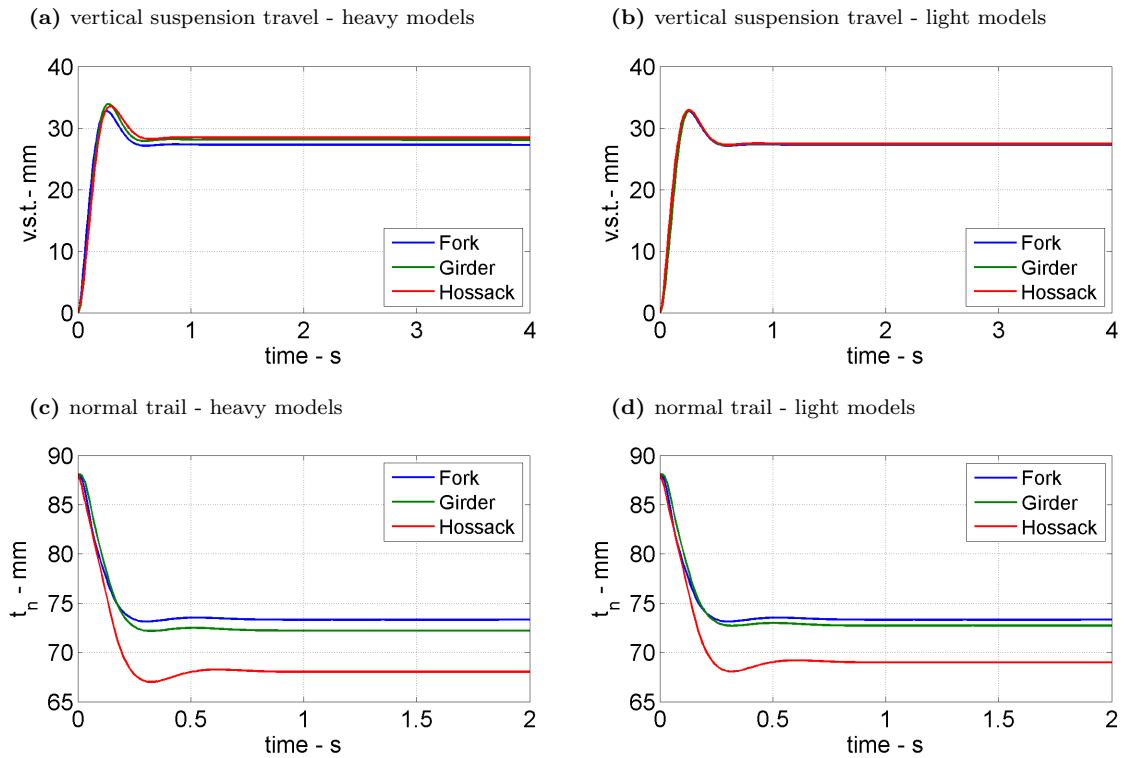


Figure 4.26: Vertical suspension travel ($v.s.t.$) and normal trail (t_n) for the telescopic fork suspension compared to the girder and Hossack systems with a telescopic fork's trajectory configuration (tft). A straight line front wheel braking manoeuvre at an initial forward speed of $v = 40$ m/s with a constant deceleration of $a = -4.9$ m/s² is performed.

When both girder and Hossack suspension systems are designed with a fork's trajectory configuration (tft), their diving properties become similar to those of the telescopic fork, as it is shown in Fig. 4.26. The vertical suspension travel reached under the braking manoeuvre is similar for the three systems. In the girder suspension and telescopic fork cases, the common steering axles and front wheel contact points trajectories, produce similar kinematics in both systems, which results in similar normal trail behaviour.

In the Hossack suspension system case, the normal trail is highly reduced from $t_n = 88$ mm up to $t_n = 68$ mm, which exceeds significantly the reduction of this pa-

parameter reached by the telescopic fork and girder suspension systems. The Hossack system's geometry magnifies the normal trail reduction. In order to obtain a front wheel contact point trajectory similar to that of the telescopic fork, the steering axis is necessarily reduced with the suspension travel. This leads to a greater normal trail reduction compared to other configurations. Finally, the lighter models show subtle differences in the vertical suspension travel and the normal trail variations with respect to the heavier models for both girder and Hossack suspension systems.

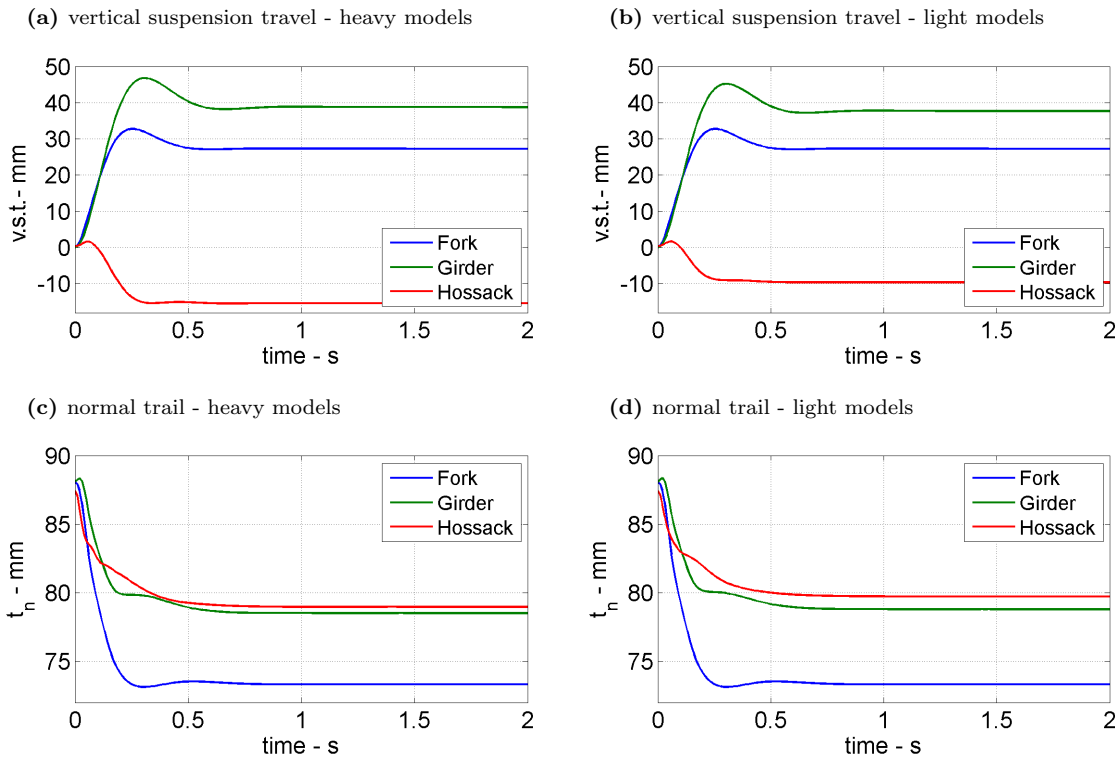


Figure 4.27: Vertical suspension travel ($v.s.t.$) and normal trail (t_n) for the telescopic fork suspension compared to the girder and Hossack systems with a constant normal trail configuration (cnt). A straight line front wheel braking manoeuvre at an initial forward speed of $v = 40$ m/s with a constant deceleration of $a = -4.9$ m/s² is performed.

Figure 4.27 shows the front wheel braking dynamics of the girder and the Hossack systems configured to present a minimal normal trail variation. The front wheel contact point trajectory becomes highly relevant on the suspension anti-dive effect. Looking at Fig. 4.12 it can be observed a trajectory of the contact point with a higher angle with the vertical, which makes this suspension configuration more prone to dive than the telescopic fork, increasing the vertical suspension travel value about 10 mm in this case. Conversely, the Hossack suspension system with this configuration shows a negative angle with the vertical of its front wheel contact point trajectory.

This results in an opposite behaviour of the front end, which rises from its nominal position, 10 mm for the heavier model and 15 mm for the lighter one. Regarding to the normal trail, both girder and Hossack suspension systems experience a reduction of this value (limited by the geometrical configuration). They were designed in order to keep this value constant. However, this can only be achieved considering the static suspension compression. Depending on the different accelerations on the motorcycle, other elastic parts different than those of the front suspension system will be compressed or extended: these are the tyres carcasses and the swinging arm assembly. This change in the geometry modifies the kinematics design and produces a normal trail reduction as shown in Fig. 4.27c and 4.27d. With this geometrical configuration, the lighter and heavier models are more influenced by the mass differences than in other configurations. Now, the heavier ones show more pronounced suspension diving effects which also have an impact on the normal trail variation.

4.3.2 Stability analysis

In order to understand how the alternative double wishbone suspension systems can affect the motorcycle oscillatory dynamics, a stability analysis is performed using root locus of the different suspension systems and various parameter variations such as geometry, mass, front frame compliance and steering damper coefficients. Following the approach stated in Chapter 3, the state space models derived from the linearized equations of motion are filled up with the quasi-equilibrium states, integrated from the nonlinear equations. These states have been obtained for each model, from four motorcycle simulations with four different roll angles (0° , 15° , 30° and 45°). In the four simulations, the forward speed is increased from 10 m/s up to 80 m/s with an acceleration of $a = 0.001 \text{ m/s}^2$.

Figure 4.28 shows these root loci of the nominal motorcycle model fitted with a telescopic front fork. The rider lean, weave and wobble oscillating modes are shown. Also the pitch mode appears in the interest area, but only for the case of a 45° roll angle. The rest of the normal modes are highly damped and are not visible in this area. The rider lean, weave and wobble are out-of-plane modes whilst the pitch mode is an in-plane one. It consists in the pitching of the motorcycle through the

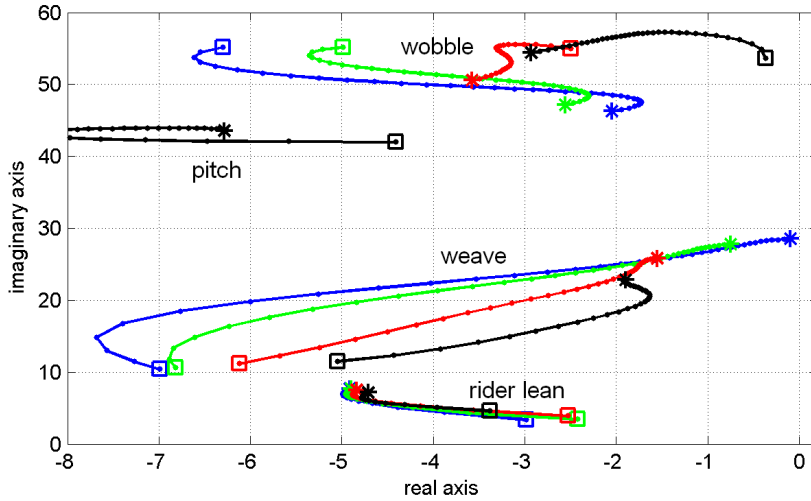


Figure 4.28: Root loci of the nominal motorcycle model fitted with a telescopic fork suspension. The speed is increased from 10 m/s (\square) up to 80 m/s ($*$) at different roll angles: 0° (blue), 15° (green), 30° (red) and 45° (black).

front and rear suspension compression and extension in an out-of-phase motion. The rider lean appears in the root locus when the rider upper-body degree of freedom is included in the mathematical model. It is an oscillation of the rider’s upper-body. The weave mode appears when the roll, yaw and steering angle oscillations are combined in a fishtailing motion. The wobble mode is characterized by a shaking of the front frame about the steering axis whilst the rear frame is slightly affected. The in-plane and the out-of-plane degrees of freedom become coupled for roll angles different to zero, when the motorcycle symmetry plane is out of the vertical. A more extensive study of these and other modes is presented in Chapter 7. Weave and wobble oscillating modes have been widely studied in the literature (e.g. (Sharp 1971), (Cooper 1974), (Roe & Thorpe 1976), (Koenen 1983), (Limebeer et al. 2001), (Evangelou et al. 2008) just to cite a few). And they are of main relevance in this chapter due to their proximity to the unstable area, which is eventually reached under some running conditions.

Geometry and mass variation

The root locus obtained for the different geometrical configurations (*prl*, *tft* and *cnt*) of both the girder and the Hossack suspension systems shows that the differences of these configurations do not affect the system’s roots positions in a significant manner. Figure 4.29a and Fig. 4.29b show the root loci for four different simulations

at various motorcycle's lean angles for the girder suspension heavier model with the telescopic fork's trajectory (*tft*) and the constant normal trail (*cnt*) configurations. No relevant difference is observed. Figure 4.29c and Fig. 4.29d represent the root loci for the lighter models under the same conditions. In these cases, the mass reduction increases slightly the wobble mode frequency and damping at medium-high speeds for all the roll angles.

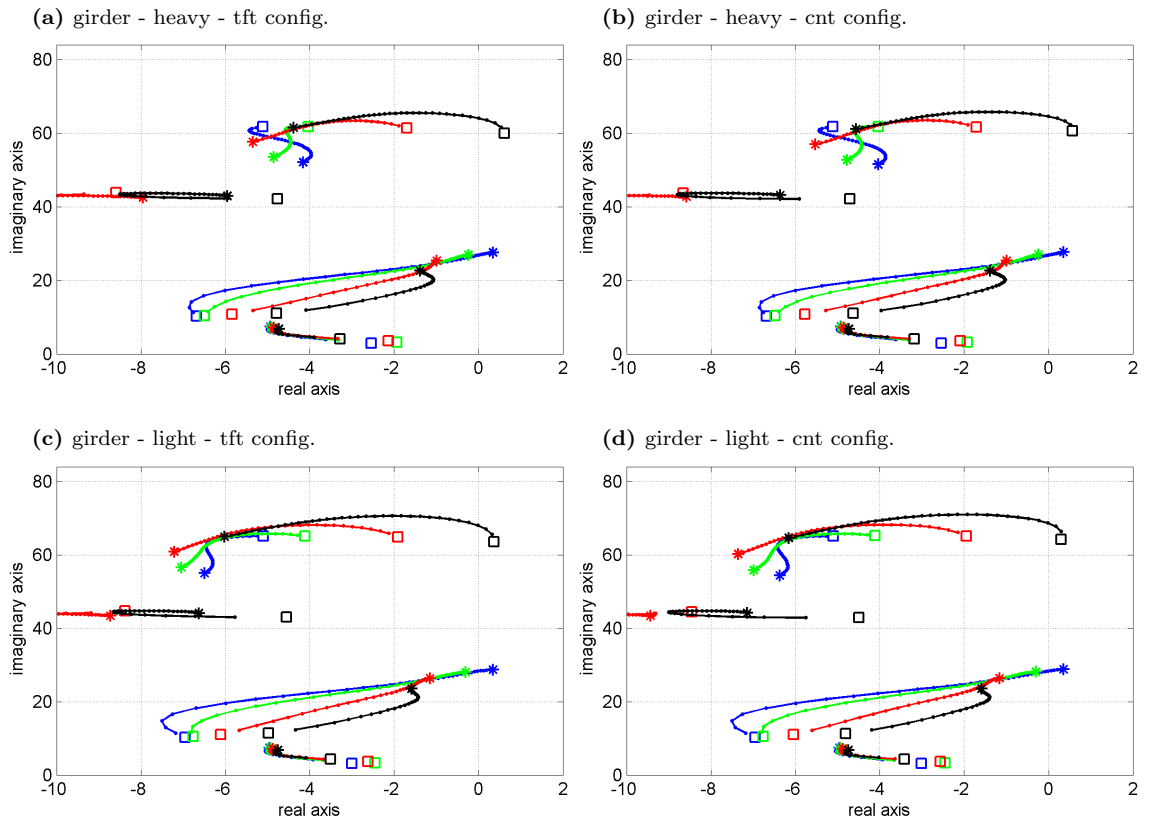


Figure 4.29: Root loci of the girder suspension for the telescopic fork's trajectory (*tft*) and the constant normal trail (*cnt*) configurations of the lighter and heavier models. The speed is increased from 10 m/s (\square) up to 80 m/s ($*$) at different roll angles: 0° (blue), 15° (green), 30° (red) and 45° (black).

Compared to the root loci of the telescopic fork suspension (Fig. 4.28), three things can be observed: first, observe the destabilization of the weave mode at zero roll angle for speeds higher than 70 m/s. At higher roll angles (15° , 30° and 45°), this mode is less damped than in the telescopic fork suspension case but does not cross the stability limit. Secondly, the wobble mode is unstable for speeds lower than 16 m/s at 45° . However, it becomes more damped for higher speeds and smaller roll angles. Finally, the third effect of fitting the motorcycle with a girder suspension system is an appreciable increase of the wobble frequency. The rest of

the modes remain mostly unaffected by the inclusion of this suspension system on the motorcycle model.

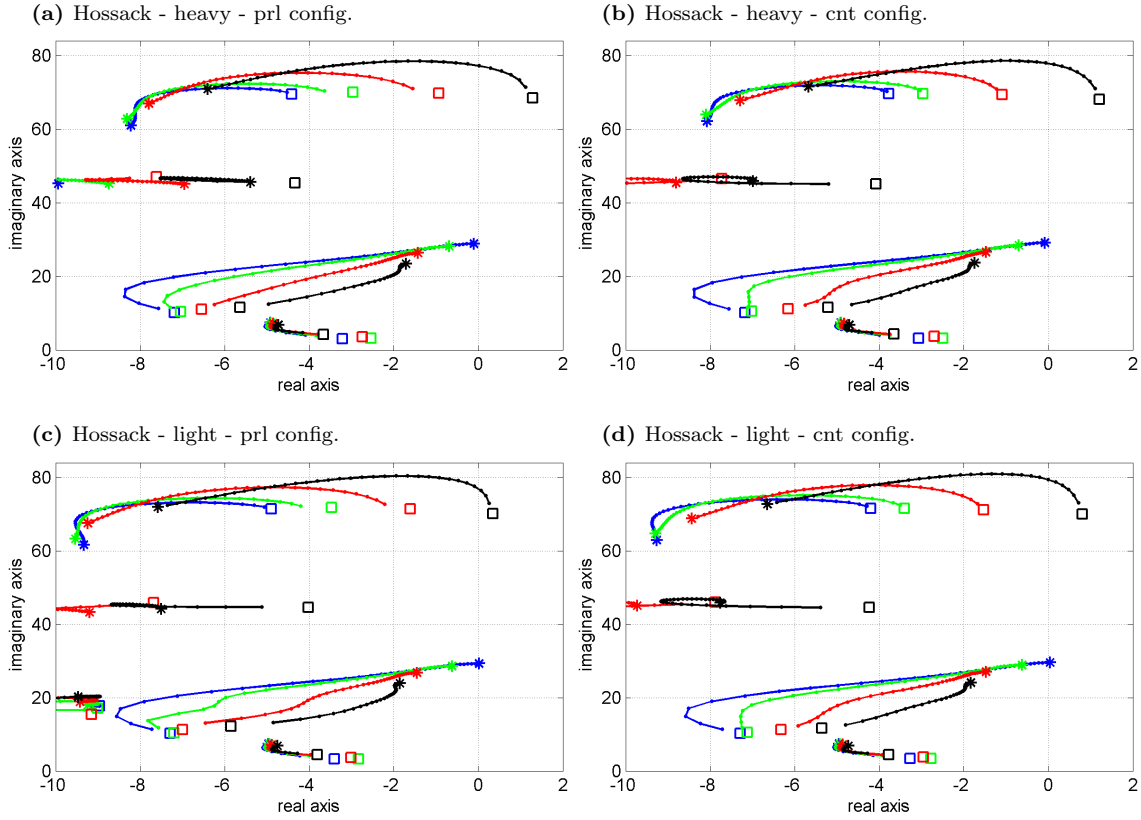


Figure 4.30: Root loci of the Hossack suspension system with parallelogram (*prl*) and constant normal trail (*cnt*) configurations of the lighter and heavier models. The speed is increased from 10 m/s (\square) up to 80 m/s ($*$) at different roll angles: 0° (blue), 15° (green), 30° (red) and 45° (black).

Figure 4.30a and Fig. 4.30b show the root loci for four lean angles simulations of the Hossack suspension system heavier model with the parallelogram (*prl*) and the constant normal trail (*cnt*) configurations respectively. Equivalent root loci for the lighter models are presented in Fig. 4.30c and Fig. 4.30d. In these cases, the mass reduction slightly increases the wobble mode frequency, and becomes more damped at high speeds for all the roll angles compared to the telescopic fork suspension case. (Fig. 4.28). The weave mode shows little variations, reaching the unstable area for 0° roll angle at a maximum forward speed of $v = 80$ m/s for the lighter models.

Compared to the root loci of the telescopic fork suspension case, the Hossack suspension system's wobble mode becomes more damped at higher forward speeds for all roll angles whilst it is less damped at lower speeds. In the case of 45° roll angle, this mode is unstable from 10 m/s up to 20 m/s. Its frequency is increased between

10 rad/s and 20 rad/s on the full speed range and for all roll angles. The remaining normal modes are not substantially affected by the inclusion of this suspension system in the motorcycle model.

Front frame compliance

The design of a front suspension system will determine its compliance and hence, the stiffness at the front end. It is interesting to study how this compliance can affect the stability of a motorcycle assembly. In the motorcycle's mathematical model, the compliance is introduced as a moment applied between the chassis and the front end about the twist axis. As it was explained in the modelling section, this is an axis perpendicular to the steering one and into the motorcycle symmetry plane.

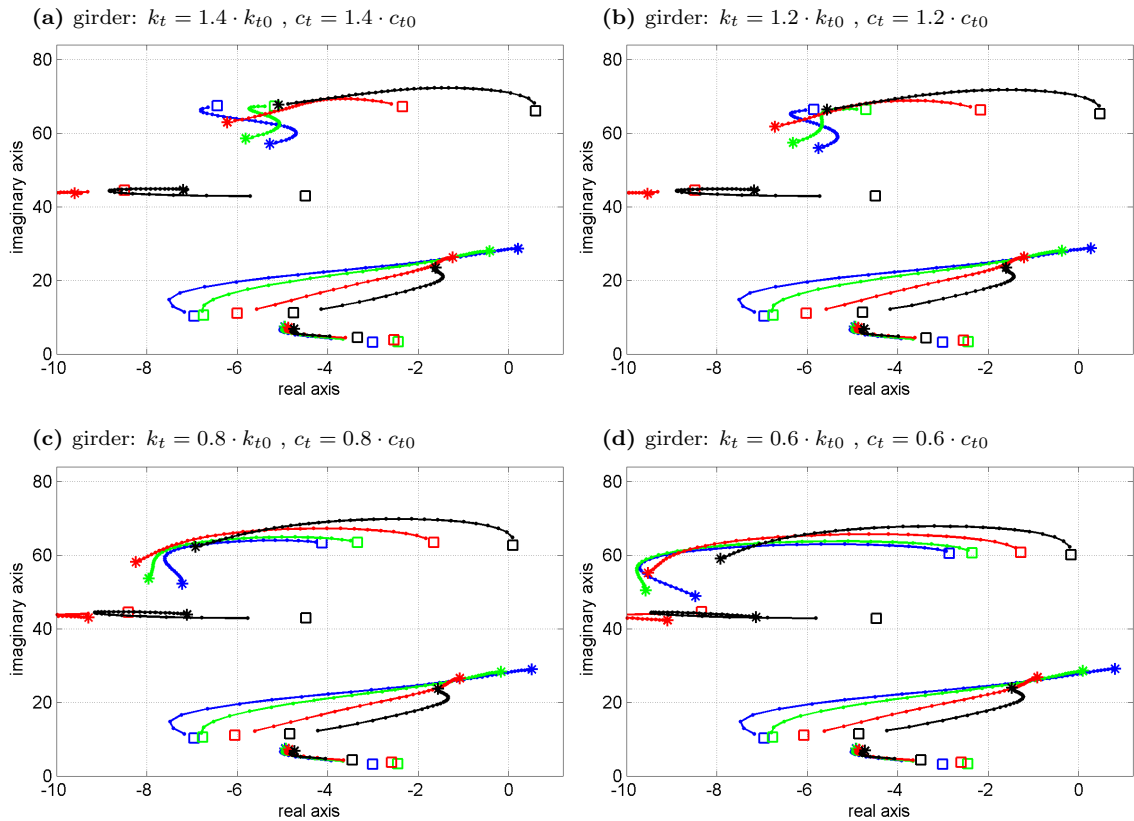


Figure 4.31: Root loci for girder suspension lighter model with a constant normal trail (*cnt*) configuration for different values of the twist moment coefficients. The speed is increased from 10 m/s (\square) up to 80 m/s ($*$) at different roll angles: 0° (blue), 15° (green), 30° (red) and 45° (black).

The twist moment is defined as a torsional spring and damper combination whose stiffness parameter has a nominal value of $k_{t0} = 100$ kNm, whilst the damping parameter nominal value is $c_{t0} = 100$ Nms. In order to study the variation on the

rigidity of both front suspension systems, these stiffness and damping coefficients are modified proportionally from 60 % of their nominal values up to the 140 %. These maximum values may be difficult to be achieved in a real mechanical implementation, but become useful to be considered in order to highlight the trends of the systems behaviour.

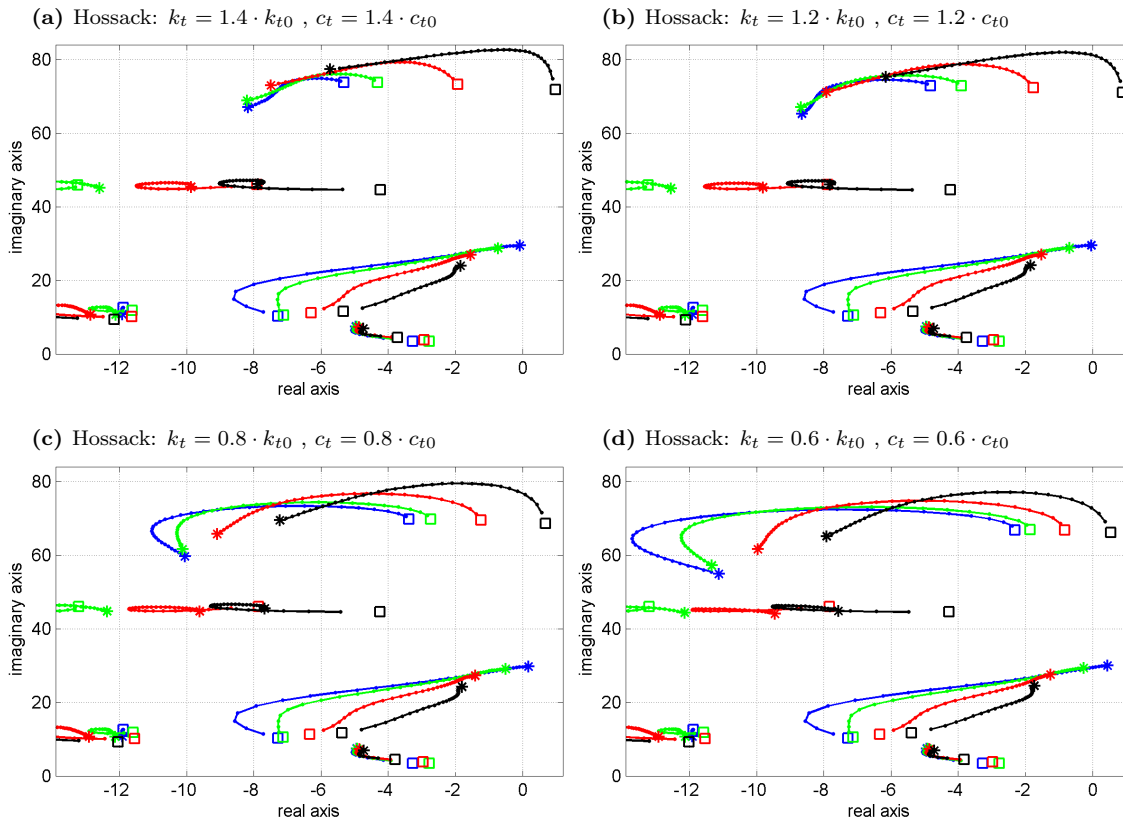


Figure 4.32: Root loci for Hossack suspension lighter model with a constant normal trail (*cnt*) configuration for different values of the twist moment coefficients. The speed is increased from 10 m/s (\square) up to 80 m/s ($*$) at different roll angles: 0° (blue), 15° (green), 30° (red) and 45° (black).

As it has been shown, since the mass differences and the variation in the geometrical configuration of both girder and Hossack suspension systems do not affect their stability properties significantly, Figs. 4.31 and 4.32 show the root-loci of the girder and Hossack systems for the different values of the twist moments only for the lighter constant trail geometrical configuration.

For the girder suspension system, the weave mode is unstable for speeds above 70 m/s at a zero roll angle, whilst the wobble mode instability happens for a 45° roll angle and forward speed values below 16 m/s. When the twist stiffness, and thus the front frame rigidity, is increased, the wobble mode becomes more unstable whilst

the weave mode's stability increases, narrowing in this way its unstable forward speed range at zero roll angle. A reduction of the twist stiffness results in the opposite effect. Consequently, weave and wobble modes stability cannot be satisfied simultaneously by modifying the front suspension system's compliance.

Considering the Hossack suspension system, the front end's compliance variation has a similar impact as in the girder suspension case on the motorcycle's stability behaviour. In this case, the wobble mode at 45° roll angle is stable for speed values larger than 20 m/s whilst the weave mode is stable for practically all the speed range at any roll angle for the nominal value of the twist moment coefficient. However, if the stabilization of the wobble mode for a 45° roll angle at the lower speed range is sought by decreasing the front frame's rigidity, the weave mode will become unstable for the straight line case at its higher speed range.

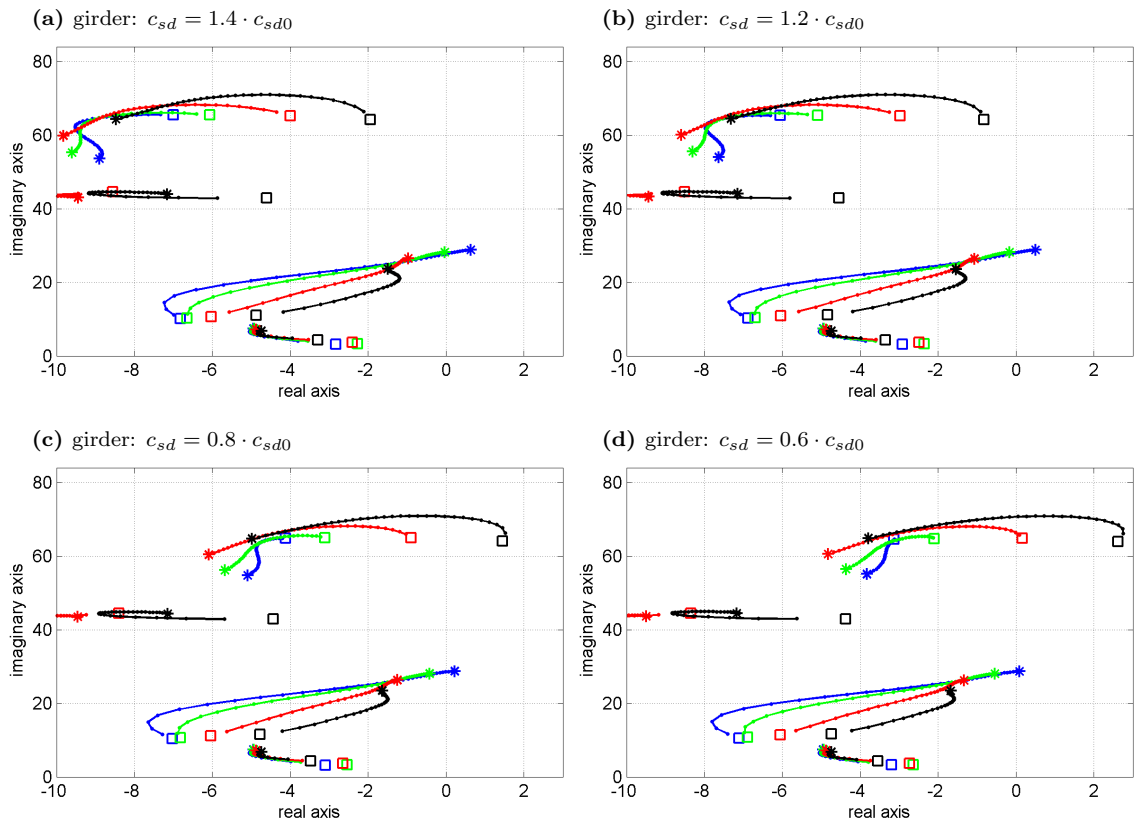


Figure 4.33: Root loci for girder suspension lighter model with a constant normal trail (*cnt*) configuration for different values of the steering damper coefficient. The speed is increased from 10 m/s (\square) up to 80 m/s ($*$) at different roll angles: 0° (blue), 15° (green), 30° (red) and 45° (black).

As it happened in the girder case, fully stable normal modes for the entire speed range at all roll angles are not found simultaneously by modifying the front end's

compliance. Nevertheless, this is a design parameter that should be taken into account if the expected motorcycle running conditions are not as demanding as in the case in which both normal modes are unstable: straight running forward speeds near to 80 m/s and large roll angles of 45° at low speeds.

Steering damper

The steering damper links the steering body and the chassis; its mission is to attenuate hard steering oscillations. Nowadays, a steering damper is fitted in most of the commercial sport motorcycle. The nominal GSX-R1000 model has a steering damper which is mathematically modelled as a linear reacting moment between the steering body and the motorcycle's main body (chassis).

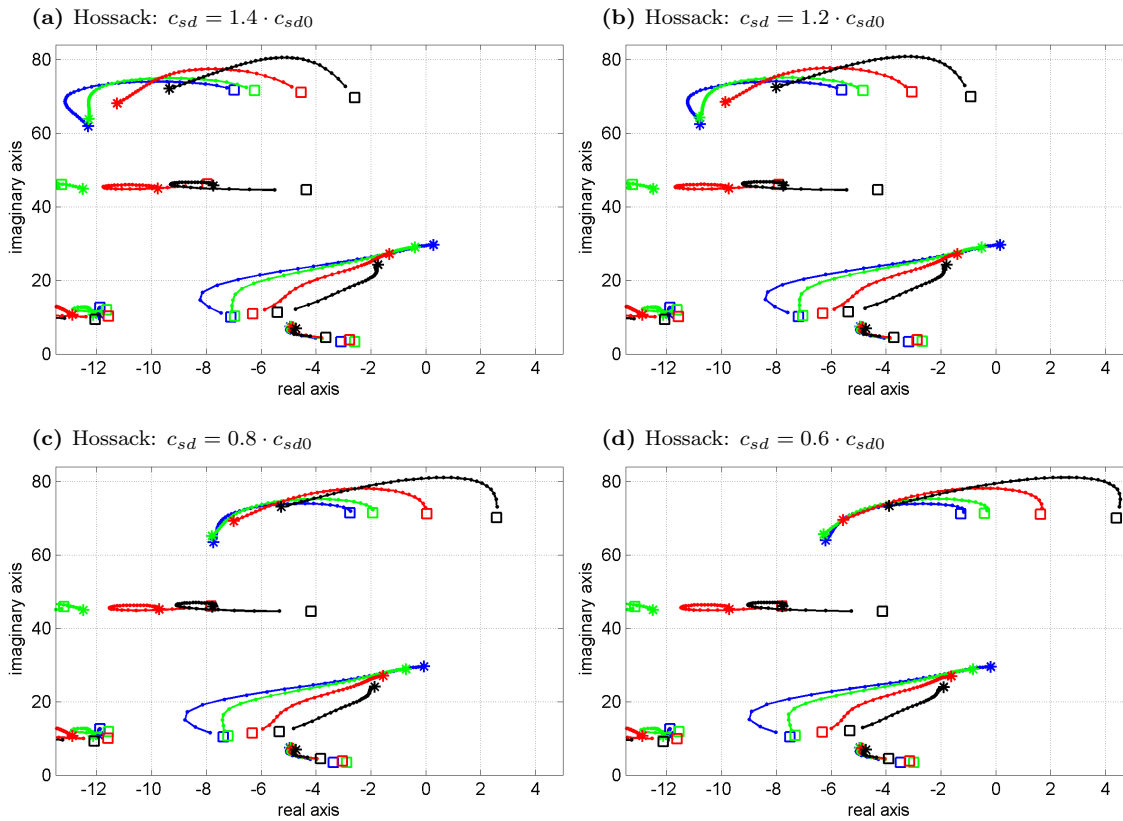


Figure 4.34: Root loci for Hossack suspension lighter model with a constant normal trail (cnt) configuration for different values of the steering damper coefficient. The speed is increased from 10 m/s (□) up to 80 m/s (*) at different roll angles: 0° (blue), 15° (green), 30° (red) and 45° (black).

For the standard motorcycle model fitted with a telescopic fork, it is well known that by increasing the steering damper coefficient, the wobble mode becomes stable since this mode consists in a violent oscillation of the steering body. However, the

weave mode stability at high forward speeds is compromised by the action of the steering damper. The opposite effect is found when the steering damper coefficient is decreased. Figure 4.33 and Fig. 4.34 show similar effects for the girder and Hossack suspension systems lighter models with a constant normal trail (*cnt*) configuration, respectively. In these simulations the steering damper coefficient has been varied from the 60 % of its nominal value ($c_{sd0} = 6.94$ Nms) up to the 140 %.

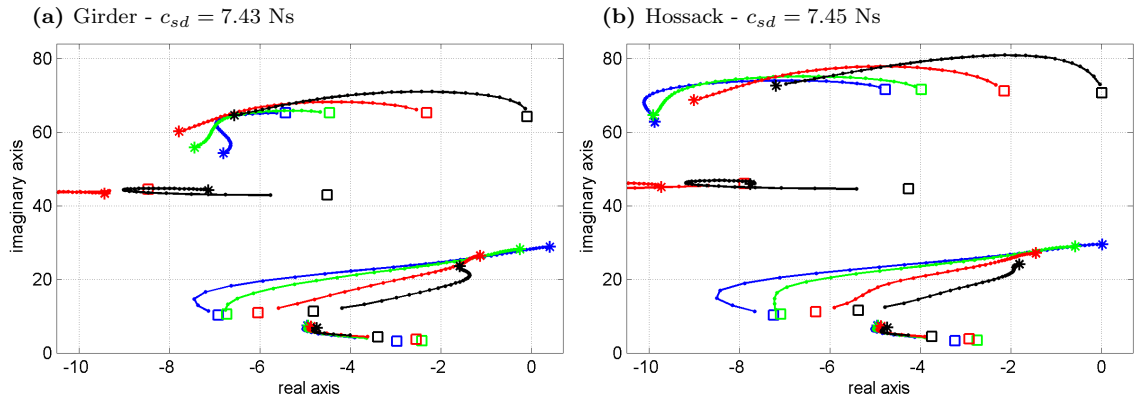


Figure 4.35: Root loci for the girder (a) and Hossack (b) suspension systems for the lighter models with the constant normal trail configurations set with steering damper coefficient values that guarantee wobble stability and only weave instability at high speeds for the girder suspension system. The speed is increased from 10 m/s (\square) up to 80 m/s ($*$) and different roll angles are considered: 0° (blue), 15° (green), 30° (red) and 45° (black).

For the steering damper coefficient variation, an opposite behaviour to that for the twist coefficients variation is found. In the case of the girder suspension, the weave mode stability is always compromised at high speeds ranges even for the smallest value of the steering damper coefficient. In this case, the wobble mode is unstable for half of the speed range at 45° roll angle. Stability of both modes cannot be achieved simultaneously with the steering damper. However, as a compromise solution, far from being optimal, it can be used to stabilize the wobble mode at lower speed and high roll angles by sacrificing the stability at higher forward speed values. For the GSX-R1000 model fitted with lighter girder suspension system with a constant normal trail configuration, the wobble mode becomes fully stable for a value of the steering damper coefficient of $c_{sd} = 7.43$ Ns, which is just slightly higher (7 %) than the nominal value. The maximum forward speed at which the weave mode still remains stable is $v = 70$ m/s, which for non racing conditions is a considerable speed (252 km/h) well above of the allowed speed limits.

For the case of a Hossack suspension system, the weave mode is better damped. A steering damper coefficient value which keeps both modes stable for almost all the studied running conditions can be found for the GSX-R1000 model fitted with this suspension system. This value is $c_{sd} = 7.45$ Ns, which is only a 8 % increase of the nominal value. Figure 4.35a and Fig. 4.35b show the root loci for the lighter girder and Hossack suspension systems respectively with a constant normal trail (*cnt*) configuration when the steering damper coefficients are the values indicated above.

4.4 Conclusions

Discussion

In this chapter the performances of the girder suspension and the Hossack system have been studied for a Suzuki GSX-R1000 motorcycle model which initially was fitted with a telescopic fork suspension. Both of them can be designed with different kinematic behaviours. From a front wheel trajectory similar to that performed by the telescopic fork to a configuration in which the normal trail (or any other handling parameter) remains constant along the full suspension travel. Three geometrical configurations have been studied for the two different suspension systems: parallelogram, fork's trajectory and constant normal trail configurations. Four handling parameters are presented: wheelbase, head angle, trail and normal trail. The first of them is relevant for the motorcycle dynamics but cannot be significantly modified by the suspension system's geometry. The three last of them are similarly related for any kind of suspension system. One of them has been taken as representative, this is the normal trail, whose variations impact has been studied in this chapter.

The principal obstacle at the time to implement the suspension systems' mathematical models is that a real Suzuki GSX-R1000 motorcycle fitted with either a girder or a Hossack suspension system was not available. Therefore, different CAD designs were built in order to obtain the accurate values for the masses, moment and products of inertia that a real suspension system of this type would have. Making use of finite element analysis techniques, the CAD models could be tested and

their masses reduced. Two different models depending on the masses values have been developed for each of these two suspension systems. The first of them keeps similar parts masses than their equivalent parts in the telescopic fork. The second was modelled to be lighter, always inside the compliance security limits.

Once the suspension systems dynamic properties were obtained from the CAD designs, the corresponding mathematical models have been built using VehicleSim multi-body software. Then, two types of simulation were performed: the in-plane dynamic simulations and the quasi-equilibrium acceleration for various representative roll angles.

In the in-plane dynamic simulations cases, the motorcycle is firstly driven through a road step bump input in order to test the front end's response for both suspension systems. A second kind of simulation is carried out to study the in-plane dynamics. It consists in a controlled front wheel braking manoeuvre that produces a 0.5 G constant deceleration on the motorcycle. With these simulations, the anti-dive properties of each suspension system can be observed as well as its actual geometrical behaviour.

On the other hand, in the quasi-equilibrium state simulations, the state space matrices are fed with the results obtained for the different models in order to study the stability properties of the motorcycle under a range of different running conditions. The forward speed is increased from 10 m/s up to 80 m/s and the roll angle varies from 0° up to 45° . Therefore, the stability of the system can be studied through root loci in which the system's states are varied.

Results

During the road bump input simulations it has been found that the behaviour of the girder and the Hossack systems do not differ much from the nominal response when the motorcycle was fitted with a telescopic fork suspension, obtaining similar settle times and maximum elongations. In most of the simulation results here presented, the girder suspension's response is similar to the telescopic fork's response, except in the parallelogram configuration, for which the Hossack suspension system behaviour remains more similar to the fork suspension response than the girder system's response. In terms of systems' weight, no major differences have been found between

the heavier models and the lighter ones.

In the front wheel braking manoeuvres, different behaviour was found for the different suspension systems and geometrical configurations. In the parallelogram configuration (*prl*) case, both suspension systems show better anti-dive properties than the telescopic fork suspension, being the Hossack suspension the system which shows less dive. During a braking manoeuvre the conventional telescopic fork suspension dives reducing the motorcycle's normal trail. In the case of the Hossack suspension system with a *prl* geometrical configuration, the normal trail is reduced in a smaller proportion. However, for the girder system with this *prl* configuration, a larger reduction in normal trail is produced compared to the telescopic fork case.

When both suspension systems are configured such that they follow the same trajectory as the telescopic fork suspension, the girder suspension behaves practically identical to it, being the dive and the normal trail variation of both models very similar to each other. However, the Hossack suspension system differs from the nominal case behaviour of the telescopic fork suspension, reaching higher levels of diving and drastically decreasing its normal trail.

The last geometrical configuration applied to the double wishbones suspension systems seeks to maintain a constant normal trail along the full suspension travel. This ideal behaviour would be reached if the motorcycle's rear frame and tyres' carcasses were rigid. However, due to their flexibilities, the motorcycle geometry is deformed depending on the accelerations. Consequently, a completely constant trail cannot be found. Nevertheless, it can be observed that the reduction of the normal trail with the suspension travel is highly restricted for both suspension systems. The effects of this geometrical configuration on the front end diving are opposed for each of the systems: whilst the girder suspension dives further than the telescopic fork, the Hossack suspension system rises the front end. These behaviours are directly related to the different trajectories followed by the front wheel's contact points for the different suspension systems. That of the girder forms an angle with the vertical axis larger than the trajectory of the telescopic fork wheel's contact point, that opposes less resistance to the motorcycle diving. On the other hand, the trajectory of the wheel's contact point for the Hossack suspension system forms a negative angle with the vertical axis, which makes the front end prone to rise under braking

manoeuvres. In all the performed deceleration simulations, the mass reduction of the lighter models shows results in which the impact of the different geometrical configurations is smoothed.

Regarding to the stability analysis, it was found that the geometrical configuration of the different suspension systems does not imply a substantial difference in terms of root locus for none of the system considered. The mass reduction does not introduce a change in the stability but, as it can be expected, the wobble mode frequency is slightly increased.

Compared to the telescopic fork suspension model, the girder suspension model presents two differences on the wobble mode behaviour. Firstly, its frequency increases for most of the running conditions. Secondly, the damping at higher speeds increases whilst for slower speeds and high roll angles (30° and 45°) it decreases. For the case of 45° roll angle, the wobble mode is unstable for forward speed below 16 m/s. On the other hand, the weave mode damping is reduced at high speeds and small roll angles (0° and 15°). For zero roll angle, the weave mode becomes unstable for speeds above the 70 m/s.

When the Hossack suspension model is compared to the telescopic fork suspension case, it is shown that the wobble mode behaves in a similar manner as in the girder suspension model case. It is unstable for forward speeds below 20 m/s at 45° , whilst for higher speeds this mode's damping is significantly increased compared to the telescopic fork suspension model. However, in the Hossack suspension case, the weave mode remains almost unaffected.

The influence the front frame compliance has on the motorcycle's stability is studied by modifying the twist moment coefficients. It was found that by increasing these coefficients, the weave mode at higher forward speeds and 0° roll angle increases its stability, whilst the wobble mode's stability at lower speeds and 45° roll angle decreases. This behaviour is similar in both girder and Hossack suspension systems.

The suspension system's compliance is a parameter that ought to be considered although it cannot be easily exploited in the motorcycle stability design process. It is for this reason that nowadays, most of the marketed sport motorcycles include a steering damper that allows to improve the wobble mode's damping. However, as it has been shown, it has a detrimental effect on the weave mode stability. The steering

damper coefficient variation in the girder and Hossack models has the opposite effect to the variation of the front end compliance. Higher values of this coefficient help to damp out the wobble mode for all the speed range whilst reducing the weave mode's damping. Nevertheless, the steering damper affects in a more pronounced manner the wobble mode than the weave mode, and for the Hossack suspension system a steering damper coefficient value that stabilizes the weave and wobble modes for almost all the running conditions is provided. For the girder suspension system it is necessary to sacrifice top speed stability (above 70 m/s) in order to get stability for all the leaning angles under study.

Conclusions

In the light of these results, both girder and Hossack suspension systems can be considered as good candidates for general sport motorcycles. In terms of stability, for the motorcycle model considered in this research, the girder suspension system maximum safe speed is restricted to values below 70 m/s due to the limits imposed by weave stability. Whilst, for the case the Hossack suspension system, the steering damper can be set to allow maximum speeds, up to 80 m/s, and still maintain safe running conditions. These systems also produce accurate responses to road bump inputs and show interesting properties in terms of anti-dive and normal trail variation that could not be exploited with a telescopic fork suspension. Furthermore, their simpler construction reduces notably the assembly's weight and could reduce the manufacturing costs.

Chapter 5

Interconnected Suspensions

System: Linear Description

Interconnected suspension systems have been widely used on car industry. Nowadays most of the marketed cars are equipped with anti-roll bars that connect mechanically the front and rear ends wheels separately. Although the connection between the front and rear ends is not as usual as the anti-roll bars, some notable examples have been marketed, being the 1948 Citroën 2CV the first mass production car fitting this system. However, in the two wheels field, these systems are not extended and have not been popularized. The main goal of this chapter is to provide the mathematical background that allows a deeper understanding of the dynamics behind the interconnected suspension systems when implemented on a motorcycle. The starting point of this study is defined by examining three prototypes, of three different manufacturers, which implement this type of suspension systems. Two of them are bicycle demonstrators built by two independent individuals whose works are presented in both websites: (Toptrail 2015) and (RaerDesign 2015). The first of them introduces the concepts behind its prototype in the technical report (Griffiths 2015). However, no mathematical models are provided to analyse the dynamics of any of the two systems.

The third interconnection system under study is that of Creuat Suspension Technology (Creuat 2015). The company provides a mathematical derivation of the proposed arrangement in (Fontdecaba i Buj 2002). In this chapter, this interconnected mechanical implementation is adapted and completed in order to find a more ade-

quate model for two-wheeled vehicles which provides a wider knowledge of this type of systems. For some manufacturers, the interconnection system is claimed as an efficient method to uncouple the bounce and pitch dynamics, and all of them declare a significant improvement in the suspensions' performance. This chapter is focused on studying the dynamics and normal modes properties, whilst in Chapter 6 the improvement on suspension performance is explored.

5.1 Interconnected suspension prototypes

5.1.1 Raer Design

The RaerDesign prototype is one of the functional demonstrators of the interconnected suspension technology on bicycles. Several models have been built based on this interconnection scheme. Fig 5.1 presents the last Rae's bicycle prototype and the sketch provided on his web site (RaerDesign 2015) showing the proposed interconnection layout.

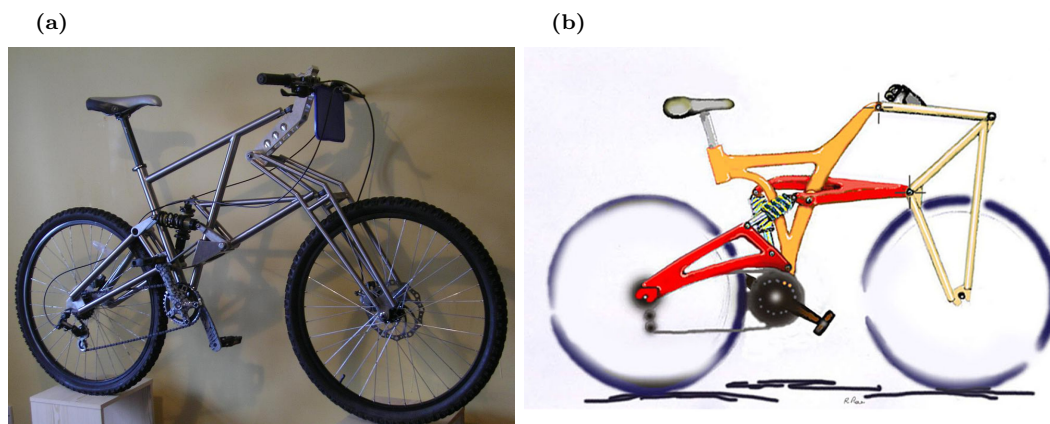


Figure 5.1: a)The last Raer Design interconnected suspension system bicycle prototype. b) Sketch used to explain the interconnection layout. - (RaerDesign 2015).

This sketch is almost the only technical explanation of the invention that can be found as per to date. So far, no technical details regarding this mechanical proposal have been found. Only one international patent of the invention (Rae 2010) is found in which this mechanical arrangement is described. However, no further theoretical discussion appears to be available neither in the patent document nor in the web site. Nevertheless, a dynamical analysis can be performed from the sketch shown in

Fig. 5.1. In order to simplify its understanding, a schematic diagram containing the most significant parameters is presented in Fig. 5.2.

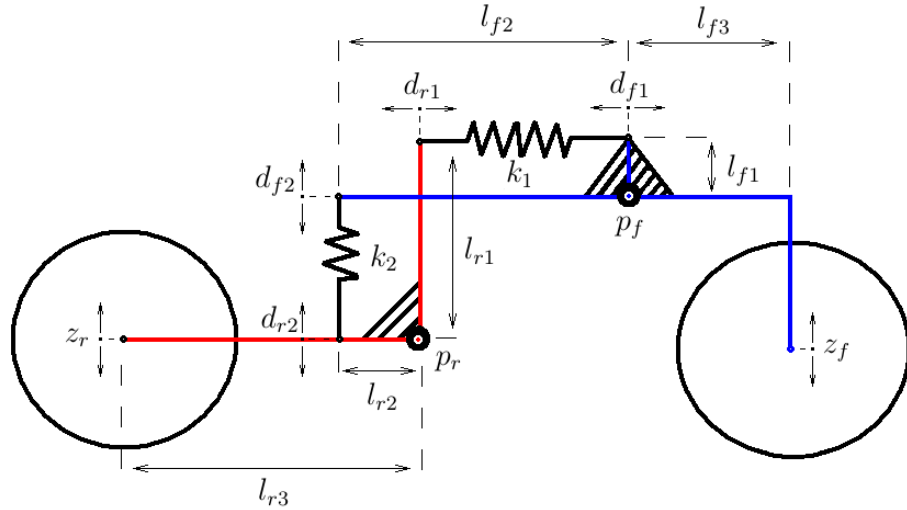


Figure 5.2: Diagram showing the interconnection layout and relevant parameters. The Raer Design system can be divided in two rigid bodies, front (blue) and rear (red). They are connected through two independent springs-damper units. In this figure only the springs are shown in order to provide a clearer view.

The interconnection layout consists of two rigid bodies attached to the front and rear wheels respectively, such that each of them pivots about its corresponding axis located at the points p_f or p_r . The corresponding front and rear bodies are connected to each other by two independent shock-absorbers, consisting of two springs and two dampers acting in parallel. In Fig. 5.2 these elements are drawn only as springs in order to provide a clearer view. The front suspension body is plotted in blue whilst the rear one is plotted in red. Both bodies are characterized by three lengths each. These lengths correspond to the distance from the pivot points to the junctions with the two shock-absorbers and the corresponding wheel. For the front suspension body, l_{f1} is the distance from the pivoting point (p_f) to the junction with the first spring (k_1); l_{f2} is the distance from the pivoting point (p_f) to the junction with the second spring (k_2) and l_{f3} is the distance from the pivoting point (p_f) to the connection with the front wheel. A similar notation is used for the rear suspension body where the subscript 'r' is used instead of 'f'. The displacements of the springs tips are named as d_{f1} and d_{r1} for the spring one and d_{f2} and d_{r2} for the spring two. Under a lineal approach, the compression of each spring is given by $d_{fi} - d_{ri}$ and it is related to the wheel's vertical displacement through the geometrical ratios:

$$\begin{aligned} d_{f1} &= \rho_{f1} \cdot z_f & ; & & d_{r1} &= -\rho_{r1} \cdot z_r \\ d_{f2} &= -\rho_{f2} \cdot z_f & ; & & d_{r2} &= \rho_{r2} \cdot z_r \end{aligned}$$

Considering that all the lengths are taken as positive values, and in order to keep a consistent notation with the sign criteria, the ratios ρ_{f2} and ρ_{r1} must be preceded by a negative sign, being these ratios also defined as positive.

$$\rho_{f1} = \frac{l_{f1}}{l_{f3}} \quad ; \quad \rho_{f2} = \frac{l_{f2}}{l_{f3}} \quad ; \quad \rho_{r1} = \frac{l_{r1}}{l_{r3}} \quad ; \quad \rho_{r2} = \frac{l_{r2}}{l_{r3}}$$

Then, the forces appearing on each springs' tip are written as:

$$f_1 = -k_1 \cdot (\rho_{f1}z_f - \rho_{r1}z_r) \quad (5.1)$$

$$f_2 = -k_2 \cdot (\rho_{f2}z_f - \rho_{r2}z_r) \quad (5.2)$$

These forces are transmitted to the wheels through the same geometrical ratio. And the total forces appearing in the wheels result in the addition of the forces exerted by the two springs:

$$f_{fz} = \rho_{f1} \cdot f_1 + \rho_{f2} \cdot f_2 \quad (5.3)$$

$$f_{rz} = -\rho_{r1} \cdot f_1 - \rho_{r2} \cdot f_2 \quad (5.4)$$

Finally the total spring forces can be written as functions of the front and rear wheels displacement:

$$f_{fz} = (-\rho_{f1}^2 k_1 - \rho_{f2}^2 k_2) \cdot z_f + (-\rho_{f1} \rho_{r1} k_1 - \rho_{f2} \rho_{r2} k_2) \cdot z_r \quad (5.5)$$

$$f_{rz} = (-\rho_{r1}^2 k_1 - \rho_{r2}^2 k_2) \cdot z_r + (-\rho_{f1} \rho_{r1} k_1 - \rho_{f2} \rho_{r2} k_2) \cdot z_f \quad (5.6)$$

Three equivalent stiffness coefficients appear in these equations. The front stiffness coefficient (k_f) is the stiffness coefficient of an equivalent spring reacting to the front wheel displacement. The rear stiffness coefficient (k_r) is that of an equivalent spring which reacts to the rear wheel displacement. The interconnection stiffness coefficient (k_s) is that corresponding to the force that appears in one wheel due to the displacement of the other one. This interconnection coefficient is similar for

both front and rear suspension forces.

$$k_f = \rho_{f1}^2 \cdot k_1 + \rho_{f2}^2 \cdot k_2 \quad (5.7)$$

$$k_r = \rho_{r1}^2 \cdot k_1 + \rho_{r2}^2 \cdot k_2 \quad (5.8)$$

$$k_s = \rho_{f1}\rho_{r1} \cdot k_1 + \rho_{f2}\rho_{r2} \cdot k_2 \quad (5.9)$$

These results are found for the springs forces. However, a similar analysis is valid for the damping forces obtaining the following equivalent damping coefficients:

$$c_f = \rho_{f1}^2 \cdot c_1 + \rho_{f2}^2 \cdot c_2 \quad (5.10)$$

$$c_r = \rho_{r1}^2 \cdot c_1 + \rho_{r2}^2 \cdot c_2 \quad (5.11)$$

$$c_s = \rho_{f1}\rho_{r1} \cdot c_1 + \rho_{f2}\rho_{r2} \cdot c_2 \quad (5.12)$$

Then, the total suspension force can be written as follows:

$$f_{fz} = k_f \cdot z_f + k_s \cdot z_r + c_f \cdot \dot{z}_f + c_s \cdot \dot{z}_r \quad (5.13)$$

$$f_{rz} = k_s \cdot z_f + k_r \cdot z_r + c_s \cdot \dot{z}_f + c_r \cdot \dot{z}_r \quad (5.14)$$

The equivalent full interconnected suspension system consists of six parameters, three of them related to the stiffness (k_f , k_r and k_s) and three related to the damping of the system (c_f , c_r and c_s). Eight independent variables are available to define the desired values of the damping and stiffness coefficients of the resultant suspension system: two stiffness coefficients corresponding to the physical springs (k_1 and k_2), two damping coefficients corresponding to the physical dampers (c_1 and c_2) and four geometrical ratios (ρ_{f1} , ρ_{r1} , ρ_{f2} , ρ_{r2}). Solving the equation system {Eq. 5.7, Eq. 5.8, Eq. 5.9} the values of the stiffness coefficient and the one of the geometrical ratios are found depending on the equivalent stiffness coefficient and the rest of the geometrical ratios:

$$k_1 = \frac{-2k_f\rho_{f2}\rho_{r2}k_s + \rho_{r2}^2k_f^2 + \rho_{f2}^2k_s^2}{(-2\rho_{f2}\rho_{r2}k_s + k_r\rho_{f2}^2 + \rho_{r2}^2k_f)\rho_{f1}^2} \quad (5.15)$$

$$k_2 = \frac{-k_s^2 + k_fk_r}{-2\rho_{f2}\rho_{r2}k_s + k_r\rho_{f2}^2 + \rho_{r2}^2k_f} \quad (5.16)$$

$$\rho_{r1} = \frac{-\rho_{f1}(-\rho_{r2}k_s + k_r\rho_{f2})}{(\rho_{r2}k_f - k_s\rho_{f2})} \quad (5.17)$$

The values of the damping coefficients and other of the geometrical ratios are found by solving the equations system {Eq. 5.10, Eq. 5.11, Eq. 5.12}

$$c_1 = \frac{c_r c_f - c_s^2}{-2c_s \rho_{r1} \rho_{f1} + \rho_{f1}^2 c_r + c_f \rho_{r1}^2} \quad (5.18)$$

$$c_2 = \frac{c_s^2 \rho_{r1}^2 - 2c_s \rho_{r1} \rho_{f1} c_r + \rho_{f1}^2 c_r^2}{\rho_{r2}^2 (-2c_s \rho_{r1} \rho_{f1} + \rho_{f1}^2 c_r + c_f \rho_{r1}^2)} \quad (5.19)$$

$$\rho_{f2} = \frac{-(-\rho_{f1} c_s + c_f \rho_{r1}) \rho_{r2}}{-c_s \rho_{r1} + \rho_{f1} c_r} \quad (5.20)$$

Finally, by solving the equations system {Eq. 5.17, Eq. 5.20} the solutions for the geometrical ratios ρ_{r1} and ρ_{f2} are found. One double solution appears for ρ_{r1} which results proportional to ρ_{f1} . For ρ_{f2} two different solutions are found where ρ_{f2} is proportional to ρ_{r2} in both cases.

$$\rho_{r1} = \rho_{f1} \cdot \frac{k_s - k_f}{k_r - k_s}$$

$$\rho_{f2} = \rho_{r2} \cdot \frac{1}{2} \frac{-k_f c_r + k_r c_f \pm \sqrt{k_f^2 c_r^2 - 2k_f c_r k_r c_f + k_r^2 c_f^2 - 4k_f c_s c_r k_s + 4k_f c_s^2 k_r + 4c_f k_s^2 c_r - 4c_f k_s c_s k_r}}{-k_f c_s + c_f k_s}$$

It can be noticed that only two independent geometry parameters do exist, being this a total of six independent variables to define the six interconnected suspension coefficients. The independent geometrical relation can be taken as:

$$\tau_1 = \frac{\rho_{r1}}{\rho_{f1}} \quad ; \quad \tau_2 = \frac{\rho_{f2}}{\rho_{r2}}$$

This interconnected suspension system is fully configurable taking advantage of its geometrical configuration. This implies both positive and negative consequences: it only needs two shock-absorbers for its implementation, reducing in this way its cost and its weight. However, once the geometrical ratios have been calculated and implemented on the vehicle, they cannot be modified. Therefore, the equivalent interconnected suspension system settings are more restricted than for other systems that may include a third shock-absorber.

5.1.2 The Toptrail Project - Citroën 2CV

Other prototype of a bicycle with interconnected suspension system is that of the Top Trail Interconnected Suspension Bicycle Project (Toptrail 2015). The author of

this project presents this work in a technical report that can be found in (Griffiths 2015). Several test of the prototype compared to conventionally suspended bicycles are presented in different videos that display the advantages that this model introduces in terms of suspension efficiency. However, a dynamical analysis of the interconnection system is not presented.

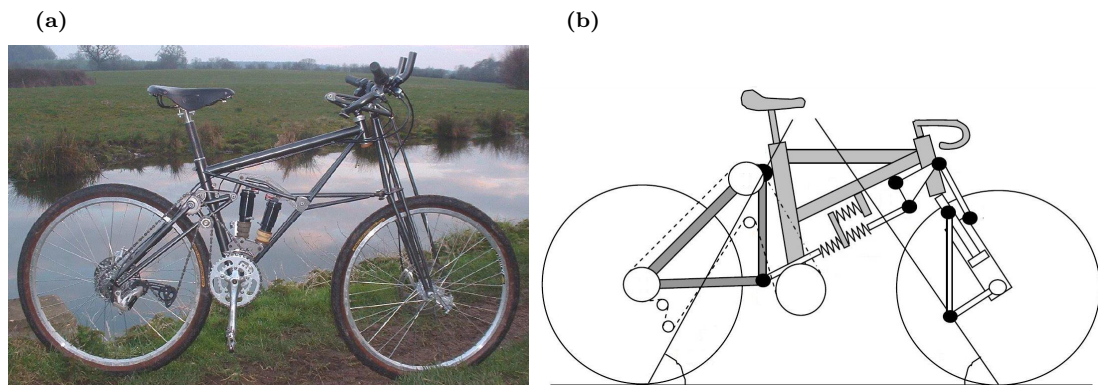


Figure 5.3: a) Toptrail interconnected suspension system bicycle prototype. b) Sketch used to explain the interconnection layout. - (Toptrail 2015).

In the technical report, the author discusses on the common ridding issues appearing in conventional bicycles and a different mechanical method is proposed in order to address those issues. The main focus is on the bicycle's dive, boobing and sag movement. Although the bounce mode's natural frequency is a factor to be considered on the bicycle's design, the interconnection mechanism is presented as a way to reduce bobbing appearing whilst pedalling instead of a design element for the bicycle normal mode. By combining this feature with other different solutions, finally the author proposes a full suspension system as in Fig. 5.3b. This proposal does not correspond to the final design of the bicycle's prototype, which looks to be closer to one of the sketches that the author presents in his international patent (Griffiths 2008). The prototype, shown in Fig. 5.3a, uses two shock-absorbers and a complex mechanical arrangement to achieve the interconnection properties stated in the technical report. This section is focused in the three stiffness-damping units arrangement presented on the technical report instead of in the final arrangement of the prototype. One of the reasons is that the two absorbing elements of the interconnected suspension system have been already presented in the previous section.

On the other hand, the three absorbing elements interconnection system presents a similar layout of that of the famous Citroën 2CV whose efficiency and reliability

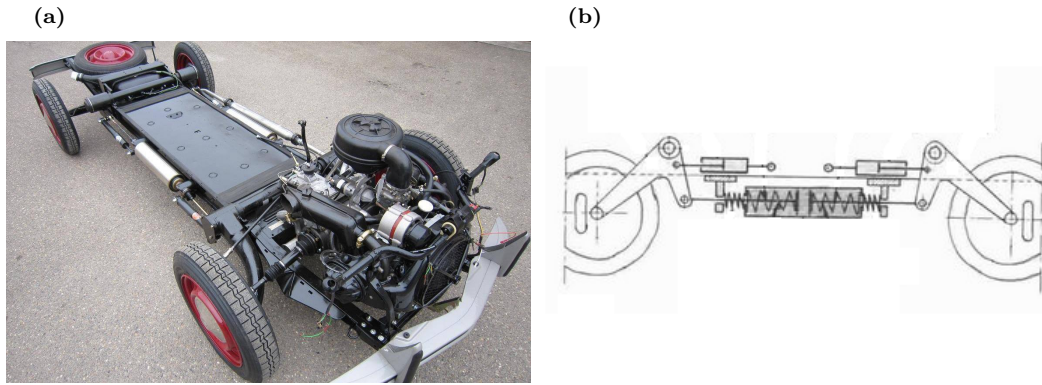


Figure 5.4: a) Citroën 2CV chassis where the interconnected suspension system can be appreciated as two longitudinal silver cylinders. - www.bringatrailer.com. b) Sketch of interconnection layout. - www.bielles.free.fr.

have been widely proven. Figure 5.4a shows a chassis of this car and the interconnected suspension system can be seen at its both sides as two silver cylinders. Figure 5.4b shows a sketch of this mechanism. In order to have a clearer view of the kinematics of the system, Fig. 5.5 shows a diagram corresponding to this interconnection systems in which all the relevant parameters can be seen.

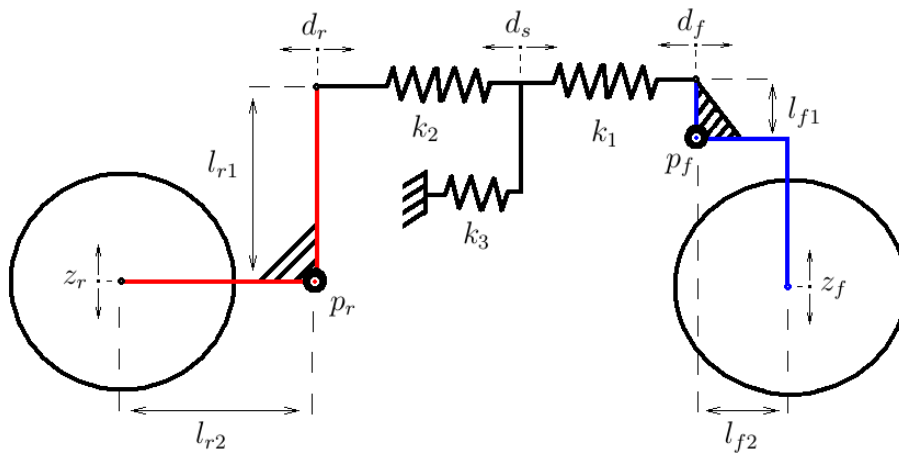


Figure 5.5: Diagram showing the interconnection layout and relevant parameters. The Toptrail system can be divided in two rigid bodies, front (blue) and rear (red). They are connected through two springs-damper units connected in series. A third spring-damper unit is connected between the bicycle main frame and a junction point of those two units. In this figure only the springs are shown in order to provide a clearer view.

As in section 5.1.1, the analysis here is firstly carried out for the springs forces and then extended to the damper's forces. The forces appearing on each of the three springs depend on the springs' tips displacements:

$$f_1 = -k_1 \cdot (d_f - d_s) \quad (5.21)$$

$$f_2 = -k_2 \cdot (d_s - d_r) \quad (5.22)$$

$$f_3 = -k_3 \cdot d_s \quad (5.23)$$

The front (d_f) and the rear (d_r) springs' tips displacements are related to the front and rear wheels' vertical displacement by the geometrical ratios:

$$d_f = \rho_f \cdot z_f \quad ; \quad d_r = -\rho_r \cdot z_r$$

Where:

$$\rho_f = \frac{l_{f1}}{l_{f2}} \quad ; \quad \rho_r = \frac{l_{r1}}{l_{r2}}$$

The displacement d_s is calculated by equating all the forces applied at this point ($f_1 = f_2 + f_3$) and this gives:

$$d_s = \frac{k_1 d_f + k_2 d_r}{k_1 + k_2 + k_3}$$

The total forces appearing on the springs' tips can be found by substituting this value in Eq. 5.21 and Eq. 5.22. Taking into consideration the geometrical ratios, the equivalent suspension forces can be written as functions of the front and rear wheels' displacement:

$$f_{fz} = \frac{-k_1(k_2 + k_3)\rho_f^2}{k_1 + k_2 + k_3} \cdot z_f - \frac{k_1 k_2 \rho_f \rho_r}{k_1 + k_2 + k_3} \cdot z_r \quad (5.24)$$

$$f_{rz} = \frac{-k_2(k_1 + k_3)\rho_r^2}{k_1 + k_2 + k_3} \cdot z_r - \frac{k_1 k_2 \rho_f \rho_r}{k_1 + k_2 + k_3} \cdot z_f \quad (5.25)$$

This result is consistent with that found in previous subsection 5.1.1, where three resulting parameters fully describe the equivalent interconnected system. These are the front spring stiffness coefficient (k_f), the rear spring stiffness coefficient (k_r) and the interconnection spring stiffness coefficient (k_s) which is equal for both front and rear suspensions. A similar analysis is valid for the damping forces. The complete resulting system is then defined by the equivalent stiffness and damping coefficients

and the total suspension forces in Eq. 5.24 and Eq. 5.25 can now be rewritten as:

$$f_{fz} = -k_f \cdot z_f - k_s \cdot z_r - c_f \cdot \dot{z}_f - c_s \cdot \dot{z}_r \quad (5.26)$$

$$f_{rz} = -k_s \cdot z_f - k_r \cdot z_r - c_s \cdot \dot{z}_f - c_r \cdot \dot{z}_r \quad (5.27)$$

Where:

$$\begin{aligned} k_f &= \frac{-k_1(k_2 + k_3)\rho_f^2}{k_1 + k_2 + k_3} & ; & & c_f &= \frac{-c_1(c_2 + c_3)\rho_f^2}{c_1 + c_2 + c_3} \\ k_r &= \frac{-k_2(k_1 + k_3)\rho_r^2}{k_1 + k_2 + k_3} & ; & & c_r &= \frac{-c_2(c_1 + c_3)\rho_r^2}{c_1 + c_2 + c_3} \\ k_s &= \frac{k_1 k_2 \rho_f \rho_r}{k_1 + k_2 + k_3} & ; & & c_s &= \frac{c_1 c_2 \rho_f \rho_r}{c_1 + c_2 + c_3} \end{aligned}$$

Three springs and three dampers are available to set the three equivalent stiffness and the three equivalent damping coefficients respectively. Thus in these cases, the geometrical ratios are free to be set as desired. For simplicity, they can be considered to be one. Under these conditions, the values of equivalent suspension coefficient will define the necessary values of the actual shock-absorbers coefficients:

$$\begin{aligned} k_1 &= \frac{k_f k_r - k_s^2}{k_r - k_s} & ; & & c_1 &= \frac{c_f c_r - c_s^2}{c_r - c_s} \\ k_2 &= \frac{k_f k_r - k_s^2}{k_f - k_s} & ; & & c_2 &= \frac{c_f c_r - c_s^2}{c_f - c_s} \\ k_3 &= \frac{k_f k_r - k_s^2}{k_s} & ; & & c_3 &= \frac{c_f c_r - c_s^2}{c_s} \end{aligned}$$

In the light of the results, the main advantage of this interconnection system is that the geometrical ratios are not needed in order to set the equivalent coefficient. Therefore the system is more flexible and its configuration might be eventually changed after the motorcycle has been built by changing the shock-absorbers' properties. However, a third spring-damper unit is needed, increasing in this way the costs and weight of the overall assembly. Nevertheless, this implementation just presented, represents a more intuitive and simpler layout than that of only two absorbing elements.

5.1.3 Creuat Suspension Technology

Creuat Suspension Technology (Creuat 2015) is a technological company specialized in developing interconnected suspension systems based on passive mechanical com-

ponents. This work is mainly focussed in four-wheeled vehicles but has also adapted the technology to be implemented in motorcycles. This technology is claimed to separate the spring and damper rates for each vehicle's movement (such as pitch and bounce) with reduced cost and complexity. The system consists of a central device hydraulically connected to the motorcycle's front fork and rear swinging arm such that it contains the spring and damper elements. Figure 5.6a and Fig. 5.6b show the system fitted in a motorcycle and a sketch representing the interconnection system respectively.



Figure 5.6: a) CREUAT interconnected suspension system. b) Concept's Explanatory diagram. - (Creuat 2015).

The CREUAT technology theoretical background is presented in (Fontdecaba i Buj 2002) and it focuses in four-wheeled vehicles dynamics: the four characteristics motions associated to the vehicle (bounce, pitch, roll and axle crossing) are analysed. Considering a four degrees of freedom model, in which the wheels' masses are neglected, the general elasticity matrix is described as diagonal matrix containing the stiffness coefficients for each of the four general motions. Through a change of basis, the individual elasticity matrix is obtained. It contains the stiffness coefficients of the forces appearing on each individual wheel. This matrix is not diagonal and its crossed terms represent the interconnection stiffness rates provided by the central device. The author states the optimal stiffness and damping properties that a suspension system should provide in terms of improving the vehicle's handling, traction and comfort. These requirements are addressed by means of the interconnected suspension system where the independence of all the characteristics motions and minimal axle crossing stiffness and damping coefficients are sought. Finally,

(Fontdecaba i Buj 2002) presents the results obtained in independent tests on a real vehicle fitted with the CREUAT interconnected suspension system to demonstrate the efficiency of the system. Although this contribution is focussed in four-wheeled vehicles, it represents a good starting point for motorcycle interconnected suspension system analysis. In the following sections a similar analysis is performed to the motorcycle's dynamics. First, a model with independent front and rear suspensions is studied. Then the effects of the interconnected system are introduced in the model.

5.2 Reduced model with two degrees of freedom

Following the work presented in (Fontdecaba i Buj 2002) and as a first approach, a two degrees of freedom model (wheel masses and tyres stiffness are not included) is studied. Taking advantage of the reduced model presented in Chapter 3, the motorcycle is represented by a rigid body connected to the ground by two sets of spring-damping units. The body's total mass (m_t) and its moment of inertia about the y axis (I_y) are equivalent to those of a GSX-R1000 motorcycle including all the unsprung masses, whilst the stiffness and damping coefficients have been calculated to produce equivalent responses to those of a nominal GSX-R1000 suspension system.

5.2.1 Independent suspensions system

Individual coordinates

Figure 5.7 represents the two degrees of freedom model where the front and rear suspension systems are independent from each other and not connected. In this model the front and the rear suspension forces are represented by the following equations:

$$f_f = -k_f \cdot (z_f - u_f) - c_f \cdot (\dot{z}_f - \dot{u}_f) \quad (5.28)$$

$$f_r = -k_r \cdot (z_r - u_r) - c_r \cdot (\dot{z}_r - \dot{u}_r) \quad (5.29)$$

z_f and z_r represent front and rear ends vertical displacement respectively whilst

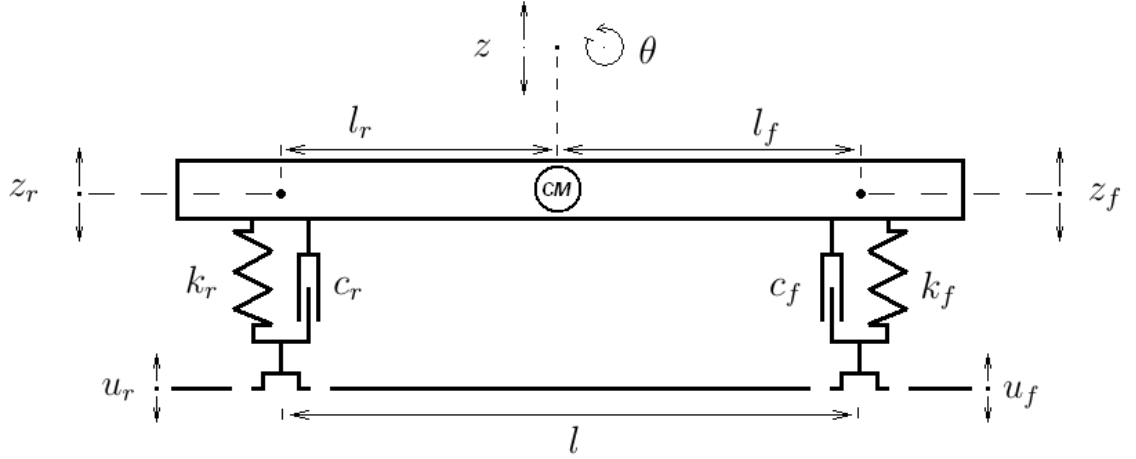


Figure 5.7: Two degrees of freedom motorcycle model with independent suspension systems. Two sets of generalized coordinates are presented: a) Front (z_f) and rear (z_r) chassis ends vertical displacement. b) Vertical displacement (z) and rotation about the y axis (θ) of the chassis centre of masses. In both cases, the system inputs are introduced through the front (u_f) and the rear (u_r) tyres.

u_f and u_r are the front and rear road inputs. The front and rear suspension spring coefficients are k_f and k_r ; c_f and c_r are the corresponding damping coefficients. For simplicity, the system inputs can be taken as zero and then Eq. 5.28 and Eq. 5.29 can be represented as:

$$F^i = R^i \cdot Q^i \quad (5.30)$$

Where Q^i is the coordinates' vector, R^i is the stiffness-damping matrix and F^i is the forces' vector.

$$F^i = \begin{pmatrix} \dot{z}_f \\ \dot{z}_r \\ f_f \\ f_r \end{pmatrix} ; \quad R^i = \begin{pmatrix} 0 & 0 & 1 & 0 \\ 0 & 0 & 0 & 1 \\ -k_f & 0 & -c_f & 0 \\ 0 & -k_r & 0 & -c_r \end{pmatrix} ; \quad Q^i = \begin{pmatrix} z_f \\ z_r \\ \dot{z}_f \\ \dot{z}_r \end{pmatrix}$$

F^i contains the speeds of the generalized coordinates in order to follow a state space representation. However, writing the equations of motion as a function of the accelerations needs the equivalent masses for the front and the rear ends, which are not directly available. Nevertheless, this masses can be found through a series of changes of basis on Eq. 5.30. The kinematics and dynamics of the model can be represented either by the individual coordinates set ($[z_f, z_r]$) or by a second set

of general coordinates ($[z, \theta]$), for which z is the vertical displacement of the rigid body center of masses and θ is the rotation about its y axis. Considering a linear small angles approximation, the new set of coordinates is:

$$z \approx \frac{l_r \cdot z_f + l_f \cdot z_r}{l} \quad (5.31)$$

$$\theta \approx \frac{-z_f + z_r}{l} \quad (5.32)$$

Same linear relations are valid for speeds and accelerations. The motorcycle's geometry determines the equivalences between one and the other coordinates system, being l_f and l_r the distances from the motorcycle's centre of masses to its front end and rear end respectively; l is the sum of these two distances. On the other hand, the equivalent force (f) and moment (μ) appearing in the rigid body due to the action of the front and the rear suspension systems are determined by:

$$f \approx f_f + f_r \quad (5.33)$$

$$\mu \approx -l_f \cdot f_f + l_r \cdot f_r \quad (5.34)$$

Two changes of basis matrix to pass from the individual coordinates system to the general coordinates system can be obtained. One of them converting the coordinates vectors (positions, speeds and accelerations) and the other one converting the individual front and rear suspension forces into general equivalent force and moment. The following equation converts the individual coordinates vectors into the general ones:

$$Q^g = Pq \cdot Q^i \quad (5.35)$$

Where Q^i is the individual coordinates vector, Q^g is the general coordinates vector and Pq is the change of basis matrix from the individual to the general coordinates systems:

$$Q^g = \begin{pmatrix} z \\ \theta \\ \dot{z} \\ \dot{\theta} \end{pmatrix} ; \quad Pq = \frac{1}{l} \begin{pmatrix} l_r & l_f & 0 & 0 \\ -1 & 1 & 0 & 0 \\ 0 & 0 & l_r & l_f \\ 0 & 0 & -1 & 1 \end{pmatrix} ; \quad Q^i = \begin{pmatrix} z_f \\ z_r \\ \dot{z}_f \\ \dot{z}_r \end{pmatrix}$$

A similar change of basis can be applied in order to convert the individual forces vector into the general force and moment vector:

$$F^g = Pf \cdot F^i \quad (5.36)$$

F^i is the individual forces vector, F^g is the general force and moment vector and Pf is the change of basis matrix from the individual to the general coordinates systems:

$$F^g = \begin{pmatrix} \dot{z} \\ \dot{\theta} \\ f \\ \mu \end{pmatrix} ; \quad Pf = \frac{1}{l} \begin{pmatrix} l_r & l_f & 0 & 0 \\ -1 & 1 & 0 & 0 \\ 0 & 0 & l & l \\ 0 & 0 & -l_f \cdot l & l_r \cdot l \end{pmatrix} ; \quad F^i = \begin{pmatrix} \dot{z}_f \\ \dot{z}_r \\ f_f \\ f_r \end{pmatrix}$$

The second Newtown's law is expressed on its matrix form as follows:

$$F^g = M^g \cdot \dot{Q}^g \quad (5.37)$$

M^g is the mass-inertia matrix and \dot{Q}^g is the time derivative of the general coordinates vector:

$$M^g = \begin{pmatrix} 1 & 0 & 0 & 0 \\ 0 & 1 & 0 & 0 \\ 0 & 0 & m_t & 0 \\ 0 & 0 & 0 & I_y \end{pmatrix} ; \quad \dot{Q}^g = \begin{pmatrix} \dot{z} \\ \dot{\theta} \\ \ddot{z} \\ \ddot{\theta} \end{pmatrix}$$

Finally, Eq. 5.30 can be written as:

$$Pf^{-1} \cdot M^g \cdot Pf \cdot \dot{Q}^i = R^i \cdot Q^i \quad (5.38)$$

The individual mass-inertia matrix is found as $M^i = Pf^{-1} \cdot M^g \cdot Pf$ and the

equations of motion can now be written as:

$$M^i \cdot \dot{Q}^i = R^i \cdot Q^i \quad (5.39)$$

Which is:

$$\begin{pmatrix} 1 & 0 & 0 & 0 \\ 0 & 1 & 0 & 0 \\ 0 & 0 & \frac{m_t l_r^2 + I_y}{l^2} & \frac{m_t l_f l_r - I_y}{l^2} \\ 0 & 0 & \frac{m_t l_f l_r - I_y}{l^2} & \frac{m_t l_f^2 + I_y}{l^2} \end{pmatrix} \cdot \begin{pmatrix} \dot{z}_f \\ \dot{z}_r \\ \ddot{z}_f \\ \ddot{z}_r \end{pmatrix} = \begin{pmatrix} 0 & 0 & 1 & 0 \\ 0 & 0 & 0 & 1 \\ -k_f & 0 & -c_f & 0 \\ 0 & -k_r & 0 & -c_r \end{pmatrix} \cdot \begin{pmatrix} z_f \\ z_r \\ \dot{z}_f \\ \dot{z}_r \end{pmatrix}$$

Looking at Eq. 5.39, it can be noticed that the front and rear ends equations of motion are coupled through the individual mass-inertia matrix. Similarly as in (Cossalter 2006, pp. 177–179), it is found here that the only case in which these two equations are uncoupled is when the following condition is satisfied:

$$I_y = m_t l_f l_r \quad (5.40)$$

In this case, the front and the rear equivalent masses are:

$$m_f = m_t \frac{l_r}{l} \quad ; \quad m_r = m_t \frac{l_f}{l}$$

Under these conditions the motorcycle can be represented as two independent masses (m_f and m_r) suspended by two independent spring-damping units ($[k_f, c_f]$ and $[k_r, c_r]$). Although this is an advantage for suspension systems design, the condition in Eq. 5.40 represents a difficult to achieve geometrical configuration for any motorcycle. A considerable amount of mass must be located beyond the front and rear ends in order to compensate for the mass in between the two ends. Such mass distribution will have an impact on the motorcycle dynamical behaviour.

General coordinates

Considering that the two normal modes of this two degrees of freedom motorcycle model are bounce and pitch (being the bounce motion related to the vertical displacement of the motorcycle centre of masses and the pitch motion related to the

rotation about its y axis), a more intuitive representation of the motorcycle dynamics can be provided if the system is expressed in its general coordinates basis. In this basis, the general stiffness-damping matrix R^g is:

$$R^g = Pf \cdot R^i \cdot Pq^{-1} \quad (5.41)$$

And this is:

$$R^g = \begin{pmatrix} 0 & 0 & 1 & 0 \\ 0 & 0 & 0 & 1 \\ -k_z & -k_{z\theta} & -c_z & -c_{z\theta} \\ -k_{\theta z} & -k_\theta & -c_{\theta z} & -c_\theta \end{pmatrix}$$

R^g contains the stiffness and damping coefficients associated to the vertical displacement $[k_z, c_z]$, the rotation about the y axis $[k_\theta, c_\theta]$ and crossed terms for the interaction between both motions $[k_{z\theta}, c_{z\theta}]$ and $[k_{\theta z}, c_{\theta z}]$. These crossed terms are equal for bounce and pitch motions.

$$\begin{aligned} k_z &= k_f + k_r & ; & & c_z &= c_f + c_r \\ k_\theta &= k_f l_f^2 + k_r l_r^2 & ; & & c_\theta &= c_f l_f^2 + c_r l_r^2 \\ k_{z\theta} &= k_{\theta z} = -k_f l_f l_r + k_r l_r & ; & & c_{z\theta} &= c_{\theta z} = -c_f l_f l_r + c_r l_r \end{aligned}$$

Given the bounce (k_z, c_z) and the pitch (k_θ, c_θ) general coefficients, the necessary front (k_f, c_f) and rear (k_r, c_r) coefficients can be found from the results above :

$$\begin{aligned} k_f &= \frac{k_h l_r^2 - k_p}{l_f^2 - l_r^2} & ; & & c_f &= \frac{c_h l_r^2 - c_p}{l_f^2 - l_r^2} \\ k_r &= \frac{k_h l_f^2 - k_p}{l_r^2 - l_f^2} & ; & & c_r &= \frac{c_h l_f^2 - c_p}{l_r^2 - l_f^2} \end{aligned}$$

However, the crossed term $(k_{z\theta} = k_{\theta z})$ cannot be cancelled and its value depends on the bounce and pitch coefficients.

$$k_{z\theta} = k_{\theta z} = \frac{l_f l_r}{l_f - l_r} \cdot k_h + \frac{1}{l_r - l_f} \cdot k_p \quad ; \quad c_{z\theta} = c_{\theta z} = \frac{l_f l_r}{l_f - l_r} \cdot c_h + \frac{1}{l_r - l_f} \cdot c_p$$

If the equations of motion are written in the general coordinates basis, the normal

modes containing both motions components can be predicted:

$$\begin{pmatrix} \dot{z} \\ \dot{\theta} \\ \ddot{z} \\ \ddot{\theta} \end{pmatrix} = \begin{pmatrix} 0 & 0 & 1 & 0 \\ 0 & 0 & 0 & 1 \\ \frac{-k_z}{mt} & \frac{-k_{z\theta}}{mt} & \frac{-c_z}{mt} & \frac{-c_{z\theta}}{mt} \\ \frac{-k_{\theta z}}{I_y} & \frac{-k_\theta}{I_y} & \frac{-c_{\theta z}}{I_y} & \frac{-c_\theta}{I_y} \end{pmatrix} \cdot \begin{pmatrix} z \\ \theta \\ \dot{z} \\ \dot{\theta} \end{pmatrix} \quad (5.42)$$

This is, each of the normal modes will be a combination of the motorcycle's vertical displacement (z) and the rotation about the y axis (θ). In bounce mode case, the vertical displacement is the predominant motion component whilst for the pitch mode case it is the rotation. By modifying the motorcycle's geometry (l_f and l_r) and its suspension configuration (k_f , c_f , k_r and c_r) the relevance of both motions on each of the normal modes will change simultaneously as their resonance frequency and their damping is varied. Bounce and pitch normal modes corresponding to a pure vertical displacement of the centre of masses and rotation about the y axis respectively can be obtained only if the following relations are satisfied:

$$k_r = \frac{l_f}{l_r} \cdot k_f \quad ; \quad c_r = \frac{l_f}{l_r} \cdot c_f$$

Then, the stiffness and damping coefficients for bounce and pitch modes become:

$$\begin{aligned} k_z &= \frac{l}{l_r} \cdot k_f & ; & & c_z &= \frac{l}{l_r} \cdot c_f \\ k_\theta &= l \cdot l_f \cdot k_f & ; & & c_\theta &= l \cdot l_f \cdot c_f \\ k_{z\theta} &= k_{\theta z} = 0 & ; & & c_{z\theta} &= c_{\theta z} = 0 \end{aligned}$$

Consequently, the equation of motion written in the general coordinates system will be uncoupled:

$$\ddot{z} + 2\zeta_z \omega_{0z} \cdot \dot{z} + \omega_{0z}^2 \cdot z = 0 \quad (5.43)$$

$$\ddot{\theta} + 2\zeta_\theta \omega_{0\theta} \cdot \dot{\theta} + \omega_{0\theta}^2 \cdot \theta = 0 \quad (5.44)$$

Clearly, the natural frequencies and the damping ratios for the bounce (ω_{0z} and ζ_z) and the pitch ($\omega_{0\theta}$ and ζ_θ) modes are defined as:

$$\omega_{0z} = \sqrt{\frac{k_z}{m_t}} \quad ; \quad \zeta_z = \frac{c_z}{2\sqrt{m_t k_z}}$$

$$\omega_{0\theta} = \sqrt{\frac{k_\theta}{I_y}} \quad ; \quad \zeta_\theta = \frac{c_\theta}{2\sqrt{I_y k_\theta}}$$

With a fixed geometry (l_f and l_r being constant values) the behaviour of both modes only depends on two parameters, which have been chosen to be as the front suspension system's stiffness (k_f) and damping (c_f) coefficients. Thus, the frequency and the damping of one normal mode will depend on the other mode's frequency and damping. A particular solution of this is when the system is completely symmetric. This is, $l_f = l_r = \frac{l}{2}$, $k_f = k_r = k$ and $c_f = c_r = c$. Then, the bounce and the pitch stiffness and damping parameters are:

$$k_z = 2k \quad ; \quad c_z = 2c$$

$$k_\theta = \frac{l^2}{2}k \quad ; \quad c_\theta = \frac{l^2}{2}c$$

In the independent suspensions system case, the natural frequencies and damping ratios of the normal modes can be set independently, however, in this case, the pitch and the bounce motions cannot be uncoupled. On the other hand, the bounce and pitch normal modes can be set as pure motions of vertical displacement and y rotation respectively, but then, their natural frequencies and damping ratios will be dependent on each other. Finally, from the point of view of the front and rear motorcycle ends, their dynamics will be coupled due to the crossed terms in the masses' matrix. Only with a difficult to implement motorcycle mass distribution, they could become independent.

5.2.2 Interconnected suspension system

Individual coordinates

When the front and rear suspension systems are interconnected, new coefficients appear on the stiffness-damping matrix that modify the dynamics of the motorcycle assembly. Figure 5.8 represents a two degrees of freedom motorcycle model with interconnection forces. These forces are defined as terms in the dynamic equations that depend on the motion of the opposed motorcycle end. This is, in the front suspension force, two additional terms appear, one depending on the position of the rear end and the other one depends on the rear end speed. In the rear suspension force, similar terms appear, depending on the front suspension elongation and speed.

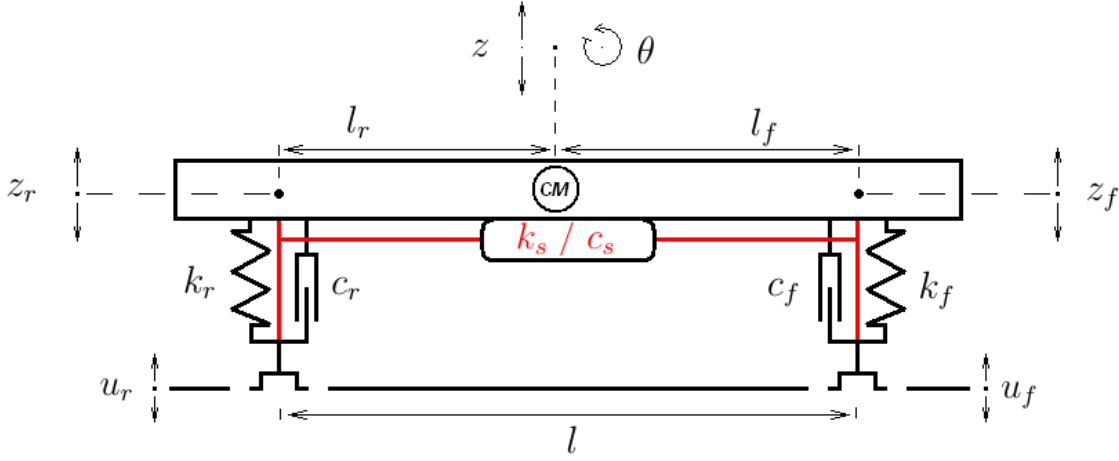


Figure 5.8: Two degrees of freedom motorcycle model with interconnected suspension system. Two sets of generalized coordinates are presented: a) Front (z_f) and rear (z_r) chassis ends vertical displacement. b) vertical displacement (z) and rotation about the y axis (θ) of the chassis centre of masses. In both cases, the system inputs are introduced through the front (u_f) and the rear (u_r) tyres.

The front and rear suspension forces are as follows:

$$f_f = -k_f \cdot (z_f - u_f) - c_f \cdot (\dot{z}_f - \dot{u}_f) - k_s \cdot (z_r - u_r) - c_s \cdot (\dot{z}_r - \dot{u}_r) \quad (5.45)$$

$$f_r = -k_r \cdot (z_r - u_r) - c_r \cdot (\dot{z}_r - \dot{u}_r) - k_s \cdot (z_f - u_f) - c_s \cdot (\dot{z}_f - \dot{u}_f) \quad (5.46)$$

Now, the stiffness-damping matrix R^i includes the stiffness and damping interconnection coefficients (k_s and c_s) and the equations of motion expressed by Eq. 5.39 result in:

$$\begin{pmatrix} 1 & 0 & 0 & 0 \\ 0 & 1 & 0 & 0 \\ 0 & 0 & \frac{m_t l_r^2 + I_y}{l^2} & \frac{m_t l_f l_r - I_y}{l^2} \\ 0 & 0 & \frac{m_t l_f l_r - I_y}{l^2} & \frac{m_t l_f^2 + I_y}{l^2} \end{pmatrix} \cdot \begin{pmatrix} \dot{z}_f \\ \dot{z}_r \\ \ddot{z}_f \\ \ddot{z}_r \end{pmatrix} = \begin{pmatrix} 0 & 0 & 1 & 0 \\ 0 & 0 & 0 & 1 \\ -k_f & -k_s & -c_f & -c_s \\ -k_s & -k_r & -c_s & -c_r \end{pmatrix} \cdot \begin{pmatrix} z_f \\ z_r \\ \dot{z}_f \\ \dot{z}_r \end{pmatrix}$$

Multiplying by the inverse of the mass-inertia matrix (M^{i-1}) the state space representation is:

$$\begin{pmatrix} \dot{z}_f \\ \dot{z}_r \\ \ddot{z}_f \\ \ddot{z}_r \end{pmatrix} = \begin{pmatrix} 0 & 0 & 1 & 0 \\ 0 & 0 & 0 & 1 \\ A_{3,1} & A_{3,2} & A_{3,3} & A_{3,4} \\ A_{4,1} & A_{4,2} & A_{4,3} & A_{4,4} \end{pmatrix} \cdot \begin{pmatrix} z_f \\ z_r \\ \dot{z}_f \\ \dot{z}_r \end{pmatrix}$$

With:

$$\begin{aligned} A_{3,1} &= -\frac{k_f+k_s}{m_t} - \frac{k_f l_f^2 - k_s l_f l_r}{I_y} & A_{3,2} &= -\frac{k_r+k_s}{m_t} - \frac{k_s l_f^2 - k_r l_f l_r}{I_y} \\ A_{4,1} &= -\frac{k_f+k_s}{m_t} - \frac{k_s l_r^2 - k_f l_f l_r}{I_y} & A_{4,2} &= -\frac{k_r+k_s}{m_t} - \frac{k_r l_r^2 - k_s l_f l_r}{I_y} \\ A_{3,3} &= -\frac{c_f+c_s}{m_t} - \frac{c_f l_f^2 - c_s l_f l_r}{I_y} & A_{3,4} &= -\frac{c_r+c_s}{m_t} - \frac{c_s l_f^2 - c_r l_f l_r}{I_y} \\ A_{4,3} &= -\frac{c_f+c_s}{m_t} - \frac{c_s l_r^2 - c_f l_f l_r}{I_y} & A_{4,4} &= -\frac{c_r+c_s}{m_t} - \frac{c_r l_r^2 - c_s l_f l_r}{I_y} \end{aligned}$$

Comparing to the previous model, the interconnection forces in this new model allow the independence of the front and rear ends dynamics even if the geometrical requirement in Eq. 5.40 is not satisfied, as far as the cross terms in matrix A are zero ($A_{3,2} = A_{3,4} = A_{4,1} = A_{4,3} = 0$). In order to tune the front and rear suspensions with the desired natural frequencies and damping ratios, the following algebraic equations system must be solved:

$$\left. \begin{aligned} 2\zeta_f \omega_{0f} - A_{3,3}(c_f, c_s, l_f, l_r) &= 0 \\ 2\zeta_r \omega_{0r} - A_{4,4}(c_r, c_s, l_f, l_r) &= 0 \\ \omega_{0f}^2 - A_{3,1}(k_f, k_s, l_f, l_r) &= 0 \\ \omega_{0r}^2 - A_{4,2}(k_r, k_s, l_f, l_r) &= 0 \\ A_{3,2}(k_r, k_s, l_f, l_r) &= 0 \\ A_{3,4}(c_r, c_s, l_f, l_r) &= 0 \\ A_{4,1}(k_f, k_s, l_f, l_r) &= 0 \\ A_{4,3}(c_f, c_s, l_f, l_r) &= 0 \end{aligned} \right\} \quad (5.47)$$

This is an eight equations system with eight independent variables, which includes the motorcycle's parameters ($k_f, k_r, k_s, c_f, c_r, c_s, l_f, l_r$). The mass and the moment of inertia could also be considered as independent variables. However, these variables together with l_f and l_r are conditioned by design restrictions. This implies that the system {5.47} must be solved during the motorcycle design process

and considering a constant rider's mass. Once the variables are set and the system built, the suspension settings could not be modified if the independence between the front and rear dynamics is to be kept. Nevertheless, a more flexible solution can be found if the motorcycle is designed with a symmetrical weight distribution, this is $l_f = l_r = \frac{l}{2}$, which is a condition commonly sought by motorcycle manufacturers. For instance, the GSX-R1000 mass distribution is almost symmetrical, the difference between l_f and l_r is about 4 mm with $l_f = 663$ mm and $l_r = 659$ mm. If a symmetrical weight distribution is achieved, the motorcycle system can be separated in two independent subsystems with similar mass, stiffness and damping coefficients. Therefore, the suspension tuning problem is reduced to a single mass-spring-damper system where $k_f = k_r = k$ and $c_f = c_r = c$. Figure 5.9 represents this system configuration whose equations of motion can be written as:

$$\begin{pmatrix} 1 & 0 & 0 & 0 \\ 0 & 1 & 0 & 0 \\ 0 & 0 & m_i & m_c \\ 0 & 0 & m_c & m_i \end{pmatrix} \cdot \begin{pmatrix} \dot{z}_f \\ \dot{z}_r \\ \ddot{z}_f \\ \ddot{z}_r \end{pmatrix} = \begin{pmatrix} 0 & 0 & 1 & 0 \\ 0 & 0 & 0 & 1 \\ -k & -k_s & -c & -c_s \\ -k_s & -k & -c_s & -c \end{pmatrix} \cdot \begin{pmatrix} z_f \\ z_r \\ \dot{z}_f \\ \dot{z}_r \end{pmatrix}$$

Where the m_i is the individual term of mass and m_c is the crossed term of mass:

$$m_i = \frac{m_t}{4} + \frac{I_y}{l^2} \quad ; \quad m_c = \frac{m_t}{4} - \frac{I_y}{l^2}$$

The system {5.48} that should be solved in order to set up the motorcycle suspension system is now reduced:

$$\left. \begin{aligned} 2\zeta\omega_0 &= -\frac{c+c_s}{m_t} - \frac{(c-c_s)l^2}{4I_y} \\ \omega_0^2 &= -\frac{k+k_s}{m_t} - \frac{(k-k_s)l^2}{4I_y} \\ 0 &= -\frac{c+c_s}{m_t} + \frac{(c-c_s)l^2}{4I_y} \\ 0 &= -\frac{k+k_s}{m_t} + \frac{(k-k_s)l^2}{4I_y} \end{aligned} \right\} \quad (5.48)$$

The damping ratio ($\zeta = \zeta_f = \zeta_r$) and the natural frequency ($\omega_0 = \omega_{0f} = \omega_{0r}$) are similar for the front and the rear subsystems and they directly depend on the suspension stiffness and damping coefficients (k and c) but no so on the

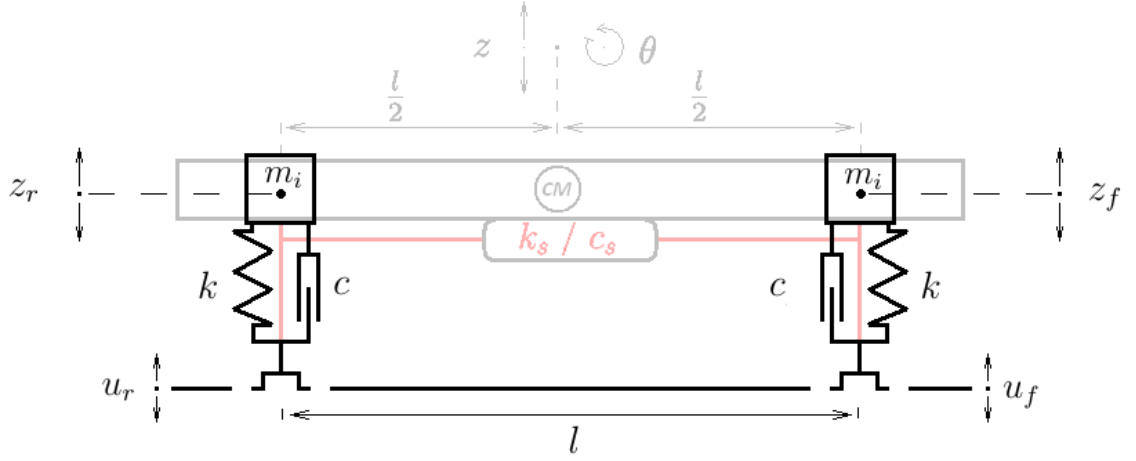


Figure 5.9: Two degrees of freedom motorcycle model where the symmetrical weight distribution ($l_f = l_r = \frac{l}{2}$) and the interconnected suspension system allow the front and rear suspensions to be set as two independent mass-spring-damper systems.

interconnection coefficients (k_s and c_s):

$$k = \omega_0^2 \cdot m_i \quad (5.49)$$

$$c = 2\zeta\omega_0 \cdot m_i \quad (5.50)$$

However, the interconnection coefficients should always satisfy the same conditions in order to guarantee the front-rear uncoupled dynamics:

$$k_s = k \cdot \frac{m_c}{m_i} \quad (5.51)$$

$$c_s = c \cdot \frac{m_c}{m_i} \quad (5.52)$$

Front and rear suspensions can be treated as two similar and independent mass-spring-damper systems by building the motorcycle with a symmetrical weight distribution between the front and rear ends and by including an interconnected suspension system. The natural frequencies and damping ratios of these subsystems can be precisely defined. Furthermore, the values of the interconnection spring and damping coefficients will be always lower than those on the suspensions.

General coordinates

In order to study the motorcycle system in its general coordinates, the individual stiffness-damping matrix (R^i), which now includes the interconnection coefficients

$(k_s$ and $c_s)$, is transformed by Eq. 5.41 resulting in:

$$R^g = \begin{pmatrix} 0 & 0 & 1 & 0 \\ 0 & 0 & 0 & 1 \\ -k_z & -k_{z\theta} & -c_z & -c_{z\theta} \\ -k_{\theta z} & -k_\theta & -c_{\theta z} & -c_\theta \end{pmatrix}$$

As in the independent suspensions system case, the matrix R^g contains the stiffness and damping coefficients $[k_z, c_z]$ associated to the vertical displacement, those associated to rotation about the y axis $[k_\theta, c_\theta]$ and crossed terms for the interaction between both motions $[k_{z\theta}, c_{z\theta}]$ and $[k_{\theta z}, c_{\theta z}]$. These crossed terms also result equal for bounce and for pitch motion. However, all these terms now include the interconnection coefficients:

$$\begin{aligned} k_z &= k_f + k_r + 2k_s & ; & \quad c_z = c_f + c_r + 2c_s \\ k_\theta &= k_f l_f^2 + k_r l_r^2 - 2k_s l_f l_r & ; & \quad c_\theta = c_f l_f^2 + c_r l_r^2 - 2c_s l_f l_r \\ k_{z\theta} = k_{\theta z} &= -k_f l_f + k_r l_r - k_s (l_f - l_r) & ; & \quad c_{z\theta} = c_{\theta z} = -c_f l_f + c_r l_r - c_s (l_f - l_r) \end{aligned}$$

The state space matrix A in the general coordinates is found multiplying the general stiffness-damping matrix by the inverse of the general mass-inertia matrix ($A^g = M^{g-1} \cdot R^g$) and the equations of motion are expressed by:

$$\begin{pmatrix} \dot{z} \\ \dot{\theta} \\ \ddot{z} \\ \ddot{\theta} \end{pmatrix} = \begin{pmatrix} 0 & 0 & 1 & 0 \\ 0 & 0 & 0 & 1 \\ \frac{-k_z}{mt} & \frac{-k_{z\theta}}{mt} & \frac{-c_z}{mt} & \frac{-c_{z\theta}}{mt} \\ \frac{-k_{\theta z}}{Iy} & \frac{-k_\theta}{Iy} & \frac{-c_{\theta z}}{Iy} & \frac{-c_\theta}{Iy} \end{pmatrix} \cdot \begin{pmatrix} z \\ \theta \\ \dot{z} \\ \dot{\theta} \end{pmatrix} \quad (5.53)$$

The interconnection stiffness and damping coefficients allow for the equations of motion to become uncoupled, as in Eq. 5.43 and Eq. 5.44. But in this case, the independence of the front and rear suspension parameters is not compromised. The bounce and pitch normal modes can now represent pure vertical displacement and pure rotation about the motorcycle y axis respectively, with independent natural frequencies and damping ratios, as far as the interconnection stiffness (k_s) and damping (c_s) parameters satisfy the following conditions:

$$k_s = \frac{k_f l_f - k_r l_r}{l_r - l_f} \quad ; \quad c_s = \frac{c_f l_f - c_r l_r}{l_r - l_f}$$

Under these conditions, the equivalent stiffness and damping coefficients associated to the vertical displacement and to the pitch rotation depend on the stiffness and damping coefficient of the front and rear suspensions as follows:

$$\begin{aligned}
k_z &= \frac{l}{l_f - l_r} \cdot (k_r - k_f) & ; & & c_z &= \frac{l}{l_f - l_r} \cdot (c_r - c_f) \\
k_\theta &= \frac{l}{l_f - l_r} \cdot (k_f l_f^2 - k_r l_r^2) & ; & & c_\theta &= \frac{l}{l_f - l_r} \cdot (c_f l_f^2 - c_r l_r^2) \\
k_{z\theta} &= k_{\theta z} = 0 & ; & & c_{z\theta} &= c_{\theta z} = 0
\end{aligned}$$

In the case of a symmetrical weight distribution, the k_s and c_s coefficients have no effect on the crossed terms of the matrix R^g and the pitch and bounce uncoupling only will happen if the front and rear suspensions' coefficients are equal ($k_f = k_r = k$ and $c_f = c_r = c$). However, the bounce and pitch modes natural frequencies and damping ratios can be defined independently with the independent coefficients k , k_s , c and c_s .

$$\begin{aligned}
k_z &= 2(k + k_s) & ; & & c_z &= 2(c + c_s) \\
k_\theta &= \frac{l^2}{2}(k - k_s) & ; & & c_\theta &= \frac{l^2}{2}(c - c_s) \\
k_{z\theta} &= k_{\theta z} = 0 & ; & & c_{z\theta} &= c_{\theta z} = 0
\end{aligned}$$

Finally, if the symmetrical weight distribution is kept and the conditions expressed by Eq. 5.51 and Eq. 5.52 are applied to the interconnection coefficients (k_s and c_s), the front-rear independence and the bounce-pitch independence are achieved at the same time. In this case, the state space matrix A for the individual coordinates is the same matrix than that for the general ones and the equations of motion in both bases are written as follows:

$$\begin{pmatrix} \dot{z} \\ \dot{\theta} \\ \ddot{z} \\ \ddot{\theta} \end{pmatrix} = \begin{pmatrix} 0 & 0 & 1 & 0 \\ 0 & 0 & 0 & 1 \\ -\frac{k}{m_i} & 0 & -\frac{c}{m_i} & 0 \\ 0 & -\frac{k}{m_i} & 0 & -\frac{c}{m_i} \end{pmatrix} \cdot \begin{pmatrix} z \\ \theta \\ \dot{z} \\ \dot{\theta} \end{pmatrix} \quad (5.54)$$

and

$$\begin{pmatrix} \dot{z}_f \\ \dot{z}_r \\ \ddot{z}_f \\ \ddot{z}_r \end{pmatrix} = \begin{pmatrix} 0 & 0 & 1 & 0 \\ 0 & 0 & 0 & 1 \\ -\frac{k}{m_i} & 0 & -\frac{c}{m_i} & 0 \\ 0 & -\frac{k}{m_i} & 0 & -\frac{c}{m_i} \end{pmatrix} \cdot \begin{pmatrix} z_f \\ z_r \\ \dot{z}_f \\ \dot{z}_r \end{pmatrix} \quad (5.55)$$

The eigenvalues (λ_i) and the eigenvectors (u_i) of matrix A are found as:

$$\lambda_{1,2,3,4} = -\zeta \pm \sqrt{\zeta^2 - \omega_0^2} ; \quad u_{1,2} = \begin{pmatrix} 1 \\ 0 \\ -\zeta \pm \sqrt{\zeta^2 - \omega_0^2} \\ 0 \end{pmatrix} ; \quad u_{3,4} = \begin{pmatrix} 0 \\ 1 \\ 0 \\ -\zeta \pm \sqrt{\zeta^2 - \omega_0^2} \end{pmatrix}$$

The damping is defined as $\zeta = \frac{c}{2m_i}$ which is related to the damping ratio through the natural frequency as $\zeta = \zeta\omega_0$ where $\omega_0 = \sqrt{\frac{k}{m_i}}$. In the light of these results, it can be concluded that under these design conditions, the system has four different normal modes whose motions depend on how the system is excited. The bounce mode appears when the front and rear inputs have the same magnitude and phase. The pitch mode occurs if the front input has similar magnitude to the rear input with an opposed phase. The front hop mode, consisting in the oscillation of the motorcycle front end whilst the rear end remains unaffected, appears in the case that only a front input excites the system. And, oppositely, the rear hop mode appears in the case that the front input is zero whilst the system is excited through the rear input. Any other system motion can be described as a linear combination of these modes, whose natural frequencies and damping ratios are equal for all of them.

5.3 Reduced model with four degrees of freedom

The springs and masses associated to the motorcycle's wheels modify its dynamics substantially. Figure 5.10 presents the four degrees of freedom motorcycle model.

Similarly to those in the previous section, the system equations of motion may be expressed on either individual (Q^i) or general (Q^g) generalized coordinates. Now, both set of coordinates include the front and rear wheels vertical displacement and two new forces appear related to them.

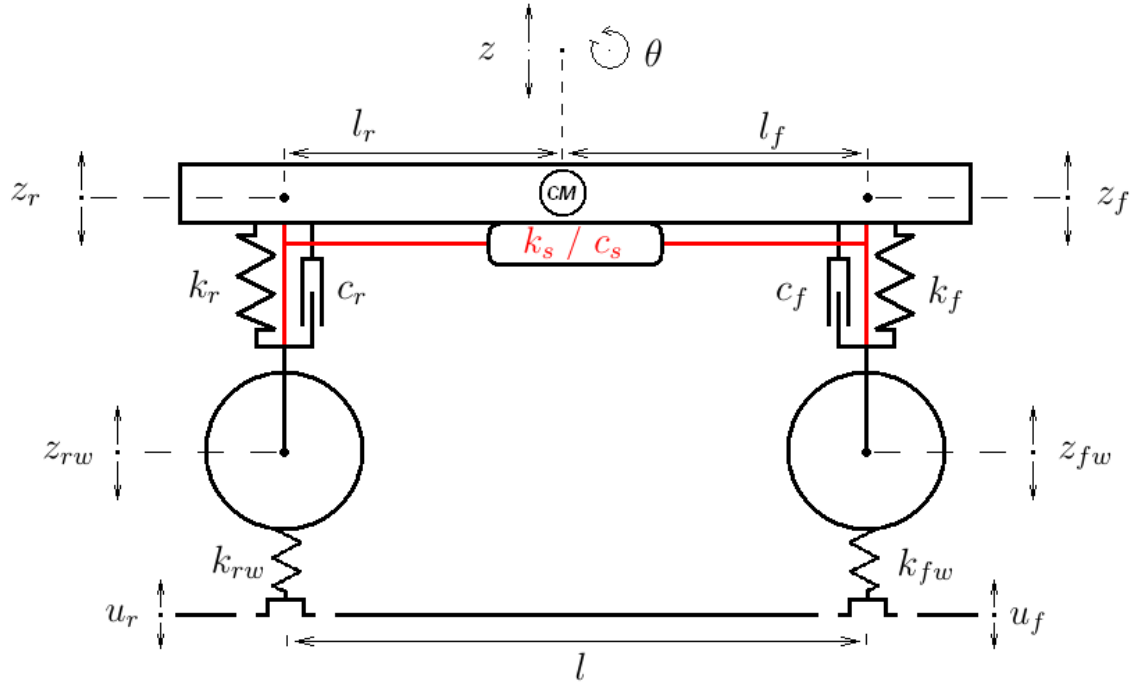


Figure 5.10: Four degrees of freedom motorcycle model. Two set of generalized coordinates are presented: a) the vertical displacement of the front (z_{fw}) and rear (z_{rw}) wheels and the vertical displacement of the front (z_f) and rear (z_r) chassis ends. b) the vertical displacement of the front (z_{fw}) and rear (z_{rw}) wheels, the vertical displacement (z) and the rotation about the y axis (θ) of the chassis centre of masses. In both cases, the system inputs are introduced through the front (u_f) and rear (u_r) tyres

Individual coordinates

In the individual system coordinates, the equations of the suspension system forces are written as follows:

$$f_f = -k_f \cdot (z_f - z_{fw}) - c_f \cdot (\dot{z}_f - \dot{z}_{fw}) - k_s \cdot (z_r - z_{rw}) - c_s \cdot (\dot{z}_r - \dot{z}_{rw}) \quad (5.56)$$

$$f_r = -k_r \cdot (z_r - z_{rw}) - c_r \cdot (\dot{z}_r - \dot{z}_{rw}) - k_s \cdot (z_f - z_{fw}) - c_s \cdot (\dot{z}_f - \dot{z}_{fw}) \quad (5.57)$$

$$f_{fw} = -f_f - k_{fw} \cdot (z_{fw} - u_f) \quad (5.58)$$

$$f_{rw} = -f_r - k_{rw} \cdot (z_{rw} - u_r) \quad (5.59)$$

Applying the second Newton's law the equations of motion are expressed by:

$$M^i \cdot \dot{Q}^i = R^i \cdot Q^i \quad (5.60)$$

The individual coordinates vector in this case includes the wheels vertical displacements (z_{fw} and z_{rw}) and speeds (\dot{z}_{fw} and \dot{z}_{rw}) whilst the individual stiffness-damping matrix contains the terms associated to them:

$$K^i = \begin{pmatrix} 0 & 0 & 0 & 0 & 1 & 0 & 0 & 0 \\ 0 & 0 & 0 & 0 & 0 & 1 & 0 & 0 \\ 0 & 0 & 0 & 0 & 0 & 0 & 1 & 0 \\ 0 & 0 & 0 & 0 & 0 & 0 & 0 & 1 \\ -k_f & -k_s & k_f & k_s & -c_f & -c_s & c_f & c_s \\ -k_s & -k_r & k_s & k_r & -c_s & -c_r & c_s & c_r \\ k_f & k_s & -k_f - k_{fw} & -k_s & c_f & c_s & -c_f & -c_s \\ k_s & k_r & -k_s & -k_r - k_{rw} & c_s & c_r & -c_s & -c_r \end{pmatrix}; Q^i = \begin{pmatrix} z_f \\ z_r \\ z_{fw} \\ z_{rw} \\ \dot{z}_f \\ \dot{z}_r \\ \dot{z}_{fw} \\ \dot{z}_{rw} \end{pmatrix}$$

As in the previous section, the individual mass matrix (M^i) can be found by a change of basis of the general mass matrix (M^g):

$$M^i = Pf^{-1} \cdot M^g \cdot Pq \quad (5.61)$$

The general mass-inertia matrix now includes the wheel masses:

$$M^g = \begin{pmatrix} 1 & 0 & 0 & 0 & 0 & 0 & 0 & 0 \\ 0 & 1 & 0 & 0 & 0 & 0 & 0 & 0 \\ 0 & 0 & 1 & 0 & 0 & 0 & 0 & 0 \\ 0 & 0 & 0 & 1 & 0 & 0 & 0 & 0 \\ 0 & 0 & 0 & 0 & m_t & 0 & 0 & 0 \\ 0 & 0 & 0 & 0 & 0 & I_y & 0 & 0 \\ 0 & 0 & 0 & 0 & 0 & 0 & m_{fw} & 0 \\ 0 & 0 & 0 & 0 & 0 & 0 & 0 & m_{rw} \end{pmatrix}$$

The change of basis matrix for the four degrees of freedom system are similar to those for the two degree of freedom ones but including the wheels terms.

$$Pq = \frac{1}{l} \begin{pmatrix} l_r & l_f & 0 & 0 & 0 & 0 & 0 & 0 \\ -1 & 1 & 0 & 0 & 0 & 0 & 0 & 0 \\ 0 & 0 & l & 0 & 0 & 0 & 0 & 0 \\ 0 & 0 & 0 & l & 0 & 0 & 0 & 0 \\ 0 & 0 & 0 & 0 & l_r & l_f & 0 & 0 \\ 0 & 0 & 0 & 0 & -1 & 1 & 0 & 0 \\ 0 & 0 & 0 & 0 & 0 & 0 & l & 0 \\ 0 & 0 & 0 & 0 & 0 & 0 & 0 & l \end{pmatrix}; Pf = \frac{1}{l} \begin{pmatrix} l_r & l_f & 0 & 0 & 0 & 0 & 0 & 0 \\ -1 & 1 & 0 & 0 & 0 & 0 & 0 & 0 \\ 0 & 0 & l & 0 & 0 & 0 & 0 & 0 \\ 0 & 0 & 0 & l & 0 & 0 & 0 & 0 \\ 0 & 0 & 0 & 0 & l & l & 0 & 0 \\ 0 & 0 & 0 & 0 & -l_f l & l_r l & 0 & 0 \\ 0 & 0 & 0 & 0 & 0 & 0 & l & 0 \\ 0 & 0 & 0 & 0 & 0 & 0 & 0 & l \end{pmatrix}$$

And the individual masses matrix results in:

$$M^i = \begin{pmatrix} 1 & 0 & 0 & 0 & 0 & 0 & 0 & 0 \\ 0 & 1 & 0 & 0 & 0 & 0 & 0 & 0 \\ 0 & 0 & 1 & 0 & 0 & 0 & 0 & 0 \\ 0 & 0 & 0 & 1 & 0 & 0 & 0 & 0 \\ 0 & 0 & 0 & 0 & \frac{m_t l_r^2 + I_y}{l^2} & \frac{m_t l_f l_r - I_y}{l^2} & 0 & 0 \\ 0 & 0 & 0 & 0 & \frac{m_t l_f l_r - I_y}{l^2} & \frac{m_t l_f^2 + I_y}{l^2} & 0 & 0 \\ 0 & 0 & 0 & 0 & 0 & 0 & m_{fw} & 0 \\ 0 & 0 & 0 & 0 & 0 & 0 & 0 & m_{rw} \end{pmatrix}$$

Looking at the individual masses matrix (M^i), it can be observed how similarly as in the two degrees of freedom model, the front and rear ends dynamics are coupled by the mass and the inertia moment due to their physical connection. However, now the front and rear wheels are also affected by the interconnection terms in the individual stiffness-damping matrix (R^i), and the displacements and the speeds of one wheel affect the opposite wheel dynamics. Due to the interconnection system, there exists an energy transfer from one wheel to the other, so that the larger value the interconnection parameters have the more energy is transferred. And this implies that front and rear ends independence cannot be achieved by the interconnection system. The wheels' interconnection terms cannot be cancelled except for $k_s = 0$ and $c_s = 0$. Thus, only in the case that the condition found in Eq. 5.40 is satisfied and the interconnection stiffness and damping parameters are zero, the motorcycle

dynamics can be treated as two independent quarter-car-models.

General coordinates

In order to study the system in the general coordinates basis, the state space A^g matrix can be found by:

$$A^g = M^{g-1} \cdot Pf \cdot K^i \cdot Pq^{-1} \quad (5.62)$$

And the equations of motion are given by:

$$\begin{pmatrix} \dot{z} \\ \dot{\theta} \\ \dot{z}_{fw} \\ \dot{z}_{rw} \\ \ddot{z} \\ \ddot{\theta} \\ \ddot{z}_{fw} \\ \ddot{z}_{rw} \end{pmatrix} = \begin{pmatrix} 0 & 0 & 0 & 0 & 1 & 0 & 0 & 0 \\ 0 & 0 & 0 & 0 & 0 & 1 & 0 & 0 \\ 0 & 0 & 0 & 0 & 0 & 0 & 1 & 0 \\ 0 & 0 & 0 & 0 & 0 & 0 & 0 & 1 \\ A_{5,1}^g & A_{5,2}^g & A_{5,3}^g & A_{5,4}^g & A_{5,5}^g & A_{5,6}^g & A_{5,7}^g & A_{5,8}^g \\ A_{6,1}^g & A_{6,2}^g & A_{6,3}^g & A_{6,4}^g & A_{6,5}^g & A_{6,6}^g & A_{6,7}^g & A_{6,8}^g \\ A_{7,1}^g & A_{7,2}^g & A_{7,3}^g & A_{7,4}^g & A_{7,5}^g & A_{7,6}^g & A_{7,7}^g & A_{7,8}^g \\ A_{8,1}^g & A_{8,2}^g & A_{8,3}^g & A_{8,4}^g & A_{8,5}^g & A_{8,6}^g & A_{8,7}^g & A_{8,8}^g \end{pmatrix} \cdot \begin{pmatrix} z \\ \theta \\ z_{fw} \\ z_{rw} \\ \dot{z} \\ \dot{\theta} \\ \dot{z}_{fw} \\ \dot{z}_{rw} \end{pmatrix}$$

Terms corresponding to \ddot{z} :

$$A_{5,1}^g = \frac{-k_f - k_r - 2k_s}{m_t} \quad A_{5,2}^g = \frac{k_f l_f - k_r l_r + k_s(l_f - l_r)}{m_t} \quad A_{5,3}^g = \frac{k_f + k_s}{m_t} \quad A_{5,4}^g = \frac{k_s + k_r}{m_t}$$

$$A_{5,5}^g = \frac{-c_f - c_r - 2c_s}{m_t} \quad A_{5,6}^g = \frac{c_f l_f - c_r l_r + c_s(l_f - l_r)}{m_t} \quad A_{5,7}^g = \frac{c_f + c_s}{m_t} \quad A_{5,8}^g = \frac{c_s + c_r}{m_t}$$

Terms corresponding to $\ddot{\theta}$:

$$A_{6,1}^g = \frac{k_f l_f - k_r l_r + k_s(l_f - l_r)}{I_y} \quad A_{6,2}^g = \frac{-k_f l_f^2 - k_r l_r^2 + 2k_s l_f l_r}{I_y} \quad A_{6,3}^g = \frac{-k_f l_f + k_s l_r}{I_y}$$

$$A_{6,4}^g = \frac{-k_s l_f + k_r l_r}{I_y} \quad A_{6,5}^g = \frac{c_f l_f - c_r l_r + c_s(l_f - l_r)}{I_y} \quad A_{6,6}^g = \frac{-c_f l_f^2 - c_r l_r^2 + 2c_s l_f l_r}{I_y}$$

$$A_{6,7}^g = \frac{-c_f l_f + c_s l_r}{I_y} \quad A_{6,8}^g = \frac{-c_s l_f + c_r l_r}{I_y}$$

Terms corresponding to \ddot{z}_{fw} :

$$\begin{aligned}
 A_{7,1}^g &= \frac{k_f+k_s}{m_{fw}} & A_{7,2}^g &= \frac{-k_f l_f+k_s l_r}{m_{fw}} & A_{7,3}^g &= \frac{-k_f-k_{fw}}{m_{fw}} & A_{7,4}^g &= \frac{-k_s}{m_{fw}} \\
 A_{7,5}^g &= \frac{c_f+c_s}{m_{fw}} & A_{7,6}^g &= \frac{-c_f l_f+c_s l_r}{m_{fw}} & A_{7,7}^g &= \frac{-c_f-c_{fw}}{m_{fw}} & A_{7,8}^g &= \frac{-c_s}{m_{fw}}
 \end{aligned}$$

Terms corresponding to \ddot{z}_{rw} :

$$\begin{aligned}
 A_{8,1}^g &= \frac{k_s+k_r}{m_{rw}} & A_{8,2}^g &= \frac{-k_s l_f+k_r l_r}{m_{rw}} & A_{8,3}^g &= \frac{-k_s}{m_{rw}} & A_{8,4}^g &= \frac{-k_r-k_{rw}}{m_{rw}} \\
 A_{8,5}^g &= \frac{c_s+c_r}{m_{rw}} & A_{8,6}^g &= \frac{-c_s l_f+c_r l_r}{m_{rw}} & A_{8,7}^g &= \frac{-c_s}{m_{rw}} & A_{8,8}^g &= \frac{-c_r-c_{rw}}{m_{rw}}
 \end{aligned}$$

By observing at matrix A^g it can be noticed that obtaining independent pitch and bounce motions is not as direct as for the two degrees of freedom system case. The front and rear wheel displacements are now included in these motions and cancelling some terms in the A^g matrix is not a possible solution. On the other hand, the eigenvalues problem has to be solved symbolically to get the natural frequencies and damping ratios of the normal modes. This problem results in a hard task considering that the characteristics polynomial is an eight degrees polynomial with six independent variables (k_f , c_f , k_r , c_r , k_s , c_s). Furthermore, it is not proven that all the desired natural frequencies and damping ratio might be reached through a combination of the suspension coefficients. In the four degrees of freedom model, an increase of the interconnection coefficients values (k_s and c_s) results in an energy transmission from one wheel to the other which will modify their rebound frequency and damping, simultaneously these rebound motions will affect the pitch and the bounce ones and modify their nature. Consequently, the results obtained for the two degrees of freedom model are not directly applicable to the four degrees of freedom model. However, they can be used as a first approach to find the closest compromise solution to the setting problem.

Application of the two degrees of freedom model results

For the two degrees of freedom model, it has been shown how the interconnected suspension system (either on its own or combined with a symmetrical distribution of masses), introduces a high flexibility in the design of the dynamics properties of the motorcycle. The damping (ς) and the resonance frequencies (ω) of the bounce and the pitch normal modes can be set through their stiffness and damping coefficients:

$$\begin{aligned} \varsigma_z &= \frac{c_z}{2m_i} & ; & & \varsigma_\theta &= \frac{c_\theta}{2m_i} \\ \omega_z &= \sqrt{\varsigma_z^2 - \frac{k_z}{m_i}} & ; & & \omega_\theta &= \sqrt{\varsigma_\theta^2 - \frac{k_\theta}{m_i}} \end{aligned}$$

The stiffness and the damping coefficients of the front, the rear and the interconnection spring-damper units can be obtained from:

$$\begin{aligned} k_f &= \frac{k_z l_r^2 + k_\theta}{l^2} & ; & & c_f &= \frac{c_z l_r^2 + c_\theta}{l^2} \\ k_r &= \frac{k_z l_f^2 + k_\theta}{l^2} & ; & & c_r &= \frac{c_z l_f^2 + c_\theta}{l^2} \\ k_s &= \frac{k_z l_f l_r - k_\theta}{l^2} & ; & & c_s &= \frac{c_z l_f l_r - c_\theta}{l^2} \end{aligned}$$

Now, the natural frequencies and the damping ratios for the bounce (ω_{0z} and ζ_z) and the pitch ($\omega_{0\theta}$ and ζ_θ) normal modes can be defined independently by appropriately setting the front, the rear and the interconnection spring and damping coefficients. As an example, the suspension coefficients are calculated for the following normal modes characteristics:

$$\begin{aligned} \zeta_z &= -10 & ; & & \zeta_\theta &= -10 \\ \omega_{0z} &= 20 \text{ rad/s} & ; & & \omega_{0\theta} &= 30 \text{ rad/s} \end{aligned}$$

The resulting suspension coefficients are calculated for the two degrees of freedom model. Then, the corresponding conversion is applied to the front and the rear stiffness coefficients in order to find the correct values for the four degrees of freedom model. Table 5.1 presents the results obtained.

Figure 5.11 shows, in red circles, the root locus of the two degrees of freedom model set with the new suspension coefficient values. Overlapped to it, plotted in blue asterisks, is the root locus of the four degrees of freedom model with the calculated suspension coefficients values. The roots of the four degrees of freedom model are far from where they are expected to be. On the other hand, two additional normal modes appear, they are the front and rear wheels hop modes that appear

	c(Ns/m)	k(N/m)–2dof	k(N/m)–4dof
f	1523	50203	81788
r	1535	50506	78695
s	559	1845	1845

Table 5.1: Stiffness and damping coefficients values for the front (f), rear (r) and interconnection (s) spring-damper units obtained with the two degrees of freedom model. The bounce and pitch normal modes characteristics for this configuration are: $\zeta_z = -10$, $\omega_{0z} = 20$ rad/s, $\zeta_\theta = -10$ and $\omega_{0\theta} = 30$ rad/s.

when the wheels are considered in the model. As it can be observed, the two degrees of freedom model results cannot be directly extrapolated to a more complex model which takes into account the wheels dynamics. In order to set the motorcycle's suspension system to obtain a desired combination of resonant frequencies and damping ratios, a four degrees of freedom model has to be considered.

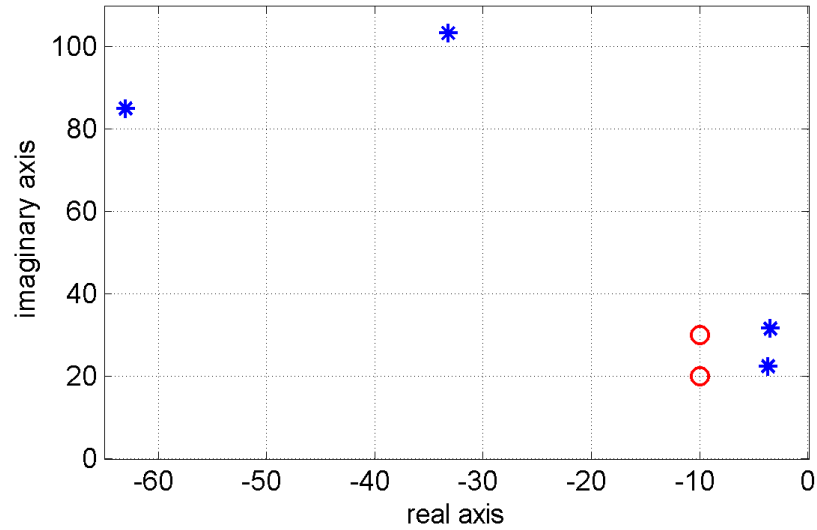


Figure 5.11: Root locus of the two degrees of freedom motorcycle model (red \circ) and the four degrees of freedom motorcycle model (blue $*$). The models have been modified with the suspension coefficients values calculated to obtain the desired damping and resonance frequencies for the bounce and the pitch normal modes: $\omega_z = 20$ rad/s, $\zeta_z = 10$ s⁻¹, $\omega_\theta = 30$ rad/s and $\zeta_\theta = 10$ s⁻¹.

However, as it has been showed previously, solving the eigenvalue problem in the four degrees of freedom model requires high computational resources. Nevertheless, a numerical approach to find closer values of the normal modes natural frequencies and damping ratios is proposed. A numerical function which returns as output the damping and resonance frequency of the bounce and the pitch motion depending on

the six inputs suspension coefficients is built. This function creates the state space of the four degrees of freedom model and calculates the eigenvalues and eigenvectors of the matrix A . The eigenvalues are classified depending on the eigenvectors components weights into Bounce, Pitch, Front Wheel Hop and Rear Wheel Hop. Once this classification is done, the frequency and damping of each of them is obtained returning only those which we are interested in.

$$g : \mathbb{R}^6 \longrightarrow \mathbb{R}^4, (\omega_b, \varsigma_b, \omega_p, \varsigma_p) = g(k_f, c_f, k_r, c_r, k_s, c_s)$$

A target function h for a multi-target optimization problem can be created including these four outputs function g . The target function returns only one value which depends on the difference between the desired frequency and damping and the actual frequency and damping of the bounce and the pitch normal modes found by the function g . As a first approach, the output value of h is defined as the root mean square of these four differences.

$$h(g) : \mathbb{R}^6 \longrightarrow \mathbb{R}$$

$$h(k_f, c_f, k_r, c_r, k_s, c_s) = \frac{1}{2} \cdot [(\omega_b - \omega_{b0})^2 + (\varsigma_b - \varsigma_{b0})^2 + (\omega_p - \omega_{p0})^2 + (\varsigma_p - \varsigma_{p0})^2]^{\frac{1}{2}}$$

	c(Ns/m)–4dof	k(N/m)–4dof
f	2876	72021
r	2198	35769
s	533	1987

Table 5.2: Stiffness and damping coefficients values for the front (f), rear (r) and interconnection (s) spring damper units returned by the optimization process using the initial values obtained with the two degrees of freedom model.

Taking advantage of the Matlab optimization toolbox, the *fminsearch* function can be used to find the minimum of h . The function g returns four six-dimensional surfaces which can be highly irregular with several local maximums and minimums. Considering that the *fminsearch* function finds a local minimum of the target function, it is important to provide it with adequate initial values to start the optimization algorithm. It is at this point where the results found for the two degrees of freedom model become relevant. The initial values provided to *fminsearch* are those which result in the desired bounce and pitch modes frequency and damping

obtained for the two degrees of freedom model. For the example, calculated with the values in Tab. 5.1 the optimization process returns the suspension coefficients appearing in Tab. 5.2.

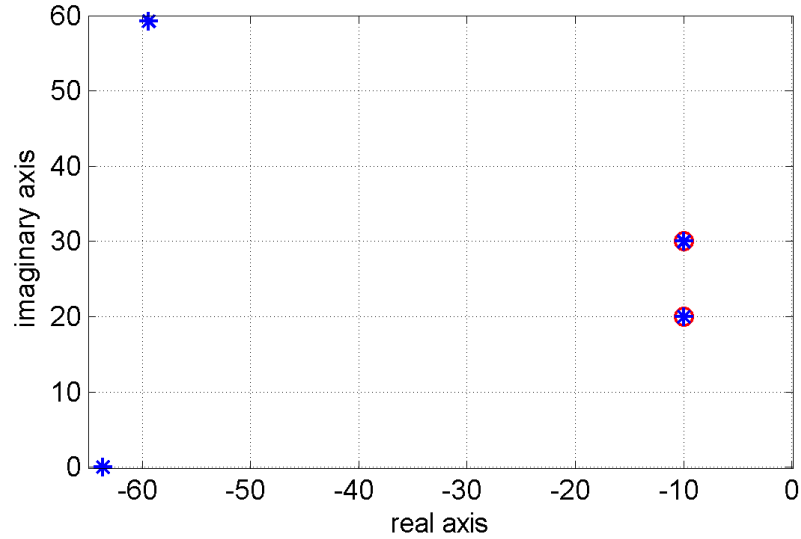


Figure 5.12: Root locus of the two degrees of freedom motorcycle model (red \circ) and the four degrees of freedom motorcycle model (blue $*$). The models have been modified with the suspension coefficients values obtained after the optimization process. The desired damping and resonance frequencies for the bounce and the pitch normal modes were: $\omega_z = 20$ rad/s, $\zeta_z = 10$ s $^{-1}$, $\omega_\theta = 30$ rad/s and $\zeta_\theta = 10$ s $^{-1}$.

The result of applying these suspension coefficients is shown in Fig. 5.12, where the root locus of the four degrees of freedom model is plotted in blue asterisks. It is overlapped to that of the two degrees of freedom model which is plotted in red circles. It can be observed that with this optimization process, satisfying results are now obtained. However, this is just an example. It is not proven that all the different combination of the natural frequencies and damping ratios of the normal modes can be achieved by this procedure, although this method to address the suspension configuration problem looks efficient at this stage.

5.4 Conclusions

In this chapter the interconnected suspension systems' dynamics has been studied returning good results. Several bicycle demonstrators of this concept have been already built and, although deep studies of the dynamics behind the different concepts are not published by the manufacturers, they are proved to achieve interesting

features that improve their overall performance. The dynamical analysis of the two concept bikes developed in this chapter shows that with different mechanical arrangement similar result are found. In an interconnected suspension system with at least six free variables (considering stiffness and damping coefficients and geometrical ratios) a full interconnected suspension system can be fully set up. The equation of motion can be written as in Eq. 5.58 and Eq. 5.59 in all this kind of systems, where the equivalent stiffness and damping coefficients depend on the different variables of them. In any case, the interconnection coefficients (k_s and c_s) are similar for the front and rear ends of the motorcycle.

On the other hand, a commercialized interconnection system mainly oriented to four-wheeled vehicles has also been adapted to the motorcycle. The mathematical theory behind this technology presented by the company, taking a vehicle model in which the wheels dynamics are not considered, allows the design of an interconnected suspension system that results in improved performance of the tested vehicles. However, when in this chapter a similar method is followed in order to find a relation that allows a full set up of the interconnected suspension system, the predictions found are not all the accurate as they should be. A more complex model including the wheels dynamics has to be considered in order to obtain a deeper understanding of the system. A promising method for setting up the bounce and the pitch normal modes properties is proposed as a combination of the two degrees of freedom model analytical solutions and a numerical optimization process on the four degrees of freedom model. However, this suspension system has also a high potential in terms of performance and suspension precision, as it can be observed in the existing prototypes. In the next chapter, the performance of the GSX-R1000 sport motorcycle featuring an interconnected suspension system will be studied.

Chapter 6

Interconnected Suspensions

System: Performance

In the previous chapter an interconnected suspension system was presented as means to introduce a more precise tuning of the general motorcycle's motion by uncoupling the pitch and bounce modes involved on it. In this chapter, the focus is on the suspension performance and on how an interconnection mechanism can improve it. By using a GSX-R1000 motorcycle nonlinear model, it can be predicted how various suspension settings will affect the vehicle's performance. The goal is to obtain the optimized interconnected suspension parameters that help to achieve an improved performance of the entire suspension system.

In a first stage, the behaviour under a road bump input is investigated. Four different optimization processes are implemented and tested to finally propose a suitable configurations of the interconnected system for four possible mechanical implementations. These implementations consider different complexity scenarios ranging from a simple passive mechanism to a more complex one based on the addition of active elements (actuators). The simplest interconnection mechanism proposed consists of a direct connection from the front suspension telescopic fork to the rear swinging arm through a damper unit with a constant damping coefficient value. An increase in mechanical complexity results from the use of dampers with speed variable coefficients in order to achieve different damping values for the different forward speeds. Finally, the most complex configuration would imply the use of active elements such as mechanical actuators to provide variable intercon-

nection stiffness coefficients. In the light of the results, configurations for springs with constant stiffness coefficient are not proposed due as far a positive value of the interconnection stiffness coefficient returns good results in terms of suspension's precision for speeds under 40 m/s, this precision is worsened for speed over 40 m/s. The opposite takes place for negative values of this coefficient, as it will be shown latter in this chapter. Furthermore, after performing the corresponding optimization process for such a configuration, the optimal spring stiffness constant value found for all the speed range is $k_s \approx 0$ N.

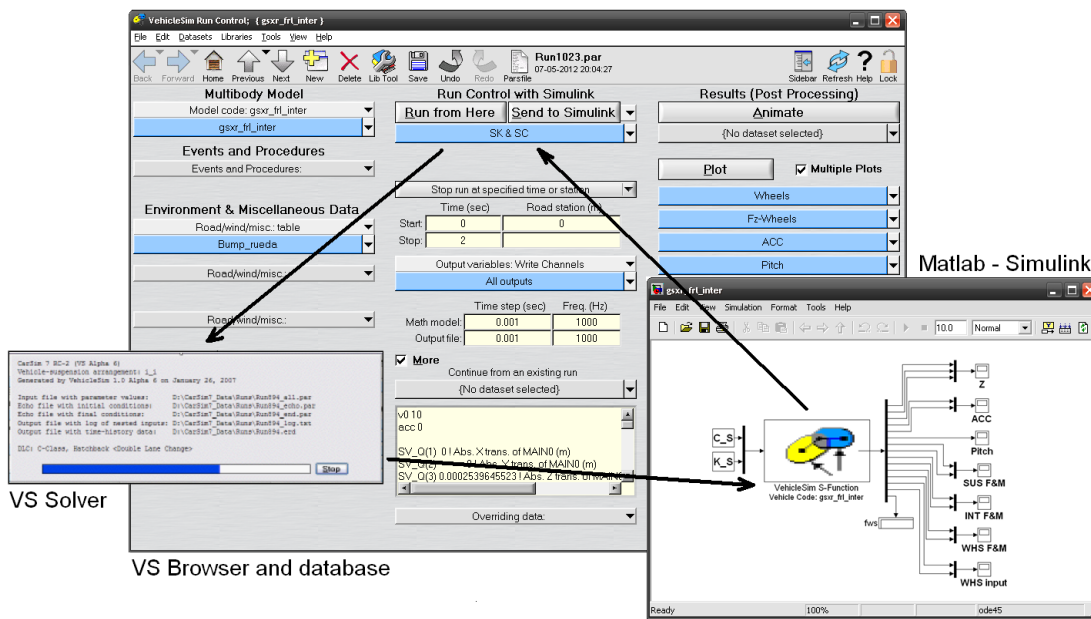


Figure 6.1: Simulink model with a VehicleSim Block to call a simulation that will be run from VS Browser.

At a second stage, the frequency responses of these four proposed interconnection configurations are studied. A sinusoidal signal is designed as a the perturbation input for the motorcycle model under straightforward running simulation at different speeds ranging from 10 m/s to 80 m/s. The magnitudes of the precision and comfort variables are mapped for the entire speed and frequency ranges and compared to the nominal independent suspension system.

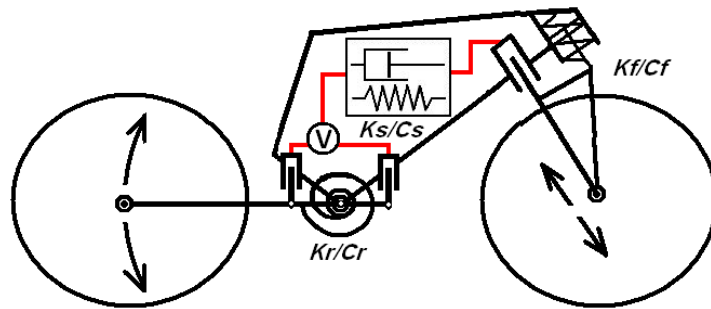
Taking advantage of the VS Browser and Matlab-Simulink compatibility, all the tasks can be carried out within the Matlab environment. This feature simplifies the data acquisition and the optimization process. Figure 6.1 shows an example of a Simulink model where the VehicleSim block calls the bump input simulation run in the VS Browser and which outputs are migrated to the various Matlab functions.

These functions can be either those used for mapping the response of the precision and comfort variables or the target functions set in the optimization processes.

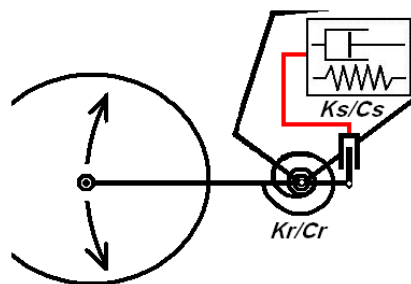
6.1 Modelling of the interconnected suspensions system

In order to illustrate the interconnection concept in an intuitive manner, Fig. 6.2a shows a sketch of an interconnected suspensions system where positive and negative values of the interconnection coefficients can be provided. Figure 6.2b and Fig. 6.2c show simpler set-ups where only negative or positive values are allowed respectively. In this approach, the coefficient sign will depend on the application point of the resulting interconnection force on the swinging arm.

(a) positive and negative interconnection



(b) negative interconnection



(c) positive interconnection

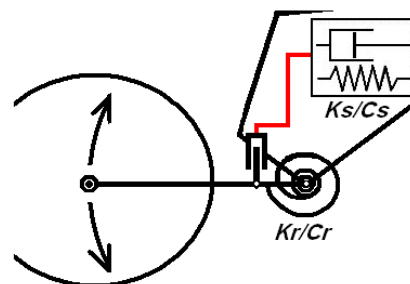


Figure 6.2: Sketches of interconnected suspension systems. a) system for positive and negative values of interconnection parameters. b) system for negative values of interconnection parameters. c) system for positive values of interconnection parameters.

The motorcycle nominal mathematical model has been updated to include the interconnection forces. In the nominal model, whilst the front suspension system consists of a telescopic fork and it is described in the model as a linear force applied

to the front wheel from the main frame, the rear suspension consists of a swinging arm and it is mathematically defined as a moment reacting between the main frame and the swinging arm. Following the approach taken in the previous chapter, the total reaction force applied by the front telescopic fork is divided into both suspension and interconnection forces, which are defined independently. The front suspension force depends linearly on the front fork position and speed, whilst the front interconnection force does so on the rear swinging arm angle and rotational speed. For the rear end, the force is modelled in a similar way. In this case the rear suspension moment depends linearly on the swinging arm angle and rotational speed, whilst the rear interconnection moment does so on the front fork position and speed. The Eq. (6.1) and Eq. (6.2) show the total front suspension force and rear suspension moment.

$$F_f = -k_f \cdot Z - c_f \cdot \dot{Z} - k_s \cdot \theta - c_s \cdot \dot{\theta} \quad (6.1)$$

$$M_r = -k_s \cdot Z - c_s \cdot \dot{Z} - k_r \cdot \theta - c_r \cdot \dot{\theta} \quad (6.2)$$

The variables Z and θ are the front fork displacement and swinging arm angle respectively. The parameters k_f (N/m) and c_f (Ns/m) are the stiffness and the damping coefficients for the front suspension. The parameters k_r (Nm) and c_r (Ns/m) are the coefficients for the rear suspension. Finally, the parameters k_s (N) and c_s (Ns) are the stiffness and damping coefficients for the interconnection system. Note that the interconnection parameters' units already consider the conversion between the angular displacement of the rear swinging arm and the linear force applied to the front fork. Similarly, the conversion between the front fork displacement and the moment applied to the swinging arm is also considered.

6.2 Road bump input response

Two essential functions of a sport motorcycle suspension system are to provide enough precision for the wheels to follow the road profile as close as possible and to keep certain comfort levels for the rider under road perturbation. The nonlinear model considered for this study introduces a discontinuity in the tires forces. As a

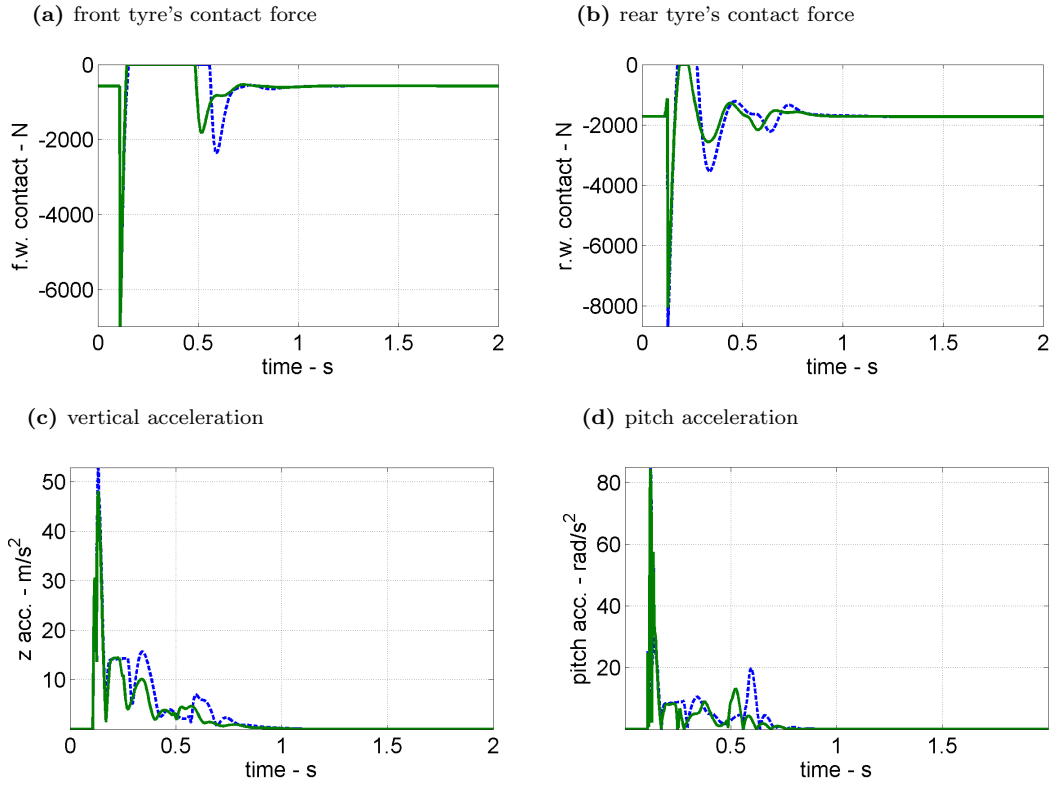


Figure 6.3: Precision and comfort variables responses at 80 m/s with interconnection coefficients $k_s = 0$ N and $c_s = -548$ Ns. The dashed blue line represents the nominal system response whilst the interconnected system response is plotted in solid green.

result, these forces become zero when the tires take off from the road.

Wheels fly times have been considered as a measurement for the suspension system's precision. Therefore, shorter fly times represent a greater precision. On the other hand, the comfort is measured through the maximum vertical acceleration and the maximum pitch angle acceleration perceived by the rider.

For this purpose, four response variables should be studied. Two of them are related to the precision of the suspension and the other two to the rider's comfort. The two first are the front and the rear wheels fly times after a bump. This is, the time whilst each tyre loses contact with the road. The control that the rider has over the motorcycle is drastically reduced if one wheel is out of the ground, being the front wheel the most critical. Shorter fly times increase the control during road perturbations and represent a better suspension precision. Flying times are calculated by the amount of time the tyre's contact forces are equal to zero. On the other hand, the maximum pitch angle acceleration and the maximum vertical acceleration perceived by the rider have been chosen as good indicators of the rider's

comfort. Smaller values of these magnitudes for a bump input represent better comfort results.

The effect of the interconnection in the above mentioned variables is illustrated in Fig. 6.3. It shows the response of the motorcycle model to a step bump with a height of 0.05 m at a forward speed of 80 m/s. The interconnection coefficients are $k_s = 0$ N and $c_s = -548$ Ns. It can be observed how, after the bump, both front and rear wheels fly times are reduced (Fig. 6.3a and Fig. 6.3b) whilst the maximum vertical and angular accelerations perceived by the rider reach similar values (Fig. 6.3c and Fig. 6.3d). The response of the independent suspension system nominal model is indicated in dashed blue line and the interconnected system's response is represented with a solid green line.

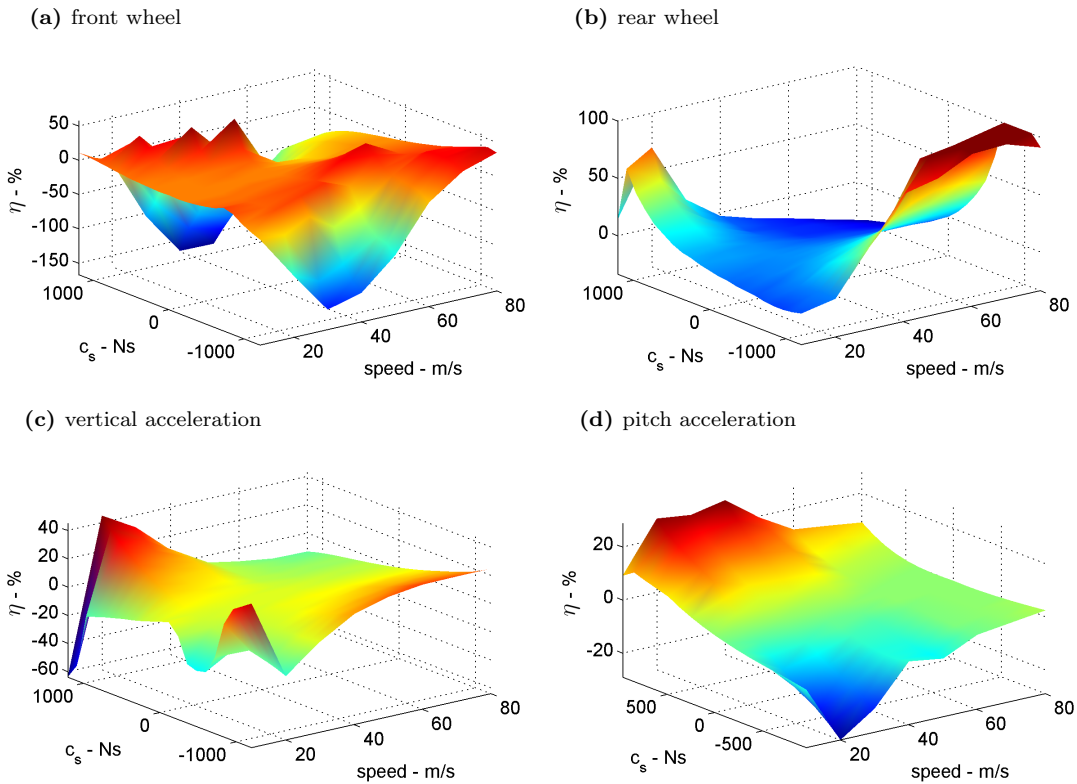


Figure 6.4: Efficiency maps of comfort and precision variables for different values of c_s with $k_s = 0$ N for a 0.05m step input at forward speeds starting at 10 m/s up to 80 m/s.

6.2.1 Efficiency mapping

In order to investigate the effects of the interconnection force and moment in the suspension response, the behaviours of these four variables are studied under straight

forward bump simulations for a wide range of stiffness (k_s) and damping (c_s) interconnection coefficients. The focus of this study is to understand the effects that the interconnection introduces in the suspension's response. Therefore, the front and rear suspension coefficients are kept constant at their nominal values.

The 'efficiency of each variable' is defined as the normalized difference between the value achieved by the variable after a bump input with ($k_s \neq 0$ N or $c_s \neq 0$ Ns) and without ($k_s = 0$ N and $c_s = 0$ Ns) interconnection forces and moments. It is defined by the Eq. (6.3) as follows:

$$\eta(x) = 100 \cdot \frac{(x - x_0)}{x_0} \quad (6.3)$$

Where x is the variable under study (it can be the maximum acceleration, the maximum pitch angle, the front wheel or the rear wheel fly times) and x_0 is the value achieved by the variable with independent suspensions. Efficiency is expressed as a percentage and it will be positive if the connection set-up provides a reduction on the variable's value.

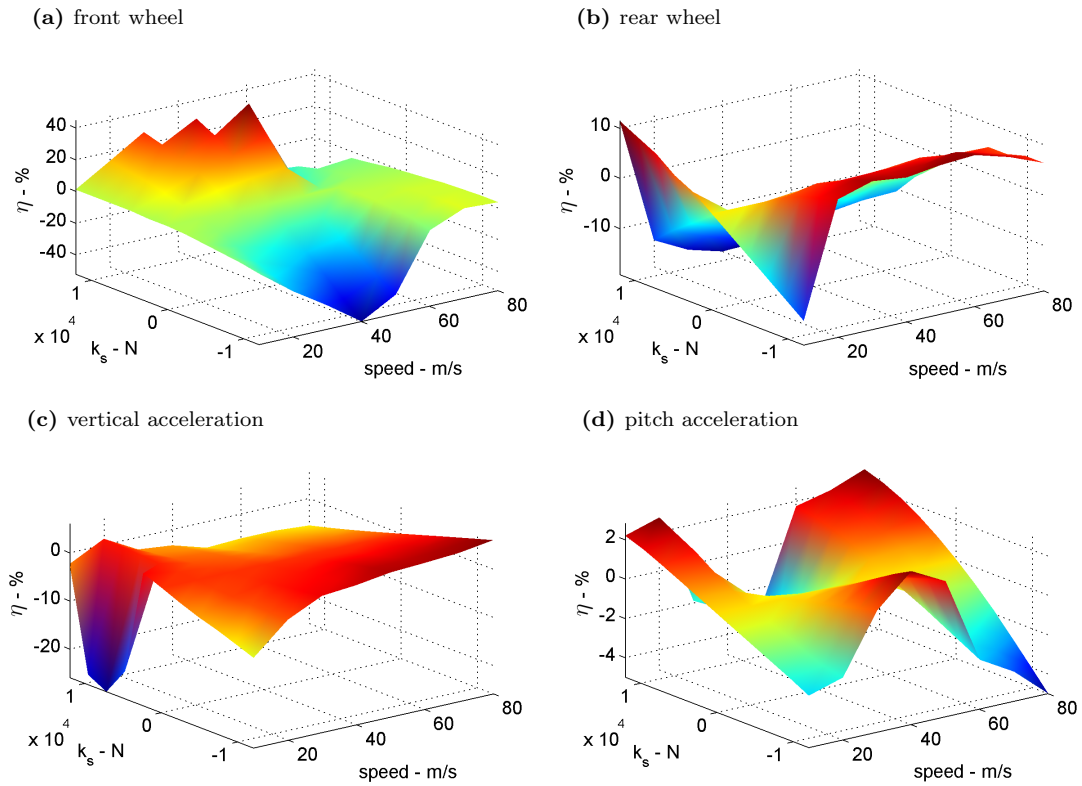


Figure 6.5: Efficiency maps of comfort and precision variables for different values of k_s with $c_s = 0$ Ns for a 0.05 m step input at forward speeds starting at 10 m/s up to 80 m/s.

Eight simulation scenarios have been created on VS Browser corresponding to eight forward speeds starting at 10 m/s and reaching 80 m/s. In these simulations the motorcycle is forced to pass through a road bump of 0.05 m at a constant speed. These scenarios are called from a Simulink model from where the stiffness and damping values are taken. The Simulink model is placed in a loop where these coefficients are varied sequentially, performing all the simulations for values of k_s ranging from -12000 N to 12000 N and values of c_s ranging from -1200 Ns to 1200 Ns. With the obtained simulation results the efficiency on the comfort and precision variables can be mapped. Figure 6.4 shows the results of varying the interconnection damping coefficient (c_s) and the speed, whilst the interconnection stiffness coefficient is $k_s = 0$ N. A difference between low and high speeds is observed. For low speeds, the front wheel efficiency is improved with high positive and negative values of damping coefficient c_s , whilst for speeds higher than 40 m/s only negative damping coefficient values would be suitable to achieve positive efficiency.

In the rear wheel and vertical acceleration cases, positive damping coefficients result in better efficiencies at low speeds, whilst for high speeds, the efficiencies are increased for negative values of c_s . In the case of the angular acceleration only positive values are suitable for the entire speed range. Due to this behaviour on the front wheel efficiency, a compromise with constant damping coefficient, c_s , to improve the overall performance can be found.

The interconnected suspension stiffness variation case presents a more complicated situation. The front wheel fly time efficiency is improved for positive values of k_s at speeds under 40 m/s whilst at higher speeds, negative values are clearly needed. However, the rear wheel and the vertical acceleration achieve positive efficiencies values only for negative interconnection stiffness coefficient for the entire the speed range, except at the slowest speed (10 m/s). The pitch acceleration efficiency presents a small variation, where negative values of the stiffness coefficient are suitable at slow speed and positive values are needed at higher speeds. These results are shown in Fig. 6.5 where k_s and the forward speed are varied and c_s is kept constant at zero.

Finally, the combination of stiffness and damping coefficients in the interconnected suspension system becomes a difficult scenario to find those coefficients that

could improve the efficiency of all the variables under study simultaneously. Automatic optimization processes should be implemented in order to find these optimal coefficients. Figure 6.6 shows, as an example, the efficiencies mapping at a forward speed of 50 m/s. Similar plots for all the forward speeds under study have been obtained and then used to choose a good set of initial values for the optimization processes for the stiffness and damping coefficients.

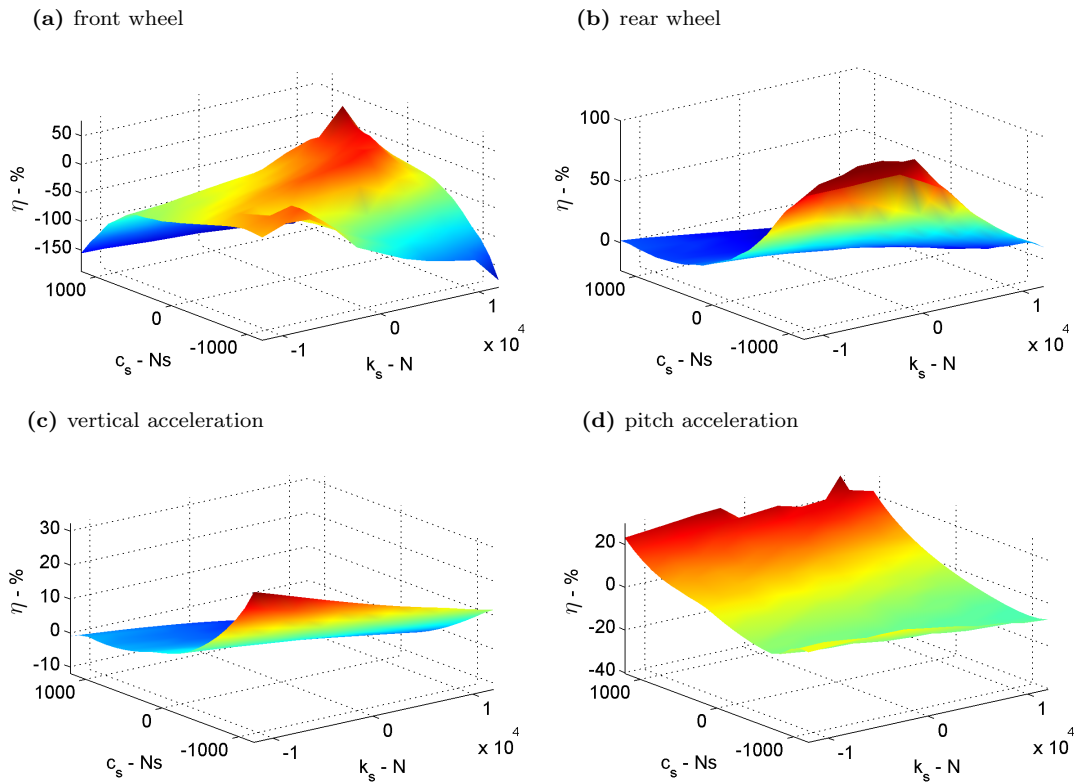


Figure 6.6: Efficiency maps of comfort and precision variables for different values of c_s and k_s for a 0.05 m step input at a constant speed of 50 m/s.

6.2.2 Optimization of the stiffness and damping coefficients

Considering that the model under study corresponds to a high performance racing motorcycle with an interconnected suspension system, the optimization process is now focused in obtaining a greater suspension precision, even if part of the comfort has to be sacrificed. Matlab optimization toolbox is a good framework to find satisfying results within a reasonable computational time. Different target functions are implemented in order to evaluate the front wheel fly time for a given desired speed. These target function correspond to the four different interconnection set-up

proposed at the beginning of this chapter:

- a) **Constant damping coefficient.** Achievable by a single constant damper unit. Consists of a direct connection of the front fork to the rear swinging arm through a damper unit with a constant damping coefficient.
- b) **Constant sign speed variable damping coefficient.** Includes a single speed variable damper with a similar mechanical design to the previous configuration, an optimal damping coefficient at each forward speed can be obtained. Following the scheme in Fig. 6.2b or 6.2c, the application point of the damper into the swinging arm would determine the sign of the coefficient, that would remain unchanged for the entire speed range.
- c) **Positive and negative speed variable damping coefficient.** Achievable by two speed variable dampers with opposed application points such as in Fig. 6.2a. Following the sign criteria defined by Eq. 6.1 and Eq. 6.2, the damper unit located ahead the swinging arm pivot point would contribute with negative interconnection damping coefficient. Oppositely, the damper unit placed behind the this pivot point would do so with a positive interconnection coefficient. The addition of each of the damper coefficients can result in positive or negative total damping coefficient for any forward speed.
- d) **Positive and negative speed variable stiffness and damping coefficients.** Achievable by electromechanical actuators. Whilst variable damping coefficient can be obtained by means of passive (dissipative) devices, a variable stiffness coefficient requires the inclusion of active devices. A couple of actuators could substitute the front and rear spring-damper units and apply the equivalent forces and moments as an interconnected suspension system would apply. This system is only proposed in here as a theoretical approach in order to explore the possibility of variable stiffness coefficients. Once actuators would be included in the suspension design, considering its elevated cost and the complexity, it constitutes a wide field of research on active suspension techniques which could be more suitable and efficient than the interconnected suspension approach.

For each of the four interconnection configurations indicated previously and for each of the eight considered forward speeds, the target function to be minimized can

be defined as the front wheel fly time efficiency. However, different consideration should be included in each function in order to meet the systems' design criteria.

The optimization process consists in using 'fmincon' Matlab function which is feed with the corresponding target function. Although the rear wheel is not a priority in this optimization process, a constriction on its efficiency is also included so that an adequate performance is kept by this wheel. This constriction is included for the case in which the rear wheel efficiency becomes negative, it restricts its value to never fall below $\eta = -10 \%$.

For the variable coefficients cases, the target functions call to a Simulink model containing the VehicleSim Block, which is configured to run the VS Browser simulation associated to a constant forward speed. The results of the simulation are processed by the target function in order to obtain the front and rear wheel fly times (time where the tyres forces become zero after a bump in the road appears). With these times and the nominal fly time of the independent system can obtained the efficiency as it was defined in Eq. (6.3).

Speed (m/s)	10	20	30	40	50	60	70	80
Weight	0.4	0.4	0.6	0.8	1	1	0.8	0.8

Table 6.1: Weights applied to the front wheel efficiency at the different forward speeds in the target function defined for the interconnection set-up a), where a constant damping value is found for all the speed range.

For the first scenario, a constant damping coefficient for the interconnected suspension (c_s) must be found for the entire speed range under consideration. Therefore the optimization process is slightly different to those cases in which different interconnection constants must be found at each different speed. In this case, the target function calls sequentially eight Simulink models that contain the different VehicleSim Blocks for the eight forward speeds under study. The sum of all the weighted efficiencies is established as the function's target to be minimized. The weight applied to the efficiency of each forward speed depends on what speed band is considered more relevant. In the case proposed in this study the middle-high speed band is more weighted than the lower speed range. Table 6.1 shows the weight values set for each forward speed.

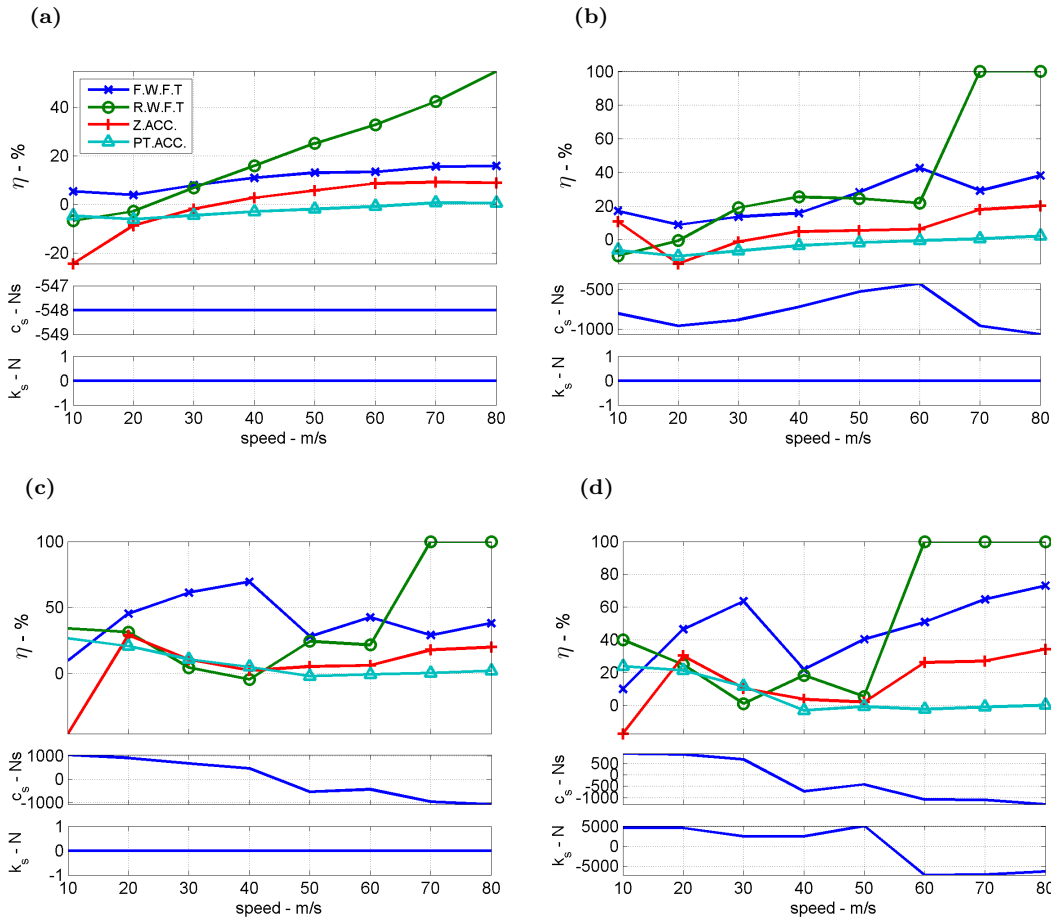


Figure 6.7: Efficiencies of the precision and comfort variables obtained for the four interconnection set-ups proposed in this section: a) Constant damping coefficient; b) Constant sign speed variable damping coefficient; c) Positive and negative speed variable damping coefficient; d) Positive and negative speed variable stiffness and damping coefficients.

The results for the four optimization processes (designed for the four different set-ups) are shown in Fig. 6.7 where the efficiencies of the front wheel (*FW*), rear wheel (*RW*), vertical acceleration (*ACC*) and pitch angle acceleration (*PTC*) are shown for the entire speed range. The units of k_s are N and c_s is in Ns.

Figure 6.7a shows the case of the constant damping coefficient. The optimal configuration found for the speed range is $k_s = 0$ N and $c_s = -548$ Ns. The improvement percentage of the suspension response of the front wheel starts around 5 % at low speeds and rises up to 17 % at high speeds. The rear suspension response is improved for high speeds and slightly worsened for very low speeds, but its efficiency never decays below the -7 %. Considering that the front wheel is relevant in terms of rider’s control and that the rear wheel fly time is only increased for very low speeds, this can be considered a good result for a very simple interconnection

system.

In Fig. 6.7b, the results for a constant sign speed variable damping coefficient are shown. Two optimization processes were implemented, one for positive and other for negative values of the damping coefficient. For positive values, the results for speeds above 50 m/s cannot be improved. Consequently a negative feedback was chosen for this set-up. The efficiencies are now higher, for the front wheel it reaches values from 10 % up to 40 %. The rear wheel efficiency is still negative at 10 m/s (above -7 %), but quickly reaches higher values (about 20 %) to a final efficiency of 100 % at high speeds. That means that for these cases the rear wheel does not lose contact with the ground.

Figure 6.7c shows the results for the positive and negative speed variable damping coefficient. In this case, positive values were found to be more suitable at slower speeds whilst negative values improved the responses at higher speeds. For speeds between 50 m/s and 80 m/s, the results are similar to those of the previous case. However, in the slow speeds range, a substantial improvement is observed in the front wheel efficiency. The rear wheel efficiency decays for medium speeds reaching its minimum value at 40 m/s, when the front wheel efficiency is maximum.

The last scenario is shown in Fig. 6.7d, positive and negative speed variable stiffness and damping coefficients are considered in this case. Higher efficiencies of the front and the rear wheels are found for all the speed range.

In all four cases, significant response improvements are found in terms of suspension precision. Although the optimization processes have not taken the comfort into account, in all the cases, it is not worsened in a substantial manner and in some cases it is improved.

Speed (m/s)		10	20	30	40	50	60	70	80
a)	$c_s(\text{Ns})$	-548	-548	-548	-548	-548	-548	-548	-548
b)	$c_s(\text{Ns})$	-801	-960	-882	-720	-528	-423	-960	-1066.5
c)	$c_s(\text{Ns})$	1305	924	682.5	468	-528	-423	-960	-1066.5
d)	$c_s(\text{Ns})$	945	903	684	-720	-420	-1080	-1100.3	-1292.5
	$k_s(\text{N})$	4.620	4.620	2.520	2520	5130	-7200	-7087.5	-6315.3

Table 6.2: Optimal coefficient values found for the four different interconnection set-ups.

Table 6.2 shows the optimal interconnection parameters found for the four interconnection set-ups previously proposed. Generally speaking, it can be said that positive spring stiffness and damping interconnection coefficients improve the suspensions precision for the lower half of the speed range whilst negative values are suitable for the higher speed range. If a simple mechanism was required, the precision of the suspension at low speeds could be improved by a constant negative interconnection damping coefficient. Nevertheless, it has to be considered that the optimization process in this case was carried out as a compromise solution for a wide range of speeds. If the motorcycle under study were to be run within a narrower speed range, such as street motorcycles, this implementation could return better results.

6.3 Frequency response

In order to understand the response of the system for different road undulations, a frequency analysis must be carried out. For this purpose, several nonlinear simulations were run in which the motorcycle model was forced to pass through sinusoidal road profiles at different constant speeds. These profiles have been designed for each forward speed in order to get an increasing frequency from 0.1 Hz to 10 Hz and an amplitude of 2 cm. For higher values of the amplitude, the discontinuity of tyre model gets relevance and the oscillatory analysis becomes less precise. The tyres take off the ground after any bump after certain speed and the distance travelled during the fly time is large enough to skip several consecutive undulations. This amplitude is chosen as a compromise that allows the study of the oscillatory behaviour of the system maintaining its nonlinear properties.

The VS Browser allows to introduce external perturbations in the simulation in different ways. One of them is in the form of a file containing a table with the values (amplitude and longitudinal distance) of the perturbation. The program can be set to fit the data contained in that table so a high data density is not needed. The VehicleSim model has to be adequately implemented to account for this perturbation. In this case, the perturbation is the road profile and it is introduced in the model through two variables associated to the tyres compression, as explained in Chapter 3.

6.3.1 Road profiles generation

Two considerations have been taken into account in the design of the road profiles. On one hand, the tyre model imposes two restrictions in terms of frequency. The first, is an upper limit in the input frequency for any perturbation, being this frequency limit about 8 Hz (Pacejka 2002). The second restriction is a lower limit in road perturbation wavelength. This wavelength cannot be shorter than the tyre radius. The largest radius of the two tyres corresponds to the rear wheel and it is equal to 0.297 m for the model under study. For the slowest speed under consideration, 10 m/s, the highest frequency allowed by this restriction is about 33 Hz. Consequently, the frequency upper limit is established by the first restriction about 8 Hz. However, the frequency range for the wave signal has been set slightly over this limit, between 0.1 Hz and 10 Hz, in order to have a wider view. Keeping this in mind, the results for frequencies above the 8 Hz must be carefully analysed.

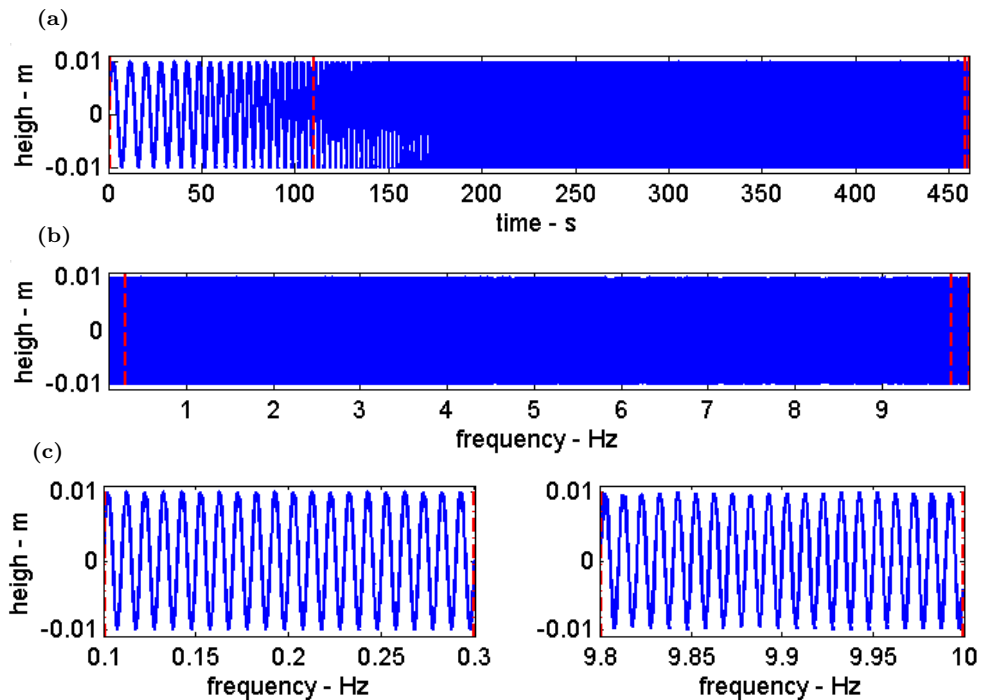


Figure 6.8: Wave signal used to build the different roads profiles. a) Signal vs. time. b) Signal vs. frequency. c) Detail of the constant peaks density for the lowest and the highest frequencies.

On the other hand, a computational efficiency criterion has been also followed: the number of sampling points for each period and the number of oscillations for each frequency interval must be constant. In that way it is not necessary to use too

many computational resources at low frequencies to ensure an adequate sampling at higher ones.

Following the approach in (Tempelaars 1996), wave modulation is achieved through its phase instead of its frequency. The instant angular frequency is defined as the time derivative of the phase $w_i = \frac{d\phi}{dt}$, the instant phase is then given by $\phi_i = \int w_i dt$ and $f_i = \frac{1}{2\pi} w_i$ is the instant frequency. In order to get a constant peaks density (peaks per hertz) for the entire frequency interval, the instant frequency can be defined as a time dependant function as:

$$f_i = f_0 e^{[\ln(f_f) - \ln(f_0)] \frac{t}{T}} \quad (6.4)$$

where the initial frequency is $f_0 = 0.1$ Hz, the final frequency is $f_f = 10$ Hz and $T = 460.52$ s is the total time for which the signal is varying. The time T is calculated in order to get a peaks density of $pph = 100$ Hz⁻¹. The phase is obtained as:

$$\phi = \frac{2\pi T}{[\ln(f_f) - \ln(f_0)]} f_0 e^{[\ln(f_f) - \ln(f_0)] \frac{t}{T}} \quad (6.5)$$

And the wave representing a sinusoidal road profile is then defined as the sine of this phase.

$$Z = Z_0 \sin(\phi(t)) \quad (6.6)$$

It can also be written as a function of the frequency as follows:

$$Z = Z_0 \sin\left(\frac{2\pi T}{[\ln(f_f) - \ln(f_0)]} f(t)\right) \quad (6.7)$$

Therefore the peaks density function is given by

$$pph = \frac{T}{[\ln(f_f) - \ln(f_0)]} \quad (6.8)$$

This is a constant from which the value of the time interval T, needed for a desired density, can be directly obtained. Figure 6.8 shows this wave, represented with respect to the time and the frequency, and shows how the peaks density is constant for all the frequency range.

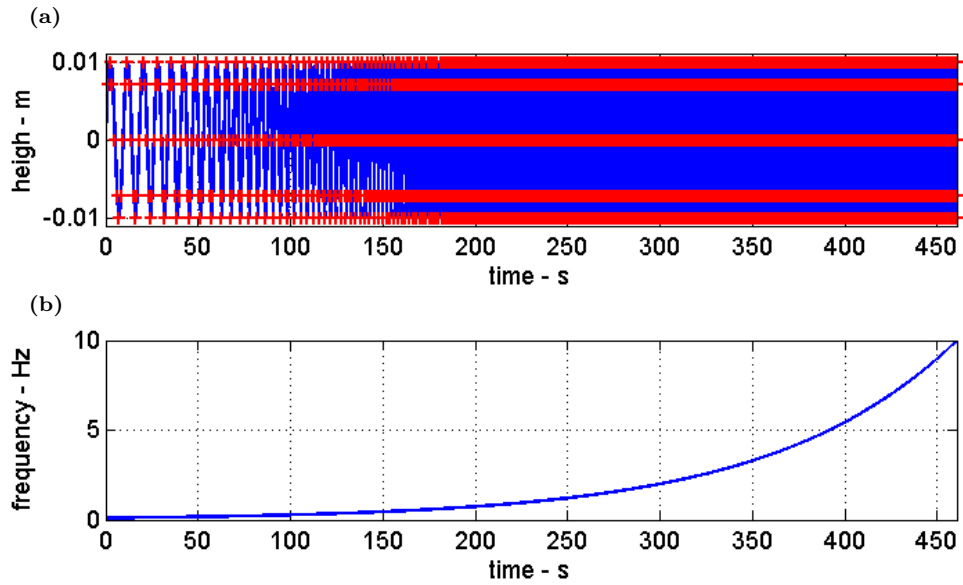


Figure 6.9: a) Wave signal (blue solid line) and sampling points (red +) used for road input. b) Frequency variation of road profile function.

In order to obtain an accurate description of the wave signal, eight sampling points were taken for each period. The time values that meet this requirement are obtained when the sine argument, ϕ , is equal to an integer multiple of $\frac{1}{4}\pi$. Figure 6.9 shows the wave signal overlapped with the sampling points and the frequency as a time dependant function. Depending on the value of the motorcycle's forward speed in each simulation, the sinusoidal road input function must be scaled with the forward speed to present the data as road perturbations, this is, to represent the amplitude of the road input with respect to the distance. The obtained data are imported to VS Browser in the form of a table. VS Browser interpolates them and reconstructs the sine wave to be used as a road perturbation along the simulation time.

6.3.2 Simulations and signal processing

As it indicated in the previous section, four configurations of the interconnected suspension were considered:

- a) Constant damping coefficient.
- b) Constant sign speed variable damping coefficient.
- c) Positive and negative speed variable damping coefficient.
- d) Positive and negative speed variable stiffness and damping coefficients.

For each of these configurations, eight simulations have been run for different forward speeds starting at 10 m/s up to 80 m/s. For all of them, a specific road input is implemented forcing the motorcycle to go through a sinusoidal undulation increasing its frequency from 0.1 Hz to 10 Hz.

Similarly to the previous section, four variables have been considered; in this case, the nature of the behavioural analysis requires a variation of them. The front and rear wheel vertical displacements are taken to study the suspension system's precision. The comfort is studied through the vertical displacement of the rider attachment point to the main frame and the pitch angle reached by the main frame.

Simulations have been run directly from the VS Browser and the data obtained were later imported to the Matlab environment. To obtain the amplitude of these four variables a low resources demanding algorithm was implemented. This algorithm finds the signal's inflection points and measures the distance from one minimum to the next maximum and vice versa. Considering the high peaks density, this distance can be taken as a good measure of the amplitude for each oscillation at a determined frequency value. After applying this algorithm it was found that, in some cases, the amplitude oscillates at some frequencies. This is caused by smaller oscillation inside the main ones due to the force transmission between the front and the rear wheel through the interconnection system. Figure 6.10a shows the front wheel frequency response for a 80 m/s forward speed simulation with $c_s = -1066.5$ Ns damping interconnection coefficient together with a detail of these nested oscillations. The effect produced by them on the amplitude is shown in Fig. 6.10b. In order clarify this oscillating behaviour, a second algorithm –also based on inflection points detection– was developed to filter these small perturbations and to keep only the maximum amplitude achieved by the variable under study at each road oscillation. Figure 6.10c shows the result of applying this filter to the amplitude obtained by the first algorithm.

The effects of the different interconnection approaches are studied for the precision and comfort variables for each of the eight forward speeds. Figure 6.11 shows the magnitude of these four variables with respect to the obtained frequency for the various interconnection configurations at a forward speed of 40 m/s. These magnitudes are represented in decibels. As it has been already mentioned, the road

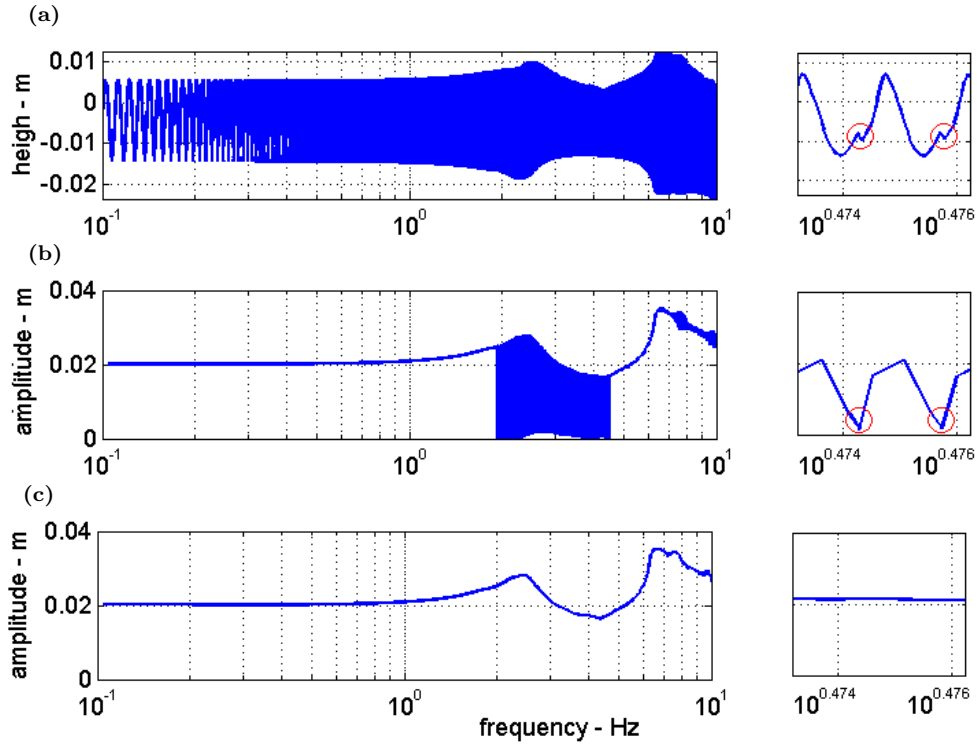


Figure 6.10: a) Front wheel frequency response for a 80 m/s forward speed simulation with $c_s = -1066.5$ Ns damping interconnection coefficient. b) Response's amplitude obtained by the inflection points algorithm. c) Response's amplitude after the filter algorithm were applied.

perturbation amplitude was 0.02 m, so the magnitude of the signals can be defined in decibels as:

$$mag = 10 \log\left(\frac{amp}{0.02}\right) \quad (6.9)$$

The low-frequency responses for the front wheel, rear wheel and vertical displacement are zero, whilst the pitch angle low-frequency response takes negative values due to the fact that the output units are radians instead of meters in this case. Similar plots can be done for all the forward speeds condition.

The results plotted in this way, although they are clear for each forward speed individually, make it difficult to understand in a global manner the effects of the interconnection system on the frequency response. In order to present these results in a clearer way, the magnitudes of the signals are mapped along all the frequencies and speeds ranges for each interconnection set-up independently. These can be shown as spectrograms where the forward speed variation belongs to the x axis and the frequency variation to the y axis. Considering that the resonance peaks occur in the high-frequency range, both axes are linearly scaled to obtain a detailed view

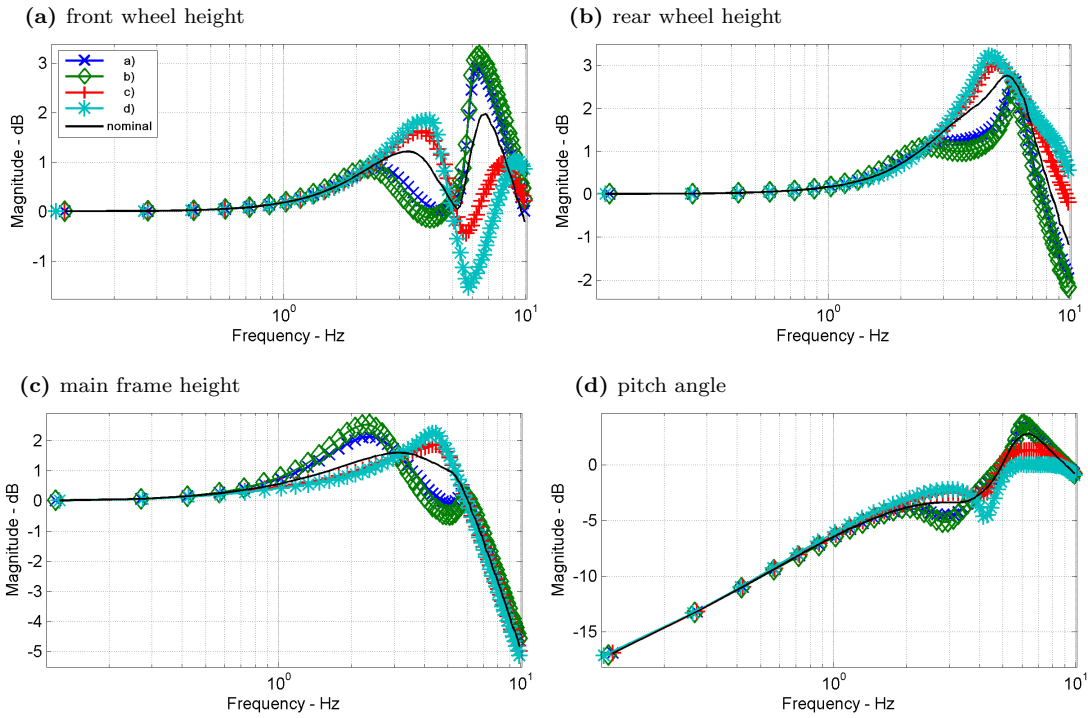


Figure 6.11: Frequency responses of the precision and comfort variables at 40 m/s for the different interconnection set-ups: a) blue \times , b) green \diamond , c) red $+$, d) cyan $*$. The nominal independent suspensions system's response is plotted in black.

at these frequencies. Figure 6.12 shows the magnitudes with respect to the speed and frequency for the nominal non-interconnected suspension model. These maps represent the behaviour of the nominal motorcycle under sinusoidal road perturbations and they are a good reference to understand how the interconnection system would affect the model's dynamics.

The resonance peaks are marked with a dashed black line. Regarding to the vertical displacement and pitch angle, their peaks appear about 3 Hz and 6 Hz respectively. These frequencies are similar to those calculated for the bounce and pitch normal mode through the eigenvalues of the state space matrix A . Figure 6.13 shows a root locus for the nominal motorcycle model with non-interconnected suspension at a roll angle of 0° and forward speed starting at 10 m/s up to 80 m/s. As it is well known, three out-of-plane normal modes can be observed. These are rider lean (3 rad/s – 8 rad/s), weave (10 rad/s – 30 rad/s) and wobble (45 rad/s – 55 rad/s). The other two normal modes, which are more damped, are the in-plane modes bounce and pitch. The bounce mode is within the frequency range 17 rad/s – 21 rad/s (2.7 Hz – 3.4 Hz). The pitch mode appears at higher frequencies, 41 rad/s

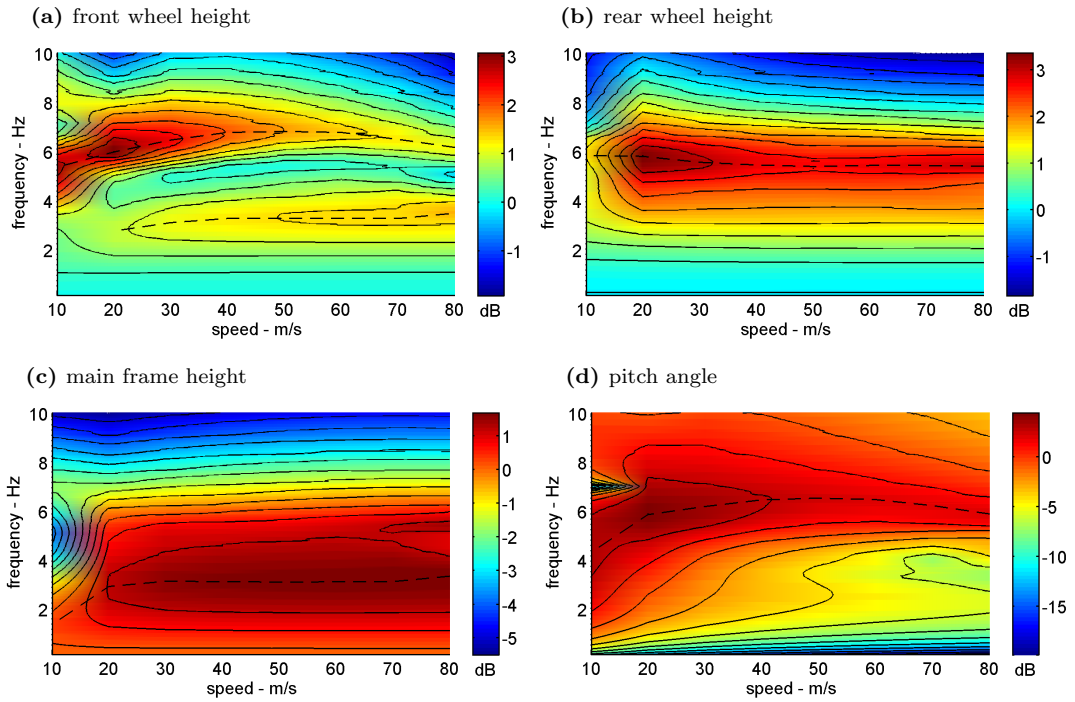


Figure 6.12: Frequency response maps of the precision and comfort variables for all the forward speeds for the nominal non-interconnected suspension model ($k_s = 0$ N and $c_s = 0$ Ns). The level curves are marked in solid black whilst the peak values of the magnitudes are marked with dashed black lines.

– 44 rad/s (6.5 Hz – 7 Hz). For the pitch angle magnitude (Fig. 6.12) the resonance frequency is not exactly the same than those predicted by the linear analysis. It is important to notice that the perturbation in this case is applied to the front and rear wheels through a sinusoidal road. Therefore, a delay exists between the rear and front wheel inputs that depends on the road wavelength. This delay introduces an irregular perturbation on the bounce and pitch motion. On the other hand, the pitch normal mode not only consists in a pure pitch motion; other degrees of freedom are involved on it with relevant relative weights that affect the resonance frequency of this normal mode. Figure 6.15 shows the relative weights of the different degrees of freedom involved in bounce and pitch normal modes. The evolution of each of them can be appreciated through the profile of the bar associated to them, starting at 10 m/s up to 80 m/s.

The delay in the front and rear wheels input produces the well known effect ”wheelbase filtering” which has been widely studied in the vehicle dynamics literature as in (Gillespie 1992), (Sharp 2002) or (Cossalter et al. 2006). This effect consists, as its name says, in the filtering of those road frequencies corresponding to

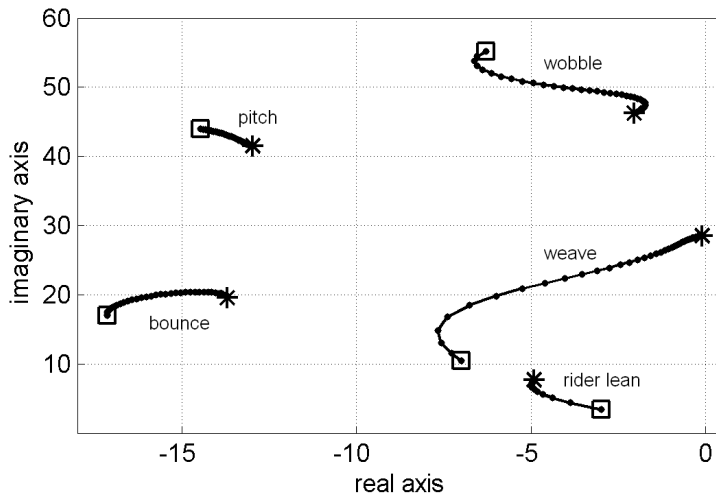


Figure 6.13: Root locus for the motorcycle model with independent suspensions at a roll angle of 0° and starting at 10 m/s (\square) up to 80 m/s (*).

wavelengths in relation to the wheelbase. In the case of the wheelbase being equal to an even multiple of half a wavelength ($wb = 2n \cdot \frac{\lambda}{2}$) the front and rear wheels inputs will be in phase, therefore, the bounce mode's perturbation will be maximum whilst the pitch mode's perturbation will be minimum. On the other hand, if the wheelbase is equal to a odd multiple of half a wavelength ($wb = (2n - 1) \cdot \frac{\lambda}{2}$) the effect will just be the opposite. In this later case, the front and rear wheels inputs are in phase opposition, resulting in maximal excitation of the pitch mode and minimal excitation of bounce mode. Figure 6.14 illustrates both cases.

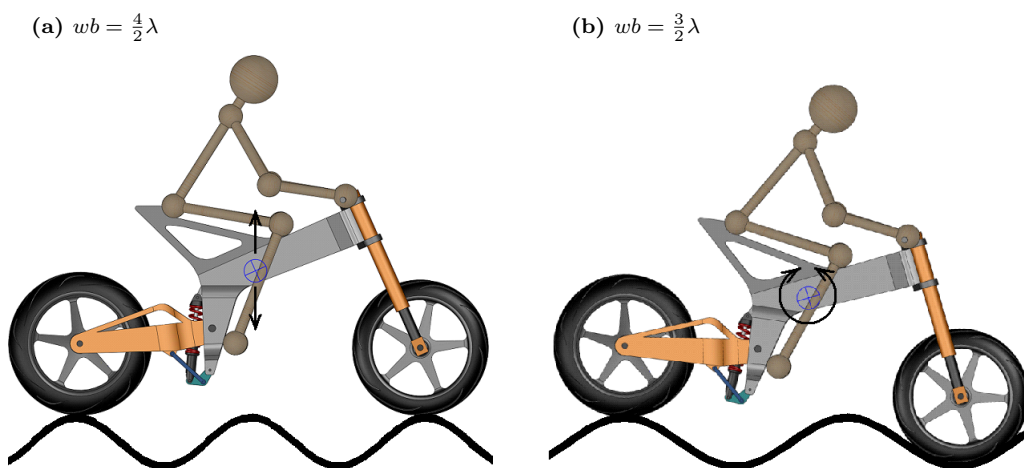


Figure 6.14: Wheelbase filtering for pitch (a) and bounce (b) motions due to the road profile wavelength.

The wheelbase of the particular motorcycle model under study is 1.41 m. Considering as a first approach the relation between the wavelength and the frequency

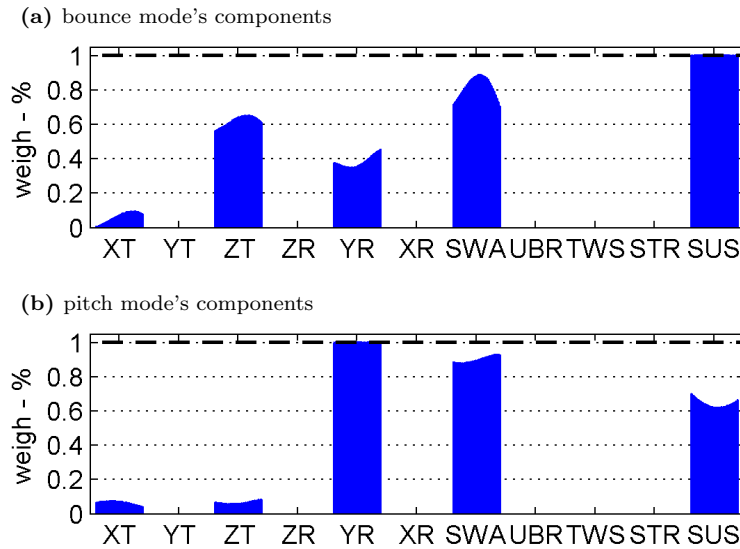


Figure 6.15: Bounce and pitch normal modes' components. The bar's edge associated to each component represents the evolution of this component along the speed range from left (10 m/s) to right hand side (80 m/s).

through the speed to be $\lambda\nu = v$, at a forward speed of 10 m/s, the filtering frequency for the pitch motion will be about 7 Hz and that for the bounce motion will be just a half of this, 3.5 Hz. For higher forward speed these frequencies are increased in proportion.

All this can be observed in Fig. 6.12. For the vertical displacement magnitude, in Fig. 6.12c, the resonance frequency is at 3 Hz for all the speed range except for 10 m/s, where the peak is at 1.5 Hz. The bounce normal mode resonance frequency coincides with the bounce wheelbase filtering frequency at 10 m/s. The competition between the normal mode resonance peak and the minimum produced by the wheelbase filtering at this frequency results in a displacement of the maximum magnitude peak towards longer wavelengths. On the other hand, the vertical displacement magnitude rises again at 7 Hz coinciding with the pitch angle wheelbase filtering frequency. Finally, these interactions produce a minimum that can be observed at 5 Hz.

In Fig. 6.12d the pitch angle magnitude at 10 m/s shows a pronounced decay at 7 Hz whilst at 3 Hz this magnitude is significantly higher than those at faster speeds. As it has been already seen, the pitch angle resonance frequency is about 6 Hz, however at 10 m/s this frequency is notably reduced due to the addition of these effects. The maximum pitch angle magnitude at this speed is found to be

about 4.5 Hz.

At 20 m/s, only the bounce wheelbase filtering frequency is inside the model frequency limits. However, the bounce motion is already highly damped at this frequency and this is not a remarkable effect. For the remaining speed range, wheelbase filtering frequencies become greater than 10 Hz, this is out of the model limits.

Figure 6.12a shows the magnitude of the front wheel frequency response. Two resonance peaks related to the bounce (3 Hz) and the pitch (6 Hz) motions appear. The wheelbase filtering is clear in the front wheel response producing both minimums at 3 Hz and 7 Hz for a forward speed of 10 m/s. The influence of the front suspension (*SUS*) in bounce and pitch normal modes is shown in Fig. 6.15a. The oscillation of this degree of freedom is directly linked to the front wheel's elevation, thus its resonance frequencies correspond to those of these two normal modes.

The rear wheel response is showed in Fig. 6.12b. The main resonance frequency corresponds to the pitch mode at 6 Hz. The increase of this tend for the entire speed range starts before the 3 Hz and at this frequency the magnitude is larger than 3.5 dB. An eventual resonance peak related to the bounce normal mode is masked behind the increase on the resonance peak corresponding to the pitch mode, whose magnitudes doubles that one of the first peak.

Various maps similar to those of Fig. 6.12 have been plotted. In order to obtain a qualitative understanding of the effects produced by the different set-ups in the frequency response of each precision and comfort variables, the level curves and peaks lines corresponding to the nominal (independent suspensions) model are overlapped with these maps. In the areas of the maps where the lines are visible the interconnection set-up under study would result in smaller magnitudes. Conversely, in the areas where the lines are covered by the surface, the interconnected suspension set-up would produce an increment of the magnitude. The color-bar legend on each map provides quantitative values of the magnitude.

Figure 6.16 shows the frequency response maps of the precision and comfort variables for the interconnected suspension set-up a) with $k_s = 0$ N and $c_s = -548$ Ns. The main frame's vertical displacement for this configuration is shown in Fig. 6.16c. The maximum amplitude is not increased significantly. However, the resonance frequency is shifted towards smaller frequencies showing its maximum at 2.5 Hz. For

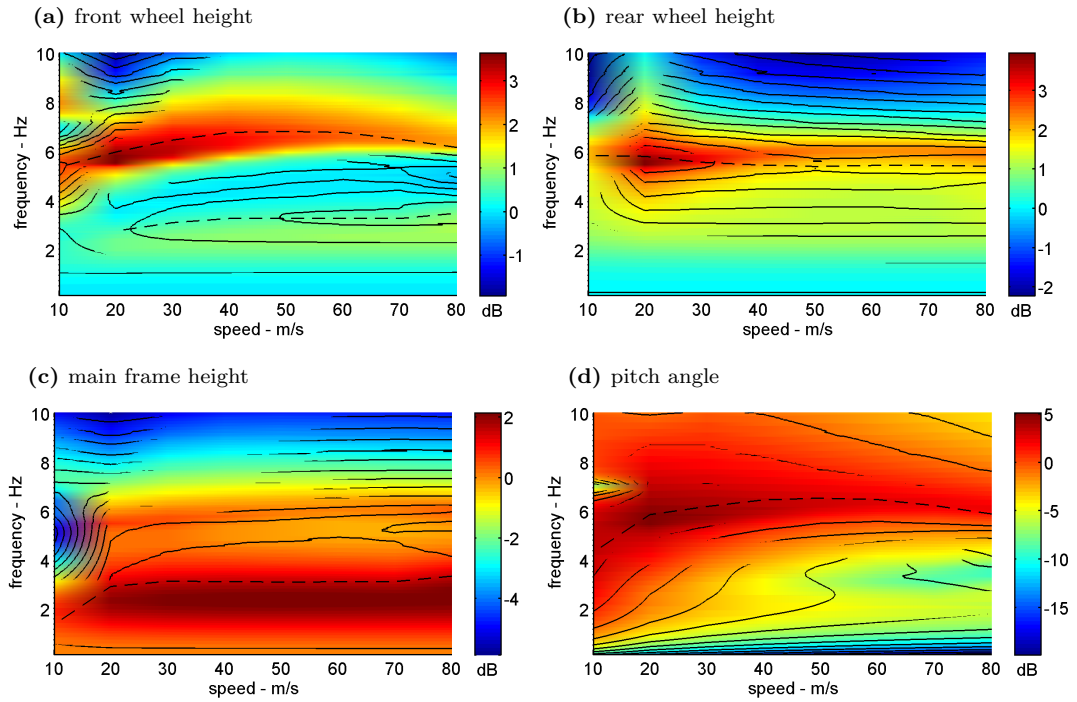


Figure 6.16: Frequency response maps of the precision and comfort variables for all the forward speeds with interconnection coefficients $k_s = 0$ N and $c_s = -548$ Ns. The level curves (solid) and the magnitude peaks values (dashed) corresponding to the independent suspensions model are overlapped with the maps as a reference.

the middle range of speeds at high frequency, the level curves are covered by the surface due to a small increment on the magnitude. The same minimum value, due to the interaction between the wheelbase filtering and the bounce mode natural frequency, is shown at 5 Hz, being in this case slightly more pronounced.

The pitch angle frequency response is mapped in Fig. 6.16d. It behaves similarly than for the nominal case although the maximum amplitude is slightly larger. A remarkable effect of the interconnected suspension configuration is that the wheelbase filtering is reduced in great manner. The minimum value found at 7 Hz for a speed of 10 m/s is now about 15 dB higher than that for the model's suspension nominal configuration.

In the front wheel height case, an increase on the magnitude for high frequencies after 20 m/s is shown in Fig. 6.16a. The resonance peak associated to the pitch motion increases its maximum value by a couple of decibels. The pitch wheelbase filtering is visible and slightly more pronounced than that for the nominal system. In the low frequency range the bounce resonance peak has been shifted and its maximum magnitude is decreased.

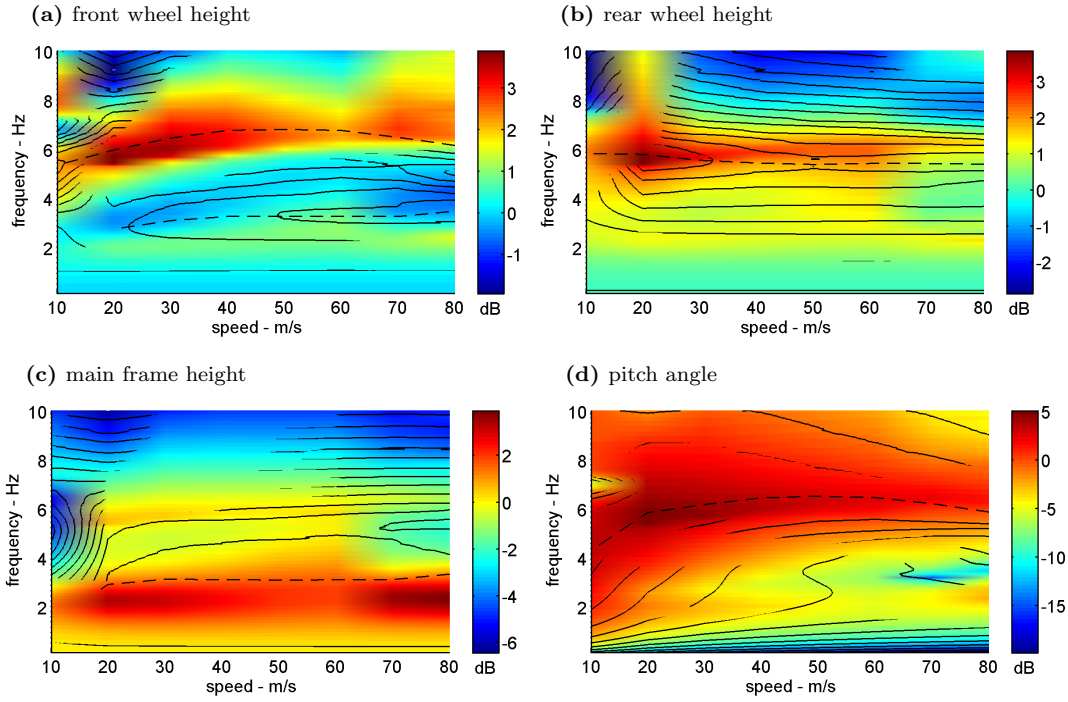


Figure 6.17: Frequency response maps of the precision and comfort variables for all the forward speeds with interconnection coefficients $k_s = 0$ N and c_s taking negative optimal values depending on the forward speed. The level curves (solid) and the magnitude peaks values (dashed) corresponding to the non-connection model are overlapped with the maps as a reference.

The rear wheel height for this configuration, in Fig. 6.16b, has a general behaviour similar to that of the nominal configuration. However, a small change can be observed: the resonance peak related to the pitch motion has a higher frequency. It also reduced its maximum magnitude except for slowest speeds (10 m/s - 20 m/s). On the other hand, at low frequencies, the rear wheel height magnitude increases and the peak related to bounce frequencies is now perceptible.

The frequency response maps of the precision and comfort variables for the interconnected suspension set-up b) are shown in Fig. 6.17. In this configuration $k_s = 0$ N and c_s takes only negative optimal values. In Fig. 6.17c similar results that those produced by the previous suspension set-up a) are found for the main frame vertical displacement. A noticeable variability of the resonance peak magnitude can be observed, the peak value decays at medium-high speeds (40 m/s - 60 m/s). A similar variation is found in the case of the front wheel height, 6 Hz peak in Fig. 6.17a.

In Fig. 6.18, the relation between the interconnected suspension coefficient value c_s and the resonance peak magnitudes becomes clear for all the speed range. In the

case of the front wheel peak, the magnitude decays with the speed. The relationship between the front wheel height and the pitch modes should be considered. In this same figure, the pitch angle highest value decays with the speed. Similarly to the bounce resonance peak magnitude, the front wheel high frequency peak magnitude is directly affected by the interconnected suspension damping coefficient although, in this last case, it is modulated by the pitch mode amplitude. Finally, the rear wheel height peak at 6 Hz follows the pitch resonance and decays with the speed showing its highest value at 20 m/s. This peak losses relevance whilst the peak at 2.5 Hz becomes clearly visible now.

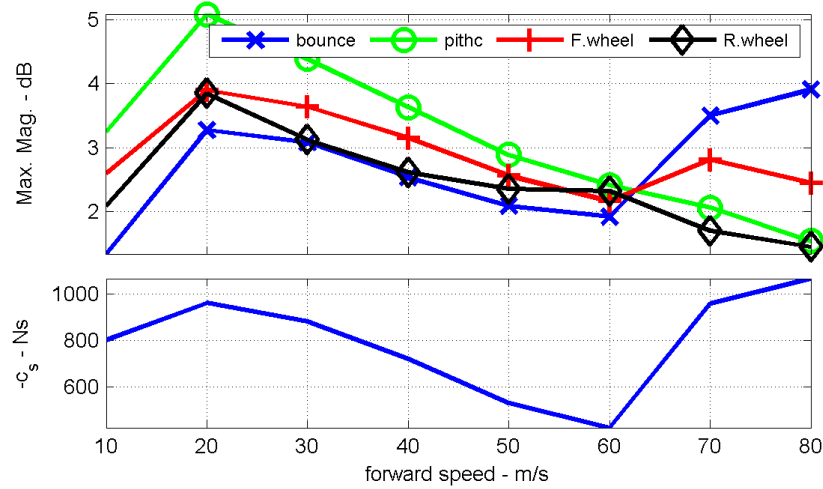


Figure 6.18: Maximum magnitudes compared to the inverse of the interconnected suspension damping coefficient of set-up b) (negative speed variable damping coefficient).

The interconnected suspension set-up c) consisted of a spring stiffness coefficient $k_s = 0$ N and a damping coefficient c_s variable with the forward speed that can adopt either positive or negative optimal values. In a similar way to previous figures, Fig. 6.19 shows the mapping of the four variables frequency responses. The optimization process carried out to find the optimal values of the damping coefficient in the previous section is similar to that for set-up c) except that in this case there is no restriction in the sign of the damping coefficient value of the interconnected suspension. In this case, for speeds under 50 m/s, positive values of c_s are more suitable for a step input. Speeds from 50 m/s up to 80 m/s require negative c_s values in order to obtain an optimal performance of the suspension precision. Therefore, the results for high forward speeds are similar in both interconnected suspension set-up b) and c). Notable differences are found for the low speeds range where the

optimal interconnected suspension damping coefficient should be always positive.

Figure 6.19c shows the main frame vertical displacement. For the low speed range, the bounce resonance peak is shifted towards higher frequencies reaching 4.5 Hz. Likewise, its magnitude is lower than for the negative c_s case. The minimum found at 10 m/s, loses relevance whilst its frequency coincides with the resonant peak. The pitch angle (Fig. 6.19d) has reduced its maximum magnitude at slow speed. However, the wheelbase filtering in this case, shows a bigger impact. At 10 m/s and about 3.5 Hz, the wavelength approximately doubles the wheelbase and the pitch angle response is clearly amplified. Meanwhile, it is deeply damped for the same speed range at a frequency about 7 Hz, where the wavelength and the wheelbase are equal.

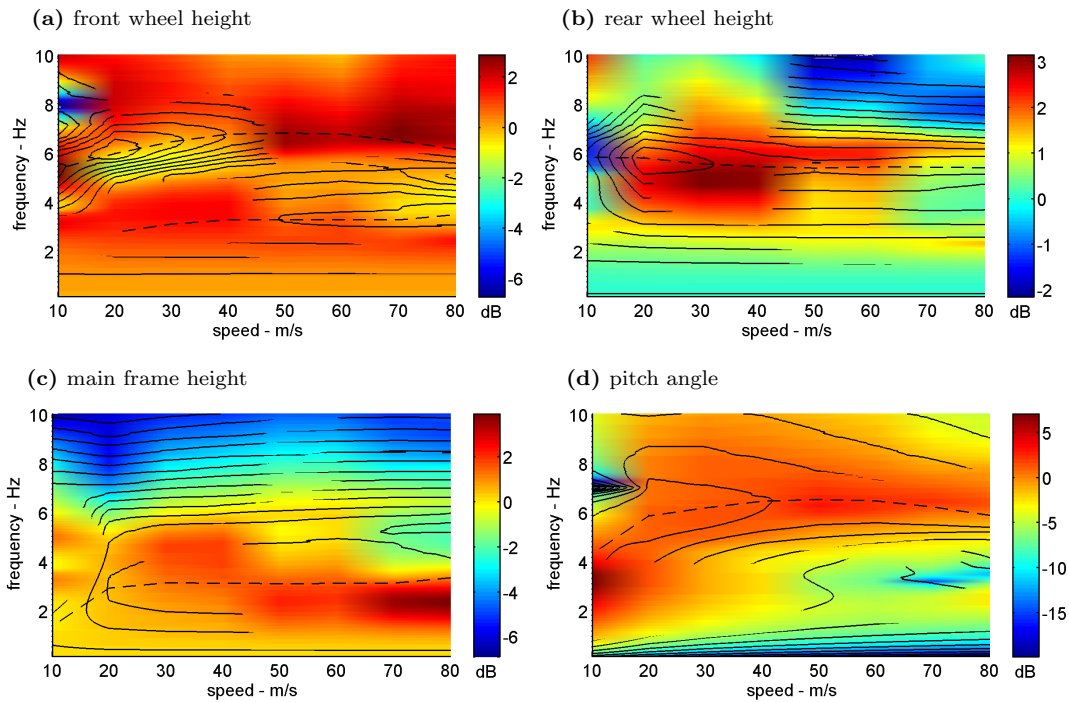


Figure 6.19: Frequency response maps of the precision and comfort variables for all the forward speeds with interconnection coefficients $k_s = 0$ N and c_s taking positive and negative optimal values. The level curves (solid) and the magnitude peaks values (dashed) corresponding to the non-connection model are overlapped with the maps as a reference.

The case of the front wheel height (Fig. 6.19a) shows also minimum value at 10 m/s, but the frequency now is slightly increased up to 8 Hz with respect to previous configurations. Its magnitude is reduced at the frequencies related to the pitch at low speed (positive c_s values) whilst it is drastically increased for those frequencies related to the bounce resonance, which now are higher. For higher speed

values, for which the interconnection damping coefficient is negative, the behaviour is similar to that in previous configurations and the pitch resonance frequencies dominate over the bounce ones.

Figure 6.19b shows the rear wheel magnitude. Once again, for the high speed range its behaviour is similar to that considered in previous configurations. However, at slower speeds, the resonance peak appears at lower frequencies, about 5 Hz. At 10 m/s, where the wheelbase filtering effect can be observed, a relevant minimum is shown at about 6 Hz. It can be observed that, whilst the connection through a negative damping produces an increase of the pitch resonance peak frequency, a positive damping connection results in a decrease of it. Finally, the resonance peak related to the bounce motion remains more or less unaffected.

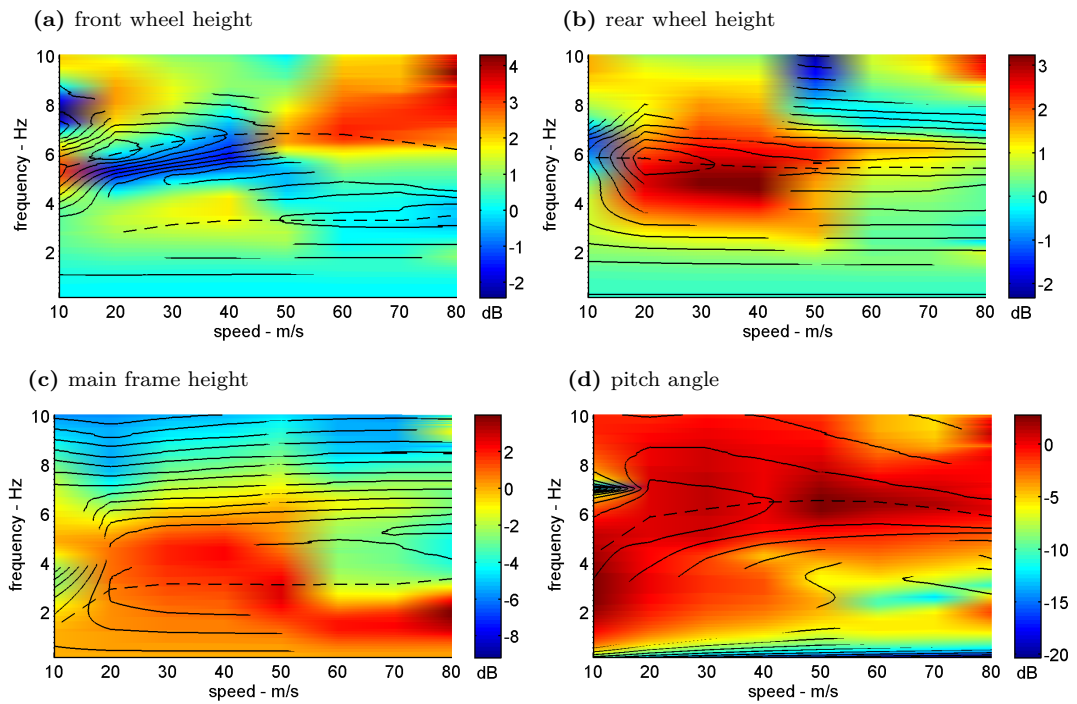


Figure 6.20: Frequency response maps of the precision and comfort variables for all the forward speeds with interconnection coefficients k_s and c_s taking positive and negative optimal values. The level curves (solid) and the magnitude peaks values (dashed) corresponding to the non-connection model are overlapped with the maps as a reference.

The interconnected suspension set-up d) was obtained by means of eight multi-variable optimization processes, one for each speed under study. The two variables to be optimized were the spring stiffness k_s and damping c_s interconnection coefficients. Both of them could take positive and negative values. The addition of a non-zero stiffness coefficient results in new optimal values for the damping coefficient at each

forward speed. The frequency response of this configuration is shown in Fig. 6.20. Similar behaviours of the two precision and two comfort variables are observed, being all of them smoother than that for the suspension set-up c).

6.4 Conclusions

This chapter presents the potential benefits in terms of performance that an interconnected suspensions system could introduce in a motorcycle, if adequately implemented.

For the motorcycle model under study, it has been shown that satisfactory results are achieved in terms of tyre fly time reduction by the connection of the front and rear suspension, just by means of a simple damper unit. By increasing the complexity of the mechanical system, better results can be achieved.

It has been found that positive damping connection coefficients are more adequate for low speeds. On the contrary, for high speeds, negative values are needed. The work presented in here considered a wide speed range. For narrower speed ranges, better result could be achieved by adding a device that connects the front and the rear suspensions with a constant coefficient damper.

By means of several optimization processes, four optimal interconnected suspension set-ups of different complexity have been proposed. The frequency response of all of them has been studied in order to detect possible undesirable effects. Although several variations of these responses could be found due to the interconnected system, none of them results in harmful behaviours. A general qualitative view of their effects on the GSX-R1000 model frequency response can be summarized in the following.

The frequency responses of the comfort and precision variables follow similar patterns along the entire speed range except at lower speed as the wheelbase filtering effect introduces maximums and minimums at its characteristic frequencies.

Positive interconnection damping coefficients increase the main frame vertical displacement resonance frequency, whilst negative coefficients decrease it. In this case, it can be observed how the peak magnitude of this variable depends directly on the coefficient's values.

The pitch resonance frequency remains unaffected by the damping coefficient values, however, positive values result in an enhancement of the wheelbase filtering effects. Meanwhile, the opposite happens for negative values.

All these could be expected considering that with negative interconnection coefficients values, the interconnection forces tend to move the front and the rear wheel in the same direction reducing the pitch motion and increasing the bounce. When the interconnection coefficients values are positive, these forces act in opposite directions, increasing the pitch oscillation and decreasing the bounce.

The front wheel vertical displacement magnitude shows two resonance peaks, associated to the bounce and pitch motions. For negative interconnection coefficients the bounce peak magnitude is much lower than the pitch peak. Nevertheless, positive interconnection coefficients values increase the bounce influence on the front wheel and attenuate the pitch influence on it. Similar effects can be observed for the rear wheel magnitude. It can be said that if the interconnected suspension system enhances one or another in-plane motion (bounce/pitch), then the wheels' responses to the resonance frequency associated to this motion are damped.

Finally, it can be concluded that interconnected suspension systems could improve significantly the suspension performance of a motorcycle of this characteristics with a minimum cost if passive elements are considered.

Chapter 7

Interconnected Suspensions

System: Stability Analysis

This chapter is focused on the study of the interconnected suspension system stability through the understanding of the normal modes presented by the GSX-R1000 linear model.

As it has been explained in Chapter 3, VehicleSim returns a state space representation of the programmed model. This is an automatically generated Matlab file containing the state matrices A, B, C and D. The terms of these matrices are expressed as functions of the state variables (positions and velocities) as well as the different dynamical parameters of the motorcycle model (masses, inertias, etc.). The parameters are numerically set in the Matlab file according to the values defined in the model programmed in VS Lisp, in contrast to the state variables that are free to be set depending on the trim state to be studied.

In order to study the evolution of the normal modes with respect to the speed and the roll variation, several simulations are run. On each simulation, the roll angle is fixed and the speed is increased from 10 m/s up to 80 m/s in a very slow manner (0.001 m/s^2) in order to obtain quasi-equilibrium trim states. The roll angles under study are 0° , 15° , 30° or 45° . They are kept constant along the simulation taking advantage of the roll angle controller included in the motorcycle model.

Once a simulation is finished, the values of the state variables for each forward speed and roll angle are taken from those of the corresponding simulation time step. The state matrices are then fed with these values, resulting in a high fidelity state

space representation for each trim state (roll angle and forward speed), from which its normal modes can be obtained.

On one hand, the weights and the phase angles of the different degrees of freedom within a normal mode can be obtained from the eigenvector components associated to it. These components weights and phases describe the mode's pattern of motion. A normal mode can be represented by two bar diagrams as in Fig. 7.2 and Fig. 7.3. In the first of them, the bars heights represent the normal mode's degrees of freedom relative normalized weights. In the second diagram, the bars heights represent the relative phase angle of each degree of freedom.

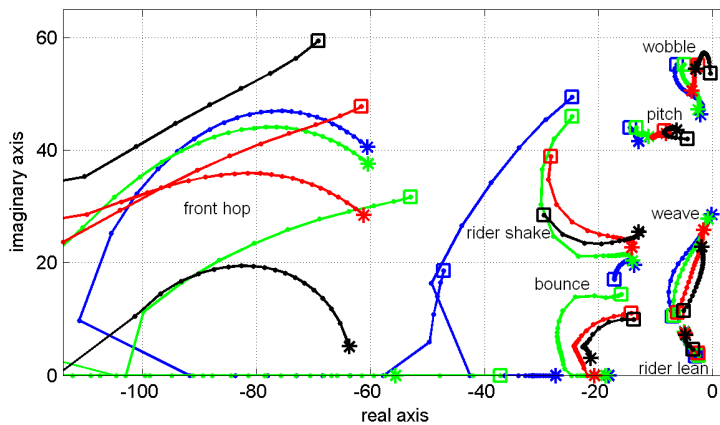


Figure 7.1: Root loci for the motorcycle nominal suspension system showing the main normal modes affected by the suspension dynamics. Speed is increased from 10 m/s (\square) up to 80 m/s (*). Different roll angles are considered: 0° (blue), 15° (green), 30° (red) and 45° (black).

On the other hand, the state space matrix A eigenvalues provide information on the normal modes' frequency and damping for a given trim state and can be represented as a root locus. Figure 7.1 shows typical root loci for the motorcycle nominal configuration in which no connection exists between the front and rear suspension systems. In this figure, the eigenvalues associated to the normal modes for the motorcycle linear model are represented for four different simulations, in which the motorcycle runs at four different roll angles: 0° (blue \times), 15° (green \circ), 30° (red $+$) and 45° (black \diamond). For each of these four simulations the speed is increased from 10 m/s (\square) up to 80 m/s (*).

This root locus shows a wide area where highly damped normal modes are visible. Clearly, these modes do not imply stability risks for the motorcycle nominal configuration. They hardly could be excited and, thus, appreciated in the motorcycle dynamics. However, once the front and rear suspension systems are connected,

these modes change its damping properties in a substantial manner reaching, in some cases, the unstable region.

The normal modes shown in this plot are divided into in-plane and out-of-plane modes. The in-plane modes are those in which only the degrees of freedom that imply a motion inside the motorcycle's symmetry plane are involved. On the other hand, the out-of-plane modes only involve the degrees of freedom that represent a motion out of the motorcycle's symmetry plane. This is valid for an equilibrium state at zero roll angle, but once the motorcycle is leant, the forces appearing between the ground and the tyres are not in-plane and consequently, the in-plane and out-of-plane degrees of freedom get coupled. However, both types of modes maintain their main motion characteristics and can be distinguished.

DOF	Description
XT, YT, ZT	Motorcycle's chassis x, y and z translation.
ZR, YR, XR	Motorcycle's chassis <i>yaw, pitch</i> and <i>roll</i> rotations.
SWA	Swinging arm rotation about the main frame's y axis.
UBR	Rider's upper-body rotation about the main frame x axis.
TWS	Front frame rotation about the <i>twist</i> axis.
STR	Front frame rotation about the <i>steering</i> axis.
SUS	Front fork compression/extension.

Table 7.1: Eigenvectors components of the GSX-R1000 multi-body system considered for the mode motion identification.

The out-of-plane modes are wobble, weave, rider lean and rider shake. Figure 7.2 shows the weights and phases of each degree of freedom involved in these modes for straight running conditions, this is, zero roll angle. The forward speed of the motorcycle is increased from 10 m/s up to 80 m/s. Consequently, the weights and phases of each degree of freedom change with the forward speed. This change is appreciated in the bars' profiles, where the speed is increased from left to right. On the other hand, the in-plane modes are pitch, bounce and front hop. Their weights and phases are plotted in Fig. 7.3 following the same representation.

These eigenvectors representations correspond to the eigenvalues in Fig. 7.1 plotted in blue \times (zero roll angle). The degrees of freedom in the \mathbf{x} coordinates of the

normal mode figures are all related to the motorcycle's reference frame and they are presented in Table 7.1.

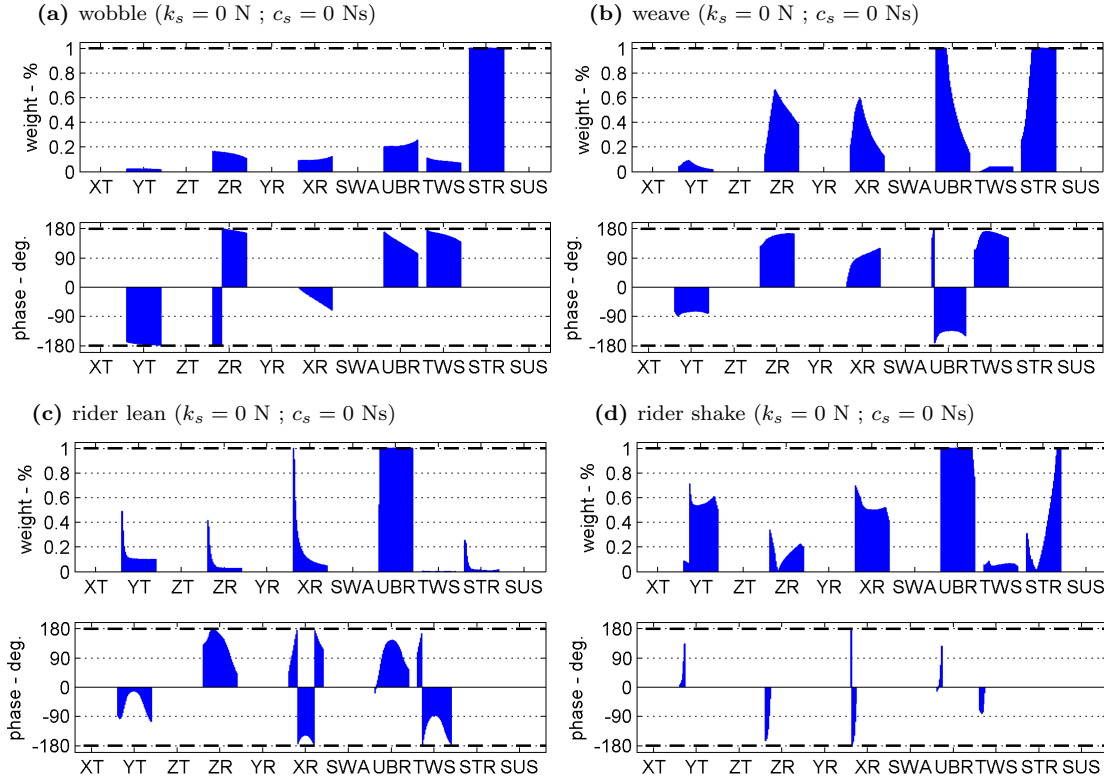


Figure 7.2: Out-of-plane normal modes' components for the motorcycle nominal configuration at 0° roll angle. The speed evolution of each component's weight and phase is represented by the bars profile, varying the speed from left (10 m/s) to right hand side (80 m/s).

Figure 7.2a shows the bar diagram for the wobble mode at 0° roll angle. It is characterized by an oscillation of the front frame about the steering axis whilst the rear frame is only slightly affected. The lateral displacement (YT), the yaw (ZR), the roll (XR), the rider's upper body (UBR) and the frame twist (TWS) oscillations are substantially smaller than the steering oscillation (STR), which is the main degree of freedom involved in this normal mode. The root loci in Fig. 7.1 show that the resonance frequencies of this mode are reduced with the speed from 55 rad/s to 45 rad/s for the different roll angles under study except for high roll angle (45°). For this roll angle the frequency is increased up to almost 58 rad/s at medium speed and reduced down to 55 rad/s for high speed. For high (45°) and medium (30°) roll angles, the wobble mode is low damped at slow speeds and becomes more stable as the speed is increased. On the other hand, for small roll (15°) and zero roll angles it becomes well damped and tends to lose its stability with

the speed increase.

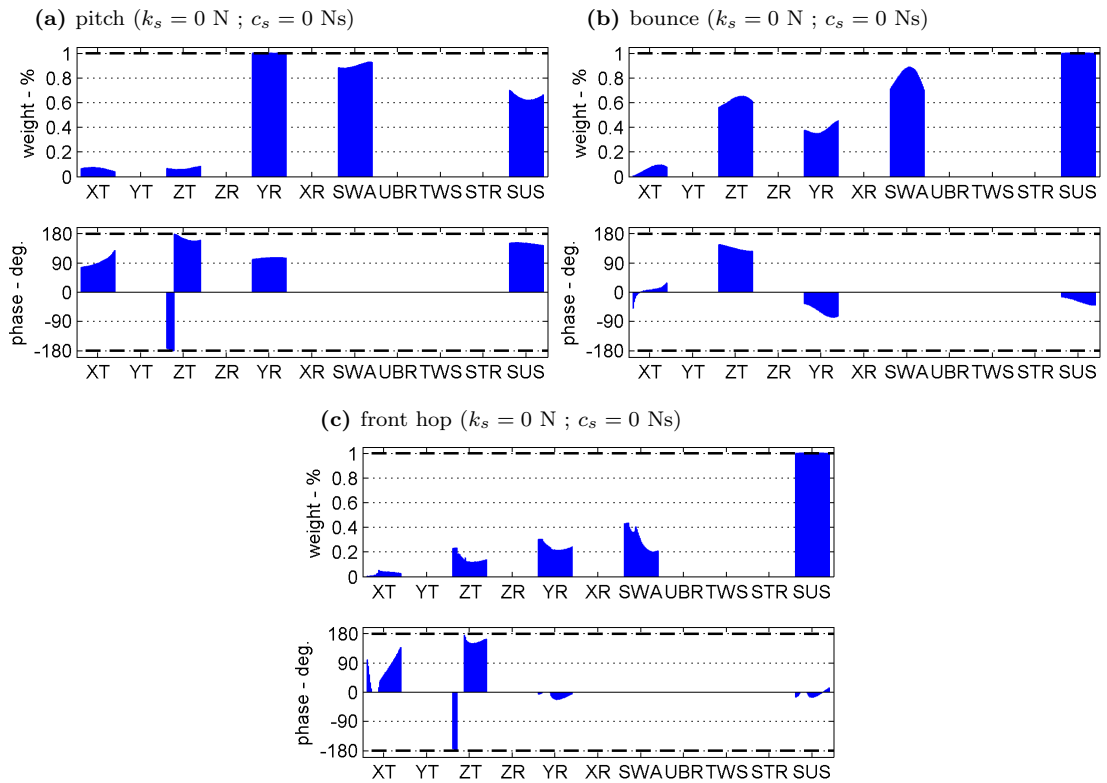


Figure 7.3: In-plane normal modes' components for the motorcycle nominal configuration at 0° roll angle. The speed evolution of each component's weight and phase is represented by the bars profile, varying the speed from left (10 m/s) to right hand side (80 m/s).

Figure 7.2b shows the weave mode eigenvector components at 0° roll angle. This mode is characterized by roll (XR), yaw (ZR) and steering angle (STR) oscillations at medium and high forward speeds. At low speed, the rider's upper-body oscillations (UBR) are relevant, but not so the steering angle. The increase in the forward speed produces a reduction in the weight of this component and a fast rise on the STR amplitude. Its resonance frequency is between 10 rad/s and 30 rad/s. It is stable for the entire speed range but it approaches the stability limit as the speed is increased. This mode becomes more stable for roll angle increases at higher speeds.

The rider lean is a mode that appears when the rider's upper-body degree of freedom is included in the mathematical model. It consists in a high oscillation of the rider's upper-body (UBR). For very low speeds, the steer (STR), the yaw (ZR), the roll (XR) and the lateral displacement (YT) present large amplitudes, being the roll angle the main degree of freedom involved in the mode. However, these components are fast reduced with the speed as it can be seen in Fig. 7.2c. It has a

low frequency, between 3 rad/s and 9 rad/s. And it is well damped for the speed range considered in the simulations. For higher speeds it becomes more stable.

Rider shake is a mode associated to the rider's upper-body degree of freedom. In this case the motion consists in an oscillation of the rider with higher frequencies starting at 50 rad/s and ending at about 23 rad/s, depending on the motorcycle roll angle. This is shown in Fig. 7.4. Only for zero roll angle, this mode becomes overcritical for speeds greater than 20 m/s. Figure 7.2d shows the eigenvector components for zero roll angle with nominal configuration. After this speed, all the phase angles become zero due to the fact that the normal mode is not oscillating at these points.

The pitch mode's components are presented in Fig. 7.3a. They are characterized by the main body pitching (YR) with large oscillations of the front (SUS) and rear (SWA) suspension. The phase angle presented by the motorcycle main frame and the front suspension with respect to the swinging arm are about 180° . For a motorcycle model with a perfect symmetry about its centre of masses there would not be other components involved and the phase angle would be exactly 180° , producing a pure pitch motion. However, this model presents differences in terms of masses, suspensions, etc. of the front and rear sides of the motorcycle, these other components such as the vertical (ZT) or the horizontal (XT) displacements are present in the mode motion, and the phase angles are smaller than 180° . It is well damped, getting smaller values of damping for higher roll angles. Its frequencies for all running conditions are constricted between 40 rad/s and 45 rad/s.

The components of the bounce mode are plotted in Fig. 7.3b. It consists in the vertical oscillation of the main frame (ZT) in phase opposition with the front (SUS) and rear (SWA) suspensions. Similarly than what happens with pitch mode, other degrees of freedom are involved on the bounce mode which presents these phase angles smaller than 180° . Once again, this is due to the model asymmetry around its centre of masses. For a symmetrical model, this mode would present a pure bounce motion pattern. Its frequencies for the straight running conditions are about 20 rad/s. If the motorcycle is leant, the evolution of this mode with the speed results in a frequency reduction until the mode becomes overcritical at higher speeds, increasing its damping ratio.

The front hop mode is the front wheel resonance whilst the rest of motorcycle assembly remains slightly affected. Figure 7.3c shows how the main component of its eigenvector is the front suspension (*SUS*) oscillation with minor lower oscillation of the rest of the in-plane degrees of freedom. For this motorcycle model, and with no interconnection established between front and rear suspensions, it is a highly damped mode with a large frequency variation with the speed. It can reach values up to 60 rad/s for 45° of roll angle at very low speeds and becomes overcritical for low-medium speed range at any roll angle.

7.1 Straight running condition

During straight running conditions, the motorcycle in-plane and out-of-plane modes are uncoupled. Therefore, their evolutions with the different interconnection parameters can be understood in a more intuitive manner.

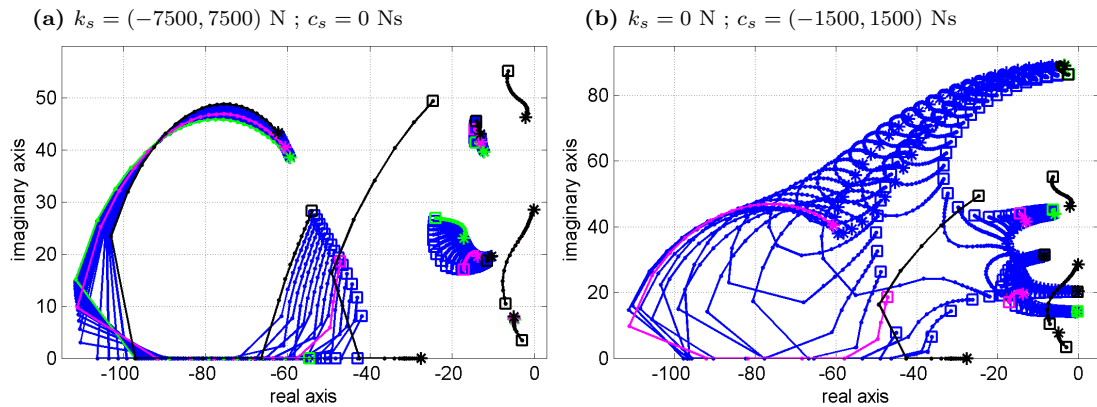


Figure 7.4: Root loci for both stiffness and damping coefficients variations. Roll angle is set at 0° and speed is increased from 10 m/s (□) up to 80 m/s (*). a) Interconnection stiffness coefficient varies from $k_s = -7500$ N up to $k_s = 7500$ N, with $c_s = 0$ Ns. b) Interconnection damping coefficient varies from $c_s = -1500$ Ns up to $c_s = 1500$ Ns, with $k_s = 0$ N.

Figure 7.4 represents the evolution of the motorcycle’s root locus when the interconnection stiffness and damping coefficients are varied within the limits established in Chapter 6. These limits are found as those maximum and minimum values for which the suspension system’s response shows minimum acceptable accuracy. The eigenvalues variation across the motorcycle forward speed is shown as a blue dotted line, ranging from 10 m/s (□) to 80 m/s (*). Several root loci are overlapped in the same figure in order to show their evolution with the interconnection parameters.

Consequently, for the same eigenvalue 20 lines are shown (one for each interconnection parameter value) with 36 points (one for each motorcycle forward speed). The nominal case, where no connection is implemented between the front and rear ends ($k_s = 0$ N and $c_s = 0$ Ns), is shown in magenta. The case for which the interconnection parameter gets its minimum value is represented in green whilst that for which the parameter reaches the maximum value allowed is shown in black.

7.1.1 Variation of interconnection stiffness coefficient

Figure 7.4a represents the motorcycle root locus evolution when the interconnection stiffness coefficient k_s is varied from -7500 N up to 7500 N and the interconnection damping coefficient c_s is zero. As expected, it can be seen how the out-of-plane modes are not affected. The roots of these modes for the different interconnection coefficient values are overlapped in the plot, being only visible those for the maximum value of the interconnection stiffness.

On the other hand, the in-plane modes are slightly affected. Although the front hop mode remains highly damped for the entire k_s range, it becomes more damped for positive values of k_s and less damped for negative values. In the nominal configuration case, it becomes in a non-oscillating mode when the forward speed falls between 28 m/s and 32 m/s. High values of negative interconnection stiffness coefficient prevent the mode from oscillating for all the forward speed values under 30 m/s. This can be seen in Fig. 7.5e, where the phase of all of its components becomes zero for this speed range. This figure shows the evolution of the eigenvectors components with forward speed for an interconnection stiffness value of $k_s = -7500$ N, whilst in Fig. 7.5f does so for a value of $k_s = 7500$ N. Comparing these two figures with the front hop mode's components for a nominal configuration, in Fig. 7.3c, it can be said that the interconnection stiffness coefficient has small effect on the behaviour of this normal mode. The Swinging arm amplitude is increased for positive values of this coefficient and it is reduced for negative values. Minor changes in some of the components' phases can also be observed.

The bounce mode becomes less damped for positive values of k_s . For negative values its damping and resonant frequency increase. In terms of eigenvectors' components, it keeps its main properties, experimenting little changes in the phases of

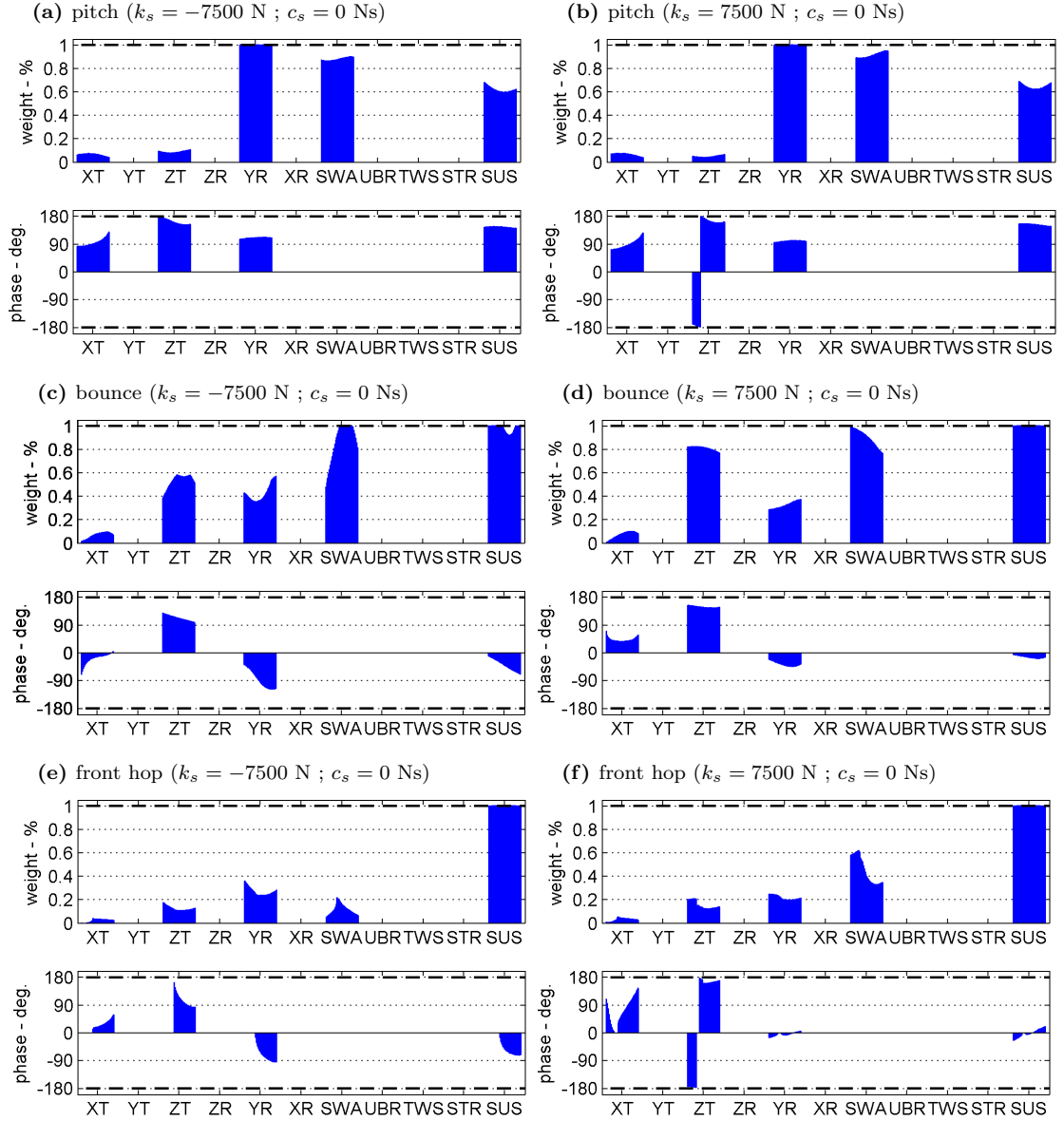


Figure 7.5: In-plane normal modes' components for the maximum and minimum values of stiffness interconnection coefficient for a roll angle of 0° . On the left-hand side $k_s = -7500$ N. On the right-hand side $k_s = 7500$ N. The interconnection damping coefficient is set to $c_s = 0$ Ns. The speed evolution of each component's weight and phase is represented by the bars profile, varying the speed from left (10 m/s) to right hand side (80 m/s).

some of them. Figure. 7.5c and Fig. 7.5d show the modal composition for values of $k_s = -7500$ N and $k_s = 7500$ N respectively, whilst Fig. 7.3b presents the eigenvector components for the nominal configuration. It also can be appreciated that the main frame vertical displacement amplitude decays for negative values of k_s and increases for positive values of k_s .

Finally, pitch mode remains almost unaffected, with similar eigenvectors components' weights and phases. The root loci in Fig.7.4a show a small variation of the mode resonant frequency with the interconnection stiffness coefficient, reaching higher frequencies for positive values of k_s and smaller frequencies for negative values.

Clearly, the choice of the interconnection stiffness coefficient does not influence greatly the main oscillating modes dynamics, although it can improve the suspension's efficiency results as shown in Chapter 6.

7.1.2 Variation of interconnection damping coefficient

When an interconnection damper is introduced in the nominal model, a complex evolution of its in-plane normal modes appears in the root loci. This is shown in Fig. 7.4b. The eigenvalues corresponding to the minimum value of the interconnection damping coefficient ($c_s = -1500$ Ns) are shown in green, the eigenvalues corresponding to the nominal configuration ($c_s = 0$ Ns) are plotted in magenta and those corresponding to the maximum value ($c_s = 1500$ Ns) are shown in black. Intermediate values are represented in a blue dotted line. Following the same representation, Fig. 7.6 separates the root loci into negative (Fig. 7.6a) and positive (Fig. 7.6b) c_s values variations in order to provide a clearer view of the roots evolution for the different interconnected suspension system configurations.

For a decrease in c_s , the eigenvalues evolve regularly with the forward speed and they can clearly be distinguished one from the others. However, for an increase in the c_s , for certain values of c_s there is not a clear trend on the eigenvalues' behaviour. This is shown in Fig. 7.6b, where the pitch and front hop modes are plotted in red for an interconnection damping coefficient $c_s = 510$ Ns. In this point, the speed evolution of these modes changes substantially. Now, the eigenvalues that could be expected to belong to the pitch mode for slow speeds actually correspond to the

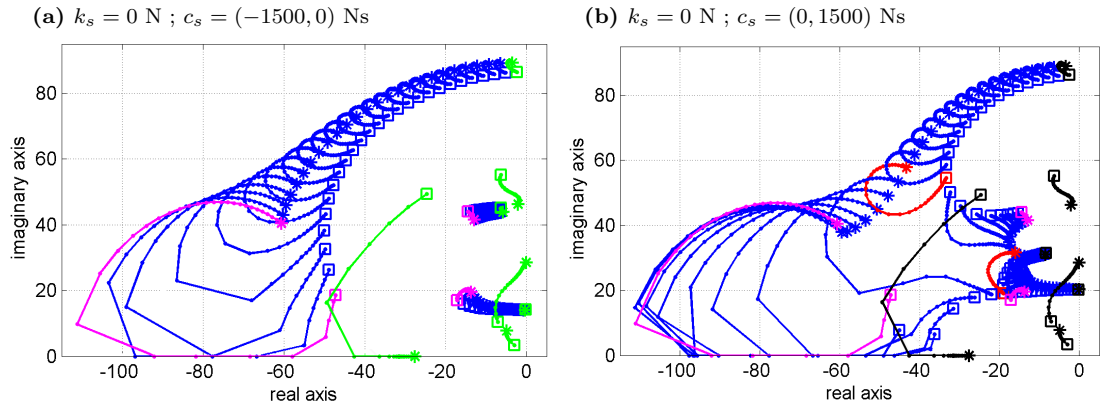


Figure 7.6: Root loci for the interconnection damping coefficient variation divided into positive and negative values. The roll angle is set at 0° and the speed is increased from 10 m/s (\square) up to 80 m/s ($*$). a) Interconnection damping coefficient ranging from $c_s = -1500 \text{ Ns}$ (green) up to $c_s = 0 \text{ Ns}$ (magenta). b) Interconnection damping coefficient ranging from $c_s = 0 \text{ Ns}$ (magenta) up to $c_s = 1500 \text{ Ns}$ (black). The interconnection stiffness coefficient is $k_s = 0 \text{ N}$ in both cases.

front hop mode, and vice versa.

Figure 7.7 shows the front hop mode's components evolution with speed for positive values of c_s . It can be seen how the YR component amplitude (pitch angle) reaches high relevance in the mode motion at slow speeds for a value of $c_s = 480 \text{ Ns}$. This typical characteristic of the pitch motion is reduced for higher speeds. For interconnection damping coefficient values larger than $c_s = 510 \text{ Ns}$, this behaviour tends to be reduced gradually until the maximum value is reached at $c_s = 1500 \text{ Ns}$, for which the pitch angle oscillation is almost zero (see Fig. 7.10f).

The main degree of freedom involved in the front hop mode for the nominal configuration (Fig. 7.3c) is the front fork translation (SUS). It presents a phase angle relative to the swinging arm oscillation (SWA) of about zero degrees. However, it can be observed in Fig. 7.7 that when an interconnection damping coefficient is introduced in the system, this phase angle swaps to 180° , whilst the swinging arm oscillation increases proportionally to the c_s value.

Being the interconnection damping coefficient positive, any input force applied to the front suspension results in a reacting force applied to the rear suspension with opposite direction. This is, if the front fork is compressed, the interconnection moment in the swinging arm will extend it. Consequently, for this kind of configuration, an energy transfer between the front and rear ends takes place, the rear suspension increases its relevance in the mode motion and 180° phase angles between the two

ends induce resonance.

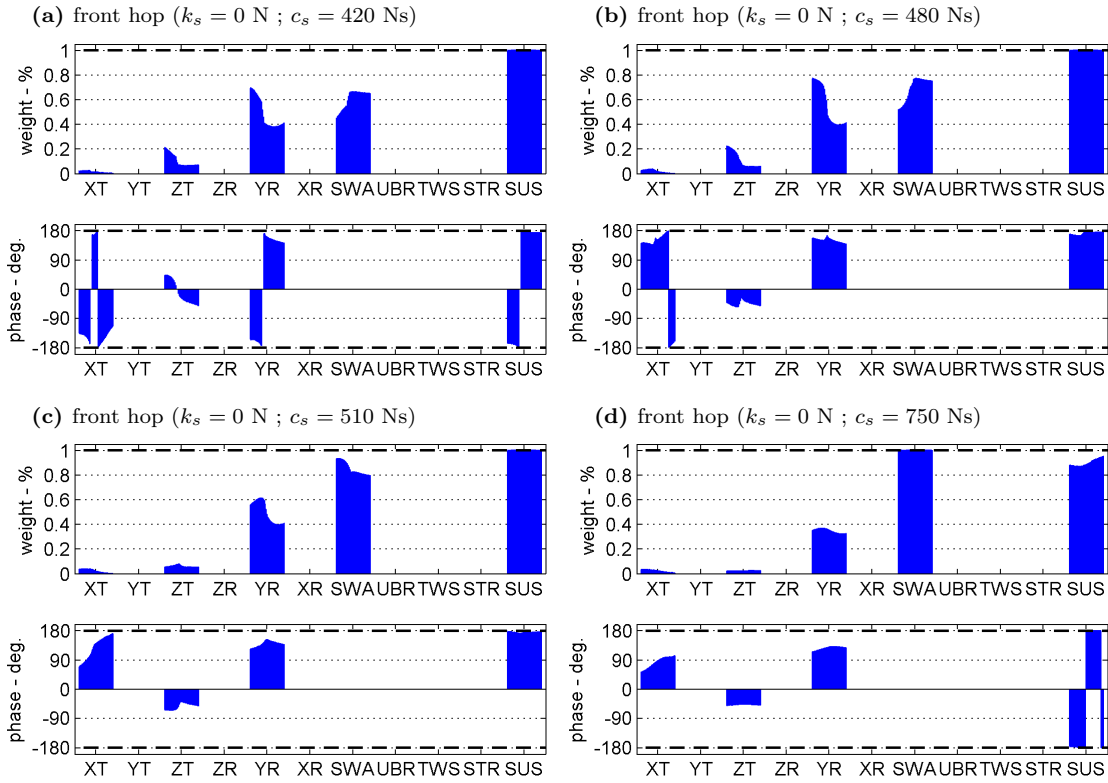


Figure 7.7: Front hop mode’s components for intermediate values of the interconnection damping coefficient and stiffness coefficient $k_s = 0$ N. The roll angle is set at 0° . The speed evolution of each component’s weight and phase is represented by the bars profile, varying the speed from left (10 m/s) to right hand side (80 m/s).

In terms of stability, the front hop eigenvalue real part approaches zero for an increment of c_s . Although that for the maximum value achieved in the simulations it does not cross the stability limit, there is a clear tendency of the front hop mode to become unstable for high values of the c_s coefficient. On the other hand, the resonance frequency is rapidly increased and it reaches values near 90 rad/s.

The interaction between modes for certain positive values of c_s happens for the three in-plane modes. For the bounce mode, this is not as visible as for the front hop and the pitch modes due to the high density of eigenvalues in the root loci interest area. Nevertheless, it can be observed in the eigenvector components plots.

In Fig. 7.8, the bounce mode eigenvectors evolution with the speed is shown for different positive values of c_s . For values of c_s comprised between 400 Ns and 700 Ns, this mode shows a clear influence of a pitch motion for higher values of the speed. The amplitude of the motorcycle vertical displacement (ZT) and swinging arm oscillation (SWA) are reduced with the speed increment whilst the pitch angle

amplitude (YR) is increased. The phase angle between the front (SUS) and the rear (SWA) suspension changes at higher speeds getting near to -180° , which is a main characteristic of pitch motion. For higher values of c_s (Fig. 7.10d), the motion of this mode is similar to that of the nominal configuration (see Fig. 7.3). The main eigenvector component is the motorcycle vertical displacement amplitude (ZT) and the pitch angle amplitude (YR) is reduced. The front suspension (SUS) and the swinging arm (SWA) amplitudes get relevance for all the speed range and their relative phase angle falls below 45° for high speeds, being almost zero for low speeds.

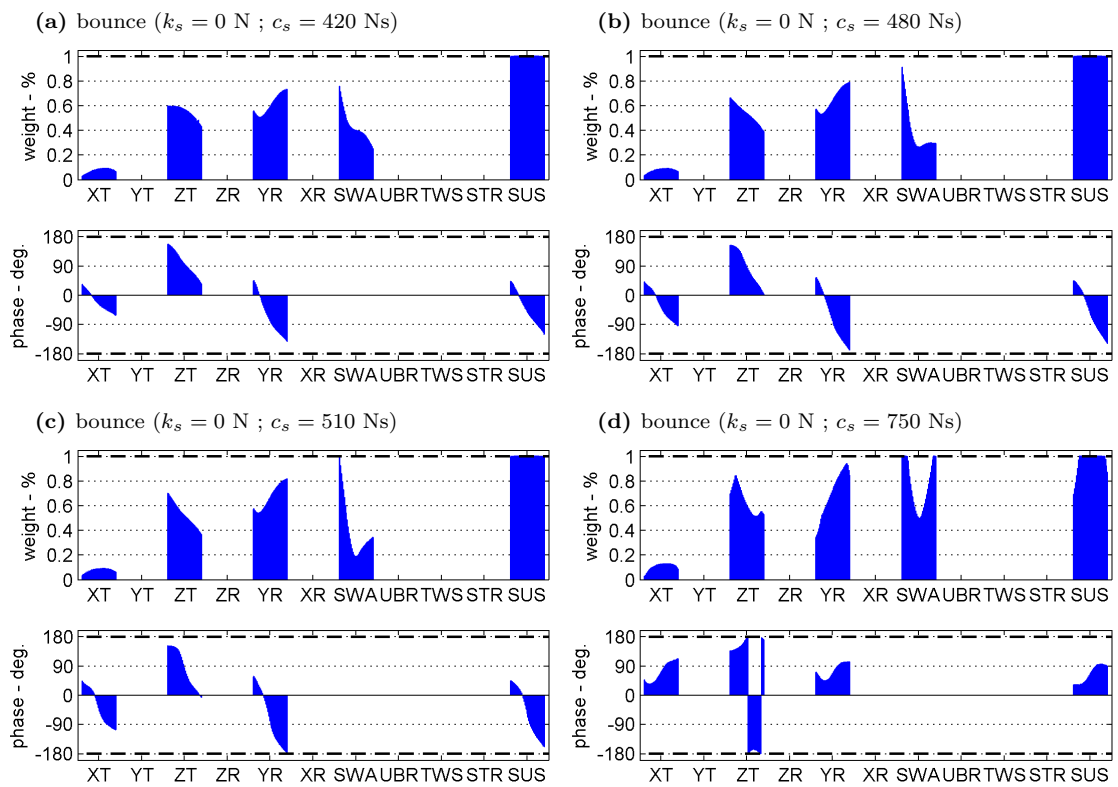


Figure 7.8: Bounce mode's components for intermediate values of the interconnection damping coefficient and stiffness coefficient $k_s = 0$ N. The roll angle is set to 0° . The speed evolution of each component's weight and phase is represented by the bars profile, varying the speed from left (10 m/s) to right hand side (80 m/s).

The root loci in Fig. 7.6b show that the bounce mode remains stable for values of c_s up to 1500 Ns, however it tends to become less damped for higher positive values while increasing its resonance frequency from 20 rad/s in the nominal configuration up to 35 rad/s for $c_s = 1500$ Ns.

The pitch mode, oppositely to the bounce mode, reduces its frequency from 45 rad/s to 20 rad/s when the interconnection damping coefficient value increases

from $c_s = 0$ Ns to $c_s = 1500$ Ns. However, its damping is also reduced reaching the imaginary axis in the root loci for the higher values of this coefficient. On the other hand, in Fig. 7.9, the interaction with bounce and front hop modes can be seen for low and middle c_s values. At low speed, the YR and the SWA amplitudes are reduced. For high speeds, the phase angle difference between the SUS and the SWA components is also reduced. For the higher interconnection damping coefficient values, these components become more regular for all the speed range and show a clearer pitch motion pattern. For $c_s = 1500$ Ns, in Fig. 7.3, a pure pitch motion pattern can be distinguished with predominant YR , SWA and SUS components and phase angles of 180° , 0° and 180° respectively.

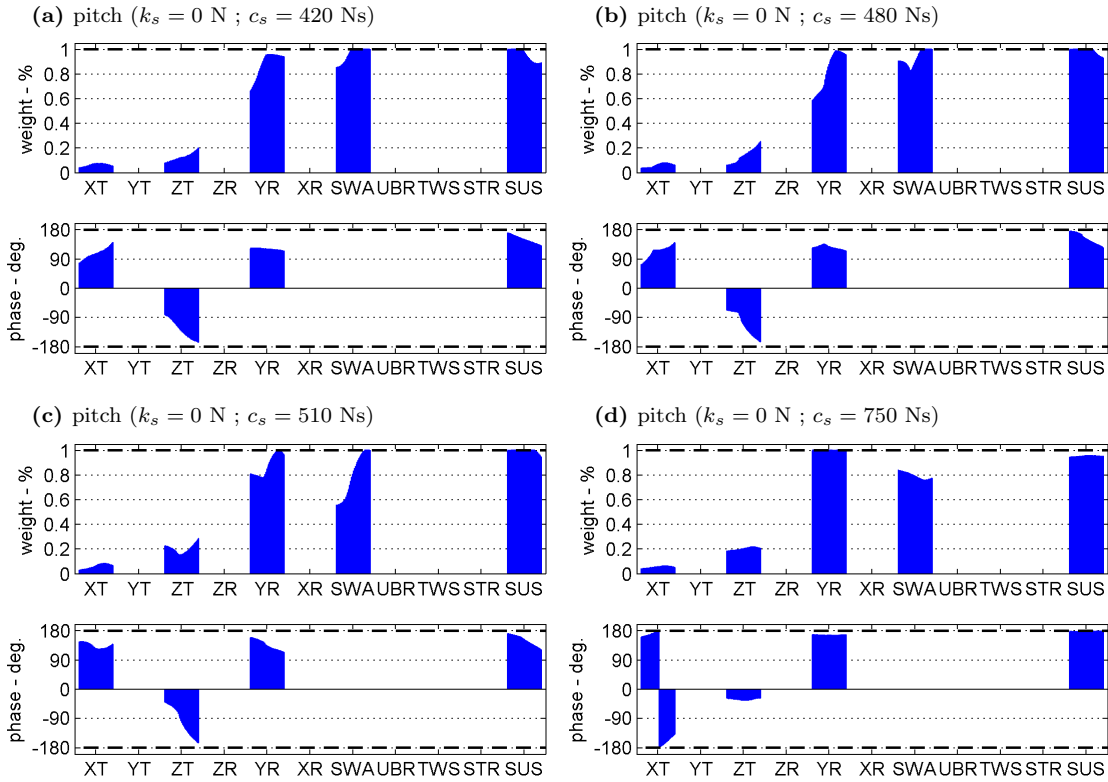


Figure 7.9: Pitch mode's components for intermediate values of the interconnection damping coefficient and stiffness coefficient $k_s = 0$ N. The roll angle is set to 0° . The speed evolution of each component's weight and phase is represented by the bars profile, varying the speed from left (10 m/s) to right hand side (80 m/s).

When the interconnection damping coefficient takes negative values, the evolution of the motorcycle normal modes with the speed is regular and they can be easily tracked for all the different c_s values. Figure 7.6a shows this eigenvalues evolution for interconnection damping coefficient ranging from $c_s = -1500$ Ns up to $c_s = 0$ Ns.

For these values, the pitch mode increases its resonance frequency and reduces

its damping, reaching an area in the root locus near the wobble mode. It stays stable for all the c_s values and forward speeds and does not change its behaviour. In Fig. 7.10a the pitch eigenvectors components are shown for a damping interconnection coefficient value of $c_s = -1500$ Ns. They do not differ much from the components at intermediate negative values of c_s , nor from that for nominal configuration in Fig. 7.3. The pitch angle amplitude (YR) is still the most relevant as well as the front (SUS) and rear (SWA) components suspensions oscillation, although these two components loose relevance in the overall mode motion.

The bounce mode resonance frequency and damping are reduced, reaching the instability region for high negative values over $c_s = -1500$ Ns (see Fig. 7.6a). Pure bounce motion is enhanced by negative interconnection damping coefficients as showed in Fig. 7.10c. Here, the main frame vertical translation amplitude (ZT) increases its relevance with respect to the rest of degrees of freedom. The phase angle difference between the front (SUS) and the rear (SWA) suspensions becomes almost zero whilst the phase angle difference between the (ZT) component and the SUS and SWA components remains around 180° for all the speed range.

The front hop mode evolves in similar manner for higher negative and positive values of c_s , as it can be observed in Fig. 7.6. In both cases, the resonance frequency is increased and the damping is reduced quickly, reaching 90 rad/s and approaching the stability limit for the extreme values of c_s . However, observing the eigenvector's components in Fig. 7.10e and Fig. 7.10f, a substantial difference is found in their phase angles. Their weights remains similar for positive and negative c_s values but their phases differ about 180° between the configuration with $c_s = 1500$ Ns and that with $c_s = -1500$ Ns. For the first configuration, the SUS phase difference with SWA phase was 180° for all the speed range. This implies that the front and rear ends oscillate in phase opposition while the main frame remains unaffected. Now, with $c_s = -1500$, this phase difference is almost zero, inducing a motion in which the main frame is unaffected whilst the front and rear suspension highly oscillate in phase. Oppositely to the case of positive interconnection coefficients, for negative values of c_s , a compression force input in the front fork results in a compression moment in the rear swinging arm. Then, in phase oscillations of both ends are prone to resonate, and the front hop mode will show this characteristic.

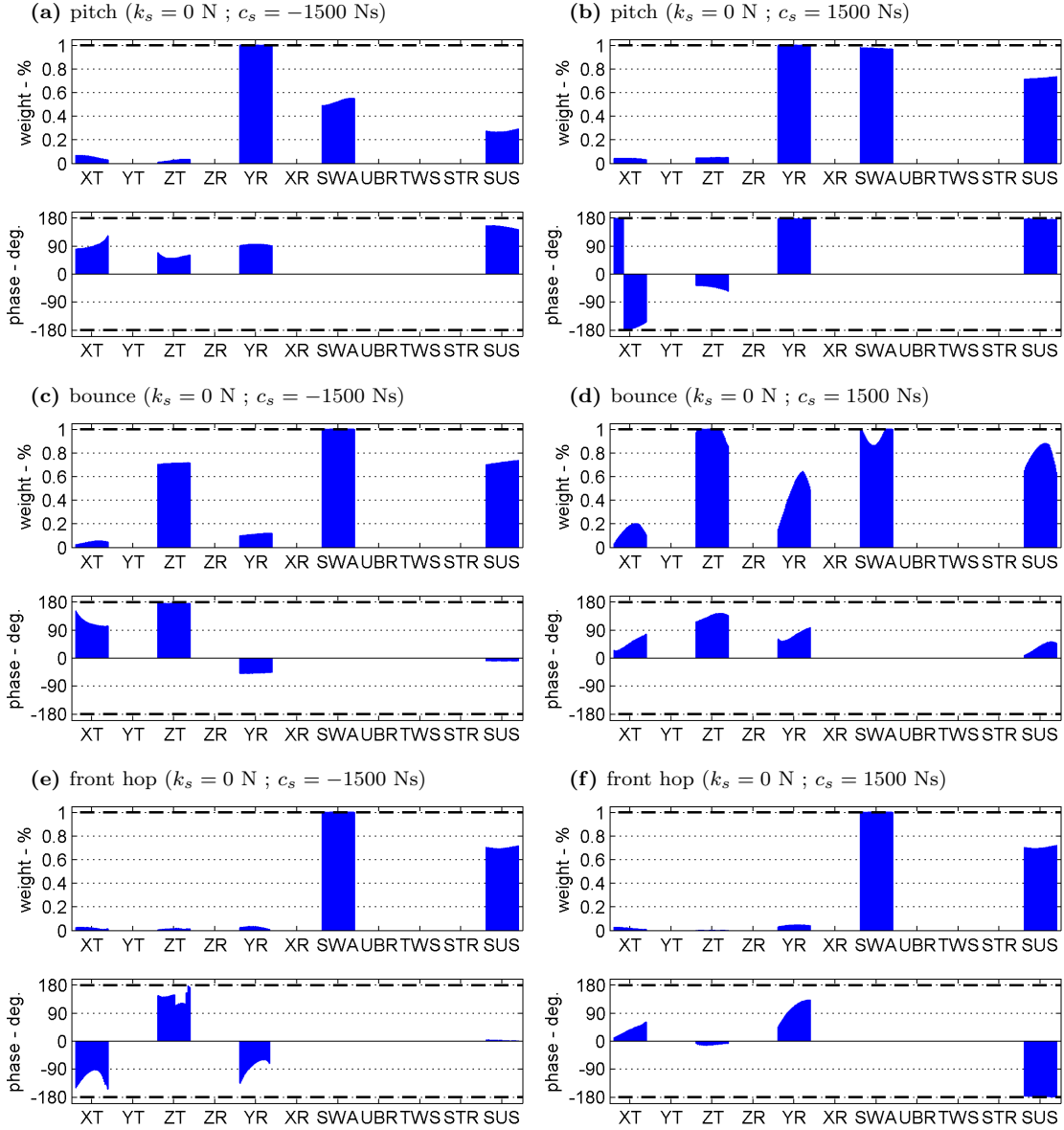


Figure 7.10: In-plane normal modes' components for the maximum and minimum values of damping interconnection coefficient for a roll angle of 0° . On the left-hand side $c_s = -1500 \text{ Ns}$. On the right-hand side $c_s = 1500 \text{ Ns}$. The interconnection stiffness coefficient is set at $k_s = 0 \text{ N}$. The speed evolution of each component weight and phase is represented by the bars profile, varying the speed from left (10 m/s) to right hand side (80 m/s).

Figure 7.10 shows the difference of the in-plane modes eigenvectors components for the two interconnection damping coefficient extreme values, $c_s = -1500$ Ns and $c_s = 1500$ Ns. It can be observed that a configuration with positive c_s values increases the pitch characteristics in any in-plane mode whilst a negative c_s value reinforces the bounce motion in these modes.

For $c_s = 1500$ Ns, the bounce mode increases the weight of its *YR* component whilst the pitch mode becomes in a pure pitch motion. This is, the three main degrees of freedom are the main frame rotation about the *Y* axis (*YR*), the swinging arm angle (*SWA*) and the front fork displacement (*SUS*), being their relative phase angles 180° , 0° and 180° respectively. This represents a motion in which the main frame pitches to the front simultaneously to the front fork being compressed and the swinging arm extended and vice versa.

On the negative extreme, for a value of $c_s = -1500$ Ns, the weights of the *SUS* and *SWA* components of the pitch normal mode are reduced. This means that their oscillations amplitudes decrease due to the interconnection forces opposing this motion. On the other hand, the bounce components represent a pattern of almost pure bounce motion. Although a small *YR* oscillation persists the main components are the main frame vertical translation (*ZT*), the front suspension compression (*SUS*) and the swinging arm rotation (*SWA*), with relative phase angles of 180° , 0° and almost 0° respectively. In this motion, the main frame moves down vertically simultaneously to the front and the rear suspensions being compressed, whilst it moves up when both suspensions are extended.

Regarding the front hop mode, it can be said that any interconnection damping parameter value induces the *SWA* amplitude to reach a high weight in the overall motion of the mode, due to the energy transfer between the front and rear ends. Positive values of c_s coefficient introduce a phase angle of 180° . Negative values of this coefficient reduce the phase angle to almost 0° . In the nominal configuration, the front hop mode consists in a shaking of the front wheel with little bounce, pitch and swinging arm oscillations. However, it is so highly damped that during normal running it is hardly noticed on the motorcycle's dynamics. For large positive and negative values of the interconnection damping coefficient, this mode becomes less damped and it approaches the instability region in the root locus. The vehicle's

motion in these cases consists in a violent shaking of the front and rear ends while the main frame remains almost unaffected. Depending on the c_s sign, the front and rear ends would oscillate in phase ($c_s < 0$) or in phase opposition ($c_s > 0$).

Positive and negative values of the interconnection damping coefficient displace the front hop eigenvalues towards the right hand side on the imaginary plane in the root locus. In the case of the pitch and bounce modes, the negative values of this coefficient produce a similar effect as could be expected. For positive values of c_s there exist a range for which these two modes damping can be increased. However, from certain values on (about $c_s = 500$ Ns) the influence of the front hop mode in the degrees of freedom involved in the pitch and bounce modes becomes relevant. This produces that the eigenvalues real part of these modes turn towards smaller values, becoming less damped for high values of c_s . The pitch mode is the most affected crossing the $X0$ axis for values above $c_s = 1500$ Ns.

7.2 Small roll angle

When the motorcycle is cornering, the in-plane and out-of-plane normal modes get coupled due to the appearing forces in the wheels contact point, which are misaligned with the motorcycle symmetry plane. The degrees of freedom typically involved in the motion of the in-plane modes are also involved in the out-of-plane modes and vice versa. In cornering conditions (the motorcycle is leant) these forces not only affect the degrees of freedom in the symmetry plane but also those out of this plane. This means that the interconnection structure will affect the out-of-plane normal modes. The evolution of the root loci for different values of these interconnection parameters c_s and k_s , must be studied carefully. When the eigenvalues evolution is observed for the different interconnection parameter values, a similar behaviour to that found on the straight running condition is found. The different roots are overlapped and their modes are combined forming new modes as the interconnection parameters are varied. For roll angles different to zero, this affects the bounce and the rider shake modes for k_s variations. When the c_s parameter is varied, the modes affected are the pitch and the bounce.

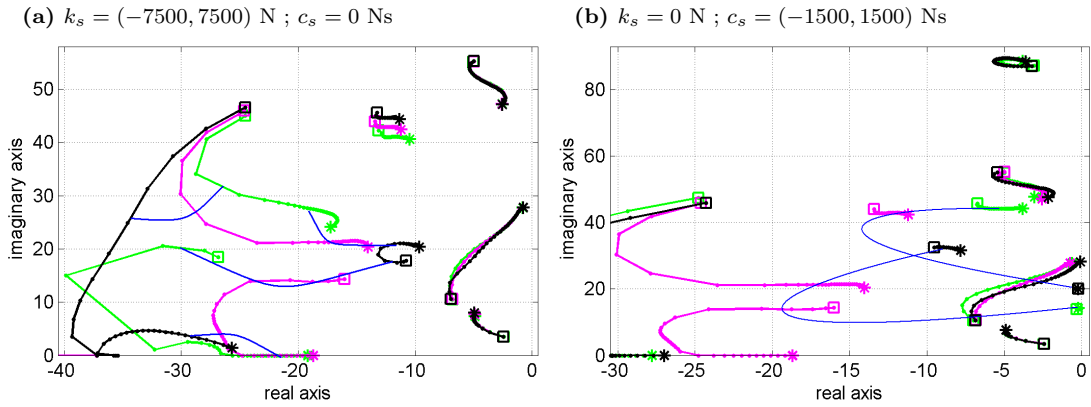


Figure 7.11: Root loci for both stiffness and damping coefficients variations. The roll angle is set to 15° and the speed is increased from 10 m/s (\square) to 80 m/s ($*$). Only modes for minimum (green), nominal (magenta) and maximum (black) values are fully plotted, whilst their evolution is represented by a blue solid line. a) Interconnection stiffness coefficient varies from $k_s = -7500$ N up to $k_s = 7500$ N. b) Interconnection damping coefficient varies from $k_s = -1500$ Ns up to $k_s = 1500$ Ns.

7.2.1 Variation of interconnection stiffness coefficient

Figure 7.11 represents the two different root locus for the motorcycle at a roll angle of 15° . The speed increase is shown by dotted lines ranging from 10 m/s (\square) up to 80 m/s ($*$). Figure 7.11a shows the modes evolution for the minimum ($k_s = -7500$ N in green), nominal ($k_s = 0$ N in magenta) and maximum ($k_s = 7500$ N in black) values of the interconnection stiffness coefficient. Intermediate eigenvalues have been removed from the plot for clarity. A blue solid line represents the mean trajectory followed by each normal mode when k_s is increased from $k_s = -7500$ N to $k_s = 7500$ N. For this roll angle, the out-of-plane eigenvalues are not affected in a significant manner when the interconnection stiffness coefficient is varied. Except for the rider shake mode, which presents substantial differences for positive and negative k_s values. With a value of $k_s = -7500$ N this mode does not show any remarkable difference compared to the nominal configuration case, except for the minor changes for the medium and high speeds range. For these speeds, the frequency is increased from 20 rad/s up to 28 rad/s, being the damping also increased. On the other hand, a bigger difference is observed for positive interconnection stiffness coefficient values. For $k_s = 7500$ N, the rider shake mode reduces its frequency and increases its damping quickly with the speed rise, becoming in some points overcritical. This mode shows a strong influence on the bounce mode. This can be observed in their eigenvector components for the nominal configuration presented in Fig. 7.12c. At

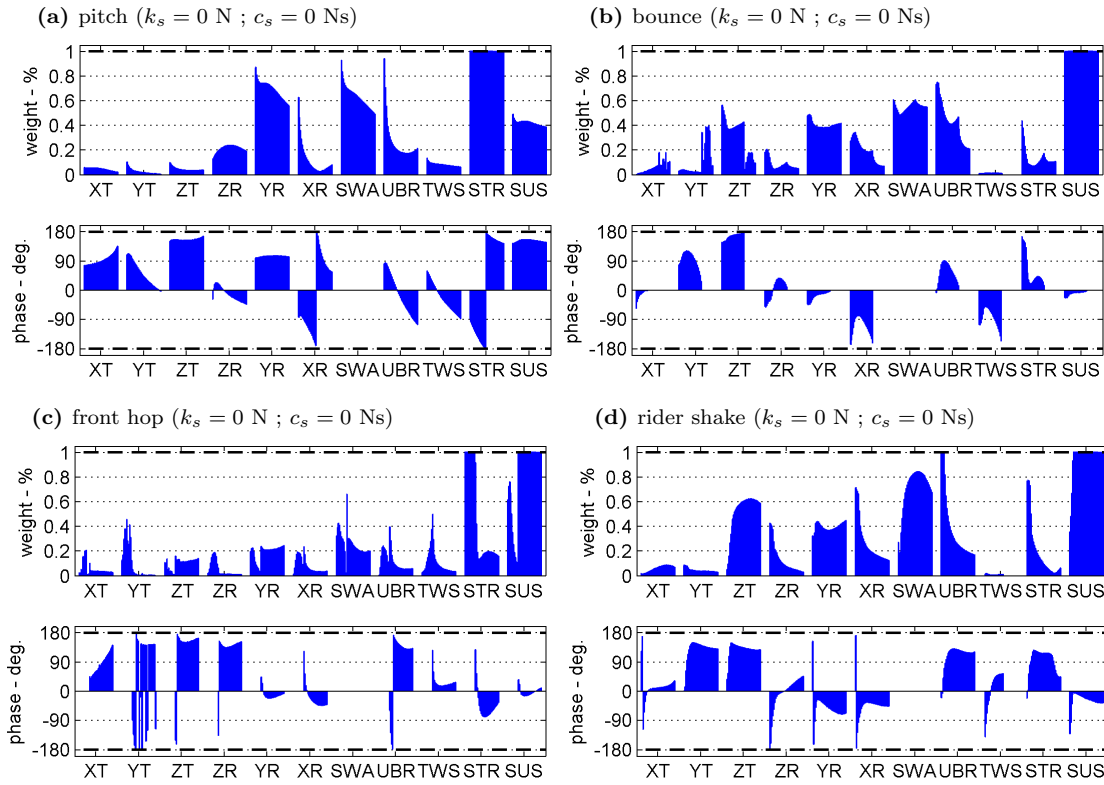


Figure 7.12: Components of normal modes affected by the interconnection coefficients at a roll angle of 15° for the nominal configuration.

low speeds, the ZT , SWA and SUS components of the rider shake mode have small weight while the UBR , XR and STR amplitudes are the main degrees of freedom involved in the motion. This changes for medium and high speeds for which the ZT , SWA and SUS components rapidly reach high relevance whilst the UBR , XR and STR components reduce their weights. The rider shake mode presents a motion pattern in the medium-high speeds range similar to that of the bounce mode for low and medium speeds. In Fig. 7.12b, the bounce mode's component does not have a regular behaviour at high speed, this is due to the fact that for those speeds this normal mode becomes overcritical and nonoscillatory.

The bounce mode for the nominal configuration starts at a frequency of 25 rad/s and rapidly decays, reducing its damping, until it becomes overcritical. Positive values of the interconnection damping coefficient result in a similar behaviour with an increase of its damping. However, negative values of k_s increase its frequency and reduce drastically its damping, concentrating all its eigenvalues in a smaller area within the root locus.

Looking at Fig. 7.13, it can be noticed that k_s affects the rider shake and bounce

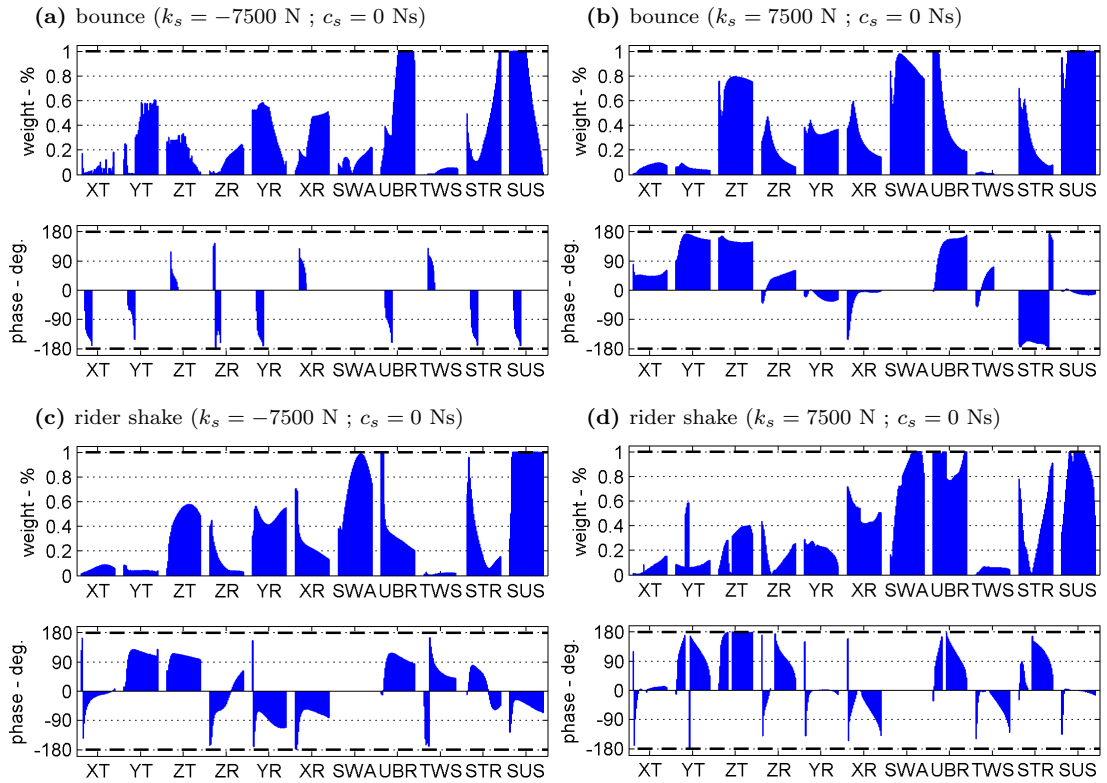


Figure 7.13: Bounce and rider shake modes' components for the maximum and minimum values of the stiffness interconnection coefficient for a roll angle of 15° . On the left-hand side $k_s = -7500$ N. On the right-hand side $k_s = 7500$ N. The interconnection damping coefficient is set to $c_s = 0$ Ns. The speed evolution of each component's weight and phase is represented by the bars profile, varying the speed from left (10 m/s) to right hand side (80 m/s).

modes in a similar manner. Positive values of k_s emphasizes the pure motion associated to each of these two modes. This is, the *UBR*, *XR* and *STR* components weights are increased for the rider shake mode whilst the *ZT*, *SWA* and *SUS* component reach major relevance in bounce mode. On the other hand, the negative values of this coefficient increase the relevance of the bounce motion in the rider shake mode, whilst the weights of the degrees of freedom associated to the rider shake are enhanced in the bounce mode.

Regarding to the pitch mode, it does not show a major change with respect to the variation of the interconnection stiffness coefficient value. Only its frequency is slightly affected. Positive values of k_s increase the resonance frequency and negative values decrease it. A variation of the parameter from $k_s = -7500$ N to $k_s = 7500$ N produces a variation in the frequency of about 4 rad/s.

Finally, the front hop mode is highly damped and does not appear in the interest area of the root locus, being its effects negligible for the motorcycle's motion.

7.2.2 Variation of interconnection damping coefficient

Figure 7.11b shows the motorcycle's root loci evolution for various interconnection damping coefficient values ranging from $c_s = -1500$ Ns up to $c_s = 1500$ Ns. Again, the out-of-plane modes remain almost unaffected except for the rider shake. However, in this case, it highly increases its damping when any positive or negative values of k_s are introduced in the model and does not affect in a significant manner the motorcycle's dynamics. Weave and wobble mode are also slightly affected, finding that they become slightly less stable for positive c_s values and more stable for negative values, in both cases for medium-high speed range. At high speeds cases, the weave eigenvalues approach the imaginary axis, nevertheless it stays stable for all the speed range. For low forward speed, weave mode becomes more stable for any value of the interconnection stiffness coefficient and wobble's damping is insignificantly reduced.

The bounce mode evolves with the variation of the interconnection damping coefficient as it did for the straight running conditions. For high negative values of c_s , it can reach the stability limits. The frequency in this case remains almost unaffected. For the positive values of this coefficient the bounce mode frequency is increased up to 38 rad/s and its damping is highly reduced. Nevertheless it remains more stable than the out-of-plane main modes. In terms of eigenvector components, the effects introduced by the interconnection damping coefficient are similar to those found in the straight running conditions. Negative values of c_s intensify the pure bounce motion. Figure 7.14c presents a clear pattern of pure bounce motion where ZT , SWA and SUS weights have major relevance being their phase angles 180° , 0° and 0° respectively, whilst the out-of-plane components weights are much smaller. As it has been stated in the previous section, positive values of c_s oppose to the bounce motion, this implies a reduction of the bounce main components and an increase of the weights of out-of-plane degrees of freedom. In this case, the steering angle oscillation (STR) becomes the main component in the motion of the bounce mode.

The pitch mode also evolves in a similar manner than that for the straight running conditions case. Although small positive values of c_s can improve the stability of this mode, higher values of this coefficient result in a drastic destabilization of it and in a reduction of its resonance frequency. Negative c_s values slightly increase

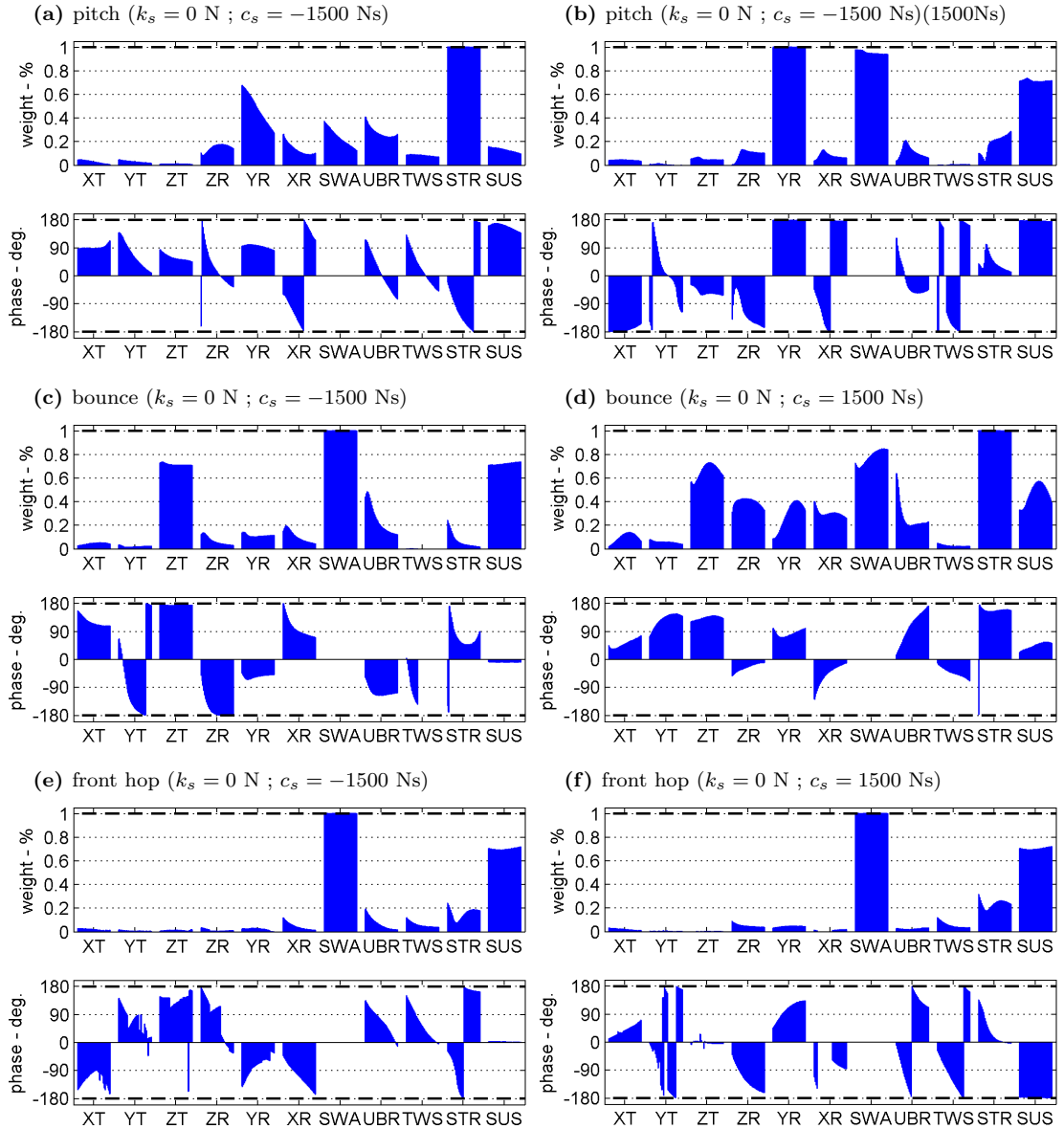


Figure 7.14: In-plane normal modes' components for the maximum and minimum values of the damping interconnection coefficient for a roll angle of 15° . On the left-hand side $c_s = -1500$ Ns. On the right-hand side $c_s = 1500$ Ns. The interconnection stiffness coefficient is set to $k_s = 0$ N. The speed evolution of each component weight and phase is represented by the bars profile, varying the speed from left (10 m/s) to right hand side (80 m/s).

the frequency of the pitch mode and reduce its damping, however it remains stable, near to the wobble region. The interconnection damping coefficient influences the eigenvector components in an opposite manner as it does with the bounce motion. Positive values of this coefficient intensify the pure pitch motion (see Fig. 7.14b), being *YR*, *SWA* and *SUS* the main component with relative phase angles of 180° for *YR* and *SUS* and 0° for *SWA*. Negative values of c_s (see Fig. 7.14a) oppose the pitch motion and its main components get overtaken by the out-of-plane ones, being the steering the most relevant.

Under straight running conditions, the front hop mode evolves in a similar way for positive and negative values of c_s . It quickly reaches areas in the root locus near to the imaginary axis (although the damping reduction is smaller than for the zero roll angle case), and increases drastically its averaged resonance frequency up to 85 rad/s. The evolution with the speed is very similar for high c_s values regardless of its sign. The main difference is found in the eigenvector components in Fig. 7.14e and Fig. 7.14f. In both cases the main components are the front suspension (*SUS*) and the rear swinging arm (*SWA*) being the rest of the components weights smaller. Positive values of c_s induce a phase opposition oscillation of these degrees of freedom whilst the negative values impose an in-phase resonance of them.

7.3 Medium roll angle

For a 30° roll angle, the variation of the normal modes with speed for the different interconnection parameters has a similar behaviour to that found for smaller roll angles. Although still some differences can be found.

7.3.1 Variation of interconnection stiffness coefficient

The effect of the interconnection stiffness coefficient becomes relevant for the rider's shake and the bounce mode. They interact similarly as they did for the small roll angle case, and the changes in their motions depend in a similar manner on the k_s coefficient. In Fig. 7.15a it can be seen the evolution of the bounce and the rider shake modes in the root locus for the minimum ($ks = -7500$ N in green), nominal ($ks = 0$ N in magenta) and maximum ($ks = 7500$ N in black) values of

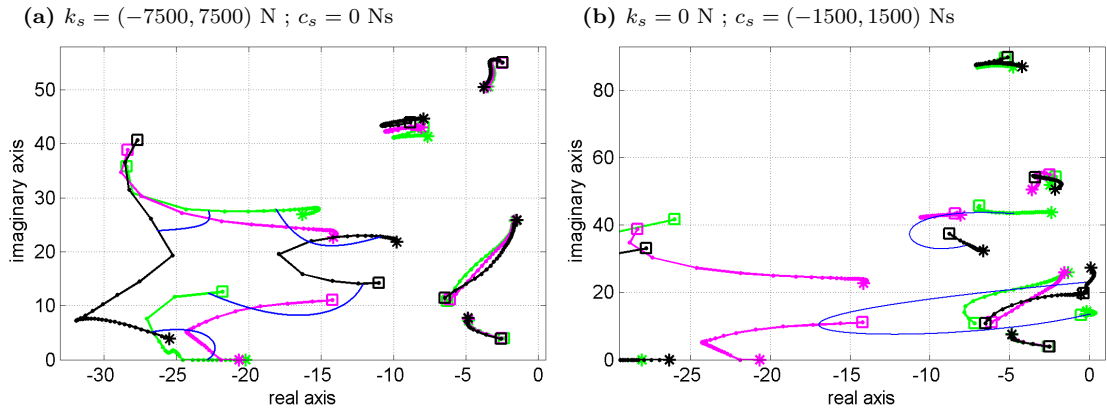


Figure 7.15: Root loci for both stiffness and damping coefficients variations. The roll angle is set at 30° and the speed is increased from 10 m/s (\square) to 80 m/s ($*$). Only modes for the minimum (green), nominal (magenta) and maximum (black) values are fully plotted, whilst their evolution is represented by a blue solid line. a) Interconnection stiffness coefficient varies from $k_s = -7500$ N up to $k_s = 7500$ N, with $c_s = 0$ Ns. b) Interconnection damping coefficient varies from $c_s = -1500$ Ns up to $c_s = 1500$ Ns, with $k_s = 0$ N.

the interconnection stiffness coefficient. The effect of the interconnection stiffness coefficient in these modes' motion patterns can be appreciated in Fig. 7.17. The positive values of k_s enhance the typical motion of each of these modes. For the bounce mode, ZT , SWA and SUS components reach main relevance with phase angles corresponding to pure bounce oscillation, this is about 180° for the main frame vertical displacement, and 0° for the front and rear suspension. The rider shake mode increases its roll amplitude (XR) and its rider oscillation (UBR) for the positive coefficient values. For the negative stiffness interconnection coefficients the rider shake mode presents bounce motion with certain pitch oscillation, whilst the bounce mode becomes closer to a pitch motion.

The pitch mode is also affected by the k_s coefficient variation. Its averaged resonance frequency is modified proportionally to the k_s values from 41 rad/s ($k_s = -7500$ N) to 45 rad/s ($k_s = 7500$ N). The rest of the normal modes are not substantially modified by the interconnection stiffness coefficient.

7.3.2 Variation of interconnection damping coefficient

Similarly to the case of 15° roll angle, the interconnection damping coefficient mostly affects the pitch, bounce and front hop modes. Although it also modifies the rider shake mode, it is rapidly damped becoming overcritical for most of the speed range and for all values of c_s . Now, it is not visible in the root loci in Fig. 7.15b. Some

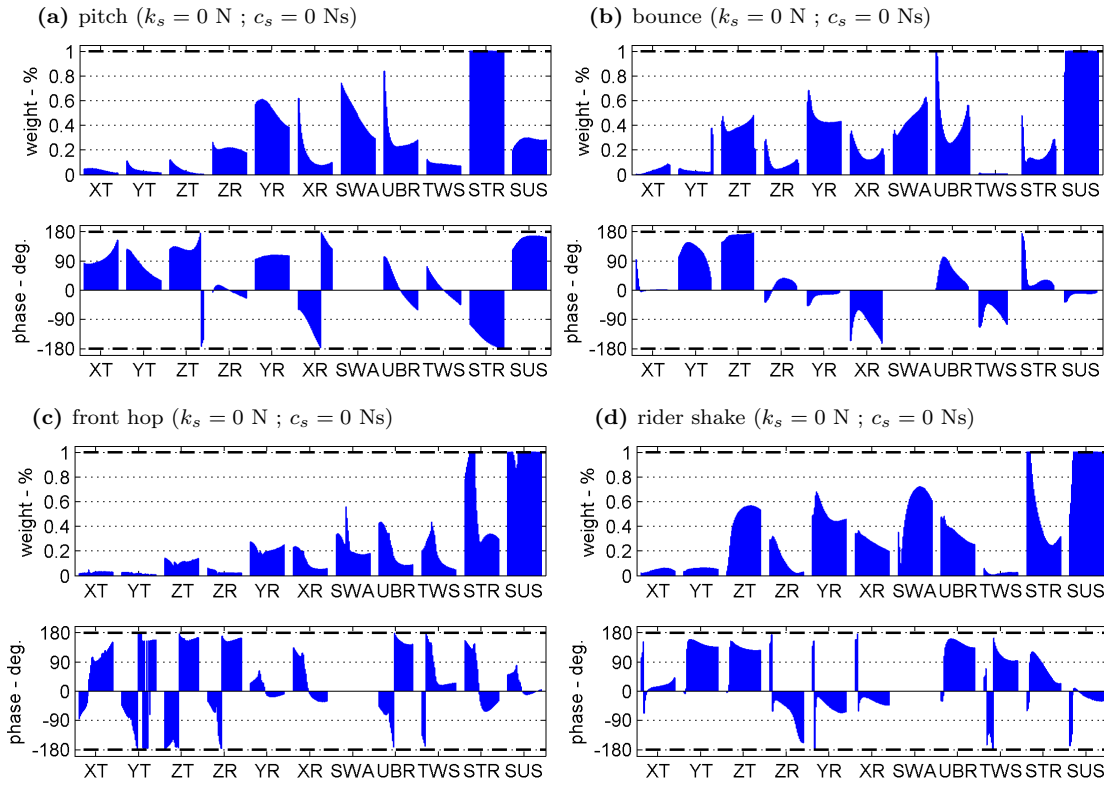


Figure 7.16: Components of the normal modes affected by the interconnection coefficients at a roll angle of 30° for the nominal configuration.

differences can be found for the pitch and the bounce modes whilst the front hop mode evolves similarly as in previous cases. This is, it increases its frequency and reaches damping values closer to the imaginary axis for both positive and negative values of c_s . However, for the minimum and maximum values of c_s , this mode is more damped than in the previous roll angle cases. Examining Fig. 7.18e and Fig. 7.18f, a similar behaviour of this mode with respect to the c_s coefficient values is observed. Positive values result in a phase opposition resonance of the front and rear suspensions whilst negative values of c_s make the front and rear ends resonate in phase. The rest of the eigenvector components are secondary except for the steer angle amplitude (STR) which is increased with respect to the previous roll angle cases.

The pitch mode for the nominal configuration, for a roll angle of 30° , is influenced by the out-of-plane dynamics as it can be observed in Fig. 7.16a, where the STR component has a main relevance. In Fig. 7.18a the eigenvector components are plotted for $c_s = -1500$ Ns. It can be seen that the pitch motion is penalized for this configuration and the components associated to it (YR , SWA and SUS) lose

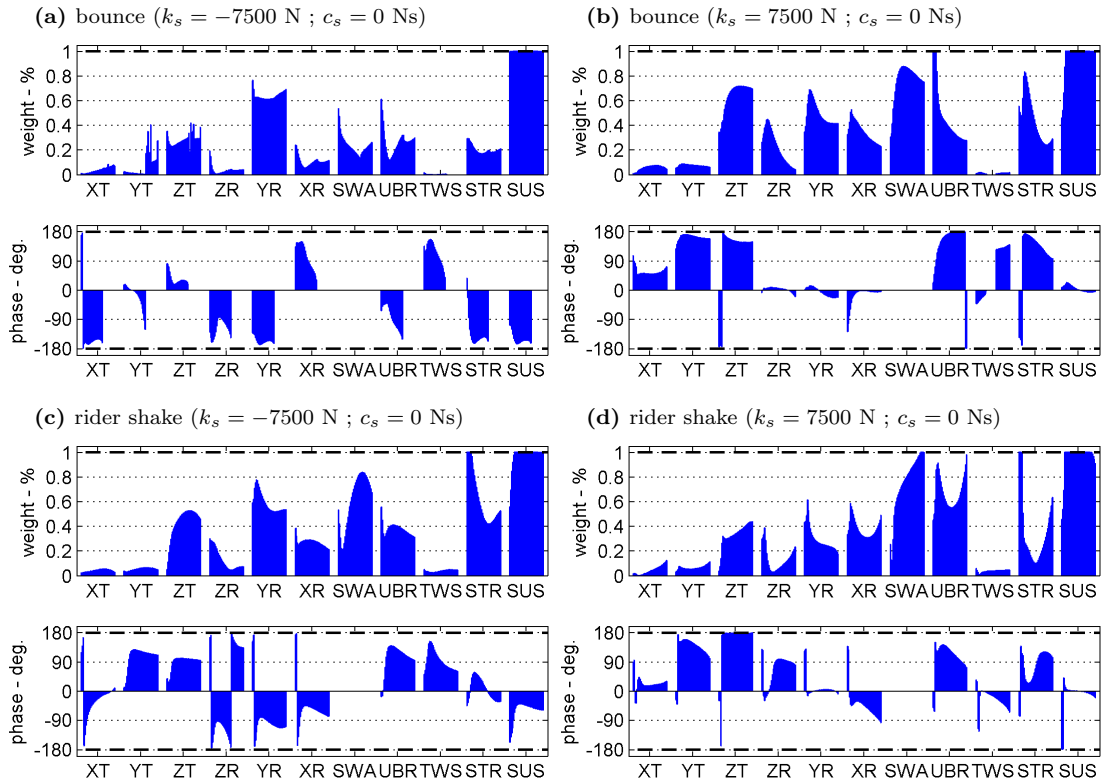


Figure 7.17: Bounce and rider shake modes' components for the maximum and minimum values of the stiffness interconnection coefficient for a roll angle of 30° . On the left-hand side $k_s = -7500$ N. On the right-hand side $k_s = 7500$ N. The interconnection damping coefficient is set to $c_s = 0$ Ns. The speed evolution of each component's weight and phase is represented by the bars profile, varying the speed from left (10 m/s) to right hand side (80 m/s).

its predominant role whilst the out-of-plane dynamics become relevant, being the steering angle (*STR*) oscillation predominant on it. On the other hand, Fig. 7.18b shows the pitch mode pattern of motion closer to a pure pitch oscillation for $c_s = 1500$ Ns. However, for this roll angle, it can be seen how the out-of plane components are more predominant than in the previous situation, mostly in the high speed range. In terms of frequency and damping, Fig. 7.15b shows how for this roll angle, their variation is restricted to a reduced area. In this case, the pitch mode is not coupled with the bounce nor the front hop mode at any value of the c_s coefficient. The different mode branches for the speed evolution stay nearer to that corresponding to the nominal configuration ($c_s = 0$) and they keep a substantial damping.

The bounce mode evolution with interconnection damping coefficient for a 30° roll angle is similar to that for smaller roll angles cases. However, there is a difference now. Both positive and negative c_s values increase the bounce mode averaged resonance frequency and reduce its damping. For absolute values of c_s equal and

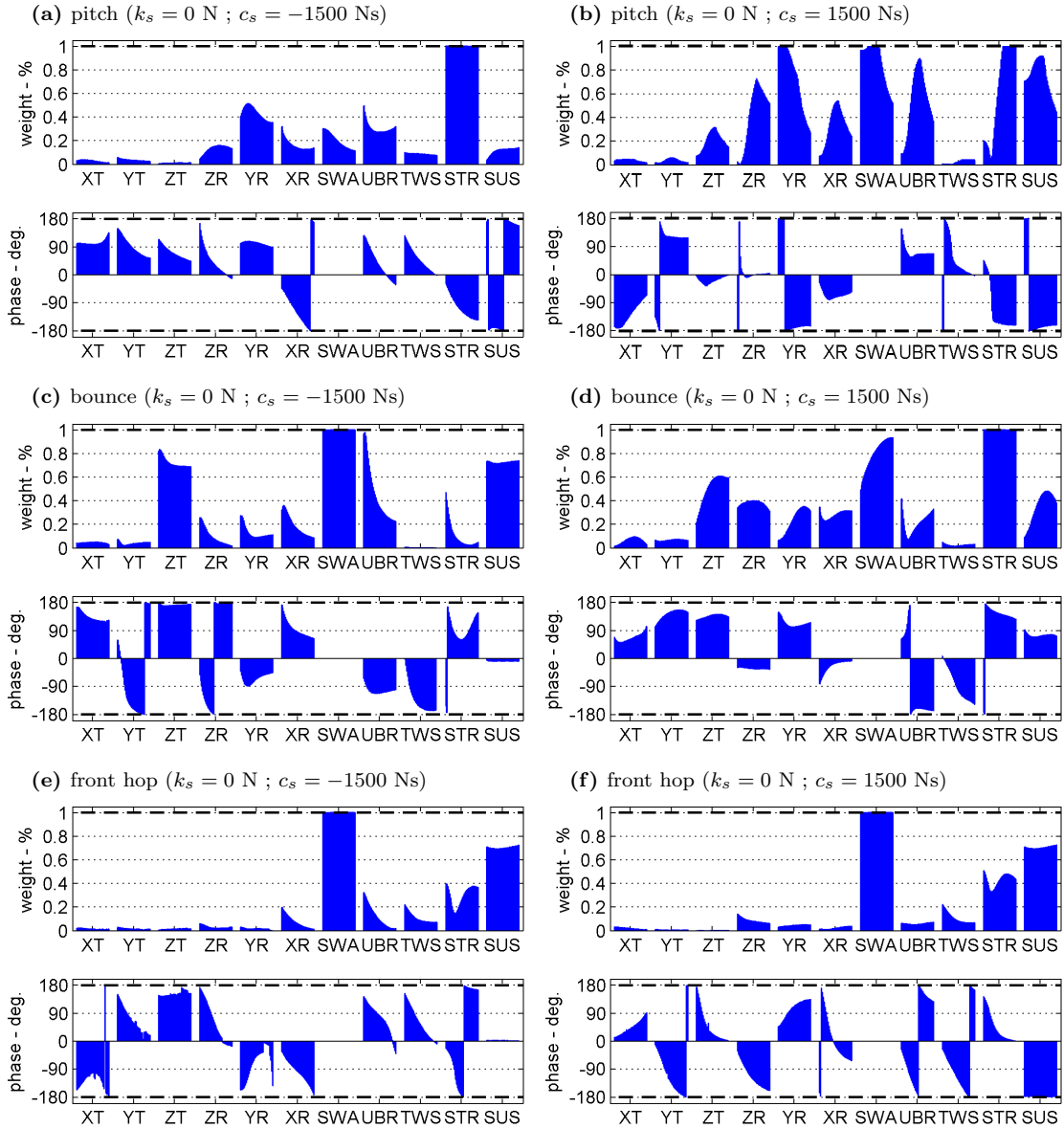


Figure 7.18: In-plane normal modes' components for the maximum and minimum values of the damping interconnection coefficient for a roll angle of 30° . On the left-hand side $c_s = -1500$ Ns. On the right-hand side $c_s = 1500$ Ns. The interconnection stiffness coefficient is set to $k_s = 0$ N. The speed evolution of each component weight and phase is represented by the bars profile, varying the speed from left (10 m/s) to right hand side (80 m/s).

larger than 1500 Ns, the bounce mode eigenvalue's real parts become positive for a wide range of speeds. Thus, the motorcycle clearly becomes unstable for this configuration.

Regarding to the eigenvector components, negative values of the c_s coefficient produce a recognizable bounce pattern with minor influence of the out-of-plane dynamics. On the other hand, positive c_s values oppose to the bounce motion and consequently the out-of-plane components weights become more relevant, being the steering angle oscillation (*STR* component) the larger of them. Nevertheless, *ZT*, *SWA* and *SUS* components oscillation keep their presence and the bounce motion can be still recognized.

For this roll angle, weave and wobble modes are affected in a more significant manner. Positive values of c_s increase both modes stability at low speeds and decrease their stability at high speeds. For negative values of c_s , the wobble mode is less stable than for the nominal case for all the speed range whilst the weave mode's stability is improved for low-medium forward speeds. Both modes maintain their averaged resonance frequencies and remain stable for the entire speeds range.

7.4 High roll angle

For a roll angle of 45° , the behaviour of the normal modes with respect to the speed and the interconnection coefficients variation is similar to that for a 30° roll angle.

7.4.1 Variation of interconnection stiffness coefficient

Figure 7.19a, shows the eigenvalues evolution with forward speed for the minimum ($ks = -7500$ N in green), nominal ($ks = 0$ N in magenta) and maximum ($ks = 7500$ N in black) values of k_s for a 45° roll angle, it is similar to that in Fig. 7.15a, which represents the root behaviour for a roll angle of 30° . Slightly differences can be observed between them, however, the overall influence of the interconnection stiffness coefficient is similar.

The interaction between bounce and rider shake modes is as well similar. In both modes, their characteristic eigenvector components' amplitudes increase with a positive k_s values and reduce with negative values. The out-of-plane components

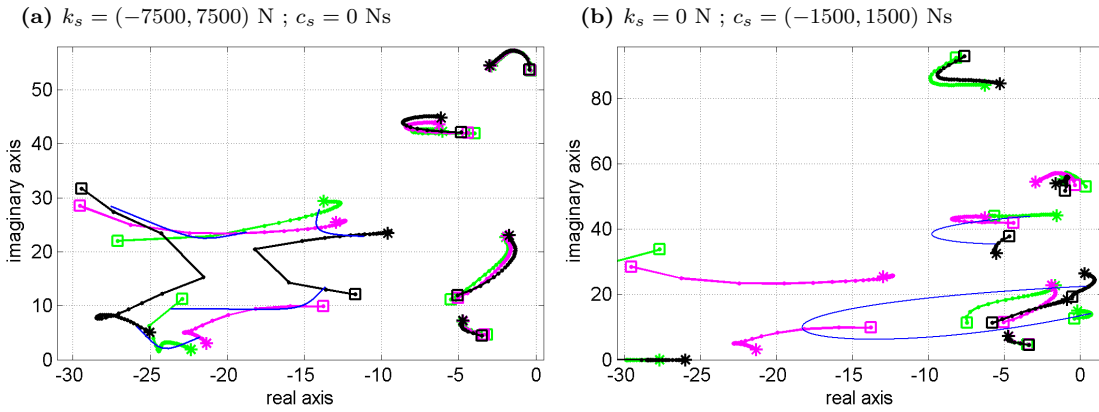


Figure 7.19: Root loci for both stiffness and damping coefficients variations. The roll angle is set to 45° and the speed is increased from 10 m/s (\square) up to 80 m/s ($*$). Only modes for the minimum (green), nominal (magenta) and maximum (black) values are fully plotted, whilst their evolution is represented by a blue solid line. a) Interconnection stiffness coefficient varies from $k_s = -7500$ N up to $k_s = 7500$ N, with $c_s = 0$ Ns. b) Interconnection damping coefficient varies from $c_s = -1500$ Ns up to $c_s = 1500$ Ns, with $k_s = 0$ N.

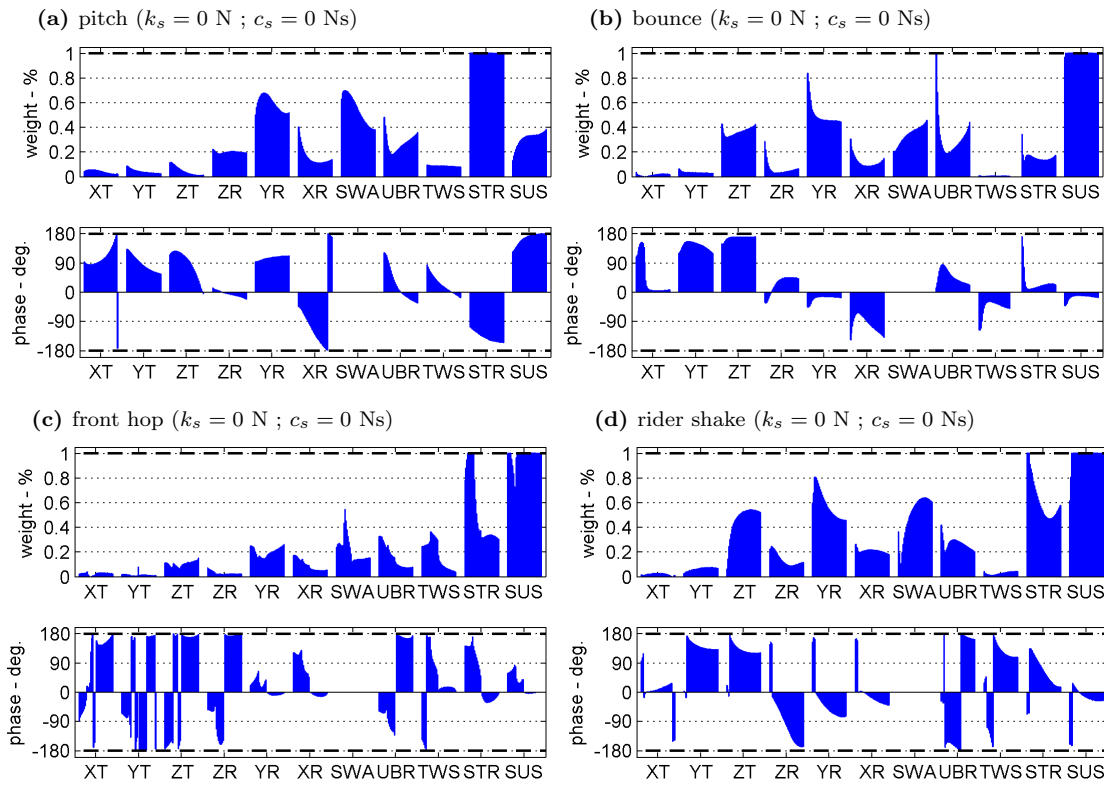


Figure 7.20: Components of the normal modes affected by the interconnection coefficients at a roll angle of 45° for the nominal configuration.

are now more relevant in both cases. On the other hand, the pitch mode modifies its average resonance frequency in a direct relation with the coefficient values. Finally, weave and wobble modes remain practically unaffected.

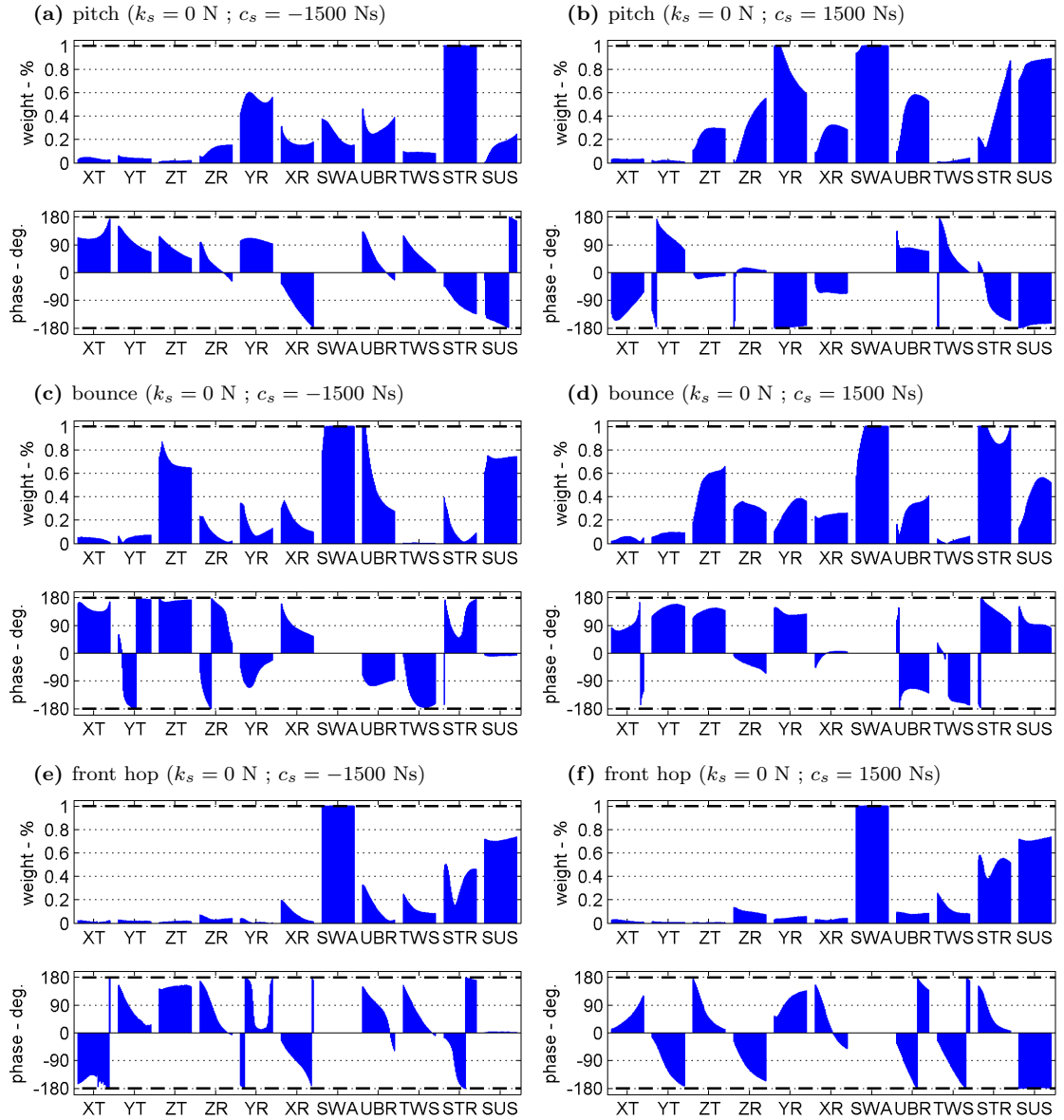


Figure 7.21: In-plane normal modes' components for the maximum and minimum values of the damping interconnection coefficient for a roll angle of 45° . On the left-hand side $c_s = -1500 \text{ Ns}$. On the right-hand side $c_s = 1500 \text{ Ns}$. The interconnection stiffness coefficient is set to $k_s = 0 \text{ N}$. The speed evolution of each component weight and phase is represented by the bars profile, varying the speed from left (10 m/s) to right hand side (80 m/s).

7.4.2 Variation of interconnection damping coefficient

When the c_s coefficient is varied (see Fig. 7.19b), similar modes behaviour as in previous section can be expected, except for the wobble mode. This mode becomes more stable for positive values of c_s whilst the negative values of this coefficient induce mode instability at low speed. The pitch mode shows similar tendency as before but now its damping is reduced for all the interconnection damping coefficient configuration and speeds. The bounce mode evolves similarly, although for the case of 45° , this mode is more unstable for the higher positive and negative values of c_s at almost all the speed range. Finally, it is worthy to mention that the front hop mode increases its frequency and reduces its damping for both positive and negative values of the interconnection damping coefficient, although its eigenvalues for the minimum and maximum values of c_s are slightly more stable than for the smaller roll angles cases. In terms of eigenvectors, the effect of the interconnection damping coefficient is similar to the smaller roll angles. c_s negative values enhance the bounce motion and, in the front hop mode, the front and rear ends resonate in phase. For positive values of this coefficient, the resonance of the front and rear suspensions in the front hop mode occurs in phase opposition and pitch mode oscillation is increased. Figure 7.20 shows the eigenvector components for the nominal configuration at a roll angle of 45° whilst Fig. 7.21 presents their evolutions for the maximum values of the interconnection damping coefficient.

7.5 Optimal interconnection coefficients

Four optimization processes were performed in Chapter 6 in order to find the best configuration of the interconnection coefficients in terms of suspension precision for four possible mechanical arrangements. Table 6.2 presents the values found for the k_s and c_s coefficients. The mechanical arrangements considered imply the following configurations:

- a) Negative constant damping coefficient.
- b) Negative speed variable damping coefficient.
- c) Positive and negative speed variable damping coefficient.
- d) Positive and negative speed variable stiffness and damping coefficients.

As it has been shown in this chapter, the values of the interconnection parameters can modify the motorcycle dynamics and, for some cases, make it unstable. A stability analysis is required at this point in order to guarantee the stability of the system for the four optimal configurations. Figure 7.22 shows the four root loci found for each of these four optimal configurations. The optimization process was carried out for eight different forward speeds, the interconnection coefficients values for the intermediate speeds were found through linear interpolation. Each root locus represents the eigenvalues evolution with the speed, ranging from 10 m/s (\square) to 80 m/s (*). Four different roll angles are studied, 0° (blue \times), 15° (green \circ), 30° (red $+$) and 45° (black \diamond). The focus of this section is to study if any stability risk exists in the proposed optimal interconnection arrangements. Therefore, the root locus area under study is the stability limits neighbourhood. Then, a clearer view of those modes that affect the general motorcycle's dynamics is obtained.

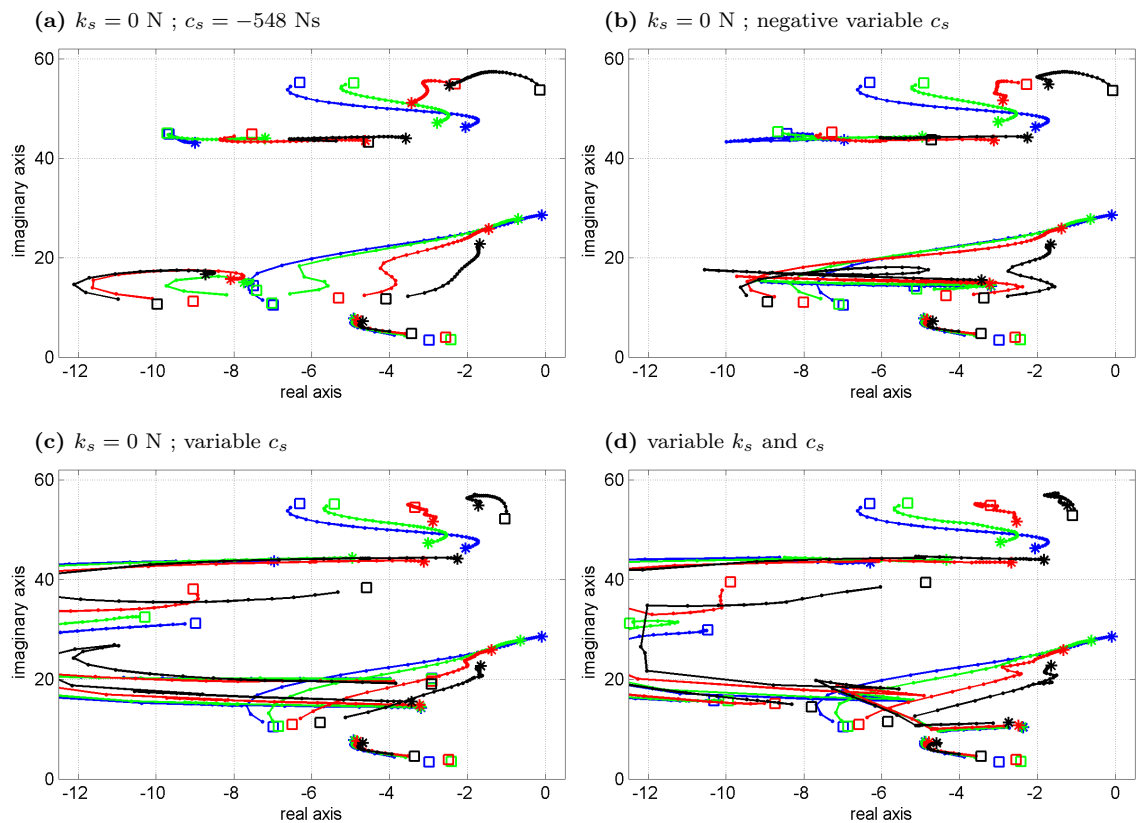


Figure 7.22: Root loci for the four optimal interconnected suspension system configurations proposed in Chapter 6. The speed is increased from 10 m/s (\square) to 80 m/s (*) and different roll angles are considered: 0° (blue), 15° (green), 30° (red) and 45° (black). a) Negative constant damping coefficient. b) Negative speed variable damping coefficient. c) Positive and negative speed variable damping coefficient. d) Positive and negative speed variable stiffness and damping coefficients.

In Fig. 7.22a the root loci for the interconnection arrangement a) is presented. The three out-of-plane normal modes (rider lean, weave and wobble) can be recognized near the stability limit, remaining almost unaffected by the interconnection. The two in-plane modes (pitch and bounce), that for the nominal case are highly damped, now appear in the interest area. The interconnection system shifts them to the right. The pitch mode approaches the wobble mode, at lower frequencies and slightly more damped. On the other hand, the bounce mode almost reaches the weave area. In some cases, their eigenvalues do overlap and, for low speeds, both modes may interact as they do share resonance frequencies. For this configuration, the in-plane modes damping remains greater than the out-of-plane ones. Figure 7.22b shows the root loci for the optimal interconnection configuration b). For this configuration, the damping of both pitch and bounce modes is reduced. In this case, the overlapping of weave and bounce mode's roots is increased at lower speeds whilst for medium and high speeds range it does not exist. The wobble mode at very low speed and for a roll angle of 45° , is near the imaginary axis, although it remains stable. Similar situation appears for weave mode at higher speeds with 0° roll angle. It can be said that this configuration does not compromise the stability of the motorcycle. The root loci for the interconnection arrangement c) are shown in Fig. 7.22c. In this configuration, the wobble mode for 45° roll angle is more stable at low speed. The weave mode does not show much variation and reaches real values near to the stability limit for 0° roll angle and high speed. The in-plane modes are now more stable for a wide range of speeds and roll angles, being located in a wider area of the root locus. Nevertheless, for certain values at higher speeds they become less damped than in the previous configuration. The root loci for the configuration d) in Fig. 7.22d do not show relevant differences to that for the configuration c). Finally, the front hop mode stays well damped for all the interconnection arrangements and does not appear in the area of interest in the root locus. It can be concluded that none of the proposed optimal interconnection configurations introduces a stability risk in the motorcycle model.

7.6 Conclusions

In this chapter, a stability analysis of the GSX-R1000 motorcycle mathematical model, modified for including a possible interconnected suspensions system, is performed. The interconnected suspensions system under study is defined with two interconnection parameters, the interconnection stiffness (k_s) and the interconnection damping (c_s) following the mathematical description in Chapter 5. The stability of the system is tested through the state space description of the model for the full coefficients ranges stated in Chapter 6. A modal analysis is also presented in order to understand the changes in the motion patterns of the motorcycle system natural modes.

The interconnected suspension system acts on the in-plane suspension forces, thus it directly affects the in-plane modes whilst the out-of-plane modes remain unaffected. In a first stage, the motorcycle model is studied under straight running conditions, where these modes are not coupled with the out-of-plane modes, in order to obtain a deeper understanding of the interconnected suspension system effects in the motorcycle oscillating dynamics.

It is found that the interconnection stiffness coefficient does not affect in a significant manner to the out-of-plane modes. Pitch frequency increases for positive values of k_s coefficient and it is reduced for negative values. The bounce mode presents higher frequencies and higher damping for negative k_s values but only its damping is reduced for positive values of this coefficient. The front hop mode is not influenced in a great manner by the interconnection stiffness coefficient, however, it can be observed how for high and low speeds its frequency and damping is increased for positive values of k_s and reduced for negative values. For the middle speed range this behaviour is inverted. Generally speaking, the interconnection stiffness coefficient, within the limits established in Chapter 6, does not affect in a substantial manner the motorcycle oscillating dynamics.

Regarding the interconnection damping coefficient it has a greater influence in the motorcycle normal modes. It affects the front hop mode by increasing its frequency drastically for both positive and negative c_s settings, whilst its damping is reduced, becoming the real parts of its eigenvalues closer to zero. The evolution of its eigenvalues is very similar for positive and negative values of the interconnec-

tion damping coefficient, mainly for the higher ones, although a main difference is found in its eigenvectors. The pattern of motion for negative c_s values shows large amplitude in phase oscillation of the front fork and the rear swinging arm of the motorcycle, while minor oscillations affect the main body. For the positive values of c_s the motion is similar except for the phase angle existing between the front and rear ends, which now oscillate in phase opposition.

For the case of the pitch mode, it becomes in a more pure pitching motion for positive values of the interconnection damping coefficient. For the bounce mode are the negative values of this coefficient which enhance the pure vertical oscillation. For both modes, the damping is reduced for negative values of the c_s coefficient. For small positive values of this coefficient, they become more damped, however, after certain values they get less damped as the coefficient values is increased. Also its frequency is modified. In the case of the pitch mode it is reduced whilst for the bounce mode is increased.

These three modes are closely related through the in-plane dynamics of the motorcycle. When the front and rear ends are interconnected the relation between the three modes become more noticeable and for certain values of the interconnection damping coefficient they become difficult to identify one from the others. The front hop mode highly affects the bounce and pitch modes and avoid that they become more damped for high positive values of c_s coefficient.

The effects mentioned above are reproduced for all the different roll angles under study. However, by increasing the roll angle, the influence of the front hop mode in the bounce and pitch modes is reduced and the out-of-plane modes become more relevant in their motion patterns and stabilities, being the rider shake mode coupled to the bounce mode.

In a final stage, the stability of the system for the four optimal interconnection configurations proposed in Chapter 6 is tested. The effects found in the previous study can be appreciated in all the configurations, nevertheless it can be concluded that all of them result stable settings for all the speed range and at any roll angle.

Chapter 8

Conclusions and Further Work

Two motorcycle alternative suspension concepts have been studied. On one hand, the girder and Hossack double-wishbone suspension systems have shown to represent a promising alternative to the conventional telescopic fork for the sport motorcycle front end. The simplicity, the structural rigidity and the wide design's options in terms of kinematics make these suspension systems to be suitable choices for commercial sport machines. On the other hand, the interconnection of the front and rear motorcycle suspension system has been demonstrated to allow better motorcycle suspension performance and to introduce interesting suspension capabilities as a whole system.

Main findings

By using a high fidelity mathematical model and computer simulations, the behaviour of a sport motorcycle including the new features could be predicted with high accuracy. In Chapter 3, the model based on a Suzuki GSX-R1000 motorcycle, previously developed by (Sharp et al. 2004), and VehicleSim (used to modify the model, obtain the equations of motion and run the different simulations) are introduced. New features were developed and included in the model in order to build a more complete model that allowed running the necessary simulations for the study of the suspension's performance under nonlinear and time variable running conditions.

The state space representation returned by VS Lisp was updated. The default state space basis was changed in order to obtain a more intuitive one in which the

normal modes could be clearly understood as motions of the system's degrees of freedom related to the motorcycle's symmetry plane.

Finally, the original three-dimensional model with thirteen degrees of freedom was reduced to a couple of two-dimensional models. The first of them, with two degrees of freedom, was created in order to study simple bounce and pitch motions. The second reduced model, with four degrees of freedom, included the front and rear wheels displacement. It was built to study the effect of these two additional degrees of freedom on the bounce and pitch normal modes. The work carried out represents a contribution that increase the capabilities of the (Sharp et al. 2004) model, which already was an excellent analysis tool for motorcycle dynamics.

By means of the model presented in Chapter 3, the performances of the girder and Hossack suspension systems were studied. These systems were proven to be highly configurable in terms of kinematic behaviour. The motorcycle's in-plane dynamics were tested for different geometrical configurations of these systems through road bump inputs and hard front wheel braking simulations. Both the girder and Hossack suspension systems showed satisfactory responses and were found to be suitable for different design requirements that could not be achieved by a conventional telescopic fork suspension system.

In the second part of the Chapter 4, the effects of the two alternative suspension systems on the motorcycle's stability were studied for different road conditions. It was demonstrated that different geometrical configurations of both girder and Hossack suspension systems do not affect in a significant manner the motorcycle's normal modes. However, by reducing the mass in both girder and Hossack systems' components, the wobble mode behaviour is modified. Its natural frequency is increased whilst it becomes more damped for higher speeds for the entire roll angle range ($0^\circ - 45^\circ$).

Under cornering conditions, for high roll angles (45°) the wobble mode becomes unstable at low speeds for both suspension systems, whilst for straight running conditions, the weave mode crosses the stability limit at high speed. In the case of the girder suspension system, the weave mode crosses this limit before than in the case of the Hossack system.

The motorcycle's torsional rigidity and damping constant of the steering damper

affect the weave and wobble stability in a similar manner as for the motorcycle fitted with a conventional telescopic fork suspension. For the case of the Hossack suspension system, an optimal value of the steering damper coefficient that keeps the motorcycle stable under any running condition was found. However, this was not possible in the case of the girder suspension system, for which the weave mode at 0° roll angle remains unstable for speeds over 70 m/s.

Interconnected suspension systems were investigated from Chapters 5 to Chapter 7. In Chapter 5, the reduced models developed in Chapter 3 were used to study the motorcycle's bounce and pitch motions and how the interconnected suspensions system can be used to define the normal modes' stiffness and damping properties as desired. For a two degrees of freedom model, it was proven that these properties could be set by defining the different values of the front, rear and interconnection spring and damper constants. However, when the wheels degrees of freedom are taken into consideration, the normal modes associated to the bounce and pitch motions become more complex and setting their stiffness and damping properties is not a simple task. It could not be proven that all the desired bounce and pitch stiffness and damping combinations could be achieved. Nevertheless, a preliminary numerical method was presented in order to obtain bounce and pitch modes stiffness and damping constants values as close as possible to the desired ones.

Other advantage introduced by the interconnected suspension system is the increase on the motorcycle's suspension accuracy. This was demonstrated in Chapter 6 where optimal values of the interconnected suspension system parameters were found improving the suspension precision along the full speed range. It was found that just with a damper unit with constant value of the damping coefficient, the suspension precision can be significantly improved. If more complex mechanisms are introduced, such as damper units with variable speed coefficients, higher values of suspension precision can be found. It was observed that for speeds under 45 m/s positive values of the interconnection damper coefficients are preferred to improve the suspension's response, whilst for speeds over 45 m/s negative interconnection coefficients values are needed.

The frequency response was also investigated through straight running simulations for sinusoidal road inputs considering the coupling between the front and rear

wheel motions. It was proven that none of the optimal interconnection configuration proposed worsens the frequency response or increments significantly the amplitude transmitted from the road to the different parts of the motorcycle. It was concluded that the interconnected suspension system may represent a competitive difference with the conventional suspension system in the GSX-R1000 model by improving the motorcycle's suspension response.

When interconnection mechanisms are introduced between the front and rear suspension systems the motorcycle's stability properties can change. In Chapter 7, the full GSX-R1000 model was used to carry out a complete modal analysis of the motorcycle for a wide range of interconnection parameters values. It was shown how not only the resonance frequency and damping ratio of each normal mode are affected, but also their pattern of motion are modified depending on how important the relation between the normal mode and the interconnection system is. The normal modes which are more influenced by the interconnection system are the in-plane modes: bounce, pitch and front wheel hop. For certain values of the interconnection coefficients, these modes interact between them and in some cases they cannot be distinguished from each other. It was observed that although the stability of these normal modes can be improved for some values of the interconnection damping coefficient, for absolute values of this coefficient above certain value, the normal modes move in the complex plane towards areas with less damping due to the interaction between modes and the energy transfer from the front wheel to the rear wheel. However, it was demonstrated that the optimal configurations that increase the suspension precision are completely stable for the different running conditions under study.

Contributions to knowledge

The contribution made in this research can be divided in two parts depending on the suspension system under study. Those regarding to the double wishbone suspension systems are summarized in the following lines:

1. The kinematic design of the front suspension system does not affect the motorcycle response to step bump inputs as far as the suspension tuning stays equivalent to the reference model.

2. The motorcycle's dynamics under front wheel braking manoeuvres is significantly affected by the front end's kinematics.
3. Anti-dive effect can be achieved with both girder and Hossack suspension systems. The use of each system will result in different behaviour of the handling geometric parameters.
4. A reduction on the mass of the front suspension system result in slight improvements of the motorcycle response in both step bump input and front wheel braking simulations.
5. The motorcycle's normal modes are not affected in a remarkable manner by the front suspension system's kinematics.
6. The reduction of the front suspension system's mass can be appreciated in the wobble mode's behaviour. Its frequency is increased at the same time that it becomes more stable, mostly at high speeds range.
7. The increase of the front end's rigidity stabilizes the weave mode, whilst the wobble mode's stability is decreased. The opposite occurs when the rigidity of the front end is reduced.
8. The effect of the steering damper on the motorcycle stability is the opposite to that of the front end's rigidity. This is, the weave stability is decreased with higher values of the steering damping coefficients, whilst the wobble mode becomes less stable. And, again, the opposite occurs with lower values of the steering damper coefficient.
9. For the model under study, conventional designs of girder suspension systems allow the motorcycle to be fully stable until high speeds of about 70 m/s. However, the maximum speeds that can be achieved with a conventional Hossack system, maintaining the motorcycle stable, is about 80 m/s.

On the other hand, the contributions made with the interconnected suspensions system research can be summarized as follows:

10. Interconnected suspensions systems introduce new setting parameters that allow modifying the motorcycle's bounce and pitch motions.

11. When the wheels' degrees of freedom are considered in the model, the suspension coefficients which produce the desired bounce and pitch motion cannot be obtained by an analytical solution. Nevertheless, a numerical method is proposed in here to obtain approximate values for the desired settings.
12. Interconnected systems improve the suspensions system's accuracy if the appropriate values of stiffness and damping interconnection coefficients are set for each speed range.
13. Positive values of interconnection coefficients are suitable for low speeds whilst for high speeds negative values are needed. In the medium speed range (about 40 - 50 m/s) the effect of interconnection is less remarkable.
14. The interconnection between the front and rear suspension systems modify the normal mode patterns of motion. Positive interconnection enhances the pitch motion whilst penalize the bounce motion. The opposite happens with negative interconnection.
15. Large absolute values of interconnection coefficients may produce a notable destabilization of some normal modes that are highly damped with an independent suspensions system.
16. Optimal values of interconnection coefficients can be found for which the suspension efficiency is improved in all the speed range whilst the motorcycle's normal modes remain stable.

Limitation of the work

It is important to consider the limitations of this work. Although the mathematical model (Sharp et al. 2004), the modelling tools (VehicleSim) and the methodology adopted to study the different suspension systems have been widely used, tested and accepted by both academia and industry, the results obtained for the new suspension systems included in the model in this research have not yet been tested with experimental results.

Building a motorcycle model including a different suspension system to the original one and carrying out the physical experiments with this machine require a large

amount of economical and human resources. The mathematical modelling allows to explore new mechanical solutions even before the prototyping stage, saving a lot of these resources. This research is framed in this context. As it has already been stated, the goal of this work is to point out the real possibilities that these alternative suspension systems can bring to the motorcycle dynamics field and to be an eventual starting point for future research on these systems. Therefore, further work is needed before these systems can be implemented in a commercial sport motorcycle.

Further work

Before physical tests with real prototypes can be carried out, several ideas for further research are suggested in a framework of mathematical modelling and numerical simulation.

Regarding the double wishbone suspension systems, more extensive research should be done following the approach of (Watanabe & Sayers 2011) in order to investigate the rider's requirements under cornering running conditions and how the variable geometry of the girder and Hossack front suspension systems can affect the riders' handling efforts depending on the different motorcycle front end geometrical relations, such as the normal trail or the steering angle.

On the other hand, further research should be done to explore new girder and Hossack suspensions designs which eventually could improve motorcycle's stability at higher speeds by investigating the effects of different location of the front frame's centre of mass, as suggested by (Sharp 1971). This characteristic differs from the conventional telescopic fork in both girder and Hossack suspension systems. However, the girder suspension presents a greater difference at the same time that the weave mode's stability is significantly reduced with this system.

In relation to the interconnected suspensions system, the new parameters introduced by his system have been demonstrated to be useful to act on the motorcycle modal behaviour. Nevertheless, setting the interconnected suspension system with the desired values is not a simple task. Although a numerical method have been proposed for it, it has not been demonstrated to be suitable for the full space of possible stiffness and damping combinations of the normal modes. Further research

is suggested in order to obtain a deeper knowledge in this matter and a more accurate methodology which would allow to set the interconnected suspension system for any desired values.

Finally, in the comparison between the responses of the interconnected and independent suspension systems, the front and rear suspension settings were not modified from their nominal values. Studying the effects on the overall suspension efficiency when also the front and rear suspension parameters are modified in combination with the interconnection ones may represent an interesting opportunity for further increasing the motorcycle's performance.

Final conclusion

Although the front telescopic fork is the most extended and almost the only system considered by manufacturers for the front end of their sport motorcycles, this research shows the possible advantages that some alternative suspension systems may introduce in motorcycles and it is intended to open the door for future research and developments of these kinds of suspension systems.

Appendix A

Motorcycle Reduced Model

In this appendix, the dynamic properties of a motorcycle reduced model with four degrees of freedom, as that described in Chapter 3, are derived from the properties of the full model developed by (Sharp et al. 2004). A diagram of the reduced model is presented in Fig. A.1, where its degrees of freedom are the front (z_{fw}) and rear (z_{rw}) wheels vertical displacements, the main frame vertical displacement (z) and the main frame pitch rotation (θ).

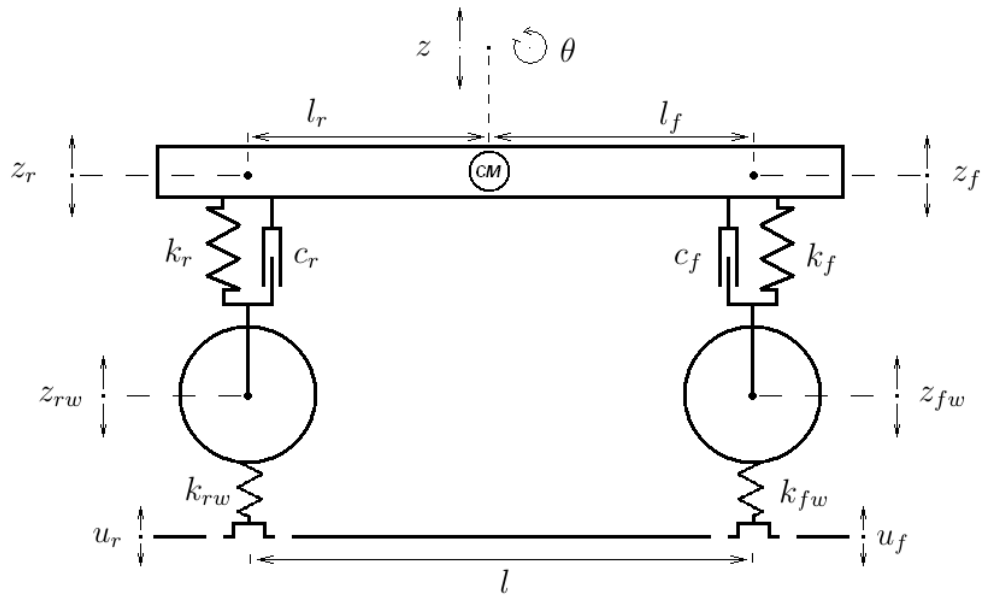


Figure A.1: Motorcycle's reduced model with four degrees of freedom.

The main body mass is calculated as the sum of the masses of the chassis, the rider's upper body and the steer body. The new moment of inertia of the main body is obtained by applying the Steiner theorem to the three bodies implied on its motion. The new model front wheel mass is the sum of the front wheel and the

suspension body in the original model. Whilst the new rear wheel mass is obtained as the sum of the former rear wheel mass and the apparent mass introduced by the swinging arm. This motorcycle part rotates about its link axle with the chassis. The torque needed to reach certain angular acceleration can be obtained by applying a linear force to the swinging arm centre of mass, being the distance from this point to the pivot point (l_{sa}) the lever arm of this torque. Applying Newton's second law, the swinging arm apparent mass (m_{sa}) becomes related to the swinging arm inertia moment (I_{sa}) by:

$$I_{sa} \cdot \ddot{\alpha}_{sa} = m_{sa} \cdot \ddot{z}_{sa} \cdot l_{sa} \cos(\alpha_{0sa}) \quad (\text{A.1})$$

$\ddot{\alpha}_{sa}$ is the rotational acceleration of the swinging arm, α_{0sa} is the swinging arm angle at the nominal position and \ddot{z}_{sa} is the swinging arm centre of mass vertical acceleration. On the other hand, the vertical displacement of this point can be approximate by Eq. A.2 at the nominal position, whilst its acceleration is given by Eq. A.3.

$$z_{sa} = (\alpha_{sa} - \alpha_{0sa}) \cdot l_{sa} \cos(\alpha_{0sa}) \quad (\text{A.2})$$

$$\ddot{z}_{sa} = \ddot{\alpha}_{sa} \cdot l_{sa} \cos(\alpha_{0sa}) \quad (\text{A.3})$$

Finally, the apparent mass of the swinging arm, when its motion is approximated as a vertical displacement, is obtained by Eq. A.4. The new rear wheel mass is computed as the sum of this apparent mass and the old rear wheel mass. The assembly's centre of mass can be directly obtained for these masses and their positions.

$$m_{sa} = \frac{I_{sa}}{l_{sa}^2 \cos^2(\alpha_{0sa})} \quad (\text{A.4})$$

While the tyres stiffness coefficient in the reduced model are the same as those in the full GSX-R1000 model, the equivalent front and rear suspensions coefficients are computed following the approach in (Cossalter 2006). For the front suspension system, both stiffness and damping coefficients can be analytically achieved by simple projection of the forces considering the motorcycle steering angle. The equivalent front stiffness (k_f) and damping (c_f) coefficients are obtained by Eq. A.5, depend-

ing on the GSX-R1000 model telescopic fork coefficients (k_{fo} and c_{fo}) and the steer angle (ϕ_h).

$$k_f = \frac{k_{fo}}{\cos^2(\phi_h)} \quad ; \quad c_f = \frac{c_{fo}}{\cos^2(\phi_h)} \quad (\text{A.5})$$

Due to the mechanical complexity of the rear suspension system, its equivalent coefficients in the reduced model have to be obtained by an energy conservation criterion. For the case of the stiffness coefficient, Eq. A.6 shows this criterion. The time variation of the energy stored by the spring unit in the original suspension system must be equal to that of the equivalent spring on the reduced model.

$$F_s \cdot \frac{dz_r}{dt} = F_{so} \cdot \frac{dq_r}{dt} \quad (\text{A.6})$$

F_s is the force needed in the reduced model rear wheel to induce a vertical displacement equal to z_r and F_{so} is the force that compresses the actual spring a distance q_r following the Hook's law:

$$F_{so} = -k_{ro} \cdot q_r \quad (\text{A.7})$$

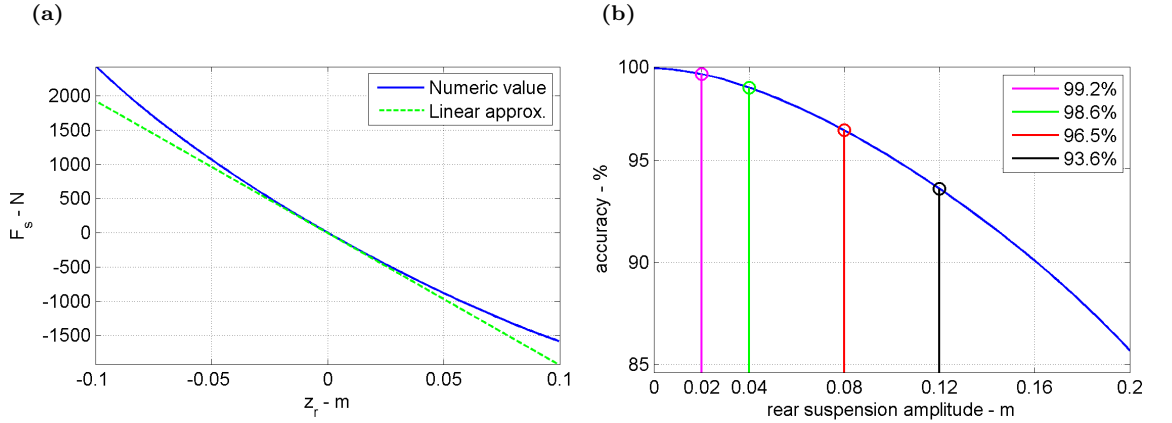


Figure A.2: a) Equivalent spring force of the reduced model rear suspension in solid blue. The linear approximation is in dashed green. b) Accuracy of using the linear approximation depending on the maximum suspension amplitude.

Taking advantage of the geometrical parametrization of the monoshock mechanical linkage presented in Fig. 3.4a, the equivalent rear suspension force of the reduced model (F_s) can be numerically computed for the full range of the possible positions

of the rear suspension by means of Eq. A.8

$$F_s = -k_{ro} \cdot q_r \frac{dq_r}{dz_r} \quad (\text{A.8})$$

A precise description of the rear suspension spring force can be found by a polynomial regression of the equivalent force with the vertical travel of the rear wheel. In order to obtain linear suspension forces in the reduced model, the equivalent spring constant (k_r) is taken as the first order coefficient absolute value of the polynomial obtained. So that the rear suspension spring force (F_s) is described as a linear function of the rear wheel vertical displacement (z_r):

$$F_s = -k_r \cdot z_r \quad (\text{A.9})$$

Figure A.2a shows the equivalent spring force in the reduced model for a wheel vertical travel of $[-10 \text{ cm}, +10 \text{ cm}]$. The numerically computed value is plotted in solid blue whilst the linear approximation obtained at the nominal position is plotted with a dashed green line. Figure A.2b shows the accuracy obtained with this approximation of F_s with respect to the rear suspension maximum amplitude.

A similar energy conservation criterion is followed to compute the equivalent rear suspension damping coefficient for the reduced model.

$$F_d \cdot \frac{dz_r}{dt} = F_{do} \cdot \frac{dq_r}{dt} \quad (\text{A.10})$$

F_d is the damping force in the reduced model rear suspension for the corresponding wheel vertical position z_r and F_{do} is the original force of the actual damper for the equivalent strut distance q_r . F_{do} depends linearly on the strut compression speed through the original damping coefficient c_{ro} . A linear relation is sought for F_d , thus Eq. A.10 can be rewritten as in Eq. A.11.

$$c_r \cdot \frac{dz_r}{dt} \cdot \frac{dz_r}{dt} = c_{ro} \cdot \frac{dq_r}{dt} \cdot \frac{dq_r}{dt} \quad (\text{A.11})$$

From which the equivalent damping coefficient for the reduced model can be

obtained by Eq. A.12.

$$c_r = c_{r0} \cdot \left(\frac{dq_r}{dz_r} \right)^2 \quad (\text{A.12})$$

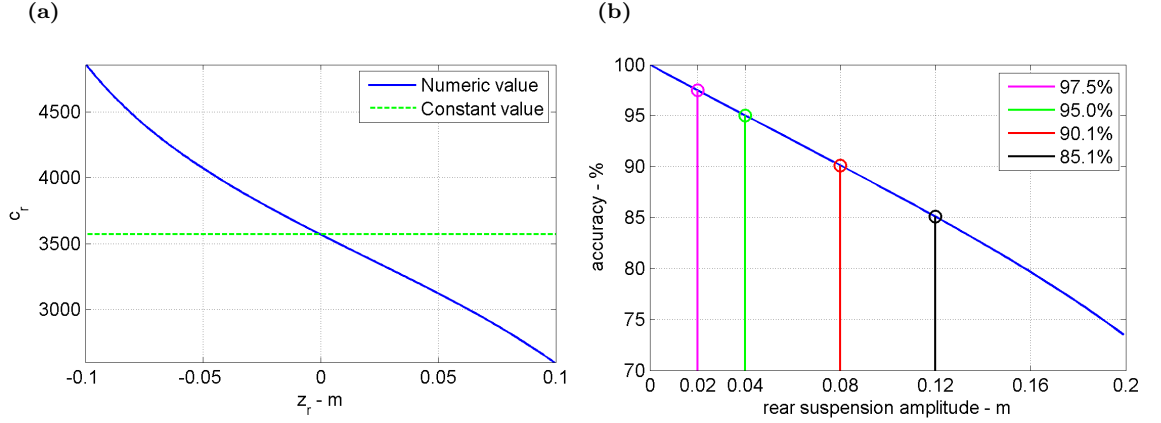


Figure A.3: a) Equivalent damping coefficient of the reduced model rear suspension plotted in solid blue. The constant value for the linear approximation is plotted in dashed green. b) Accuracy of using the linear approximation depending on the maximum suspension amplitude.

Similarly than for the spring constant, taking advantage of the monoshock link geometrical description, the values of the q_r and z_r can be numerically obtained and differentiated. An equivalent damping coefficient (c_r) which varies with the rear wheel's vertical position is obtained.

In the reduced front suspension case, the damping force is a linear function of the front wheel vertical speed which damping coefficient (c_f) is already constant for the full suspension travel. However, in the rear suspension case, the value for the equivalent rear damping coefficient must be approximated to that corresponding to the nominal wheel position. Figure A.3a shows the c_r value variation with the wheel's vertical displacement, whilst Fig. A.3b shows the accuracy of using the constant value approximation with respect to the rear suspension maximum amplitude. Finally, the suspensions coefficients and the masses and inertia moment of the four degrees of freedom reduced model are shown in Table 3.3.

If a more accurate description of the rear suspension is sought, the equivalent spring force and the equivalent damping coefficient can be given as two polynomial functions depending on the rear wheel's vertical displacement. This kind of suspension description was carried out during a collaboration with the Department of Structural and Mechanical Engineering at Universidad de Cantabria, Spain (see

García-Fernández et al. 2014). In that work, a motorcycle mathematical model was built in MSC Adams software. The goal of the study was to replicate the in-plane dynamics results obtained in the GSX-R1000 model developed in VehicleSim. For this purpose, a full parametrization of the model was needed, including a precise rear suspension description. The comparison of both models under a complete set of manoeuvres showed that the MSC Adams model was able to replicate the GSX-R1000 VehicleSim model in-plane dynamics with high accuracy.

Appendix B

New Basis for the State Space

In this appendix it is explained how the nominal base of the motorcycle model's state space provided by VehicleSim is translated into a more understandable base in which the degrees of freedom included in the motorcycle model are directly related to its symmetry plane.

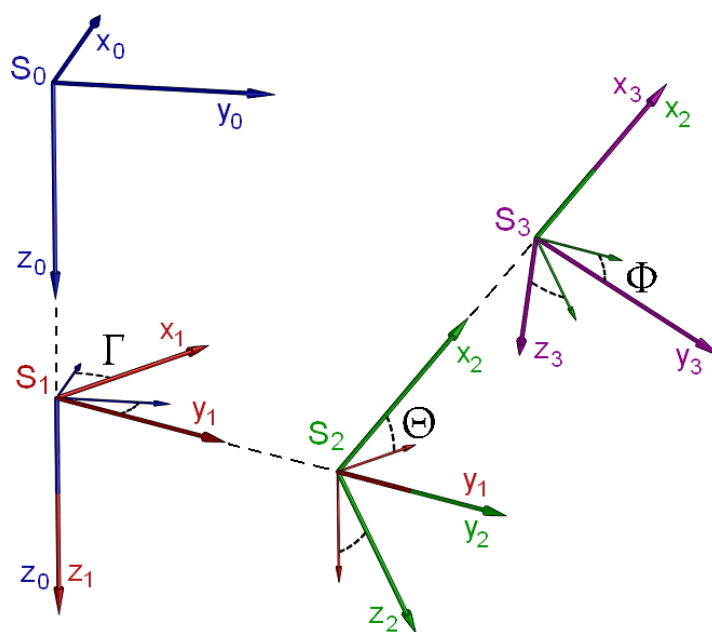


Figure B.1: Auxiliary frames created by VS Lisp with each rotation of the body. Note that the frames are represented separately in order to show a clearer view of each rotation, nevertheless, the origins of all of them are coincident.

As it has been explained in Chapter 3, VehicleSim creates an intermediate reference frame for each rotational degree of freedom of a body. However, the translational degrees of freedom are defined in the inertial reference frame. In the motorcycle model, the chassis is the main body and it is defined in the inertial reference

frame (S_0). It has three translational and three rotational degrees of freedom. The translational ones describe rectilinear motion along the x , y and z axes of the S_0 frame. On the other hand, the three rotational degrees of freedom are related to three different auxiliary reference frames. For the yaw angle (rotation about the z axis of the inertial reference frame S_0) a new reference frame (S_1) is created. It shares the z axis with S_0 and it is rotated Γ° about it. The pitch angle (rotation about the y axis of S_1) introduces another reference frame (S_2) which shares the y axis with the S_1 frame and which is rotated Θ° about it. Finally, the roll angle (rotation about the x axis of S_2) creates the reference frame S_3 , which is rotated Φ° about the x axis of S_2 . This axis is shared by both S_2 and S_3 reference frames. Figure B.1 shows the three auxiliary reference frames created by VehicleSim for each rotation about the main axes.

Translational degrees of freedom

Regarding to the translational degrees of freedom, a change of basis matrix between the S_0 and the S_3 reference frames can be found as a change of basis matrices sequence between the consecutive intermediate reference frames.

S_1 is defined by a rotation of the inertial reference frame about its z axis by the rotation matrix R^z , therefore, the change of basis matrix from S_0 to S_1 is the inverse of this matrix, $P_{10} = (R^z)^{-1}$:

$$R^z(\Gamma) = \begin{pmatrix} \cos \Gamma & -\sin \Gamma & 0 \\ \sin \Gamma & \cos \Gamma & 0 \\ 0 & 0 & 1 \end{pmatrix} ; \quad P_{10} = \begin{pmatrix} \cos \Gamma & \sin \Gamma & 0 \\ -\sin \Gamma & \cos \Gamma & 0 \\ 0 & 0 & 1 \end{pmatrix}$$

Similarly, the S_2 basis is defined by R^y as a rotation of the S_1 reference frame about its y axis, for which the change of basis matrix from S_1 to S_2 is obtained as $P_{21} = (R^y)^{-1}$:

$$R^y(\Theta) = \begin{pmatrix} \cos \Theta & 0 & \sin \Theta \\ 0 & 1 & 0 \\ -\sin \Theta & 0 & \cos \Theta \end{pmatrix} ; \quad P_{21} = \begin{pmatrix} \cos \Theta & 0 & -\sin \Theta \\ 0 & 1 & 0 \\ \sin \Theta & 0 & \cos \Theta \end{pmatrix}$$

Finally, the rotation of the S_2 reference frame about its x axis defines the S_3 basis, being the rotation matrix R^x . The change of basis matrix from S_2 to S_3 is $P_{32} = (R^x)^{-1}$:

$$R^x(\Phi) = \begin{pmatrix} 1 & 0 & 0 \\ 0 & \cos \Phi & -\sin \Phi \\ 0 & \sin \Phi & \cos \Phi \end{pmatrix} ; \quad P_{32} = \begin{pmatrix} 1 & 0 & 0 \\ 0 & \cos \Phi & \sin \Phi \\ 0 & -\sin \Phi & \cos \Phi \end{pmatrix}$$

The resultant change of basis matrix from S_0 to S_3 is obtained as:

$$P_{30} = P_{32}P_{21}P_{10} \quad (\text{B.1})$$

Which results in:

$$P_{30} = \begin{pmatrix} \cos \Theta \cos \Gamma & \cos \Theta \sin \Gamma & -\sin \Theta \\ \sin \Phi \sin \Theta \cos \Gamma - \cos \Phi \sin \Gamma & \sin \Phi \sin \Theta \sin \Gamma + \cos \Phi \cos \Gamma & \sin \Phi \cos \Theta \\ \cos \Phi \sin \Theta \cos \Gamma + \sin \Phi \sin \Gamma & \cos \Phi \sin \Theta \sin \Gamma - \sin \Phi \cos \Gamma & \cos \Phi \cos \Theta \end{pmatrix}$$

Finally, any translational degree of freedom described in S_0 is expressed in S_3 as:

$$Q_3^t = P_{30}Q_0^t \quad (\text{B.2})$$

Where Q_0^t is the translational components vector of the motorcycle's chassis provided by VehicleSim and Q_3^t is the same components vector expressed in the chassis reference frame (S_3).

$$Q_3^t = \begin{pmatrix} XT_3 \\ YT_3 \\ ZT_3 \end{pmatrix} ; \quad Q_0^t = \begin{pmatrix} XT_0 \\ YT_0 \\ ZT_0 \end{pmatrix}$$

Rotational degrees of freedom

The chassis rotational degrees of freedom need a different approach. As it has been said, the yaw (Γ), the pitch (Θ) and the roll (Φ) angles are defined in S_0 , S_1 and S_2 respectively and they fix the orientation of the motorcycle's chassis reference frame (S_3) in the space. Thus, for the eigenvectors directly obtained from the state space returned by VS Lisp, the ZR component represents the rotational oscillations of the chassis about the z axis in the S_0 reference frame. This is the same axis as in the S_1 frame. The YR component represents the rotational oscillations about the y axis of S_1 and S_2 reference frames. And the XR component represents the rotational oscillation about the x axis of S_2 and S_3 reference frames.

Following the nomenclature used for yaw, pitch and roll angles, the symbols used for the small rotational oscillations about the z , the y and the x axes will be γ , θ and

ϕ respectively, followed by a subscript index indicating which is the reference frame which the considered axis belongs to. Therefore, the chassis eigenvector's rotational component ZR corresponds to γ_1 , YR corresponds to θ_2 and XR to ϕ_3 . In order to find which motion these components represent in the chassis reference frame, the components values provided by the eigenvector must be transformed to γ_3 , θ_3 and ϕ_3 . Note that ϕ_3 is already indicated in the appropriate basis.

The rotation about the y axis in the basis of S_2 is given by $R_2^y(\theta_2)$ which in this case is written as:

$$R_2^y(\theta_2) = \begin{pmatrix} \cos \theta_2 & 0 & \sin \theta_2 \\ 0 & 1 & 0 \\ -\sin \theta_2 & 0 & \cos \theta_2 \end{pmatrix}$$

In the S_3 basis, this is a linear application that can be found by means of the change of basis matrices as:

$$R_3^y(\theta_2) = P_{32}R_2^y(\theta_2)P_{32}^{-1} \quad (\text{B.3})$$

The subscripts are the index of the reference frame in which the matrix is expressed. The superscripts represent the axis in which the rotation is produced about in the original reference frame used by VehicleSim, in this case it is S_2 .

This matrix results in:

$$R_3^y(\theta_2) = \begin{pmatrix} \cos \theta_2 & \sin \Phi \sin \theta_2 & \cos \Phi \sin \theta_2 \\ -\sin \Phi \sin \theta_2 & \cos^2 \Phi + \sin^2 \Phi \cos \theta_2 & -\cos \Phi \sin \Phi + \sin \Phi \cos \theta_2 \cos \Phi \\ -\cos \Phi \sin \theta_2 & -\cos \Phi \sin \Phi + \sin \Phi \cos \theta_2 \cos \Phi & \sin^2 \Phi + \cos^2 \Phi \cos \theta_2 \end{pmatrix}$$

Being the state space description a linear approximation of the motorcycle dynamics, the rotational oscillation of the chassis should be considered as small angle. Thus, the matrix above can be simplified as:

$$R_3^y(\theta_2) \simeq \begin{pmatrix} 1 & \theta_2 \sin \Phi & \theta_2 \cos \Phi \\ -\theta_2 \sin \Phi & 1 & 0 \\ -\theta_2 \cos \Phi & 0 & 1 \end{pmatrix}$$

This linear application can be decomposed in three rotations about the main axes of the system S_3 . For any rotation composition, the resultant matrix will

depend on the rotations sequence applied. However, in this case, after the small angle approximation is performed, the resultant matrix becomes independent from the rotations sequence. A general rotation matrix about the three main axes of an arbitrary reference frame S_i can be obtained as:

$$R(\gamma, \theta, \phi) = R_i^z(\gamma)R_i^y(\theta)R_i^x(\phi) \quad (\text{B.4})$$

Which results in:

$$R(\gamma, \theta, \phi) = \begin{pmatrix} \cos \gamma \cos \theta & -\sin \gamma \cos \phi + \cos \gamma \sin \theta \sin \phi & \sin \gamma \sin \phi + \cos \gamma \sin \theta \cos \phi \\ \sin \gamma \cos \theta & \cos \gamma \cos \phi + \sin \gamma \sin \theta \sin \phi & -\cos \gamma \sin \phi + \sin \gamma \sin \theta \cos \phi \\ -\sin \theta & \cos \theta \sin \phi & \cos \theta \cos \phi \end{pmatrix}$$

After applying the small angle approximation, the general rotation matrix for the S_3 reference frame is:

$$R(\gamma_3, \theta_3, \phi_3) \simeq \begin{pmatrix} 1 & -\gamma_3 & \theta_3 \\ \gamma_3 & 1 & -\phi_3 \\ -\theta_3 & \phi_3 & 1 \end{pmatrix}$$

By comparing the terms in $R(\gamma_3, \theta_3, \phi_3)$ to the terms in $R_3^y(\theta_2)$, the contribution on the γ_3 , θ_3 and ϕ_3 rotations in S_3 reference frame of the θ_2 rotation in S_2 frame is found as:

$$\left. \begin{aligned} \gamma_3^y &\simeq -\theta_2 \sin \Phi \\ \theta_3^y &\simeq \theta_2 \cos \Phi \\ \phi_3^y &\simeq 0 \end{aligned} \right\} \quad (\text{B.5})$$

A similar approach is followed for the ZR eigenvectors component provided by VS Lisp. This is, the rotational oscillation about the z axis (γ_1) on the S_1 reference frame. To obtain the contribution on the three different rotations about the main axis of the chassis reference frame (S_3), it is first transformed into the equivalent rotations in S_2 . Then, the equivalent rotation about the z axis (γ_2^z) in this frame is transformed to those equivalent rotations on S_3 frame (γ_3^z , θ_3^z and ϕ_3^z). The change of basis for the ZR rotations in S_1 to S_2 is:

$$R_2^z(\gamma_1) = P_{21}Rz(\gamma_1)P_{21}^{-1} \quad (\text{B.6})$$

After applying the small angle approximation about the S_2 main axes, the equivalent matrix in S_2 results in:

$$R_2^z(\gamma_1) \simeq \begin{pmatrix} 1 & -\gamma_1 \cos \Theta & 0 \\ \gamma_1 \cos \Theta & 1 & \gamma_1 \sin \Theta \\ 0 & -\gamma_1 \sin \Theta & 1 \end{pmatrix}$$

And comparing with $R(\gamma_2, \theta_2, \phi_2)$, the equivalent rotations to γ_1 in S_2 are found by:

$$\left. \begin{aligned} \gamma_2^z &\simeq \gamma_1 \cos \Theta \\ \theta_2^z &\simeq 0 \\ \phi_2^z &\simeq -\gamma_1 \sin \Theta \end{aligned} \right\} \quad (\text{B.7})$$

From these equivalent rotations, only the one about the z axis is considered; VS Lisp description already provides the rotation about the y axis in S_2 and the one about the x axis on S_3 .

A new transformation of the rotation γ_2^z is performed to obtain its contribution on the γ_3 , θ_3 and ϕ_3 rotations by means of Eq. B.8:

$$R_3^z(\gamma_2) = P_{32} R_z(\gamma_2) P_{23} \quad (\text{B.8})$$

And the resultant matrix considering the small angle approximation is expressed by:

$$R_3^z(\gamma_2) \simeq \begin{pmatrix} 1 & -\gamma_2 \cos \Phi & \gamma_2 \sin \Phi \\ \gamma_2 \cos \Phi & 1 & 0 \\ -\gamma_2 \sin \Phi & 0 & 1 \end{pmatrix}$$

Comparing with $R(\gamma_3, \theta_3, \phi_3)$, the equivalent rotations in S_3 due to the original rotation in S_1 are obtained by:

$$\left. \begin{aligned} \gamma_3^z &\simeq \gamma_2 \cos \Phi = \gamma_1 \cos \Theta \cos \Phi \\ \theta_3^z &\simeq \gamma_2 \sin \Phi = \gamma_1 \cos \Theta \sin \Phi \\ \phi_3^z &\simeq 0 \end{aligned} \right\} \quad (\text{B.9})$$

The final rotational oscillations on the S_3 reference frame are, on one hand, the rotation about the x axis in this reference frame (provided by the XR eigenvector component), and, on the other hand, the contributions of the rotation about the y axis in the reference frame S_2 and the rotation about the z axis in the reference frame S_1 , given by:

$$\left. \begin{aligned} \gamma_3 &\simeq \gamma_3^z + \gamma_3^y = \gamma_1 \cos \Theta \cos \Phi - \theta_2 \sin \Phi \\ \theta_3 &\simeq \theta_3^z + \theta_3^y = \gamma_1 \cos \Theta \sin \Phi + \theta_2 \cos \Phi \\ \phi_3 &= \phi_3 \end{aligned} \right\} \quad (\text{B.10})$$

The eigenvector's rotational components related to the chassis's degrees of freedom expressed in the S_3 reference frame can be obtained from those directly provided by VS Lisp through Eq. B.11.

$$Q_3^r = R_{30} Q_0^r \quad (\text{B.11})$$

R_{30} is the change of basis matrix:

$$R_{30} = \begin{pmatrix} \cos \Theta \cos \Phi & -\sin \Phi & 0 \\ \cos \Theta \sin \Phi & \cos \Phi & 0 \\ 0 & 0 & 1 \end{pmatrix}$$

Q_3^r and Q_0^r correspond to the eigenvector's rotational components of the chassis:

$$Q_3^r = \begin{pmatrix} ZR_3 \\ YR_3 \\ XR_3 \end{pmatrix} \quad ; \quad Q_0^r = \begin{pmatrix} ZR_1 \\ YR_2 \\ XR_3 \end{pmatrix}$$

Finally, the six degrees of freedom of the motorcycle's chassis directly provided by VS Lisp can be transformed into the equivalent eigenvector oscillatory components expressed in the motorcycle's symmetry plane:

$$\begin{pmatrix} Q_3^t \\ Q_3^r \end{pmatrix} = \begin{pmatrix} P_{30} & 0 \\ 0 & R_{30} \end{pmatrix} \begin{pmatrix} Q_0^t \\ Q_0^r \end{pmatrix} \quad (\text{B.12})$$

Appendix C

Maximum Loads on the Front End

In this appendix the maximum load applied to the front suspension systems under extreme running conditions are estimated. Both longitudinal and lateral maximum loads appear in extreme deceleration manoeuvres. The longitudinal maximum load is reached under a straight line front wheel brake, when the total of the braking force reaction is transmitted from the front wheel to the chassis through the front fork spindle. Figure C.1 shows a diagram of the forces appearing under this braking condition. The brake force between the front wheel and the road (F_b) generates an inertial force on the motorcycle's centre of masses (F_i). The resultant moment produced by this force and the gravity force (F_g) about the front wheel axis becomes zero at the maximum braking force, reached just before the overturning of the motorcycle. The resultant force (R) appearing on the motorcycle's centre of masses is the addition of the inertial and gravity forces projections on the line connecting to the fork spindle. Consequently, the maximum load that the fork must resist (F_d) can be modelled as

a force applied to the fork spindle with equal magnitude and opposite direction to the resultant force (R), being the front end attachment with the chassis fixed to the inertial frame. It can be obtained by Eq. C.1 where m_t is the rider and motorcycle total mass, g is the gravity acceleration, and β is the angle of the resultant force with respect to the vertical.

$$F_d = \frac{m_t \cdot g}{\cos(\beta)} \quad (\text{C.1})$$

The resultant force magnitude has been calculated for the motorcycle's nominal

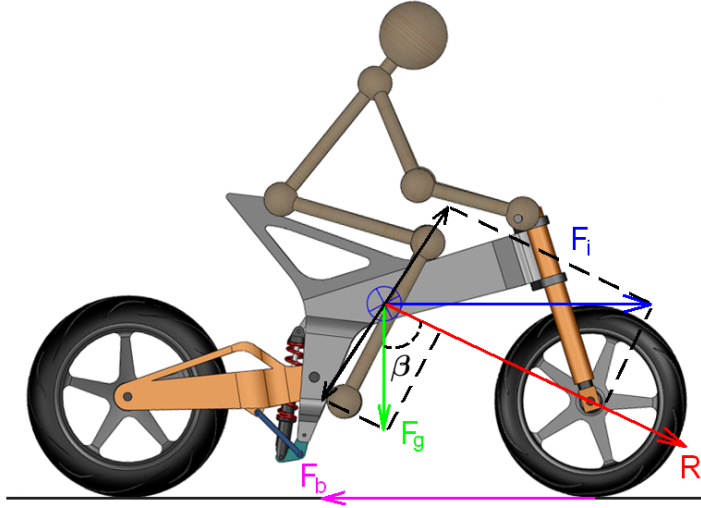


Figure C.1: Forces appearing under straight line front wheel braking. F_b is the braking force between the ground and the tyre. F_i is the fictitious force appearing in the motorcycle centre of masses, which has a similar magnitude and an opposite direction to the braking force. F_g is the gravity force. R is the resultant force in the motorcycle's centre of masses.

position and for the system's maximum deflection. This is, the front suspension is compressed whilst the rear suspension is extended. The maximum load calculated for this last case has a magnitude of $R = 5.3$ kN. This is obtained with a corresponding braking of $F_b = 4.8$ kN. Considering a rider's and a motorcycle's total mass of 228 kg this represents a deceleration of 21.1 m/s² which is approximately 2.2 G (being $G = 9.81$ m/s² the gravity acceleration units). The typical maximum decelerations experienced in MotoGP races are below 1.7 G on extreme braking actions (Brembo 2015). It also should be considered that both front and rear braking systems are used in these cases and that for the middle-high forward speed range (above 30 m/s), the aerodynamic drag becomes relevant for speed reduction. Nevertheless, an extra safety factor of 50 % is added to this maximum load obtaining a rounded longitudinal load requirement of $F_d = 8$ kN.

The maximum lateral load is calculated considering severe braking action on cornering manoeuvres with maximum lean and steering angles. The maximum lean angles achieved in MotoGP races are below $\phi = 65^\circ$ (MotoGP 2015). Considering the wide margin of error included in the resultant force for the longitudinal load, a rough approximation of the lateral load, which covers more than enough the maximum requirements of any front suspension fork, can be obtained by projecting this resultant force into the front wheel axis. Although such a severe braking manoeuvre would not be supported neither by the rider nor the tyres.

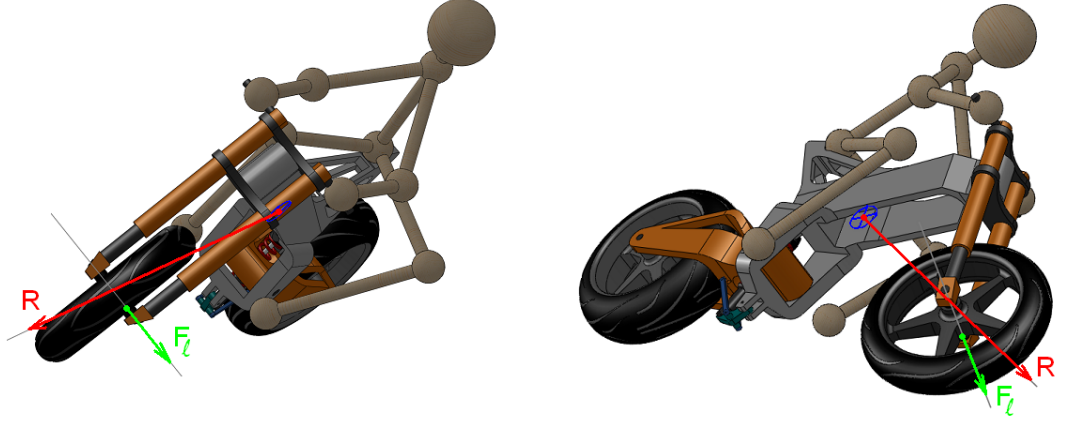


Figure C.2: The maximum lateral load (F_l) is calculated as the projection of the maximum longitudinal load on the front wheel axis for maximum lean and steering angles. The maximum longitudinal load is a force applied to the fork spindle with equal magnitude and opposite direction than the resultant force (R).

The maximum steering angle value achieved under this conditions is calculated following the approach in (Cossalter 2006). The equilibrium of moments for a steady turn can be expressed as a good approximation by Eq. C.2.

$$\tan(\phi) = \frac{v^2}{g \cdot r_t} \quad (\text{C.2})$$

v is the forward speed, g is the gravity acceleration and r_t is the turning radius. The effective kinematic steering angle can be approximated by:

$$\Delta = \delta \cdot \frac{\cos(\varepsilon)}{\cos(\phi)} \quad (\text{C.3})$$

Being δ the steering angle and ε the head angle. The turning radius can be approximated using Eq. C.4 where w_b is the motorcycle's wheelbase.

$$r_t = \frac{w_b}{\tan(\Delta)} \quad (\text{C.4})$$

The steering angle is obtained combining Eq. C.2, Eq. C.3, Eq. C.4 as a function of the forward speed and the roll angle:

$$\delta = \tan\left(\frac{w_b \cdot g}{v^2} \cdot \tan(\phi)\right) \cdot \frac{\cos(\phi)}{\cos(\varepsilon)} \quad (\text{C.5})$$

The maximum steering angle is obtained numerically for maximum lean angle ($\phi = 65^\circ$) and minimum forward speed ($v = 10$ m/s) as $\delta = 8.1^\circ$. Finally, the

maximum lateral load is calculated as the projection of the maximum longitudinal load in to the front wheel axis and applied to the fork spindle as:

$$F_l = -R \cdot \sin(\beta - \varepsilon) \cdot \sin(\delta) \quad (\text{C.6})$$

β is the angle between the resultant force and the vertical, ε is the head angle and δ is the steering angle. Figure C.2 shows the motorcycle under cornering conditions where the resultant force (R) and the lateral load (F_l) are presented. For the most demanding case, the maximum lateral load magnitude is $F_l = 492$ N. Adding a safety factor of 50 %, the lateral load taken as the maximum load requirement for the front suspension systems is equal to $F_l = 750$ N.

Smaller and more precise values of the load requirements can be calculated. However, as it has already been mentioned, the scope of this part of the research is not to designing the most efficient front suspension systems but to obtain the dynamical properties of their parts with the certainty that they could be possible candidates to real implementation. With the values calculated here, the reliability of the system is guaranteed whilst the systems' masses can be reduced in comparison to the original telescopic fork suspension system.

Bibliography

- Bakker, E., Pacejka, H. B. & Lidner, L. (1989), A new tire model with an application in vehicle dynamics studies, SAE Technical Paper 890087, SAE International.
- Boresi, A. P. & Schmidt, R. J. (2002), *Advanced Mechanics of Materials*, 6th edn, John Wiley & Sons.
- Brembo (2015), ‘MotoGP Brake Circuit Identity Cards’, **url:** www.motogp.brembo.com. Accessed: 2015-05-25.
- Bultaco Motors (2015), ‘Bultaco’, **url:** www.bultaco.es. Accessed: 2015-05-25.
- Cooper, K. (1974), The effects of aerodynamics on the performance and stability of high speed motorcycles, *in* ‘2nd AIAA Symp. Aerodynamics Sport Competition Automobiles’.
- Cossalter, V. (2006), *Motorcycle Dynamics*, 2nd edn, Lulu.com.
- Cossalter, V., Doria, A., Garbin, S. & Lot, R. (2006), ‘Frequency-domain method for evaluating the ride comfort of a motorcycle’, *Vehicle System Dynamics* **44**(4), pp. 339–355.
- Cossalter, V., Doria, A. & Lot, R. (1999), ‘Steady turning of two-wheeled vehicles’, *Vehicle System Dynamics* **31**(3), pp. 157–181.
- Cossalter, V. & Lot, R. (2002), ‘A motorcycle multi-body model for real time simulations based on the natural coordinates approach’, *Vehicle System Dynamics* **37**(6), pp. 423–447.
- Cossalter, V., Lot, R. & Maggio, F. (2002), The influence of tire properties on the stability of a motorcycle in straight running and curves, SAE Technical Paper 2002-01-1572, SAE International.

- Cossalter, V., Lot, R. & Massaro, M. (2008), ‘The chatter of racing motorcycles’, *Vehicle System Dynamics* **46**(4), pp. 339–353.
- Creuat (2015), ‘Hydropneumatic suspension systems LTT - Creuat’, **url:** www.lleidatracciotechnology.com/suspensions.php. Accessed: 2015-05-25.
- Dassault Systems (2015), ‘SolidWorks’, **url:** www.solidworks.com. Accessed: 2015-05-25.
- de Vries, E. & Pacejka, H. (1998), ‘Motorcycle tyre measurements and models’, *Vehicle System Dynamics* **29**, pp. 280–298.
- Evangelou, S. (2003), The control and stability analysis of two-wheeled road vehicles, PhD thesis, University of London.
- Evangelou, S. (2010), Control of motorcycles by variable geometry rear suspension, *in* ‘2010 IEEE International Conference on Control Applications (CCA)’, pp. 148–154.
- Evangelou, S. A., Limebeer, D. J. N. & Tomas-Rodriguez, M. (2012), ‘Suppression of burst oscillations in racing motorcycles’, *Journal of Applied Mechanics* **80**(1), pp. 011003–011016.
- Evangelou, S., Limebeer, D. J. N., Sharp, R. S. & Smith, M. C. (2006), ‘Mechanical steering compensators for high-performance motorcycles’, *Journal of Applied Mechanics* **74**(2), pp. 332–346.
- Evangelou, S., Limebeer, D. J. & Tomas Rodriguez, M. (2008), ‘Influence of road camber on motorcycle stability’, *Journal of Applied Mechanics* **75**(6), pp. 061020–061020.
- Evangelou, S., Limebeer, D. & Tomas-Rodriguez, M. (2010), Suppression of burst oscillations in racing motorcycles, *in* ‘2010 49th IEEE Conference on Decision and Control (CDC)’, pp. 5578–5585.
- Fontdecaba i Buj, J. (2002), Integral suspension system for motor vehicles based on passive components, SAE Technical Paper 2002-01-3105, SAE International.

- Fujioka, T. & Goda, K. (1995), ‘Tire cornering properties at large camber angles: mechanism of the moment around the vertical axis’, *JSAE Review* **16**(3), pp. 257–261.
- García-Fernández, P., Gutiérrez de Quevedo, J., Moreno-Ramírez, C. & Fernández del Rincón, A. (2014), Simulation tool for motorbike prototype design, *in* ‘New Advances in Mechanisms, Transmissions and Applications’, number 17 *in* ‘Mechanisms and Machine Science’, Springer Netherlands, pp. 17–24.
- Giles, C. G. & Sharp, R. S. (1983), Static and dynamic stiffness and deflection mode measurements on a motorcycle, with particular reference to steering behaviour, *in* ‘Proc. Inst. Mech. Eng./MIRA Conference on Road Vehicle Handling’, pp. 185–192.
- Gillespie, T. D. (1992), *Fundamentals of Vehicle Dynamics*, SAE International.
- Griffiths, A. (2008), ‘Suspension systems’. EP Patent 1,572,524.
- Griffiths, A. (2015), ‘Mountain bike suspension design constraints, solutions and opportunities’, **url:** www.toptrail.co.uk/docs/MB_suspension_technical_paper_050606.pdf. Accessed: 2015-05-25.
- Hand, R. (1988), Comparisons and stability analysis of linearized equations of motion for a basic bicycle model, MSc Thesis, Cornell University.
- Jennings, G. (1974), A study of motorcycle suspension damping characteristics, Technical Report 740628, SAE International, Warrendale, PA.
- Kane, T. R. & Levinson, D. A. (1983), ‘Multibody Dynamics’, *Transactions of the ASME, Journal of Applied Mechanics* **50**(4b), pp. 1071–1078.
- Kane, T. R. & Levinson, D. A. (1985), *Dynamics: theory and applications*, Series in Mechanical Engineering, McGraw-Hill.
- Koenen, C. (1983), The dynamic behaviour of motorcycles when running straight ahead and when cornering, PhD thesis, Delft University of Technology.
- Koenen, C. & Pacejka, H. B. (1982), The influence of frame elasticity, simple rider body dynamics and tyre moments on free vibrations of motorcycles in curves, *in*

- ‘Proceedings of the 7th IAVSD Symposium on the Dynamics of Vehicles on Roads and Tracks’, pp. 53–65.
- Koenen, K. & Pacejka, H. B. (1980), Vibrational modes of motorcycles in curves, *in* ‘International Motorcycle Safety Conference Proceedings’, Vol. 2, pp. 501–544.
- Limebeer, D. J. N., Sharp, R. S. & Evangelou, S. (2001), ‘The stability of motorcycles under acceleration and braking’, *Journal of Mechanical Engineering Science* **215**(9), pp. 1095–1109.
- Limebeer, D. J. N., Sharp, R. S. & Evangelou, S. (2002), ‘Motorcycle steering oscillations due to road profiling’, *Transactions of the ASME, Journal of Applied Mechanics* **69**(6), pp. 724–739.
- Limebeer, D. J. & Sharp, R. S. (2006), ‘Bicycles, motorcycles, and models’, *IEEE Control Systems Magazine* **26**(5), pp. 34–61.
- Mavroudakos, B. & Eberhard, P. (2006), ‘Analysis of alternative front suspension systems for motorcycles’, *Vehicle System Dynamics* **44**, pp. 679–689.
- Mechanical Simulation Corporation (2015), ‘Vehiclesim technology’, **url**: www.carsim.com. Accessed: 2015-05-25.
- Meijaard, J. P., Papadopoulos, J. M., Ruina, A. & Schwab, A. L. (2007), ‘Linearized dynamics equations for the balance and steer of a bicycle: a benchmark and review’, *Proceedings of the Royal Society of London A: Mathematical, Physical and Engineering Sciences* **463**(2084), pp. 1955–1982.
- Moreno-Ramírez, C., García-Fernández, P., de Juan, A. & Tomas-Rodríguez, M. (2014), Interconnected suspension system on sport motorcycles, *in* ‘New Advances in Mechanisms, Transmissions and Applications’, number 17 *in* ‘Mechanisms and Machine Science’, Springer Netherlands, pp. 9–16.
- Moreno-Ramírez, C. & Tomas-Rodríguez, M. (2014), Nonlinear optimization of a sport motorcycle’s suspension interconnection system, *in* ‘2014 UKACC International Conference on Control (CONTROL)’, pp. 319–324.

- Moreno-Ramírez, C., Tomas-Rodríguez, M. & Evangelou, S. (2012*a*), Dynamical analysis of a duolever suspension system, *in* ‘2012 UKACC International Conference on Control (CONTROL)’, pp. 1106–1111.
- Moreno-Ramírez, C., Tomas-Rodríguez, M. & Evangelou, S. A. (2011), Efecto de una suspensin hossack en la estabilidad de motocicletas de carreras, *in* ‘Actas de XXXII Jornadas de Automática’.
- Moreno-Ramírez, C., Tomas-Rodríguez, M. & Evangelou, S. A. (2012*b*), Analisis dinamico y modelado de suspensiones hossack en motocicletas de competición, *in* ‘Actas de XXXIII Jornadas de Automática’, pp. 621–628.
- MotoGP (2015), ‘The Lean Angle Experience’, **url**: www.motogp.com. Accessed: 2015-05-25.
- Nishimi, T., Aoki, A. & Katayama, T. (1985), Analysis of straight running stability of motorcycles, SAE Technical Paper 856124, SAE International.
- Pacejka, H. B. (2002), *Tire and Vehicle Dynamics*, 2nd revised edn, Elsevier.
- Pacejka, H. B. & Bakker, E. (1992), ‘The magic formula tyre model’, *Vehicle System Dynamics* **21**, pp. 1–18.
- Pacejka, H. B. & Besselink, I. J. M. (1997), ‘Magic formula tyre model with transient properties’, *Vehicle System Dynamics* **27**, pp. 234–249.
- Pacejka, H. B. & Sharp, R. S. (1991), ‘Shear force development by pneumatic tyres in steady state conditions: A review of modelling aspects’, *Vehicle System Dynamics* **20**(3-4), pp. 121–175.
- Rae, R. (2010), ‘Connected suspension for two-wheeled vehicles, namely bicycles and motorcycles’. WO Patent App. PCT/IE2009/000,063.
- RaerDesign (2015), ‘Raer Design’, **url**: www.raerdesign.com. Accessed: 2015-05-25.
- Rankine, W. (1869), ‘On the dynamical principles of the motion of velocipedes’, *The Engineer* pp. pp. 79–175.

- Roe, G. E. & Thorpe, T. E. (1976), ‘A solution of the low-speed wheel flutter instability in motorcycles’, *Journal of Mechanical Engineering Science* **18**(2), pp. 57–65.
- Routh, G. R. R. (1899), ‘The motion of a bicycle’, *The Messenger of Mathematics* **28**, pp. 151–169.
- Sayers, M. W. (1991), ‘Symbolic vector/dyadic multibody formalism for tree-topology systems’, *Journal of Guidance, Control, and Dynamics* **14**(6), pp. 1240–1250.
- Shaeri, A., Limebeer, D. J. N. & Sharp, R. S. (2004), Nonlinear steering oscillations of motorcycles, *in* ‘Decision and Control, 2004. CDC. 43rd IEEE Conference on’, Vol. 1, pp. 773–778 Vol.1.
- Sharp, R. S. (1971), ‘The stability and control of motorcycles’, *Journal of Mechanical Engineering Science* **13**(5), pp. 316–329.
- Sharp, R. S. (1974), ‘The influence of frame flexibility on the lateral stability of motorcycles’, *Journal of Mechanical Engineering Science* **16**(2), pp. 117–120.
- Sharp, R. S. (1976*a*), ‘The influence of the suspension system on motorcycle weave-mode oscillations’, *Vehicle System Dynamics* **5**(3), pp. 147–154.
- Sharp, R. S. (1976*b*), The stability of motorcycles in acceleration and deceleration, *in* ‘Conference Proceeding on Braking of Road Vehicles’, Inst. Mech. Eng., pp. 45–50.
- Sharp, R. S. (1992), ‘Tyre structural mechanisms influencing shear force generation: Ideas from a multi-radial-spoke model’, *Vehicle System Dynamics* **21**, pp. 145–155.
- Sharp, R. S. (1994), ‘The application of multi-body computer codes to road vehicle dynamics modelling problems’, *Proceedings of the Institution of Mechanical Engineers, Part D: Journal of Automobile Engineering* **208**(1), pp. 55–61.
- Sharp, R. S. (2000), Variable geometry active rear suspension for motorcycles, *in* ‘Proc. of the 5th International Symposium on Automotive Control (AVEC 2000).’, pp. 585–592.

- Sharp, R. S. (2001), ‘Stability, control and steering responses of motorcycles’, *Vehicle System Dynamics* **35**(45), pp. 291–318.
- Sharp, R. S. (2002), ‘Wheelbase filtering and automobile suspension tuning for minimizing motions in pitch’, *Proceedings of the Institution of Mechanical Engineers, Part D: Journal of Automobile Engineering* **216**(12), pp. 933–946.
- Sharp, R. S. (2007), ‘Motorcycle steering control by road preview’, *Journal of Dynamic Systems, Measurement, and Control* **129**(4), pp. 373–382.
- Sharp, R. S. (2012), ‘Rider control of a motorcycle near to its cornering limits’, *Vehicle System Dynamics* **50**(8), pp. 1–16.
- Sharp, R. S. & Alstead, C. J. (1980), ‘The influence of structural flexibilities on the straight-running stability of motorcycles’, *Vehicle System Dynamics* **9**(6), pp. 327–357.
- Sharp, R. S. & El-Nashar, M. A. (1986), ‘A generally applicable digital computer based mathematical model for the generation of shear forces by pneumatic tyres’, *Vehicle System Dynamics* **15**(4), pp. 187–209.
- Sharp, R. S., Evangelou, S. & Limebeer, D. J. N. (2004), ‘Advances in the modelling of motorcycle dynamics’, *Multibody System Dynamics* **12**(3), pp. 251–283.
- Sharp, R. S. & Jones, C. J. (1977), ‘The straight-running stability of single track vehicles’, *Vehicle System Dynamics* **6**(2-3), pp. 190–191.
- Sharp, R. S. & Limebeer, D. J. N. (2001), ‘A motorcycle model for stability and control analysis’, *Multibody System Dynamics* **6**(2), pp. 123–142.
- Smith, M. (2002), ‘Synthesis of mechanical networks: the inerter’, *IEEE Transactions on Automatic Control* **47**(10), pp. 1648–1662.
- Splerings, P. T. J. (1981), ‘The effects of lateral front fork flexibility on the vibrational modes of straight-running single-track vehicles’, *Vehicle System Dynamics* **10**(1), pp. 21–35.
- Steele, G. L. (1990), *Common LISP: The Language*, Digital Press.

- Tempelaars, S. (1996), *Signal Processing, Speech and Music*, Routledge.
- Tezuka, Y., Ishii, H. & Kiyota, S. (2001), ‘Application of the magic formula tire model to motorcycle maneuverability analysis’, *JSAE Review* **22**(3), pp. 305–310.
- Toptrail (2015), ‘The Toptrail interconnected suspension bicycle project’, **url**: www.toptrail.co.uk. Accessed: 2015-05-25.
- Watanabe, Y. & Sayers, M. W. (2011), The effect of nonlinear suspension kinematics on the simulated pitching and cornering behavior of motorcycles, SAE Technical Paper 2011-01-0960, SAE International.
- Weir, D. H. & Zellner, J. W. (1979), Experimental investigation of the transient behavior of motorcycles, SAE Technical Paper 790266, SAE International.
- Whipple, F. (1899), ‘The stability of the motion of a bicycle’, *Quarterly Journal of Pure and Applied Mathematics* **30**, pp. 312–348.